

# A CENTER OF COMPETENCE IN SOLID STATE MATERIALS AND DEVICES

by

Fred A. Lindholm, Arthur J. Brodersen, Eugene R. Chenette,  
• Stephen W. Director, Larry L. Hench, Sheng S. Li  
Aldert van der Ziel



Electrical Engineering Department  
College of Engineering  
University of Florida  
Gainesville, Florida 32601

Contract No. F 19628-68-C-0058

Project No. 8687

Scientific Report No. 7

10 March 1971

Contract Monitor  
Andrew C. Yang  
Solid State Sciences Laboratory

This document has been approved for public  
release and sale; its distribution is unlimited.

Sponsored by

Advanced Research Projects Agency  
ARPA Order No. 1060

Monitored by

Air Force Cambridge Research Laboratories  
AIR FORCE SYSTEMS COMMAND  
United States Air Force  
Bedford, Massachusetts 01730

Reproduced by  
NATIONAL TECHNICAL  
INFORMATION SERVICE  
Springfield, Va. 22151



**BEST  
AVAILABLE COPY**

## DOCUMENT CONTROL DATA - R&amp;D

(Security classification of title, body of abstract and indexing annotation must be entered when the overall report is classified)

1. ORIGINATING ACTIVITY (Corporate author) University of Florida Engineering and Industrial Experiment Station Gainesville, Florida 32601		2a. REPORT SECURITY CLASSIFICATION Unclassified	
		2b. GROUP	
3. REPORT TITLE  A CENTER OF COMPETENCE IN SOLID STATE MATERIALS AND DEVICES			
4. DESCRIPTIVE NOTES (Type of report and inclusive dates) Scientific Interim			
5. AUTHOR(S) (First name, middle initial, last name) Fred A. Lindholm                      Stephen W. Director Arthur J. Brodersen                  Larry L. Hench                      Aldert van der Ziel Eugene R. Chenette                  Sheng S. Li			
6. REPORT DATE 10 March 1971		7a. TOTAL NO. OF PAGES 223	7b. NO. OF REFS 199
8a. CONTRACT OR GRANT NO. F 19628-68-C-0058 ARPA Order No.		8a. ORIGINATOR'S REPORT NUMBER(S) Scientific Report No. 7	
b. PROJECT, TASK, WORK UNIT NOS. 8687      n/a      n/a      1060			
c. DOD ELEMENT 61101D		9b. OTHER REPORT NO(S) (Any other numbers that may be assigned this report) AFCRL-71-0309	
d. DOD SUBELEMENT n/a			
10. DISTRIBUTION STATEMENT 1 - This document has been approved for public release and sale; its distribution is unlimited.			
11. SUPPLEMENTARY NOTES This research was supported by Advanced Research Projects Agency		12. SPONSORING MILITARY ACTIVITY Air Force Cambridge Research Laboratories (I&Q) L. G. Hanscom Field Bedford, Massachusetts 01730	
13. ABSTRACT : In semiconductor and semiconductor device research, a complete equivalent circuit for the noise performance of phototransistors is developed and the current gain and cutoff frequency are derived from noise measurements. Study of the design of a detector using the PME effect in gold-doped silicon shows the compromises required in the concentrations of gold and shallow-level impurities to yield both speed and sensitivity. Measurement of conductivity and Hall effect in In-doped and Cu-doped CdS reveals the impurity levels and dominant scattering mechanisms. Measurement of the PME and PC effects in gold-doped silicon yields the recombination parameters. A method is described that so selects model complexity in the simulation of transistor circuits as to save cpu time and to accommodate larger circuits than heretofore possible. In glass and semiconducting glass research, experiments demonstrate that crystallite size determines the threshold of fast-neutron damage in heterogeneous amorphous semiconductors. Various methods for surface characterization of ceramic powders are detailed. A computer program is described that calculates and plots pertinent behavior of electronic ceramic materials based on humidity-dependent dielectric data.			

Unclassified

Security Classification

14.	KEY WORDS	LINK A		LINK B		LINK C	
		ROLE	WT	ROLE	WT	ROLE	WT
	semiconductors semiconducting glasses phototransistors irradiation properties transistor models						

Unclassified

Security Classification

Program Code No. ....1D10  
Effective Date of Contract ..... 11 September 1967  
Contract Expiration Date ..... 31 August 1972  
Principal Investigator and Phone No. .... Dr. Fred A. Lindholm/904/392-0904  
Project Scientist or Engineer and Phone No. .... Dr. Andrew C. Yang/617/861-2225

Qualified requestors may obtain additional copies from the  
Defense Documentation Center. All others should apply to the  
National Technical Information Service.

10/21/71

WHITE SECTION		<input checked="" type="checkbox"/>
BREF SECTION		<input type="checkbox"/>
UNCLASSIFIED		<input type="checkbox"/>
INVESTIGATION		
BY		
DISTRIBUTION/AVAILABILITY CODES		
DIST.	AVAIL. CODE	SPECIAL
A		

AFCRL-71-0309

## **A CENTER OF COMPETENCE IN SOLID STATE MATERIALS AND DEVICES**

by  
Fred A. Lindholm, Arthur J. Brodersen, Eugene R. Chenette,  
Stephen W. Director, Larry L. Hench, Sheng S. Li  
Aldert van der Ziel

Electrical Engineering Department  
College of Engineering  
University of Florida  
Gainesville, Florida 32601

Contract No. F 19628-68-C-0058

Project No. 8687

**Scientific Report No. 7**

10 March 1971

Contract Monitor  
Andrew C. Yang  
Solid State Sciences Laboratory

This document has been approved for public  
release and sale; its distribution is unlimited.

Sponsored by  
Advanced Research Projects Agency  
ARPA Order No. 1060

Monitored by  
Air Force Cambridge Research Laboratories  
**AIR FORCE SYSTEMS COMMAND**  
United States Air Force  
Bedford, Massachusetts 01730

Program Code No. . . . . ID10  
Effective Date of Contract . . . . . 11 September 1967  
Contract Expiration Date . . . . . 31 August 1972  
Principal Investigator and Phone No. . . . . Dr. Fred A. Lindholm/904/392-0904  
Project Scientist or Engineer and Phone No. . . . . Dr. Andrew C. Yang/617/861-2225

Qualified requestors may obtain additional copies from the  
Defense Documentation Center. All others should apply to the  
National Technical Information Service.

## ABSTRACT

In semiconductor and semiconductor device research, a complete equivalent circuit for the noise performance of phototransistors is developed and the current gain and cutoff frequency are derived from noise measurements. Study of the design of a detector using the PME effect in gold-doped silicon shows the compromises required in the concentrations of gold and shallow-level impurities to yield both speed and sensitivity. Measurement of conductivity and Hall effect in In-doped and Cu-doped CdS reveals the impurity levels and dominant scattering mechanisms. Measurement of the PME and PC effects in gold-doped silicon yields the recombination parameters. A method is described that so selects model complexity in the simulation of transistor circuits as to save cpu time and to accommodate larger circuits than heretofore possible. In glass and semiconducting glass research, experiments demonstrate that crystallite size determines the threshold of fast-neutron damage in heterogeneous amorphous semiconductors. Various methods for surface characterization of ceramic powders are detailed. A computer program is described that calculates and plots pertinent behavior of electronic ceramic materials based on humidity-dependent dielectric data.



## SUMMARY

This report for the seventh semiannual period of contract support describes technical findings in two main subject areas: semiconductors and semiconductor devices, and insulating and semiconducting glasses.

### SEMICONDUCTORS AND SEMICONDUCTOR DEVICES:

Analytical and experimental results are reported on the noise performance of phototransistors. The noise performance of phototransistors depends on fluctuations traceable to two main sources: (a) the random fluctuations in the rate of photon arrival; and (b) mechanisms inherent in the device such as fluctuations in the generation of free carriers, diffusion and recombination fluctuations, and  $1/f$  mechanisms, to cite a few. On the basis of corpuscular arguments, it is shown that the important fluctuations may be represented by simple, partially-correlated, shot noise generators in parallel with the device junctions for a wide range of frequencies. Use of the hybrid- $\pi$  transistor model together with these noise generators yields expressions for the noise current at the short-circuited output of a phototransistor. Attention has focussed primarily on the low-frequency expression for noise since correction terms due to high-frequency effects are negligible. The output noise spectra of commercially available silicon phototransistors and of silicon units fabricated at the Microelectronics Laboratory of the University of Florida have been measured. The measurements agree well with the predictions of the model. The current gains and Beta cut-off frequencies of these devices have been computed by interpreting the noise spectra with the aid of the analytical results. Independent ac and dc measurements of these noise parameters agree satisfactorily with values determined from noise measurements. This demonstrates, therefore, that noise measurements on phototransistors can be used to characterize the current gain and Beta cut-off frequency.

We describe considerations pertinent to the design of a fast solid-state light detector using the photomagnetolectric effect in gold-doped silicon. One desirable attribute of such a device is that it would be very economical to fabricate using modern silicon technology. Our study demonstrated the compromises relevant to the design of such a detector. For cells with high internal resistance the speed is low while the sensitivity is high. Conversely, samples with low internal resistance show much higher speed but lower sensitivity. The construction of a detector with considerable sensitivity and speed requires that a compromise be made between the doping concentrations of gold and the shallow

donor impurities in the silicon host material.

Electrical conductivity and Hall effect measurements have been made on In-doped and Cu-doped CdS single crystals between the temperatures: 300°K and 4.2°K. To interpret the empirical observations we make use of an energy-band model containing two impurity levels. This yields conclusions regarding the dominant scattering mechanisms and the energy levels of the impurity states.

Measurements of the photomagnetoelectric and photoconductive effects in thin gold-doped silicon are reported. In contrast to previous work the measurements made here are reported for room temperature. From the data we determine recombination parameters such as electron and hole lifetimes and the electron and hole capture probabilities associated with the gold levels. The results obtained agree well with experimental data available in the literature determined from Hall effect, photoconductivity decay and photovoltaic effect experiments.

A method is described that selects, for each transistor in a circuit, the model of least complexity that will give acceptable accuracy. At the heart of the method is the capability to assess model adequacy. This capability derives from a self-consistency test in which the values of currents and voltages computed in the simulation of the circuit behavior are compared with onset parameters. By this comparison one determines whether these computed values are consistent with the approximations underlying the device models used in the simulation. The onset parameters for a model are the terminal currents and voltages beyond which the model fails to give a satisfactory representation of device behavior. We set forth the onset parameters for the Ebers-Moll model and discuss their determination by terminal measurement and by calculation based on the transistor make-up. To illustrate the method of model assessment we simulate the performance of an operational amplifier. The effectiveness of the method in selecting model complexity is demonstrated.

The addition of a single parameter, termed the Early voltage, enables incorporation of the Early effect (base-width modulation) in the Ebers-Moll model for the large-signal static behavior of transistors. The consequent voltage dependences of collector current, common-emitter current gain, and small-signal output conductance are set forth.

#### INSULATING AND SEMICONDUCTING GLASSES:

The unique range of properties exhibited by both insulating glass-ceramics

and amorphous semiconductors makes them potentially useful in a variety of applications which may involve exposure to nuclear irradiation. We demonstrate here the importance of crystallite size on the fast neutron damage threshold in heterogeneous amorphous semiconductors. Electrical properties of heterogeneous glasses governed by sub-micron crystals suffer fast neutron damage at fluences of  $1-2 \times 10^{17}$  nvt. The size of the crystals influences the damage threshold. Ionizing radiation produces electronic complications in addition to the neutron-related structural changes that occur in semiconducting glasses.

Analyzing the surface properties of ceramic powders is one of the most important and most difficult procedures in the field of ceramics. A comprehensive study is reported of various direct and indirect methods for surface characterization. A series of studies is suggested to enable the development of a structural theory of ceramic surfaces. Such a theory can be used to yield understanding of the changes in behavior associated with the handling and wet or dry processing of ceramic powders.

In an earlier report in this series we demonstrated the severe dependence borne between humidity and the electric and dielectric properties of electronic substrates, insulators, radomes and other electronic ceramic materials. Analysis of humidity-dependent dielectric data is extremely time-consuming. We describe here a computer program that will calculate and plot material behavior based on the humidity-dependent dielectric data.

## TABLE OF CONTENTS

	<u>Page</u>
I. <u>Introduction</u>	1
II. <u>Semiconductors and Semiconductor Devices</u> (A. J. Brodersen E. R. Chenette, S. W. Director, S. S. Li, F. A. Lindholm, A. van der Ziel)	2
A. NOISE IN PHOTOTRANSISTORS (F. De La Moneda, E. R. Chenette, A. van der Ziel)	2
Introduction	3
Phototransistor Operation	4
Noise Characterization	7
Collector-Base Photodiode Noise Current	7
Output Noise Current	8
Noise Equivalent Power	12
Experimental Results	13
Conclusions	15
Appendix	16
References	20
B. A FAST SOLID-STATE PME LIGHT DETECTOR USING AU-DOPED SILICON (S. S. Li and H. F. Tseng)	34
Introduction	34
Theoretical Aspect of the Photomagnetolectric Effect	34
Analysis of a PME Detector	36
Effect of surface treatment on the sensitivity of the PME voltage	36
Response time ( $\tau_r$ )	36
Sample internal resistance and capacitance	37
Noise consideration	38
Results and Discussion	40
References	42
C. ELECTRON MOBILITY AND SHALLOW IMPURITY LEVELS IN In-DOPED AND Cu-DOPED CdS (S. S. Li and C. I. Huang)	50
Introduction	50
Experimental Details	51
Results and Analysis	52
Single-Donor Level Model for In-doped CdS	52
Two-Donor-Level Model for In-doped CdS	53
Conclusions	55
References	56

	<u>Page</u>
II. Cont.	
D. STUDY OF ROOM TEMPERATURE PHOTOMAGNETOELECTRIC AND PHOTOCONDUCTIVE EFFECTS IN Au-DOPED SILICON (S. S. Li and H. F. Tseng)	60
Introduction	60
Theory	60
Excess Carrier Lifetimes and the Ratio of Excess Carrier Density	61
The Photomagnetolectric and Photoconductive Effects	64
Results and Analysis	66
Conclusions	68
References	69
E. ASSESSING MODEL ADEQUACY AND SELECTING MODEL COMPLEXITY IN INTEGRATED-CIRCUIT SIMULATION (F. A. Lindholm, S. W. Director, D. L. Bowler)	77
Introduction	77
The Method	79
Onset Parameters for the Ebers-Moll Model	81
Onset Parameters for Emitter Crowding	82
Onset Parameter for High Injection in the Base	85
Space-Charge-Limited Flow in the Collector	86
Onset Parameter for Voltage Breakdown	89
Illustrative Example	89
Discussion	91
References	93
F. INCORPORATION OF THE EARLY EFFECT IN THE EBERS-MOLL MODEL (F. A. Lindholm)	103
References	105
III. <u>Insulating and Semiconducting Glasses</u> (L. L. Hench, R. W. Gould)	108
A. FAST NEUTRON EFFECTS IN GLASS-CERAMICS AND AMORPHOUS SEMICONDUCTORS (L. L. Hench, W. D. Tuohig and A. E. Clark)	108
Introduction	108
Experimental Procedure	109
V <sub>2</sub> O <sub>5</sub> -P <sub>2</sub> O <sub>5</sub> Amorphous Semiconductors	111
Partially Crystallized Semiconducting Glasses	113
Li <sub>2</sub> O-SiO <sub>2</sub> Glass-Ceramics	114
Conclusions	116
References	117

III. Cont.	<u>Page</u>
B. CHARACTERIZATION OF POWDER SURFACES (L. L. Hench)	123
Introduction	123
Direct Means of Characterization	124
Indirect Means of Characterization	125
Surface Forces	126
Long range interactions	129
Surface charges in liquids	131
Surface Energy	134
Surface Structure	141
Powder-Liquid Interface Techniques	142
Electrophoresis	142
Sedimentation Potential	143
Electroosmosis	143
Shearing Potential	144
Powder-Gas Interface Techniques	144
Types of Adsorption	145
Langmuir Model	146
Multilayer Models	149
Applications	154
Dielectric techniques	156
Conclusions	156
References	157
C. DIELECTRICS COMPUTING PROGRAMS (G. J. Scott and L. L. Hench)	186
Introduction	186
IV. <u>Discussion</u>	216

**BLANK PAGE**

## I. Introduction

The original general objective of this research program was to establish at the University of Florida a "Center of Competence in Solid State Materials and Devices." From the efforts expended in developing this center of competence have evolved technical findings: technical findings concerning such materials as glass ceramics, semiconducting glasses, magnetic films, degenerate materials and degenerate semiconductors; concerning devices made from these materials; concerning measurement techniques; and concerning methods of fabrication. The first of the findings in these various areas are described in six previous scientific reports<sup>1-6</sup>. To Scientific Report No. 1 the reader is referred for a more detailed statement of the research objectives than given here and for a discussion of the means to be used in achieving these objectives. The present report sets forth major findings of the seventh semiannual period of contract support. In the presentation to follow, Section II describes the results of research concerning semiconductors and semiconductor devices, and Section III reports findings concerned with insulating and semiconducting glasses.

## REFERENCES

1. F. A. Lindholm et al, Scientific Report No. 1, Contract #F 19628-68-C-0058, College of Engineering, University of Florida, 10 April 1968.
2. F. A. Lindholm et al, Scientific Report No. 2, Contract #F 19628-68-C-0058, College of Engineering, University of Florida, 10 October 1968.
3. F. A. Lindholm et al, Scientific Report No. 3, Contract #F 19628-68-C-0058, College of Engineering, University of Florida, 10 April 1969.
4. F. A. Lindholm et al, Scientific Report No. 4, Contract #F 19628-68-C-0058, College of Engineering, University of Florida, 10 October 1969.
5. F. A. Lindholm et al, Scientific Report No. 5, Contract #F 19628-68-C-0058, College of Engineering, University of Florida, 10 April 1970.
6. F. A. Lindholm et al, Scientific Report No. 6, Contract #F 19628-68-C-0058, College of Engineering, University of Florida, 10 October 1970.



II. Semiconductors and Semiconductor Devices (A. J. Brodersen, E. R. Chenette, S. W. Director, S. S. Li, F. A. Lindholm, A. van der Ziel)

A. NOISE IN PHOTOTRANSISTORS (F. H. De La Moneda, E. R. Chenette, A. van der Ziel)

The phototransistor was first suggested in 1951 by Shockley, Sparks, and Teal [1] as a variation on the "hook" transistor. It was relatively unimportant until recently when considerations of cost, size, reliability and the planar semiconductor technology have catapulted it into a prominent position in the image sensing area.

Several studies on characterization of phototransistors [2], [3] and their modes of operation [4] have been published recently. The problem of noise in these devices was treated by Daughters [5] who estimated the output noise current. His analysis was brief and no attempt was made to correlate it with his experimental data. It is the purpose of this paper to examine analytically and experimentally the noise performance of phototransistors. The results will establish the fundamental limit to the usefulness of a phototransistor as a radiation detector and amplifier. In addition, it will be shown that noise measurements on phototransistors can be used to characterize them, a particularly useful technique since often the base lead of the device is not available for normal small signal measurements.

Expression for the d.c. currents flowing across the emitter and collector junctions are derived. These expressions are then used to obtain the corresponding shot noise generators which are located in parallel with the device junctions. From these generators, a phototransistor noise model is set up. Using this model, an expression for the output noise current is obtained. The analytical development concludes with the derivation of the noise equivalent power. Finally, spectra for the output noise covering a wide frequency range and operating currents are presented. These data are interpreted with the aid of the analytical results.

a.c. and d.c. measurements of these parameters are in satisfactory agreement with values determined from noise measurements. It is thereby ascertained that noise measurements on phototransistors can be used to characterize them in terms of current gain and beta cut-off frequency.

## I. Introduction

The phototransistor was first suggested in 1951 by Shockley, Sparks, and Teal [1] as a variation on the "hook" transistor. It stayed in a dormant state until recently when considerations of cost, size, reliability and the planar semiconductor technology have catapulted it into a prominent position in the imaging sensing area.

Several studies on characterization of phototransistors [2], [3] and their modes of operation [4] have been published recently. The problem of noise in these devices was treated by Daughters [5] who estimated the output noise current. His analysis was brief and no attempt was made to correlate it with his experimental data. It is the purpose of this paper to examine analytically and experimentally the noise performance of phototransistors. The results will establish the fundamental limit to the usefulness of a phototransistor as a radiation detector and amplifier. In addition, it will be shown that noise measurements on phototransistors can be used to characterize them, a particularly useful technique since often the base lead of the device is not available for normal small signal measurements.

Expressions for the d.c. currents flowing across the emitter and collector junctions are derived. These expressions are then used to obtain the corresponding shot noise generators which are located across the device junctions. From these generators, a phototransistor noise model is set up. Using this model, an expression for the output noise current is obtained. The analytical development concludes with the derivation of the noise equivalent power. Finally, spectra for the output noise covering a wide frequency range and operating currents are presented. This data is interpreted with the aid of the analytical results.

## II. Phototransistor Operation

Irradiation of the top surface of the planar phototransistor shown in Fig. 1 by a uniform photon flux density,  $F(\nu)$ , causes generation of excess electron-hole pairs throughout the whole device. Therefore, both junctions act as photodiodes. To achieve good phototransistor performance, it is desired to suppress the photogenerated leakage current flowing across the emitter-base junction. In practice, this is accomplished by making the emitter area relatively small in comparison with the collector area. Reflection and absorption of the incoming radiation by the emitter metal contact also helps to relegate the emitter-base junction to a secondary role as a photodiode. Consequently, in what follows only the collector-base photodiode will be taken into account and the phototransistor will be regarded as a photodiode in parallel with the collector-base junction of a conventional transistor. This modeling is shown in Fig 2.

Excess electron-hole pairs are continuously generated on both sides of the collector-base photodiode. The excess majority carriers stay in their corresponding side of the junction whereas the excess minority carriers within one diffusion length of the junction edge glide over to the opposite side of the collector-base junction giving rise to the photogenerated current  $I_{PH}$  as illustrated in Fig. 1.  $I_{PH}$  is then a majority carrier current and flows in the same direction as the thermogenerated leakage current,  $I_{3C}$ .  $I_{PH}$  is related to  $F(\nu)$  through the quantum efficiency  $\eta_{PTD}$ . The relationship is [2]

$$I_{PH} = \eta_{PTD}(\nu)F(\nu)A_b \quad (1)$$

The incoming radiation,  $F(\nu)$ , then increases the collector-base leakage current from its dark value,  $I_{3C}$ , to  $(I_{PH} + I_{3C})$ . Since the net base current is zero, this majority carrier current must be

compensated by injection of minority carriers by the emitter-base junction otherwise charge neutrality is not maintained in the base region. It is then clear that  $(I_{PH} + I_{BC})$  play the role of a current source which keeps the emitter-base junction forward biased.

Minority carriers are not only injected from emitter to base but also from base to emitter. It is convenient to introduce the familiar concept of emitter efficiency,  $\gamma_N$ , to relate the resulting diffusion currents. In addition, there is also a leakage current. Reddi [6] has analytically and experimentally shown that recombination through a single level generation-recombination center explains the behaviour of the leakage component of the emitter current. Usually, this component is represented by means of a diode with a non-ideal exponential dependence. For moderate levels of operation, the total emitter current is

$$I_E = \frac{I_D}{\gamma_N} \exp (q V_{BE} / kT) + I_{ET} \exp (q V_{BE} / m' kT) \quad (2)$$

where  $m' \neq 1$ .

The collector current is composed of the current  $(I_{PH} + I_{BC})$  plus the fraction  $\alpha_F$  of the current injected by the emitter reaching the collector.

$$I_C = \alpha_F I_D \exp (q V_{BE} / kT) + (I_{PH} + I_{BC}) \quad (3)$$

The net base current must be zero. This constraint and Eqs. (2) and (3) yield

$$\frac{I_D}{\gamma_N} \exp (q V_{BE} / kT) = \frac{(I_{PH} + I_{BC}) - I_{ET} \exp (q V_{BE} / kT)}{(1 - \gamma_N \alpha_F)} \quad (4)$$

This expression clearly shows how the forward bias of the emitter junction is controlled by  $I_{PH}$ . Substituting Eq. (4) into Eq. (3) yields an

expression for the output current,  $I_{CEO}$ , as a function of  $I_{PH}$ . The subscript here indicates that  $I_C = I_E = I_{CEO}$  with the base floating

$$I_{CEO} = \frac{I}{1 - \gamma_N \alpha_F} \cdot \left[ (I_{PH} + I_{BC}) - \gamma_N \alpha_F I_{ET} \exp( q V_{BE} / m' kT) \right] \quad (5)$$

It has already been pointed out, that  $(I_{PH} + I_{BC})$  play the role of a base current source. Hence, by rearranging Eq. (5) to yield the ratio  $I_{CEO} / (I_{PH} + I_{BC})$ , the current gain of the phototransistor,  $(h_{FE} + 1)$ , is obtained.

$$(h_{FE} + 1)^{-1} = (1 - \gamma_N \alpha_F) - \frac{\gamma_N \alpha_F I_{ET} \exp( q V_{BE} / m' kT)}{I_{CEO}} \quad (6)$$

This last expression indicates the dependence of  $h_{FE}$  on current bias due to emitter leakage. It is well known that due to this dependence, the incremental current gain,  $h_{fe}$ , is larger than  $h_{FE}$ . This observation will become relevant when the noise experiments on phototransistors are discussed later.

From the definition of  $(h_{FE} + 1)$  and Eq. (1), the output current  $I_{CEO}$  can also be expressed in terms of the input photon flux. That is

$$I_{CEO} = (h_{FE} + 1) \gamma_{PTD} F(\nu) A_b \quad (7)$$

This relationship clearly shows that the phototransistor has an effective quantum efficiency which is  $(h_{FE} + 1)$  times larger than that of the collector-base photodiode.

### III. Noise Characterization

In a phototransistor, the two main categories into which radiation sensitive devices are classified are found combined into a single device. That is, a power sensitive device corresponding to the collector-base photodiode and an amplifier corresponding to the transistor. Their noise mechanisms are quite different. In the former, the noise is associated with random arrivals of the incoming photons and the random excitation of output carriers by these photons. For the latter, the input signal may be considered noiseless but the amplifying mechanism adds noise power to the signal. In what follows, the phototransistor noise model is developed by representing these noise sources with appropriate shot noise generators. The analysis culminates by formulating from these generators and the gain of the device an expression for the short-circuited output noise current.

#### Collector-Base Photodiode Noise Current

The noise in the collector-base photodiode partly arises from the randomness with which the incoming photons arrive. To some extent, then, this noise depends on the type of radiation source. In the experiments to be described in section IV, an incandescent lamp has been used. In practice, daylight is the commonest source of radiation to which phototransistors are exposed. Both of these sources are good examples of blackbody radiators. It is then sufficient to just consider noise due to fluctuations in blackbody radiators. A lucid treatment of this problem has been given by van Vliet [7]. His analysis gives that, for most practical circumstances, the fluctuations of  $I_{PH}$  can be represented by a shot noise generator.

As indicated earlier, the only difference between  $I_{PH}$  and  $I_{BC}$  is that the former is caused by photon excitation while the latter is phonon (thermal) excitation. The statistics of photons and phonons are the same, consequently the noise of the thermogenerated  $I_{BC}$  is also shot noise. The total noise associated with the collector-base photodiode is then represented by a shot noise generator of a strength corresponding to  $(I_{PH} + I_{BC})$ , located across the collector-base

junction

$$\overline{i_{ph}^2} = 2q(I_{PH} + I_{BC})\Delta f \quad (8)$$

#### Output Noise Current

As in the case of the p-n junction, it will be assumed that the passage of carriers across a junction potential barrier contributes full shot noise. In light of Eqs.(3) and (8), the noise of the collector current is then given by

$$\overline{i_c^2} = 2q \left[ \alpha_F I_D \exp (qV_{BE}/kT) + (I_{PH} + I_{BC}) \right] \Delta f \quad (9)$$

The two types of currents flowing through the emitter junction have different noise spectral densities. The diffusion component has full shot noise but the leakage due to generation-recombination levels does not. Lauritzen [8] has analytically proved that this type of mechanism has a noise spectrum with a strength varying from full shot noise at very low voltage bias to 3/4 of full shot noise for  $V_{BE} > .3$  volt. Then, it does not introduce great error to assume full shot noise for the leakage current. The noise of the emitter current is then

$$\overline{i_e^2} = 2q \left[ \frac{I_D}{\gamma_N} \exp (qV_{BE}/kT) + I_{ET} \exp (qV_{BE}/m'kT) \right] \Delta f \quad (10)$$

At frequencies low in comparison with  $f_\alpha$ , the transit time of minority carriers across the base region can be neglected and one can consider the current pulses of the injected carriers that do not recombine in the base as simultaneously appearing at both the emitter and collector junctions. This fraction of injected current common to both junctions gives the correlation between emitter and collector noise currents

$$\overline{i_c i_e^*} = 2q \left[ \alpha_F I_D \exp (qV_{BE}/kT) \right] \Delta f \quad (11)$$

Since only a fraction of the total instantaneous emitter and collector currents is composed of simultaneous pulses, there exists an instantaneous base current inasmuch as  $i_c \neq i_e$ . The mean square value of this base current is

$$\overline{i_b^2} = \overline{(i_c - i_e)(i_c^* - i_e^*)} = \overline{i_c i_c} + \overline{i_e i_e^*} - \overline{i_c^* i_e} - \overline{i_e^* i_c} \quad (12)$$

Substituting Eqs. (9), (10), (11) into Eq. (12) yields

$$\overline{i_b^2} = 2q \left[ \left( \frac{1 - \gamma_N \alpha_F}{\gamma_N} \right) \cdot I_D \exp(qV_{BE}/kT) + I_{ET} \exp(qV_{BE}/m'kT) + (I_{PH} + I_{BC}) \right] \Delta f \quad (13)$$

From Eq. (4), it is straightforward to show that the first two terms in this last equation equal  $(I_{PH} + I_{BC})$ . This is apparent since the first two terms correspond to the fraction of the emitter current that compensates  $(I_{PH} + I_{BC})$ . Hence, the base current generator has twice the shot noise corresponding to  $(I_{PH} + I_{BC})$ ; that is,

$$\overline{i_b^2} = 2q \left[ 2(I_{PH} + I_{BC}) \right] \Delta f \quad (14)$$

Physically, this comes about because  $i_b$  is made up of the fluctuations of  $(I_{PH} + I_{BC})$  and of the fluctuations of that portion of emitter current that compensates  $(I_{PH} + I_{BC})$ . These two currents flow in opposite directions and cancel through recombination in the base region whereas their shot noises are independent and consequently add quadratically.

It is interesting to compare this situation with the case of a conventionally biased transistor. For that case, the majority carriers sustaining  $i_b$  are supplied through an ohmic contact where no potential



barrier exists. Therefore, the shot noise associated with  $I_{PH}$  disappears from Eq. (13) causing a reduction of 3 db in the noise power of  $i_b$  if  $I_{BC}$  is negligible.

Finally, the correlation between  $i_b$  and  $i_c$  is

$$\overline{i_b i_c} = \overline{(i_c - i_e) i_c} = \overline{i_c^2} - \overline{i_e i_c} \quad (15)$$

Combining Eqs. (9) and (11) in Eq. (15) gives

$$\overline{i_b i_c} = 2q(I_{PH} + I_{BC})\Delta f \quad (16)$$

This is the expected result since  $(I_{PH} + I_{BC})$  is common to both the instantaneous collector and base currents.

The hybrid-pi equivalent circuit is next used to accommodate the shot noise generators given by Eqs. (9) and (14). The resulting noise equivalent circuit is shown in Fig. 3. From this equivalent circuit, the short-circuited output noise current is obtained

$$\overline{i_o^2} = \overline{(\beta i_b + i_c)^2} = |\beta|^2 \overline{i_b^2} + \overline{i_c^2} + \text{Re}(\beta \overline{i_b i_c}) \quad (17)$$

where

$$\beta = h_{fe} / (1 + jf/f_\beta)$$

With the aid of Eqs. (9), (14), and (16), Eq. (17) transforms to

$$\overline{i_o^2} = 2qI_{CEO} \left[ 1 + \left( \frac{I_{PH} + I_{BC}}{I_{CEO}} \right) \cdot \left( \frac{2h_{fe}^2 + h_{fe}}{(1 + f/f_\beta)^2} \right) \right] \Delta f \quad (18)$$

Recalling that  $(h_{FE} + 1) = I_{CEO} / (I_{PH} + I_{BC})$  and using the fact that  $h_{fe}$  is usually sufficiently large so that  $h_{fe}^2 > h_{fe}$ , Eq. (18) simplifies to

$$\overline{I_o^2} = 2q I_{CEO} \left[ 1 + \frac{2h_{fe}^2 / h_{FE}}{1 + (f/f_\beta)^2} \right] \Delta f \quad (19)$$

This is the sought-after expression for the output noise current. This approach is not fully correct for frequencies near the  $f_T$ , where  $|\beta| \approx 1$ , but the device is not very useful there either. High frequency effects have been dealt with elsewhere [9] and found to be negligible.

The physical interpretation of Eq. (19) is straightforward. Its low-frequency plateau gives the shot noise of the base current amplified by the gain of the device plus the shot noise of  $I_{CEO}$ . As the gain decreases with frequency, the output noise approaches a high-frequency plateau given by the shot noise of the collector current.

At a given  $I_{CEO}$  the unknown parameters of Eq. (19) can be determined from a measurement of the output current spectrum ranging from the low-frequency plateau up to some frequency above the 3 db fall-off point. For the purpose of interpreting the measured spectrum, it is convenient to define an  $I_{eq}$  by imagining that Eq. (19) gives the shot noise of a frequency-dependent current  $I_{eq}$ ; namely

$$I_{eq} = I_{CEO} \left[ 1 + \frac{2h_{fe}^2 / h_{FE}}{1 + (f/f_\beta)^2} \right] \quad (20)$$

The value of  $I_{eq}$  corresponding to the low-frequency plateau gives the parameter  $h_{fe}^2 / h_{FE}$ . With this parameter known, it is then a simple manipulation to find  $f_\beta$  from the measured frequency at which  $I_{eq}$  is 3 db below its low-frequency value.

In conclusion, Eq. (19) not only gives the magnitude of the output

noise of a phototransistor but it can also be used to characterize it by means of the parameters  $h_{fe}^2/h_{FE}$  and  $f_{\beta}$ . This can be a very useful characterization technique when the base lead of the device is not available

#### Noise Equivalent Power

If it is desired to characterize the phototransistor noise performance at its input, the concept of noise equivalent power or NEP must be used. The NEP is defined as the r.m.s. value of the sinusoidally modulated radiant power falling on the detector which will produce an r.m.s. output signal current equal to the r.m.s. noise current from the detector. This definition can be written in a way which makes clear the relationship

$$\frac{NEP}{\sqrt{i_o^2}} = \frac{(h\nu_s j_s) A_b}{\sqrt{i_s^2(\nu_s, f)}} \quad (21)$$

This equality implies that if one knows the right-hand relationship between the phototransistor response,  $i_s$ , and the signal power excitation  $h\nu_s j_s A_b$ , then one can find a noise equivalent power which causes the output noise current,  $i_o$ . By extending Eq. (9) to the small signal case, one obtains the right-hand relationship

$$i_s(\nu_s, f) = (\beta + 1)i_b = q(\beta + 1)\eta_{PTD} j_s A_b \quad (22)$$

After substituting Eqs. (19), and (22) into Eq. (21) and rearranging, the NEP can be written as

$$NEP = h\nu_s \frac{(2qI_{CEO})^{1/2}}{q\eta_{PTD}} \left\{ \frac{\left[ 1 + \frac{2h_{fe}^2/h_{FE}}{1 + (f/f_{\beta})^2} \right]^{1/2}}{\left[ 1 + \frac{h_{fe}^2}{1 + (f/f_{\beta})^2} \right]} \right\} (\Delta f)^{1/2} \quad (23)$$

Inspection of this expression shows that the NEP of a phototransistor is practically constant up to frequencies close to  $h_{fe} f_{\beta}$  and it equals the NEP of the collector-base photodiode times  $\sqrt{2}$ . That is, the NEP of these two detectors are practically the same.

#### IV. Experimental Results

Noise measurements were performed as described in the Appendix. As discussed in connection with Eq. (20), the measured noise has been interpreted using the concept of  $I_{eq}$ . From the measured plots of  $I_{eq}$ , the parameters  $h_{fe}^2/h_{FE}$  and  $f_{\beta}$  have been extracted. These results have been compared with independent a.c. measurements of  $h_{fe}$  and  $f_{\beta}$  and d.c. measurements of  $h_{FE}$ . A transit-time bridge [10] has been used to measure transit time,  $T_e$ , and  $h_{fe}$  from which  $f_{\beta}$  has been computed by means of the relationship derived by Lindmayer and Wrigley [11]

$$f_{\beta} = \frac{1}{2\pi \left[ T_e + \frac{kT}{qI_E} \cdot C_{CB} \right] h_{fe}} \quad (24)$$

where  $C_{BC}$  is the collector-base transition capacitance.

To show that no inconsistency is introduced by comparing measured parameters obtained under different sources of excitation, measurements were also performed using a GaAs light-emitting diode. The measured frequency response of the tested devices to an amplitude-modulated light signal from a GaAs diode has been used to determine  $f_{\beta}$ .

The room temperature spectra of Motorola phototransistor type MRD-310 and units fabricated with the facilities of the University of Florida Microelectronics Laboratory are discussed next. Both devices are silicon units with the base lead available.

The measured  $I_{eq}$  vs. frequency plots for the Motorola unit are shown in Fig. 4. The low-frequency plateau predicted by Eq. (20) is observed although it is masked by  $1/f$  noise at the lowest frequencies.

The high-frequency plateau corresponding to full shot noise of  $I_{CE0}$  is also observed.

For a given  $I_{CE0}$ , the value of  $I_{eq}$  for the low-frequency plateau and Eq. (20) yield  $h_{fe}^2/h_{FE}$ . Because of the dependence of  $h_{FE}$  on  $I_E$  indicated by Eq. (6), the current gains  $h_{FE}$  and  $h_{fe}$  are different;  $h_{fe}$  is larger than  $h_{FE}$ . The ratio  $m(I_E) = h_{fe}/h_{FE}$  which is a slow function of  $I_E$  is useful in the discussion of our experimental results. For this purpose, the plot of  $h_{fe}^2/h_{FE}$  vs.  $I_E$  in Fig. 5 has been labeled  $m^2 h_{FE}$ . In this figure, plots of  $h_{fe}$  from transit-time bridge measurements and  $h_{FE}$  are also shown.  $m(I_E)$  can then be computed by three different ways. In Fig. 6,  $m(I_E)$  has been plotted from comparison of noise and bridge measurements and via  $h_{fe}/h_{FE}$ . The good agreement between these two independent approaches indicates that all these measurements are accurate and that our noise model is accurate at low frequencies.

From the measured  $h_{fe}^2/h_{FE}$  and  $I_{eq}$  plots, the corresponding  $f_\beta$  have been computed and plotted in Fig. 7. In addition,  $f_\beta$  from the transit-time bridge measurement and the GaAs diode experiment are also plotted in Fig. 7. These data agree very well.

The output spectra of another MRD-310 unit was measured for both the phototransistor and transistor modes of operation. For the transistor mode, the base current was supplied through a 3 M $\Omega$  resistor. The measured  $I_{eq}$  are compared in Fig. 8. It is clear that the low-frequency plateau of the phototransistor is twice as large as that of the transistor with conventional bias. This is the expected result as explained in connection with Eq. (14). To repeat, the phototransistor is 3 db noisier on account of the shot noise contributed by  $I_{PH}$ .

Using the facilities of the Microelectronics Laboratory of the University of Florida, three-lead silicon phototransistors were fabricated. Fig. 9 shows a representative plot of  $I_{eq}$  for these units. The familiar spectrum shape of the MRD-310 device is recognized here. Fig. 10 compares  $m^2 h_{FE}$ ,  $mh_{FE}$ , and  $h_{FE}$ . From these plots,  $m(I_E)$  has been computed as explained before. The results are plotted in Fig. 11.

The agreement is again good between values of  $m$  computed by independent approaches. Fig. 12 compares values of  $f_{\beta}$  obtained from the three independent measurements used earlier. Agreement is again excellent.

## V. Conclusions

The excellent agreement obtained between values of  $h_{fe}^2/h_{FE}$  and  $f_{\beta}$  obtained from noise measurements and the other independent measurements coupled with the convergence of  $I_{eq}$  to  $I_{CEO}$  at the higher frequencies indicate that the noise model of Fig. 3 is valid except where  $1/f$  noise predominates. An immediate consequence of this agreement is that noise measurements on phototransistors can be used to characterize them in terms of  $mh_{FE}^2$  and  $f_{\beta}$ . To extend the usefulness of the basic results, an expression for the NEP has been derived. With this expression, a comparison between a photodiode and a phototransistor leads to the conclusion that they practically have the same NEP. However, the phototransistor has the advantage of its gain.

## APPENDIX

### NOISE MEASUREMENTS

The objective of these measurements was to obtain plots of  $I_{eq}$  vs. frequency. This was accomplished by measuring  $i_o^2$  given by

$$\overline{i_o^2} = 2qI_{eq}\Delta f \quad (25)$$

Since it was desired to measure a noise current, the phototransistor was biased with a current source. A block diagram of the noise measurement apparatus as shown in Fig. 12. The special low-noise preamplifier was built in our laboratory. It has an equivalent noise resistance of 220 ohms, and a flat frequency response from 10Hz to 200 KHz.

At a given frequency  $f_o$ , two measurements were needed in order to obtain  $I_{eq}$ . For the first measurement, let  $M_1(f_o)$  be the spectrum analyzer reading obtained after the amplified input noise was filtered through the bandwidth  $\Delta f$  of the spectrum analyzer

$$M_1(f_o) = (\overline{i_o^2} + \overline{i_{bg}^2}) \cdot |G| \quad (26)$$

where  $G$  is the power gain of the whole system and it is unknown,  $\overline{i_o^2}$  is given by Eq. (25), and  $\overline{i_{bg}^2}$  is the background noise. The second measurement was used to calibrate the system since  $G$  was unknown. For this latter measurement, a calibrating signal was added to the input of the preamplifier. As the diagram of Fig. 12 shows, two options were available for calibrating signals: a signal-generator-variable-attenuator combination and a noise diode. A 100K resistor was inserted between the attenuator and the preamplifier input so that the calibrating signal behaved as a current source,  $i_{cal}^2$ .

The calibrating measurement,  $M_2(f_o)$ , was normally done at a power level several db above  $M_1(f_o)$ .

$$M_2(f_o) = (\overline{i_o^2} + \overline{i_{bg}^2} + \overline{i_{cal}^2}) \cdot |G| = 10^n M_1(f_o) \quad (27)$$

Since the preamplifier used was low noise,  $i_{bg}^2$  was negligible in comparison with  $i_o^2$ . Hence, from Eqs. (26) and (24)

$$i_o^2 = \frac{\overline{i_{cal}^2}}{(10^n - 1)} \quad (28)$$

or in terms of  $I_{eq}$

$$I_{eq} = \frac{1}{2q\Delta f} \frac{\overline{i_{cal}^2}}{(10^n - 1)} \quad (29)$$

If a noise diode is used for calibration  $\overline{i_{cal}^2} = 2qI_{ND}\Delta f$  and there is no need to know the effective noise bandwidth of the spectrum analyzer. Since the majority of the noise measurements performed during this investigation used a sinusoidal calibrating signal, it was necessary to measure the noise bandwidths of the spectrum analyzers listed in Fig. 12. This was done by replacing the phototransistor in Fig 12 with a noise diode and using a sinusoidal signal for calibration. The measuring frequency was above the  $1/f$  region of the diode spectrum, hence  $\Delta f$  was readily determined from Eq. (29) since, in this case,  $I_{eq} = I_{ND}$ . This procedure gave the bandwidths listed in Fig. 12.



## ACKNOWLEDGMENT

The authors wish to thank Dr. K. B. Cook who graciously provided assistance with making the lab-built transistor.

## LIST OF SYMBOLS

$A_b$	Area of the base region exposed to radiation
$C_{ET}$	Emitter-base junction transition capacitance
$F(\nu)$	Photon flux rate per unit area at optical frequency $\nu$
$f$	Electrical frequency
$f_\beta$	Beta cut-off frequency
$h_{FE}$	D.C. current gain, Eq. 6
$h_{fe}$	Incremental current gain
$I_C$	D.C. collector current
$I_{BC}$	Collector leakage current due to thermal excitation
$I_{CEO}$	D.C. collector or emitter current
$I_D$	Coefficient of the electron current injected from emitter to base
$I_E$	D.C. emitter current
$I_{ET}$	Coefficient of the emitter-junction leakage current
$I_{eq}$	Equivalent shot noise current corresponding to the phototransistor output noise current, Eq. (20)
$I_{PH}$	Photogenerated current
$i_b$	Instantaneous base current
$i_c$	Instantaneous collector current
$i_e$	Instantaneous emitter current
$i_o$	Instantaneous short-circuited output current
$i_{ph}$	Instantaneous photogenerated current
$i_s(\nu_s, f)$	Small signal output current due to $j_s(\nu_s, f)$
$j(\nu_s, f)$	Small signal photon rate per unit area at optical frequency $\nu_s$ and electrical frequency $f$

$m(I_E)$	Ratio of $h_{fe}$ to $h_{FE}$
$m'$	Reciprocal slope of the emitter-leakage current vs. forward junction voltage
NEP	Noise equivalent power
T	Absolute temperature
$T_e$	Emitter-collector transit time
$V_{BE}$	Base-emitter junction voltage
$\alpha_F$	Fraction of the current injected from emitter to base that reaches the collector
$\beta$	A.C. current gain
$\gamma_N$	Emitter injection efficiency
$\Delta f$	Bandwidth

# REFERENCES

- 1 W. F. Shockley, M. Sparks, and G. K. Teal, "p-n Junction Transistors," Phy. Rev., 83, p. 151, 1951.
- 2 P. A. Gary and J. G. Linvill, "A Planar Silicon Photosensor with an Optimal Spectral Response for Detecting Printed Material," IEEE Trans. on Electron Devices, ED - 15, p. 30, 1968.
- 3 S. B. Schuldt and P. W. Kruse, "Optical Gain and Spatial Resolution in a Broad-Area Phototransistor," Journal of Applied Physics, 39, p. 5573, 1968.
- 4 IEEE Trans. on Electron Devices, ED - 15, p. 189, 1968.
- 5 G. T. Daughters II, "Noise Behavior of the 1N3754 Photodiode, and 2N986 & 2N2452 Phototransistors," Fairchild Application Data #46, 1962.
- 6 V. C. K. Reddi, "Influence of Surface Conditions on Silicon Planar Transistor Current Gain," Solid-State Electronics, 10, p. 305, 1967.
- 7 K. M. van Vliet, "Noise Limitations in Solid State Photodetectors," Journal of Applied Optics, 6, p. 1145, 1967.
- 8 P. O. Lauritzen, "Noise Due to Generation and Recombination of Carriers in p-n Junction Transistor Regions," IEEE Trans. on Electron Devices, ED - 15, p. 770, 1968.
- 9 F. H. De La Moneda, "Noise in Phototransistors," Ph.D Thesis, University of Florida, Gainesville, Fla., 1970.
- 10 M. B. Das and A. R. Boothroyd, "Determination of Physical Parameters of Diffusion and Drift Transistors," IRE Trans. on Electron Devices, ED - 8, p. 15, 1961.
- 11 J. Lindmayer and C.Y. Wrigley, "Beta Cutoff Frequencies of Junction Transistors," Proc. IRE, 50, p.194, 1962.

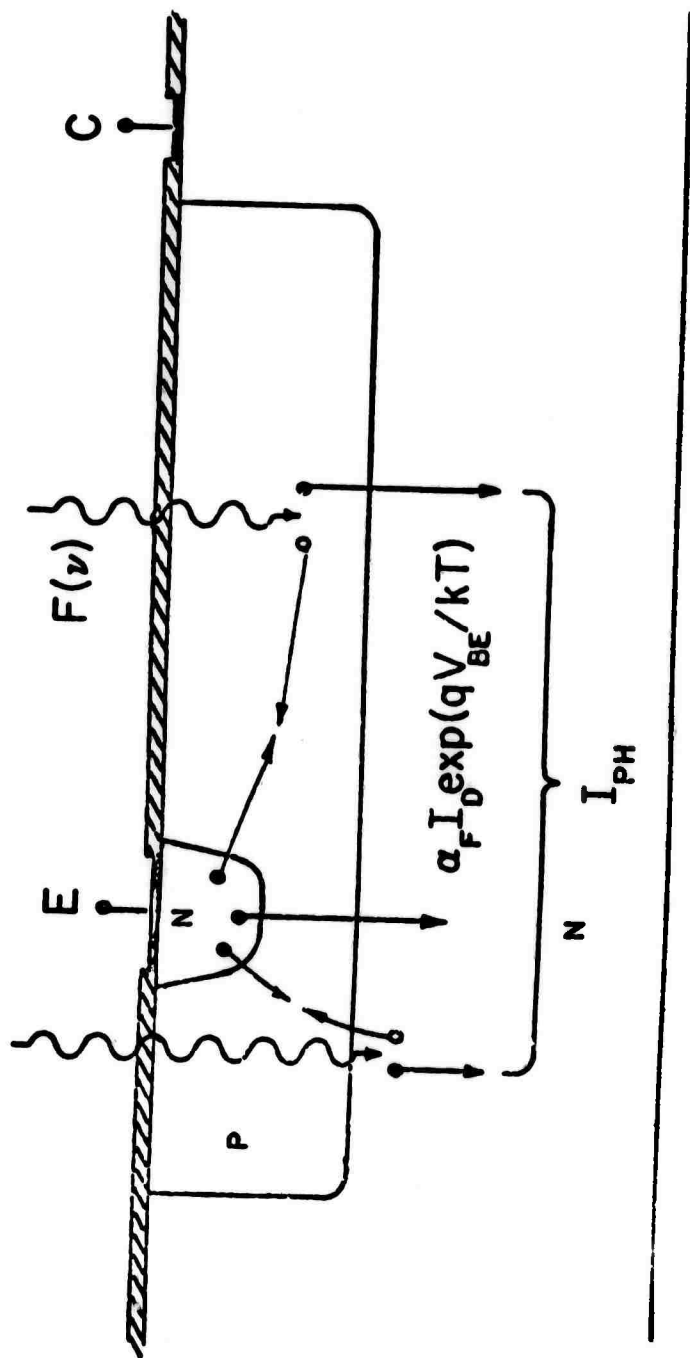


Fig. 1 CROSS-SECTIONAL VIEW OF PLANAR PHOTOTRANSISTOR

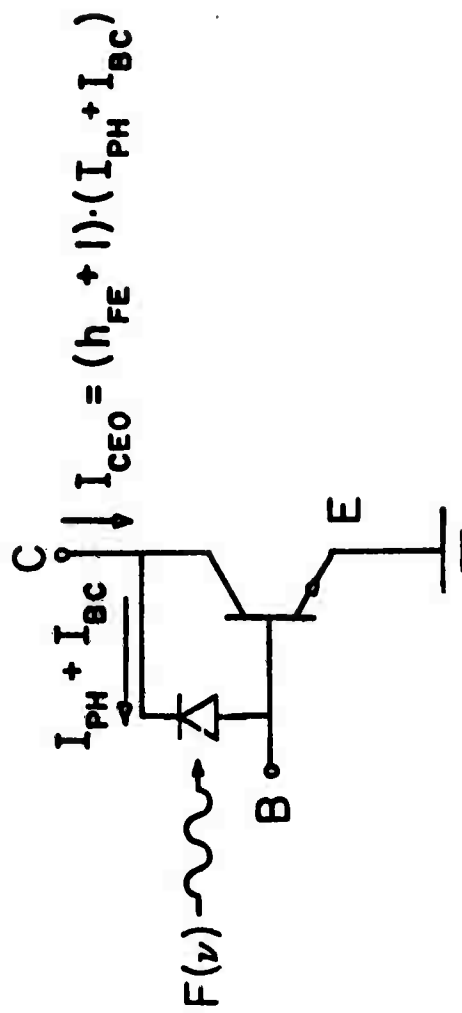
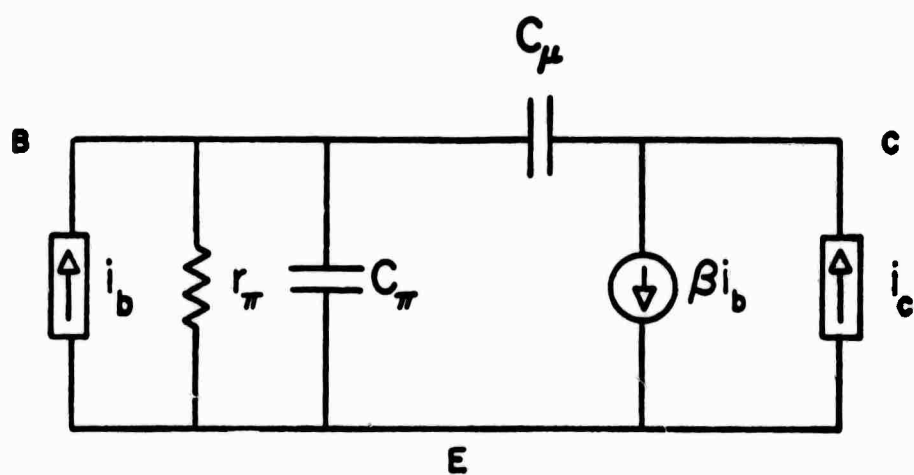


Fig. 2 ONE-DIMENSIONAL MODEL OF PHOTOTRANSISTOR



$$\overline{i_c^2} = 2q \left[ a_F I_D \exp(qV_{BE}/kT) + (I_{BC} + I_{PH}) \right] \Delta f$$

$$\overline{i_b^2} = 2q \left[ 2(I_{BC} + I_{PH}) \right] \Delta f$$

$$\overline{i_c i_b^*} = 2q(I_{BC} + I_{PH}) \Delta f$$

Fig. 3 PHOTOTRANSISTOR NOISE MODEL

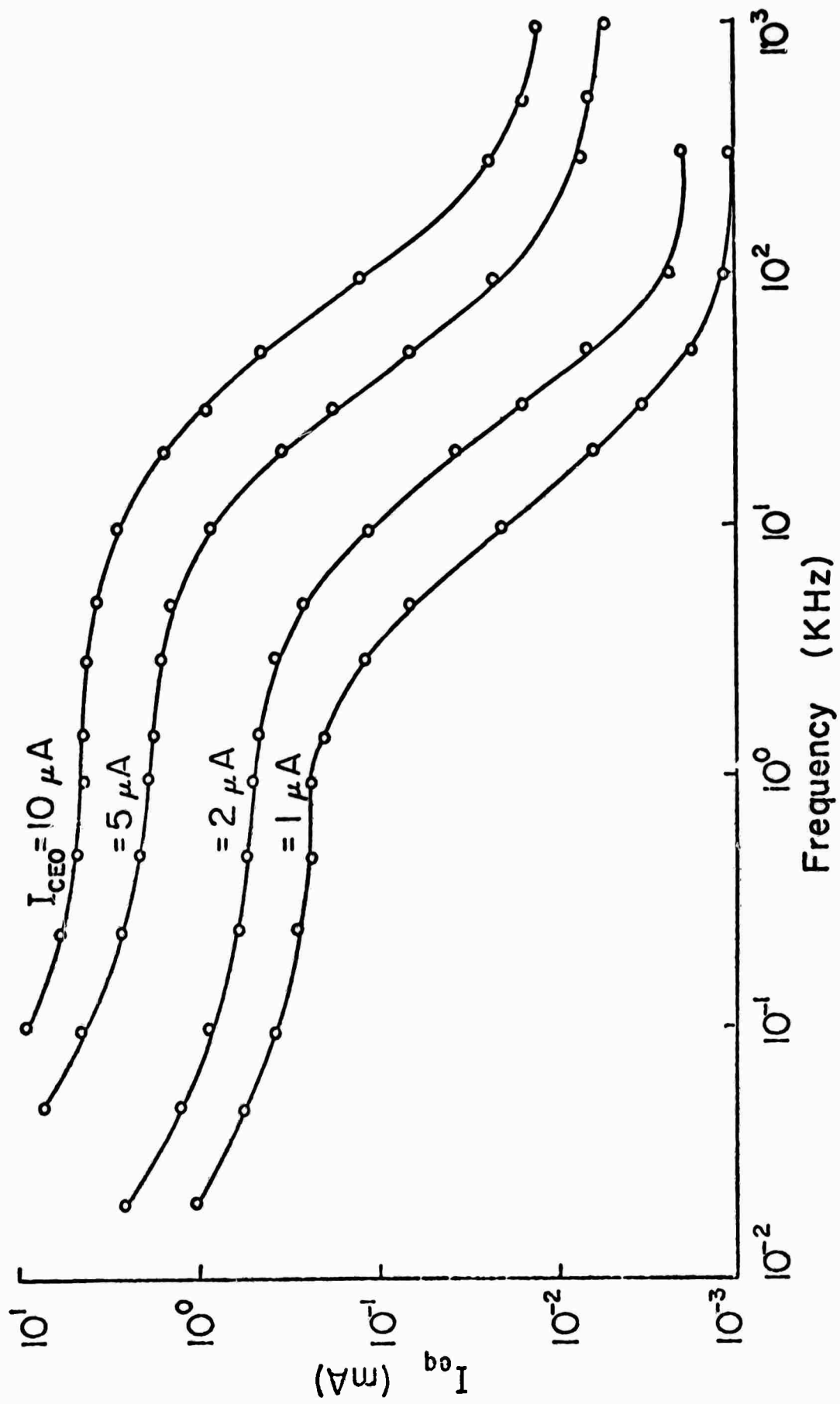


Fig. 4 MEASURED  $I_{EQ}$  vs. FREQUENCY FOR MOTOROLA MFD-310 PHOTOTRANSISTOR FOR  $I_{CEO}$  UP TO  $10 \mu A$ .

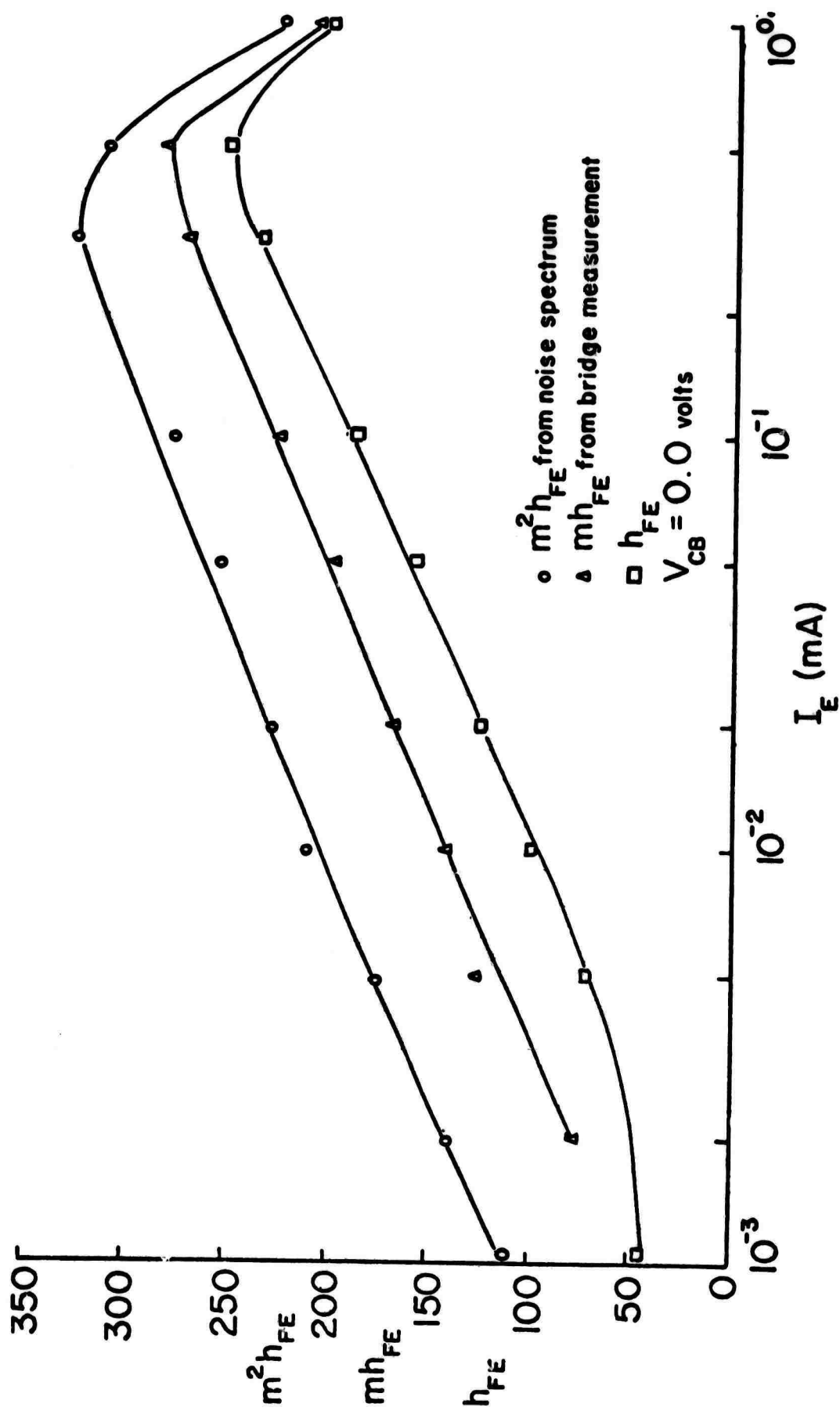


FIG. 5 PLOTS OF  $m^2 h_{FE}$ ,  $m h_{FE}$ , AND  $h_{FE}$  VS.  $I_E$  FOR MOTOROLA MFD-317 DEVICE.  
 VALUES OF  $m^2 h_{FE}$  WERE OBTAINED USING MEASURED SPECTRA AND EQ. (20).



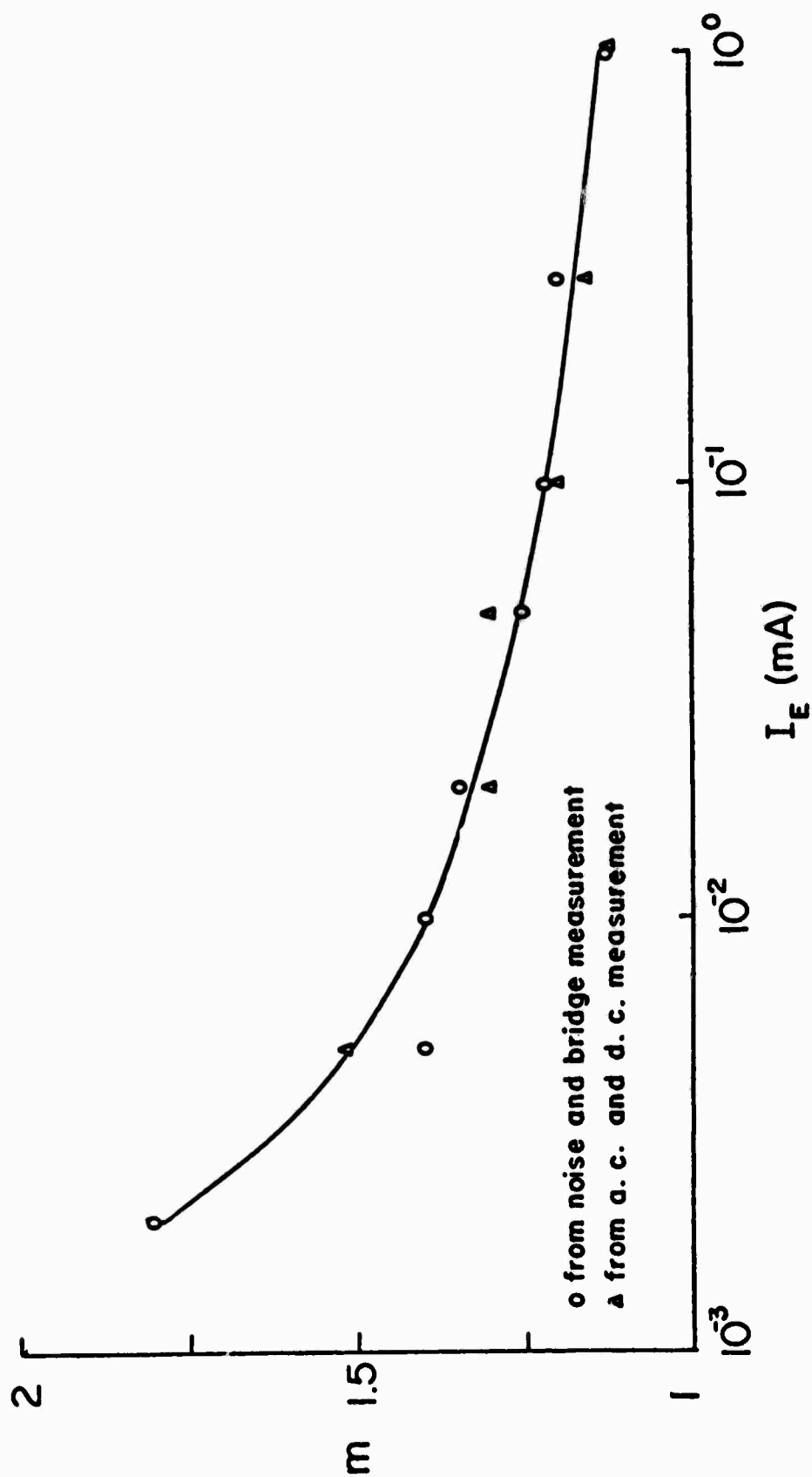


Fig. 6  $m$  vs.  $I_E$  computed from curves in Fig. 5.

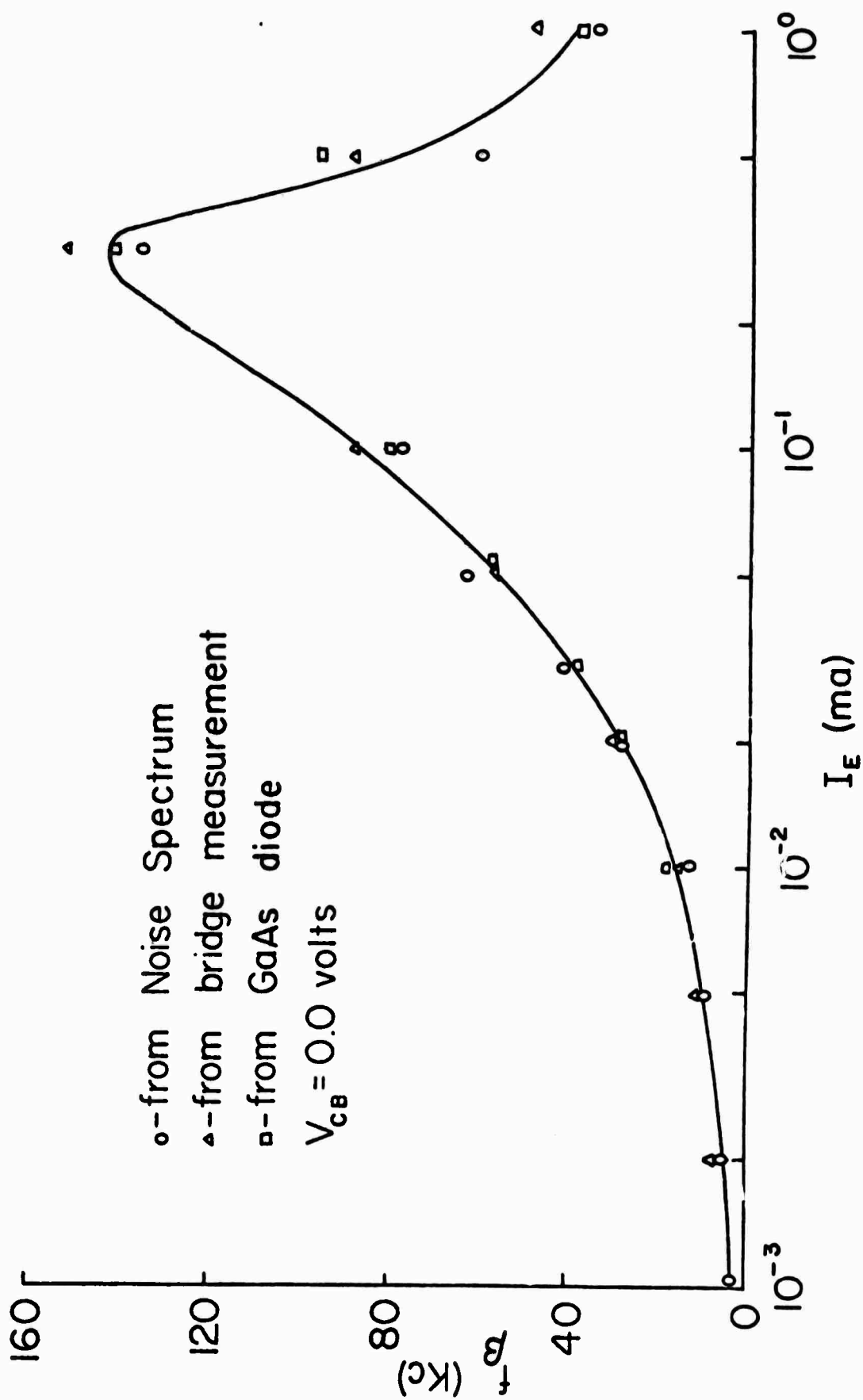


Fig. 7  $F_B$  vs.  $I_E$  for Motorola MRD-310 device.

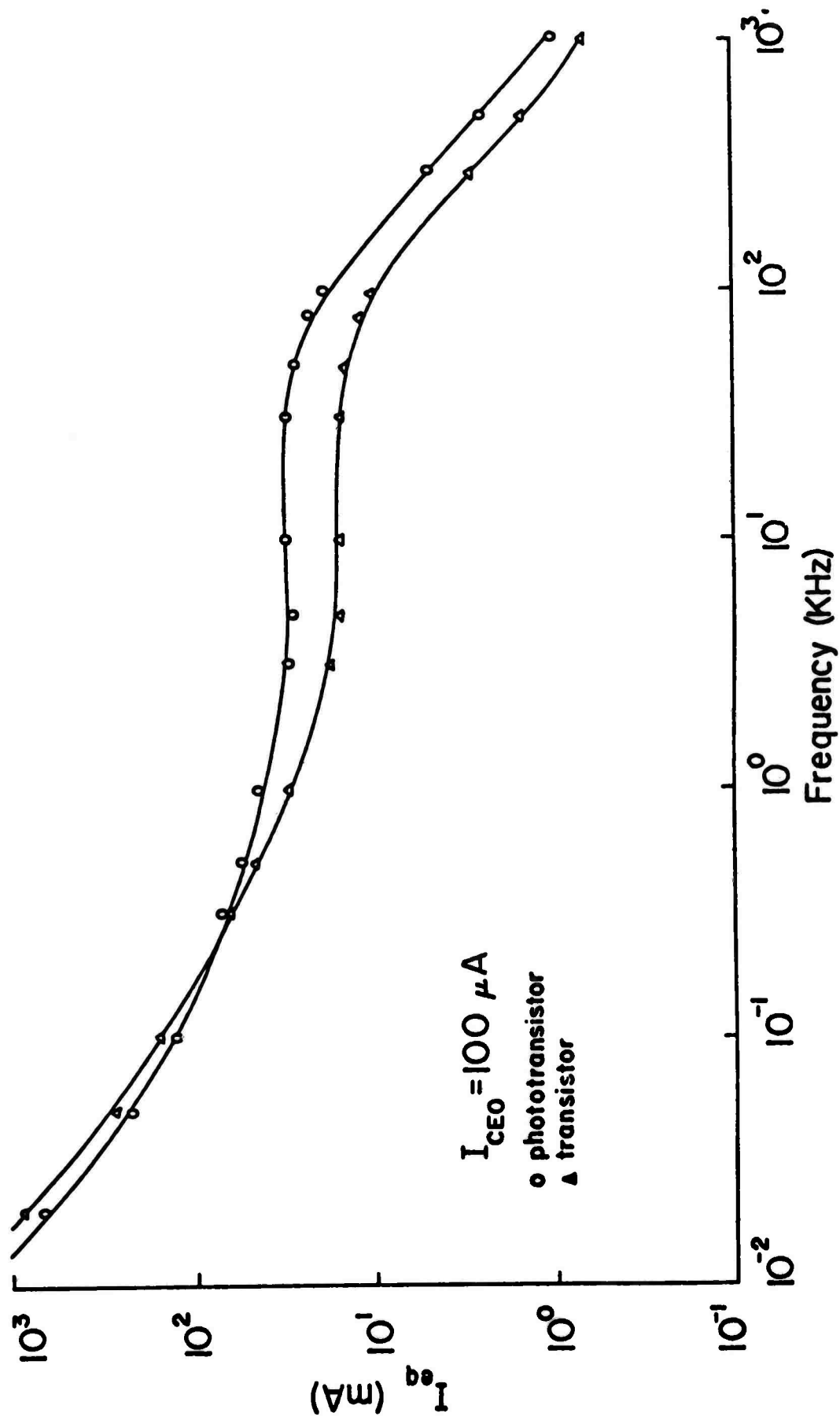


Fig. 8 MEASURED  $I_{EQ}$  VS. FREQUENCY FOR BOTH PHOTOTRANSISTOR AND TRANSISTOR MODES OF DEVICE OPERATION.

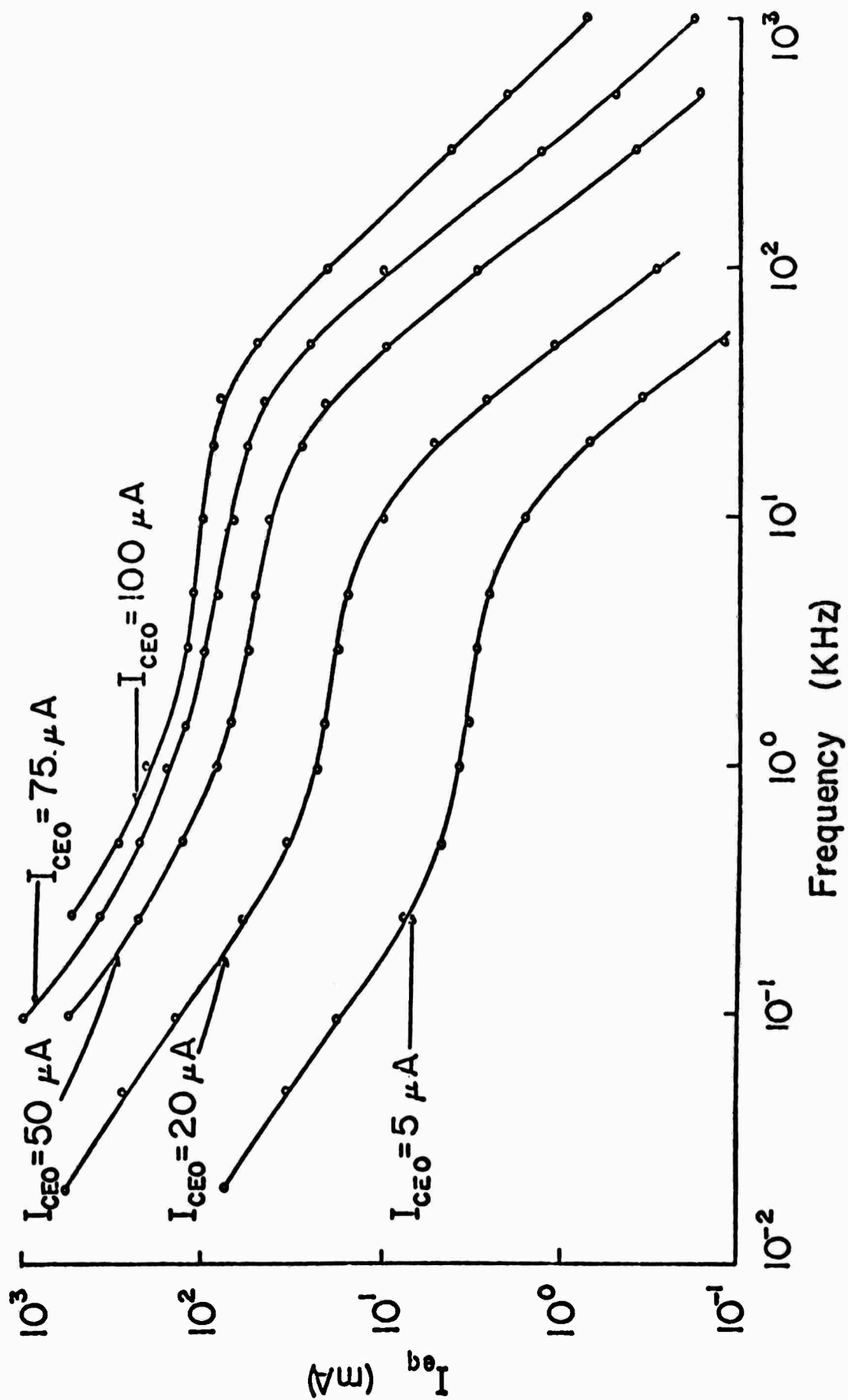


Fig. 9 MEASURED  $I_{EQ}$  VS. FREQUENCY FOR UNIVERSITY OF FLORIDA PHOTOTRANSISTOR.

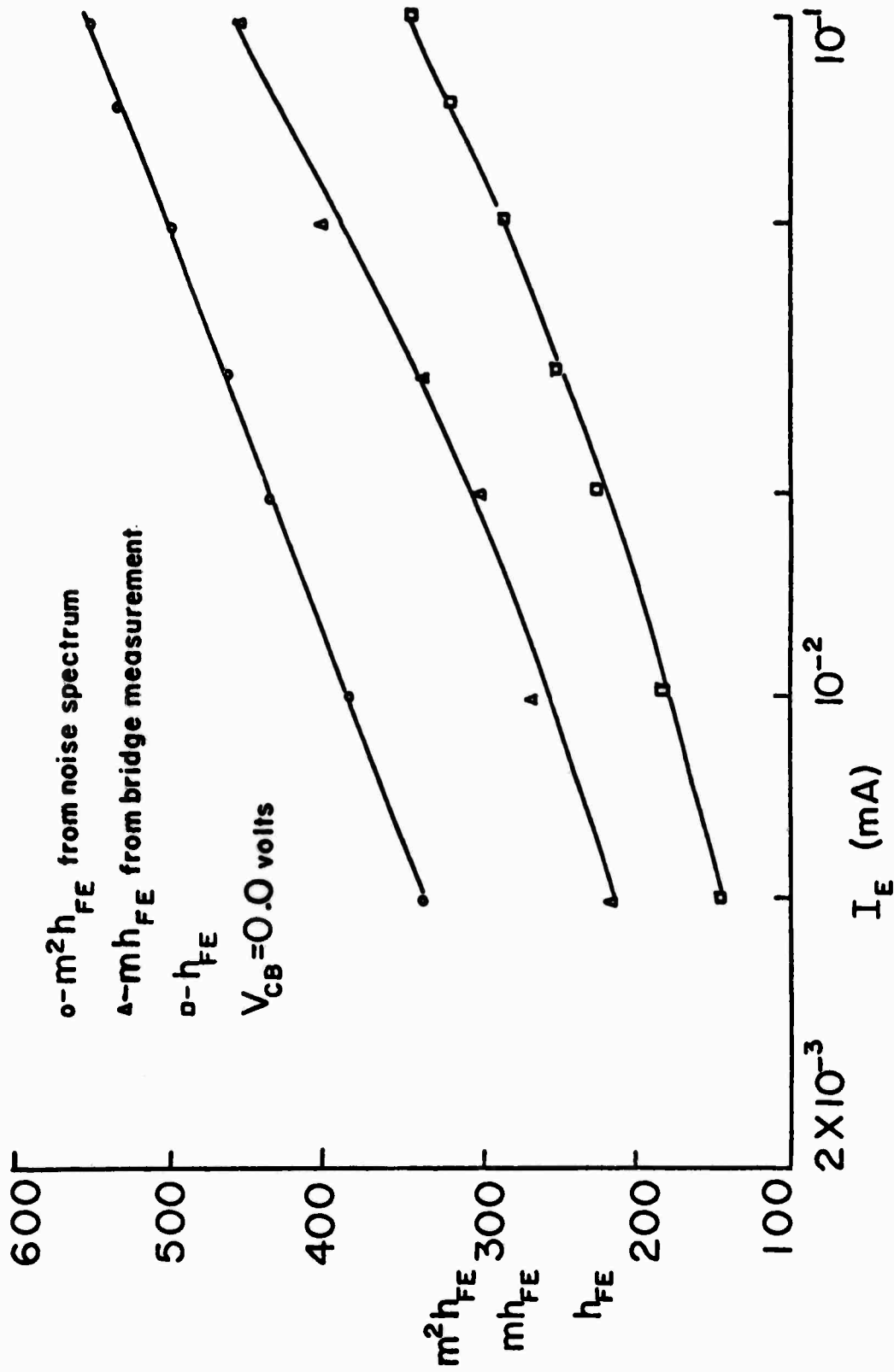


Fig. 10 Plots of  $m^2 h_{FE}$ ,  $m h_{FE}$ , and  $h_{FE}$  vs.  $I_E$  for University of Florida Device.  
 Values of  $m^2 h_{FE}$  were obtained using spectra of Fig. 9 and Eq. (20).

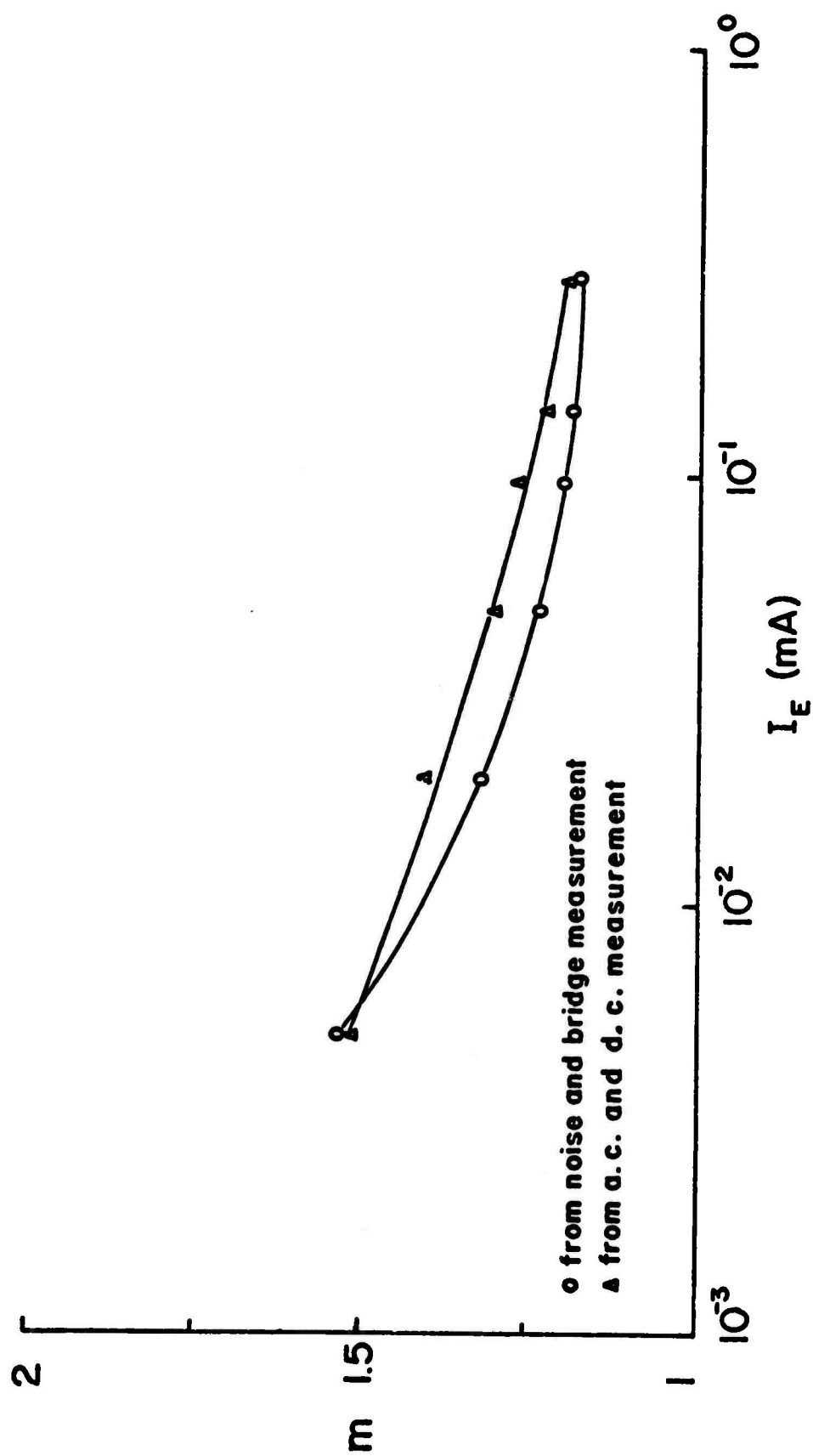


Fig. 11  $m$  vs.  $I_E$  computed from curves in Fig. 10.

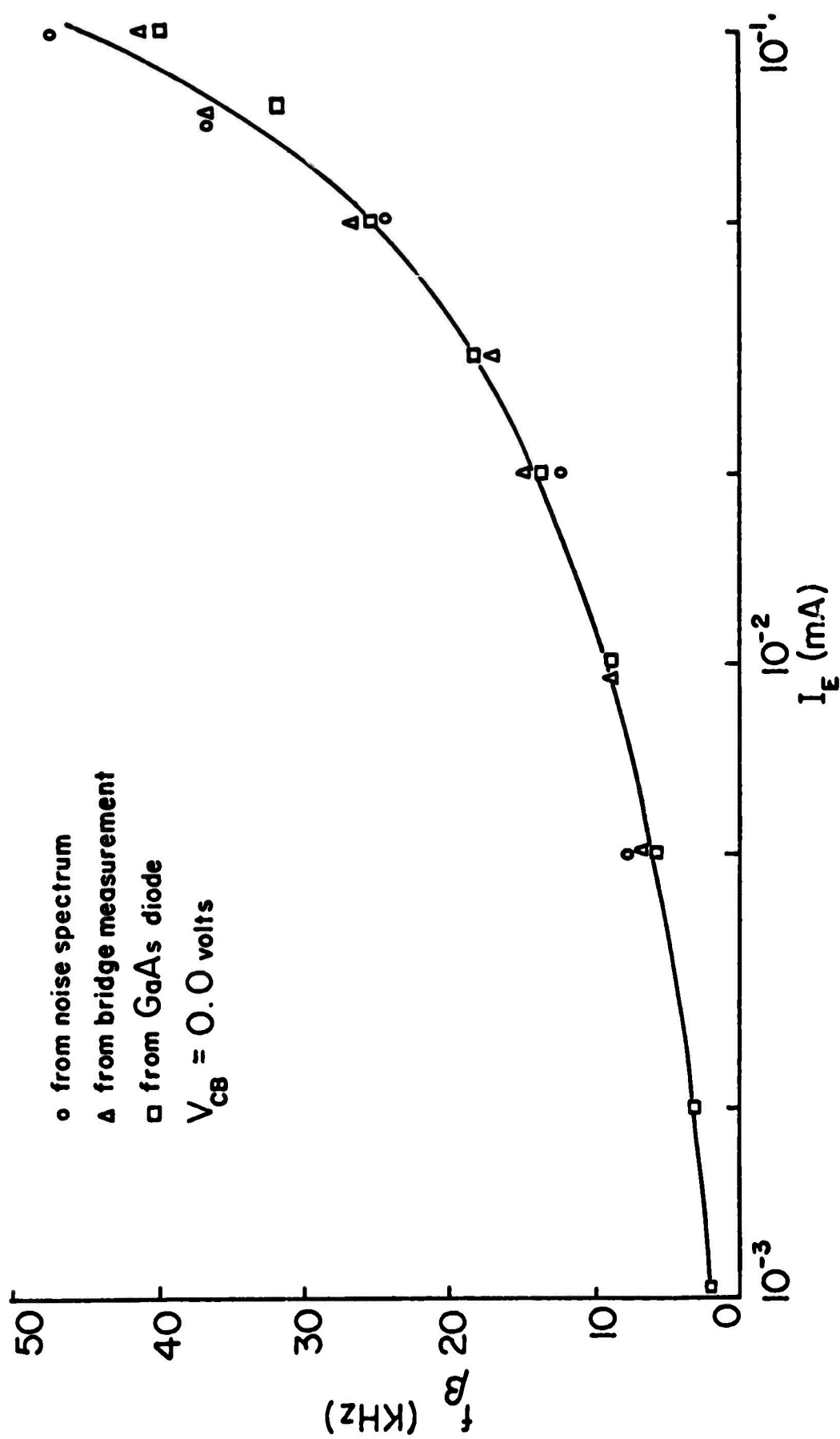


FIG. 12  $f_B$  VS.  $I_E$  FOR UNIVERSITY OF FLORIDA DEVICE.

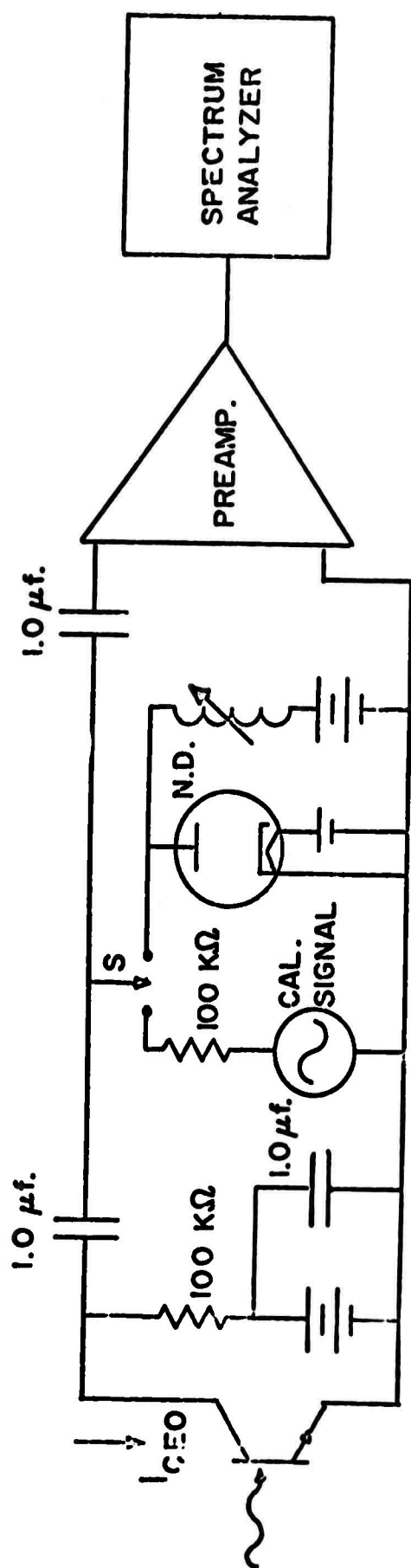


Fig. 13 NOISE-MEASUREMENT SET UP.



## B. A FAST SOLID-STATE PME LIGHT DETECTOR USING AU-DOPED SILICON (S. S. Li and H. F. Tseng)

### I. Introduction

The photomagnetolectric (PME) effect is due to the interaction of an applied magnetic field on the diffusion of optically-injected carriers. The relative orientations of the incident illumination, the magnetic field and the resulting PME voltage are shown in Fig. 1. This effect was discovered by Kikoin and Noskov<sup>1</sup> in  $\text{Cu}_2\text{O}$  in 1934. Since then, a considerable amount of research activity has been carried out by using the PME effect in semiconductors owing to its usefulness in the investigation of material properties<sup>2-9</sup>.

Application of the PME effect in light detection was first made by Boatright and Mette<sup>10</sup> for laser signal demodulation. They developed a germanium PME light detector which is capable of overcoming some of the difficulties encountered with photomultipliers as light demodulators. In addition, they also used such a device to investigate the fine structure of laser signals. Zitter<sup>11</sup> developed a fast InSb PME detector for optical maser studies up to 7 microns. This detector responds to modulation frequencies of at least 150 Mc, and the use of more highly-doped material could result in speeds up to 1 kMc. These are the historical background for the PME detector.

In our recent study of the PME effect in Au-doped silicon<sup>12,13</sup>, we have found that the PME response in silicon can be greatly enhanced by doping gold in silicon. This is particularly so for n-type silicon overcompensated with gold impurity. It has been demonstrated by us that in such material the PME open-circuit voltage of several volt/cm at liquid  $\text{H}_2$  and several hundred mV/cm at room temperature could be obtained without much difficulty. This large PME response was observed in the visible spectrum range in such material. In addition, the recombination lifetime in Au-doped silicon is extremely short (of the order of  $10^{-8} \sim 10^{-9}$  sec) which implies a fast response detector could be built by using such material. It is the objective of this paper to discuss the feasibility of using an Au-doped silicon bar as a PME light detector. The advantage of such a device lies mainly in the fact that it would be very economical to fabricate a PME detector using gold-doped silicon due to the efficacy of modern silicon technology.

### II. Theoretical Aspect of the Photomagnetolectric Effect

In our recent paper<sup>13</sup> we have developed the theory for the photomagneto-electric effect in gold-doped silicon. The results relevant to the present work

will be discussed here. The theory is valid under the following assumptions:

- i) Low injection (i.e.,  $\Delta n < n_o$ ,  $\Delta p < p_o$ ) case.
- ii) Small magnetic field (i.e.,  $\mu B < 1$ ).
- iii) Large gold density (i.e.,  $N_{Au} \geq N_D$  or  $N_{Au} \geq N_A$ ).
- iv) Incident photons only absorbed near the illuminated surface.
- v) Carrier lifetime is independent of injection for small injection case.
- vi) Sample thickness is greater than the carrier diffusion length.
- vii) One-dimensional approximation is valid.

Under the above assumptions, the expression for the photomagnetolectric open-circuit voltage per unit length for gold-doped silicon can be written in the form:

$$V_{PME} = B \frac{(1+b)}{(b+\Gamma^{-1})} \left( \frac{n_o \Gamma^{-1} + p_o}{n_o b + p_o} \right)^{1/2} \left( \frac{D_n}{\tau_n} \right)^{1/2} \left( \frac{\Delta G}{G} \right) \quad (1)$$

where

$B$  denotes the magnetic flux density

$b = \mu_n/\mu_p$  is the electron and hole mobility ratio

$\Gamma = \tau_n/\tau_p$  is the ratio of electron and hole lifetimes

$n_o, p_o$  are electron and hole concentrations in thermal equilibrium, respectively

$D_n$  is the electron diffusion constant

$\tau_n$  is the electron lifetime

$G = G_o + \Delta G$ ;  $G_o$  is the dark conductance per unit length to width ratio, and  $\Delta G$  is the photoconductance per unit length to width ratio which is related to the surface electron concentration,  $\Delta n_o$ , and can be expressed by:

$$\Delta G = q(b + \Gamma^{-1})\mu_p L^* \Delta n_o \quad (2)$$

Equation (1) shows that the PME open-circuit voltage is directly proportional to the magnetic flux density,  $B$ , and also varies linearly with light intensity for low injection (under this condition,  $\Delta G \ll G_o$ ,  $G \approx G_o$ ). Eqn. (1) also provides a direct means for determining electron lifetime by concurrent measurements of the steady-state PME open-circuit voltage, photoconductance, Hall coefficient and dark electrical conductivity. In the next section, we will discuss in detail the possible application of using this effect in gold-doped silicon as a light detector.

### III. Analysis of a PME Detector

The linear relation between the  $V_{PME}$  and the incident light intensity at low injection, and the very short electron lifetime possessed by the gold-over-compensated n-type silicon, make this material very attractive for fabricating a fast response and high sensitivity photodetector. In this section, the photoelectric characteristics of the PME light detector are discussed.

#### a) Effect of surface treatment on the sensitivity of the PME voltage

The dependence of the photosensitivity and the range of the linearity on the surface recombination velocity,  $S_o$ , can be seen from the dependence of  $\Delta G$  on  $S_o$ . The photoconductance,  $\Delta G$ , is directly proportional to the injected surface electron density  $\Delta n_o$ , and  $\Delta n_o$  is linearly related to the incident photon flux density and the surface velocity through the following relation:

$$\Delta n_o = \frac{L^* Q}{L^* S_o + D^*} \quad (3)$$

where  $Q$  is the photon flux density

$L^* = \sqrt{D^* \tau_n}$  is the effective diffusion length

$D^* = \frac{D_n (n_o \Gamma^{-1} + p_o)}{(n_o b + p_o)}$  is the effective electron diffusion constant

Combining Eqs. (2) and (3) yields the photoconductance

$$\Delta G = q(b + \Gamma^{-1})\mu_p \frac{L^* Q}{(S_o + D^*/L^*)} \quad (4)$$

From Eq. (4) it is noted that  $\Delta G$  is independent of  $S_o$  if  $D^*/L^* \gg S_o$  (i.e., for a well-etched illuminated surface one should expect the maximum PME responsivity). However, if  $S_o > D^*/L^*$ , the photosensitivity will decrease with increasing surface recombination velocity, while the range of linearity between  $V_{PME}$  and  $I_o$  will increase with increasing surface recombination velocity.

#### b) Response time ( $\tau_r$ )

It is shown in Eq. (1) that the PME voltage is directly proportional to the photoconductance for small injection cases. Therefore, the response time of the PME voltage should be equal to that of the photoconductance. It has been pointed out by Rose<sup>14</sup> that in a trap-free material, the response time will be equal to the carrier lifetime, and is dominated by the majority carrier lifetime. In the presence of trapping centers, the response time will in general be longer than the carrier lifetime when the trapping states are in "thermal contact" (i.e., trapping time is smaller than one-half of the recombination lifetime) with the conduction

band (or valence band for p-type). Under this condition the response time of excess carriers can be expressed as:

$$\begin{aligned}\tau_{rn} &= \tau_n \left(1 + \frac{\Delta n}{\Delta n_t}\right) \\ &= \tau_n \left[1 + \left(\frac{N}{N_c} \frac{t_n}{\tau_n}\right) \exp(E_C - E_{tn})/kT\right]\end{aligned}\quad (5)$$

where  $\tau_{rn}$  is the response time for the electron, and

$$\begin{aligned}\tau_{rp} &= \tau_p \left(1 + \frac{\Delta p}{\Delta p_t}\right) \\ &= \tau_p \left[1 + \left(\frac{N}{N_v} \frac{t_p}{\tau_p}\right) \exp(E_{tp} - E_v)/kT\right]\end{aligned}\quad (6)$$

where  $\tau_{rp}$  is the response time for holes.

In the case where the trapping time is much longer than the carrier recombination lifetime, i.e.,

$$\tau_{nt} = \frac{1}{v_t \sigma_{tn} n_{t1}} \gg \tau_p \quad (7)$$

and

$$\tau_{pt} = \frac{1}{v_t \sigma_{tp} p_{t1}} \gg \tau_n \quad (8)$$

then the response time will approach the lifetime of the free carriers. Under this condition, the photomagnetolectric response time should, in principle, be the same as for the trap free case.

For gold-doped silicon, the gold donor-level will act as hole traps in the n-type silicon, while the acceptor level will act as electron-traps in the p-type silicon. These are minority-carrier trappings, and will not in general have much influence on the response time. To see whether Eqs. (7) and (8) hold for gold-doped silicon, we use the electron and hole capture cross section data given by Fairfield et al.<sup>15</sup> for gold-doped silicon to calculate the electron and hole lifetimes. The results indicate that the minority carrier trapping times are indeed several orders of magnitude greater than the recombination lifetime. Therefore, the effect of minority carrier trapping on the response time in gold-doped silicon can be ignored (e.g.,  $\tau_{pt} = 1.3 \times 10^{-6}$  sec. and  $\tau_n = 1.38 \times 10^{-8}$  sec. at the gold acceptor levels). The PME response time is therefore controlled by the majority carrier lifetimes in such detectors.

### c) Sample internal resistance and capacitance

The internal resistance of the PME cell depends greatly on the compensation ratio of gold and shallow impurity in silicon. The sample resistance may vary from a few hundred kilohms to several tenths of megohms for the present case. The internal conductance of the cell remains constant under small light intensity

(i.e.,  $G_0 \gg \Delta G$ ). Since no p-n junction exists in such a cell, the total capacitance of the cell is extremely low ( $C < 1.5$  pf), and mainly comes from the connecting wires and external circuits. Since the RC time constant is relatively large as compared to the majority carrier lifetimes in the cell, it is the RC time constant that controls the decay of the PME open-circuit voltage signal. In order to shorten the response time of the detector, it is necessary to reduce the RC time constant of the cell.

#### d) Noise consideration

There are three major sources of noise existing in the PME detector that need to be considered.

##### (1) Thermal Noise (or Johnson noise)

The thermal noise is due to the thermal agitation of the carriers, which can be expressed as<sup>16</sup>:

$$v_{n,th} = (4kT \cdot R\Delta B)^{1/2} \quad (9)$$

where  $R$  is the detector internal resistance and  $\Delta B$  is the bandwidth of the detector. The thermal noise of a typical gold-doped silicon PME detector, with internal resistance of the order of 100 kilohms operating at room temperature and for 100 kHz bandwidth, will be of the order of 10  $\mu$ V. As will be shown later, this component of noise will constitute the lower limit for the detection of weak signals.

##### (2) The Generation-recombination noise (or G-R noise)

The G-R noise is due to statistical fluctuations of the generation-recombination of the excess carriers under illumination. The G-R noise can be expressed by<sup>16</sup>:

$$v_{n,g-r} = 2 \left( \frac{\Delta B}{Q} \right)^{1/2} v_s \quad (10)$$

where  $Q$  is the photon flux density and  $v_s$  is the PME voltage. As can be seen from Eq.(10), the signal noise ratio for this case is proportional to the square root of the input photon flux density. Therefore, this ratio will decrease with decreasing photon flux density. It is found that even at very low light intensity, the ratio is in the order of one thousand. In comparison with thermal noise, the G-R noise can be ignored in a PME detector.

##### (3) 1/f noise

The 1/f noise is prominent at low frequencies. This noise may be associated with surface states, barriers and poor ohmic contacts, and is only important when operating at frequencies below 1 kHz. This noise can be reduced by careful preparation of the sample.

From the above discussion and noting that the detector is designed to operate at rather high frequencies, it is obvious that the thermal noise will

constitute the lower limit for the detection of weak signals for such devices. Therefore, low noise performance is one of the outstanding features of such a detector.

e) Temperature dependence of the PME response

Boatwright and Mette<sup>10</sup> have reported that the PME voltage change in a germanium detector is less than 1%/C° within ± 10°C change around room temperature. In the gold-doped silicon PME detector, the PME response is more sensitive to the temperature. The change of the PME output voltage in such a cell is found to be 2%/C° around 25°C ± 10°C, which is about two times more sensitive than that of the Ge-cell. This is mainly due to the high internal resistance of the silicon cell.

f) Magnetic field dependence

The PME open-circuit voltage of the gold-doped silicon PME detector is linearly proportional to the magnetic flux density up to 10 kilogauss at room temperature (this is the maximum B available in our laboratory). The general criterion for such linearity to hold is that  $\mu B < 1$ , where  $\mu$  is the carrier mobility and B is the magnetic flux density. To obtain a large PME output signal, the magnetic flux density should be as high as possible.

g) Spectral response

The incident photon flux is related to the incident light intensity by

$$Q = \frac{\eta(\lambda)[1-R(\lambda)]\alpha(\lambda) I_o}{h\nu} \quad (11)$$

where  $\eta(\lambda)$ ,  $R(\lambda)$  and  $\alpha(\lambda)$  are quantum efficiency, reflection coefficient and absorption coefficient, respectively, which are functions of the incident photon wavelength  $\lambda$ . The spectral response of the PME effect in gold-doped silicon samples is found to be relatively flat (constant) over the wavelength interval from 0.45  $\mu\text{m}$  to 0.65  $\mu\text{m}$ . Therefore, the detector is adequate for detection of the modulating light signals in the visible spectrum range from 0.5  $\mu\text{m}$  to 0.7  $\mu\text{m}$ .

h) Selection of the material

It is found that gold-doped n-type silicon is superior to that of p-type silicon. This is due to the facts that: (1) the electron mobility is higher than the hole mobility; this is important for high PME responsivity; (2) the compensation of donor impurities by gold atoms is more complete than that of acceptor impurities (see for example, Wilcox<sup>17</sup>). Therefore, with equal amounts of substrate concentration and gold concentration, the resultant thermal equilib-

rium carrier concentration is much less in n-type material than in p-type material. This means that with equal amounts of incident photon flux, the change in  $\Delta G$  for n-type is much larger than that for p-type, and thus results in a higher sensitivity for n-type samples.

Another important aspect needs to be considered in connection with the selection of the material. This is the determination of the gold and donor concentration. The higher the gold concentration, the shorter the electron lifetime, and therefore the faster the response time can be achieved. The maximum attainable gold concentration is limited by the maximum solubility of gold in silicon, which is about  $10^{17} \text{ cm}^{-3}$ , as reported by Collins<sup>18</sup>. Under this maximum gold density, the electron lifetime is about  $6 \times 10^{-9} \text{ sec.}$ , and therefore the detector is capable of operating up to the frequency of 165 MC. The selection of substrate concentration (donor concentration for n-type) is more critical than gold doping. For small substrate concentration,  $N_D$ , the thermal equilibrium electron density,  $n_0$ , will be small, and thus results in a high responsivity and large RC time constant. On the other hand, the hole lifetime (minority carrier lifetime in this case) will increase with decreasing  $N_D$ . In order to achieve the goal of minority carrier trapping in the detector (i.e.,  $\tau_n > \tau_p$ ) rather than the majority carrier trapping,  $\tau_n$  should be greater than  $\tau_p$ . Under these conditions, the optimum doping concentration of  $N_D$  varies from  $N_D = 10^{16} \text{ cm}^{-3}$  ( $\rho \approx 0.5 \Omega\text{-cm}$ ) to  $9 \times 10^{16} \text{ cm}^{-3}$  depending on the desired sensitivity and RC time constant of the cell.

#### 1) Dimensions of the cell

The PME open-circuit voltage is inversely proportional to the sample conductance which varies directly with the sample thickness, as shown by Eq. (1). To ensure maximum sensitivity of the PME response, it is necessary to fabricate a thin PME cell. In addition, the PME open-circuit voltage is linearly proportional to the length of the cell and independent of the width of the cell. As a consequence, for optimum operation, a long, narrow cell should be mounted in between a small Arnold C-magnet with tapering pole pieces that concentrate the field near the PME cell.

### VI. Results and Discussion

We have fabricated and tested more than twenty gold-doped silicon PME detectors with various gold, shallow donor and acceptor concentrations. Some typical data and calculated material parameters are summarized in Table 1 for comparison. The typical sample dimensions are  $5 \times 2 \times 0.1 \text{ mm}^3$ .

Figure 2 shows the variation of the PME open-circuit voltage versus mag-

netic flux density for various light intensities for sample (4-d). The results indicate that a linear relationship between  $V_{PME}$  and  $B$  is obtained for various light intensities and for  $B$  up to 10 kG.

Figure 3 demonstrates the  $V_{PME}$  versus light intensity,  $I_0$ , for various magnetic flux densities, which also shows a linear relationship between  $V_{PME}$  and  $I_0$  for low light levels.

Figure 4 shows the spectral-response of the PME voltage versus wavelength for a typical gold-doped silicon sample. The results indicate that the maximum response occurs between 0.5 - 0.6  $\mu m$  and decreases with both increasing and decreasing photon wavelength.

Figure 5 shows the normalized  $V_{PME}$  (with  $V_{PME}$  at 25°C as reference) as a function of temperature between -20°C to +60°C for samples 1-d, 2-d and 4-d. The results indicate that the maximum  $V_{PME}$  shifts to the lower temperature side as the resistivity of the sample decreases.

Figure 6 illustrates the noise figure of a typical PME detector. The results indicate that for frequencies below  $10^3$  Hz, the 1/f noise dominates. And for frequencies greater than  $10^3$  Hz, the thermal noise is the only major noise component that exists in the sample.

In conclusion, we have studied the PME effect in gold-doped silicon samples and analyzed the feasibility of using this material as a PME light detector.

It was found that for cells with high internal resistance, the RC time constant is rather long, while the sensitivity is very high. On the other hand, samples with lower internal resistance have shown a much shorter RC time constant, while the sensitivity is greatly reduced. In order to construct a PME light detector of considerable sensitivity, and with fast response time, one has to compromise the doping concentrations of gold and shallow donor impurities in silicon.



### References

1. I. K. Kikoin and M. M. Noskov, Physik. Z., Sowjet Union 5, 586 (1934).
2. W. van Roosbroeck, Phys. Rev. 101, 1713 (1956).
3. G. Bemski, Phys. Rev. 111, 1515 (1958).
4. S. S. Li and C. Wang, Proc. of the 3rd Photoconductivity Conf., E. M. Pell, Pergamon Press (1970).
5. M. Ishigame, Japan J. of Appl. Phys. 3, 720 (1964).
6. S. w. Kurnick and R. N. Zitter, J. of Appl. Phys. 27, 278 (1956).
7. S. S. Li, Phys. Rev., 188, 1246 (1969).
8. W. van Roosbroeck, Phys. Rev. 119, 636 (1960).
9. A. Amith, Phys. Rev. 116, 793 (1959).
10. A. Boatwright and H. Mette, Proc. of the 1962 Army Science Conf., West Point, N. Y., vol. 1, pp. 31-46.
11. R. N. Zitter, Rev. of Scien. Instr. 35, 5 594 (1964).
12. J. Agraz-G and S. S. Li, Phys. Rev., B 15, Sept. (1970).
13. S. S. Li and H. F. Tseng, Phys. Rev., (to be published).
14. A. Rose, Photoconductivity and its Associated Problems (1962).
15. J. M. Fairfield and B. V. Gokhale, J. Solid State Elec., 8., 685 (1965).
16. A. D. van der Ziel, Solid State Physical Electronics, 2nd Edition, Prentice-Hall (1968).
17. W. R. Wilcox, T. J. LaChapelle, J. of App. Phys. 35, 240 (1964).
18. C. B. Collins, R. O. Carlson and C. J. Gallagher, Phys. Rev. 105, 1168 (1957).

TABLE I Performance Characteristics of Au-doped Si PME Detector at 300°K.

Sample No.		Type	$N_D$ or $N_A$ $\text{cm}^{-3}$	$N_{\text{Au}}$ $\text{cm}^{-3}$	$R(\Omega)$	Responsivity $(\text{V/W}/\text{cm}^2)$	Response Time (sec)	Detectivity $(\text{cm}^2\text{H}_z/\text{W})$	NEP $(\text{W}/\text{H}_z)$
(1)* measured at B = 10 kG	P-1-d	n	$5 \times 10^{15}$	$8 \times 10^{16}$	$2.7 \times 10^6$	100	$8.1 \times 10^{-9}$	$1.49 \times 10^8$	$6.7 \times 10^{-9}$
	P-2-d	n	$10^{16}$	$8 \times 10^{16}$	$2 \times 10^6$	13	$8.7 \times 10^{-9}$	$7.15 \times 10^7$	$1.4 \times 10^{-8}$
	P-3-d	n	$10^{16}$	$5 \times 10^{16}$	$10^6$	4	$1.5 \times 10^{-8}$	$3.12 \times 10^7$	$3.2 \times 10^{-8}$
	P-4-d	n	$1.5 \times 10^{16}$	$2 \times 10^{16}$	$0.125 \times 10^6$	0.7	$1.2 \times 10^{-7}$	$1.54 \times 10^7$	$6.5 \times 10^{-8}$
(2) capacitance for each sample is less than 1.5 pf.	M-5-d	p	$10^{15}$	$3 \times 10^{16}$	$0.19 \times 10^6$	0.5	$1.6 \times 10^{-8}$	$8.94 \times 10^8$	$1.12 \times 10^{-9}$
	M-6-d	p	$10^{14}$	$10^{16}$	$0.25 \times 10^6$	1	$1.6 \times 10^{-7}$	$1.56 \times 10^9$	$6.43 \times 10^{-10}$

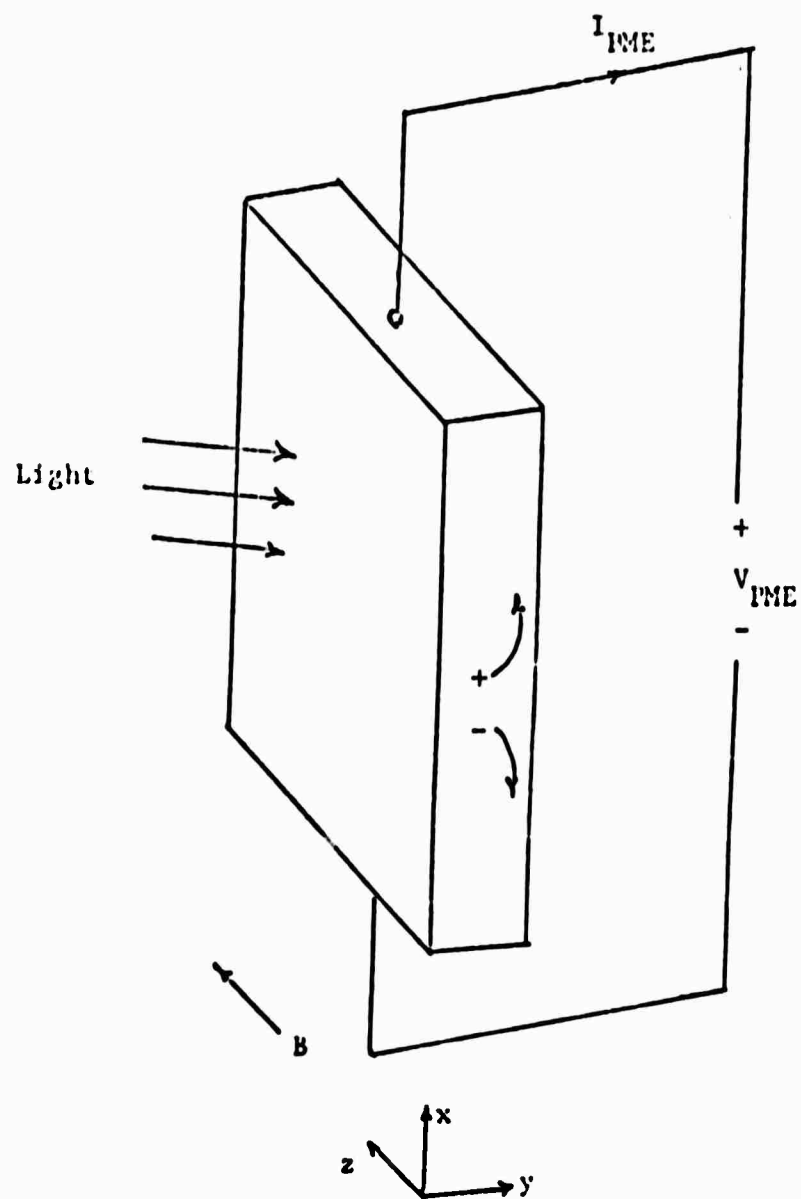


Fig. 1 The relative orientations of the incident illumination, magnetic field, and resulting PHE voltage.

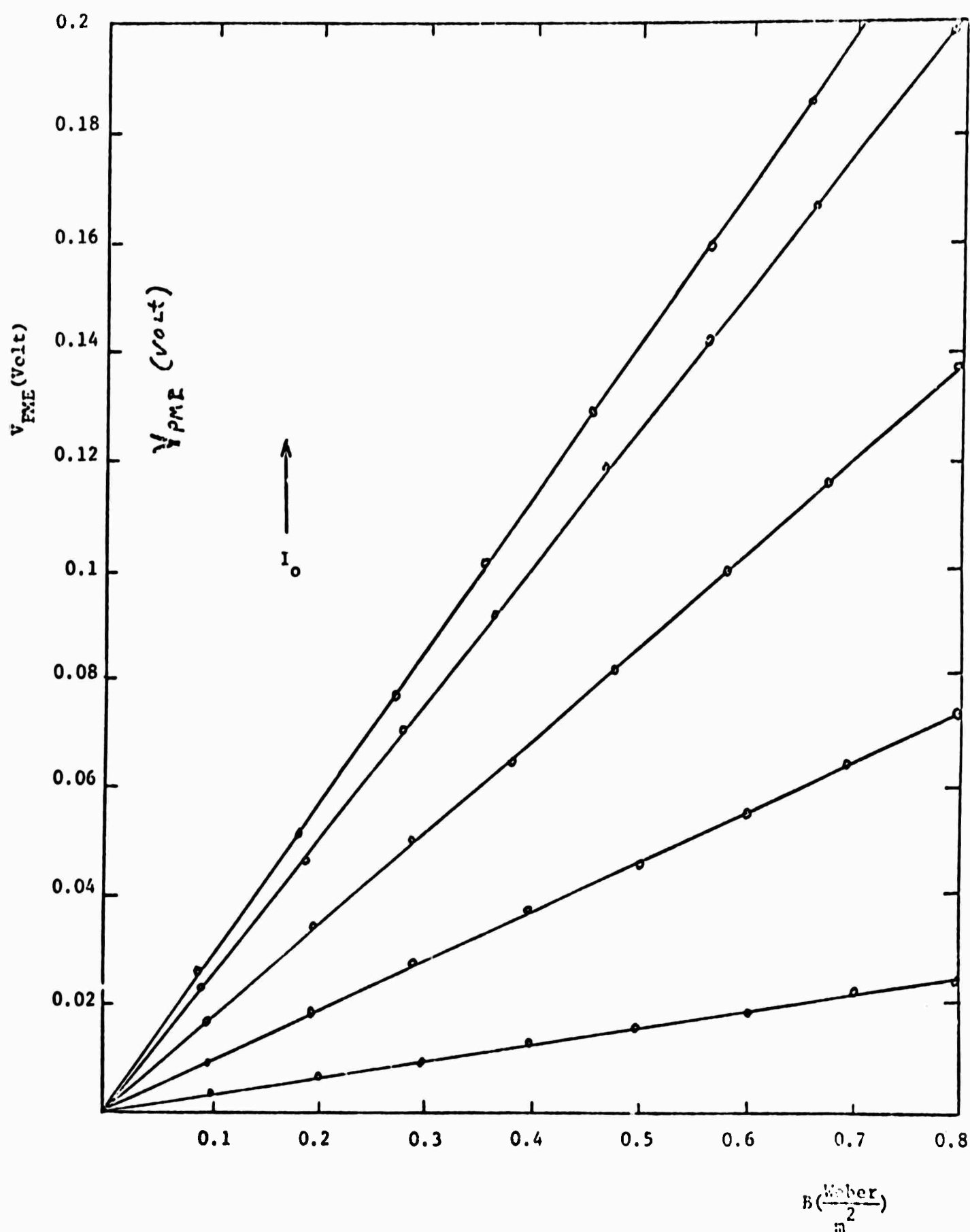


Fig. 2 The PNE open-circuit voltage,  $V_{PNE}$  versus magnetic flux density,  $B$ , with light intensity,  $I_0$ , as a parameter, for  $T = 300^\circ\text{K}$  and for sample (4-d).

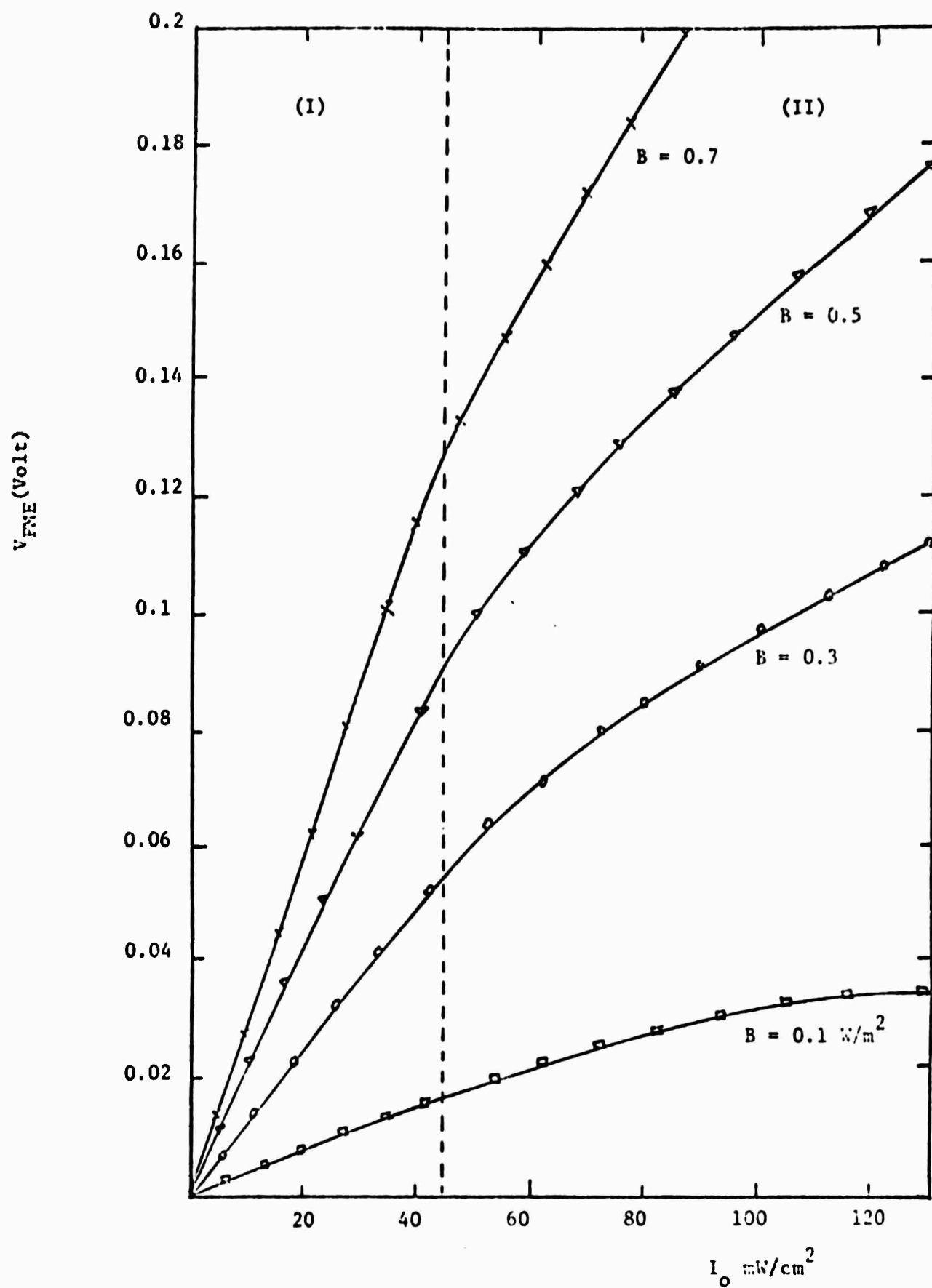


Fig. 3  $V_{PME}$  versus  $I_0$  with  $B$  as a parameter, for sample (4-d).

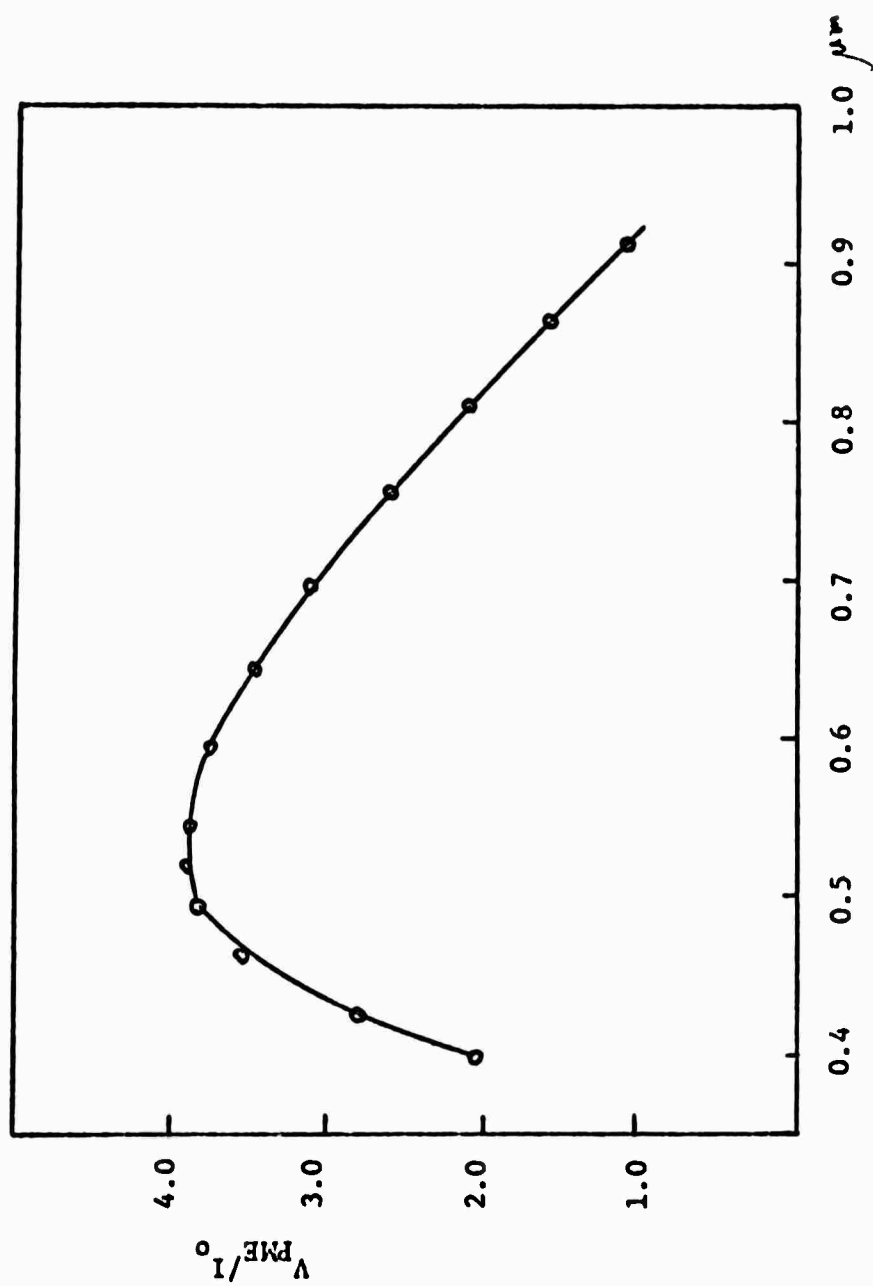


Fig. 4  $V_{PME}/I_0$  versus photon wavelength,  $\lambda$ , for sample (1-d).

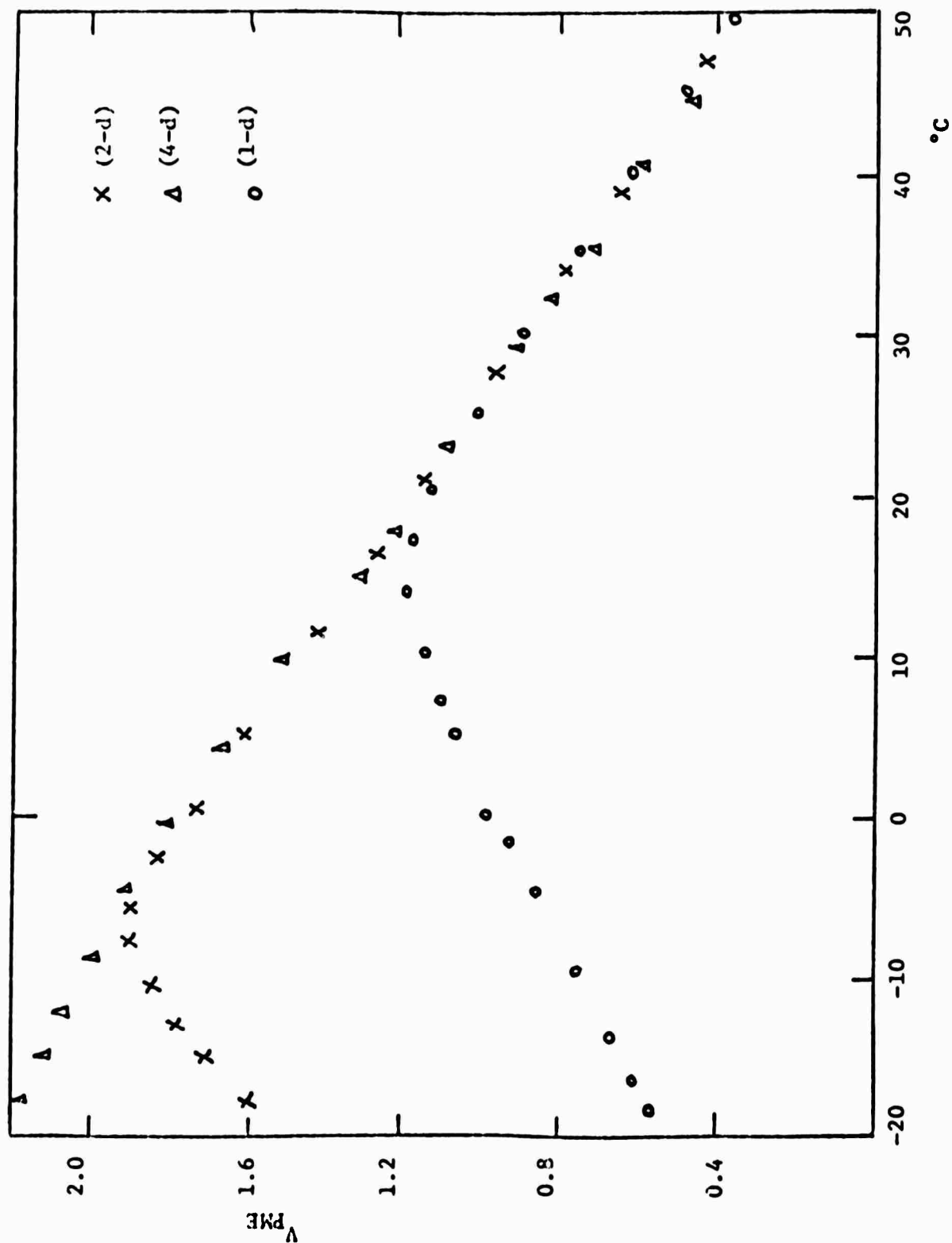


Fig. 5 Normalized  $V_{PME}$  ( $V_{PME} / V_{PME}$  at 25°C) versus temperature, T. for samples (1-d), (2-d), and (4-d).

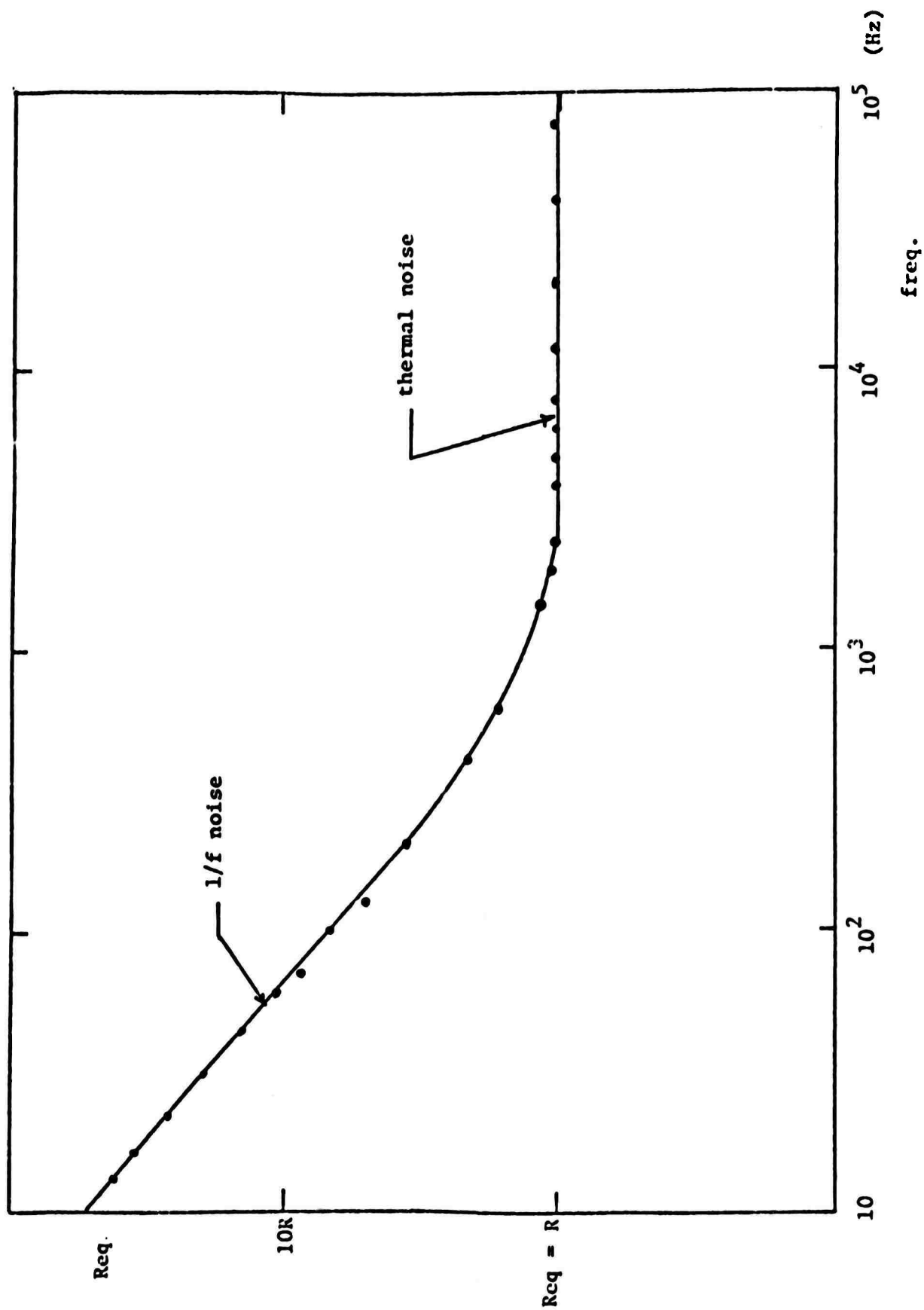


Fig. 6 Noise figures of a PME detector versus frequency, for sample (1-d).



C. ELECTRON MOBILITY AND SHALLOW IMPURITY LEVELS IN In-DOPED AND Cu-DOPED CdS (S. S. Li and C. I. Huang)

I. Introduction

Although a considerable amount of work has been done on the photoconductive and luminescent properties in II-VI compounds, only a small part of this work has been on the conventional transport properties.

Much of the work on CdS has been concerned with the intrinsic scattering mechanism. Kroger et al<sup>1</sup> attempted to fit their data to a simple expression for optical mode scattering. Migazawa et al<sup>2</sup> also attempted to fit their data with a combination of optical mode and impurity scattering. Devlin<sup>3</sup> used the variational method to find the effect of two simultaneous scattering mechanisms on the Hall mobility. Fugita et al<sup>4</sup> measured the Hall mobility under pulsed illumination using the Redfield<sup>5</sup> technique. Monikowa<sup>6</sup> measured the Seebeck coefficient of several n-type CdS crystals having room temperature carrier concentrations of the order of  $10^{15} \text{ cm}^{-3}$ , and gave a value of 0.024 eV as the shallow donor ionization energy. Woodbury<sup>7</sup> reported a double acceptor 0.09 eV below the conduction band edge. Bradberry and Spear<sup>8</sup> observed trapping effects in their drift mobility measurement due to a level 0.16 eV below the conduction band. They attributed this level to native defects, tentatively singly ionized sulfur vacancies. Buget and Wright<sup>9</sup> measured the temperature dependence of the carrier concentration in n-type CdS and found it determined by unknown donors with ionization energies of 0.45, 0.63 and 0.82 eV in different crystals.

Kroger and Vink<sup>1</sup> have studied the effect of additions of Cl and Ga which act as shallow donors after firing in Cd atmosphere, but the defects were in such high concentration that the samples were degenerate or indicated impurity band conduction. Piper and Halsted<sup>10</sup> observed a donor level at 0.032 eV in samples with carrier density of  $10^{15} \text{ cm}^{-3}$  which is sufficiently low to avoid impurity banding or screening effects. This energy is in close agreement with the value predicted on the assumption that the donor is hydrogen-like. Itakura and Toyada<sup>11</sup> measured the Hall effect in undoped CdS in which two donor levels were found: one 0.014 eV and the other 0.007 eV below the conduction band edge.

The transport measurements reported in the literature so far yield a relatively well-understood knowledge with regard to the intrinsic scattering mechanism in CdS. Longitudinal optical mode and acoustical mode scattering

dominates the scattering of electrons at high temperatures, while piezo-electric scattering dominates the scattering mechanism at low temperatures. Identification of impurity levels in CdS is still far from ideal due to the fact that native defects resulting from nonstoichiometry and residual impurities exist in the crystal, controlling the electrical properties of such a material.

In this paper, we attempt to identify the impurity levels in In-doped CdS from a study of electrical conductivity and Hall effect measurements between 4.2°K to 300°K. The doping density of indium is chosen such that the material is non-degenerate in certain temperature ranges. An elaborate study of the carrier concentration versus temperature between 4.2°K and 300°K is made for In-doped CdS samples. A two-impurity level model is proposed to interpret the observed results. In addition, the conductivity and the Hall effect measurements are also studied for Cu-doped CdS. This allows us to draw conclusions with regard to the scattering mechanism as well as shallow impurity states in In-doped CdS.

## II. Experimental Details

The undoped CdS crystal was supplied by the Clevite Corporation, and has the following impurities before doping with indium or copper:

Fe < 0.1 ppm	Ni < 0.5 ppm	Zn < 30 ppm
Cu < 0.1 ppm	Pb ~ 5.0 ppm	Cl < 5 ppm

The last three elements are greatly reduced in the process of vacuum sintering and growing the crystal. The indium doping density is chosen such that its concentration is high enough to control the electrical properties of the sample by indium atoms alone, rather than by native defects or residual impurities. In addition, the material has to be non-degenerate in a wide temperature range so that the study of the shallow impurity states can be made in such materials. The optimum concentration chosen for In and Cu is about  $5 \times 10^{17} \text{ cm}^{-3}$  for the purpose of this study. The sample was cut into a rectangular bar with dimensions of  $5 \times 3 \times 1 \text{ mm}^3$ , after chemical etching. In-Ga paste was used for ohmic contacts, which is found to be satisfactory over the measuring temperature range. The electrical and Hall effect measurements were performed between 4.2°K and 300°K, using standard techniques. An AC-310 liquid helium refrigeration system was used for low-temperature measurements. The magnetic fields used were between 1 and 8 kG. To assure that no irreversible changes had occurred in the bulk of the crystals or the electrodes during

the thermal cycling, several of the crystals were re-measured over the entire covered temperature range. A few crystals were removed from the cryostat, provided with electrodes, and re-measured. It was found that the maximum fluctuation was less than 3%.

### III. Results and Analysis

The Hall effect and electrical conductivity measurements were made between 4.2°K and 300°K on In-doped and Cu-doped CdS single crystals. Detailed analyses of the Hall coefficient and electrical conductivity data will be given for the In-doped CdS. For Cu-doped CdS, only qualitative descriptions will be given due to the non-conclusive results obtained from the present measurements.

#### Single-Donor-Level Model for In-doped CdS

In analyzing the carrier concentration data versus temperature for In-doped CdS, we first try a single-donor-level model and use the well-known formula<sup>12</sup> for nondegenerate statistics, e.g.,

$$n(n + N_A)/(N_D - N_A - n) = \left(\frac{N_C}{g}\right) \exp(E_D/kT) \quad (1)$$

for the electron concentration  $n$ . Here  $N_C = 2(2\pi m_e kT/h^2)^{3/2}$ ,  $m_e$  being the density-of-states electron mass and  $g$  the degeneracy factor which depends on the nature of the impurity states and the band edge involved. Later when considering the carrier concentration associated with two shallow donor states, we set up the generalization of (1) appropriate to that case. The electron concentration is assumed to be given by  $|R_H e|^{-1}$  for simplicity, where  $R_H$  is the Hall constant and  $e$  is the electronic charge. The factor  $r = \mu_H/\mu_d$ , the ratio of Hall to drift mobilities is, thus, taken to be unity. This is, in fact, a fairly good approximation for CdS moderately doped with indium impurity. We take the electron effective mass,  $m_e = 0.2 m_0$ , for calculating the donor level from Eq. (1), which is the most acceptable value obtained so far<sup>3</sup> for CdS. If Eq. (1) were used for calculating the shallow impurity level in In-doped CdS, a linear slope with  $E_{D1} = 0.0154$  eV was obtained for  $77^\circ\text{K} < T < 300^\circ\text{K}$  from  $\ln[n(n + N_A)/(N_D - N_A - n) T^{3/2}]$  versus  $\frac{1}{T}$  plot.

The assumed values for  $N_D$  and  $N_A$  for this case are  $N_D = 5 \times 10^{17} \text{ cm}^{-3}$  and  $N_A = 1 \times 10^{17} \text{ cm}^{-3}$ , respectively. The ionization energy  $E_{D1} = 0.154$  eV

---

<sup>†</sup>  $N_A = 1 \times 10^{17} \text{ cm}^{-3}$  is chosen so that consistent results in the curve fit of Fig. 2 can be obtained for  $20^\circ\text{K} < T < 300^\circ\text{K}$ .

obtained from this curve-fit for In-level is about two times lower than the reported values<sup>13</sup>. In addition, the experimental points deviated considerably from the theoretical curve for  $T < 77^\circ\text{K}$ , indicating the inadequacy of using a single-impurity level model for In-doped CdS. In fact, this discrepancy can be eliminated if a two-donor-level mode is used to fit the electron concentration data between  $300^\circ\text{K} > T > 20^\circ\text{K}$ .

#### Two-Donor-Level Model for In-doped CdS

Fig. 1 shows the electrical conductivity and Hall coefficient versus  $1/T$  for In-doped CdS, for  $4.2^\circ\text{K} < T < 300^\circ\text{K}$ . It is noted from the conductivity versus  $1/T$  curve, shown in Fig. 1, that normal band conductivity was observed for  $300^\circ\text{K} > T > 20^\circ\text{K}$ , and impurity band hopping conductivity was observed for  $T < 20^\circ\text{K}$ . In the normal band conductivity region where non-degenerate statistics hold, we use the two-donor-level model to perform the curve-fit from the electron concentration data versus  $1/T$ . The results indicate that the indium-donor level is responsible for the electron conduction between  $300^\circ\text{K}$  and  $77^\circ\text{K}$  (range I), while another unidentified donor state dominates the conduction mechanism for temperatures between  $20^\circ\text{K}$  and  $77^\circ\text{K}$  (range II). In order to analyze the electron concentration data for the above temperature regions, we start with the charge-neutrality equation, and assume that  $N_{D1}$  and  $E_{D1}$  are the indium density and ionization energy, respectively;  $N_{D2}$  and  $E_{D2}$  are the density and ionization energy of the unknown defects, respectively. The acceptor density for this sample is assumed to be  $N_A$ . The electron concentration data can be analyzed in two temperature regions, using nondegenerate statistics as given by Eq. (1). For range (I) the following expression is obtained for  $n$  versus  $T$ :

$$\frac{n(n + N_A - N_{D2})}{(N_{D1} + N_{D2} - N_A - n)} = \frac{n \left[ \frac{n}{N_A} - \left( \frac{N_{D2}}{N_A} - 1 \right) \right]}{\left[ \frac{N_{D1}}{N_A} - \frac{n}{N_A} + \left( \frac{N_{D2}}{N_A} - 1 \right) \right]} = \frac{1}{g} N_c \exp(E_{D1}/kT) \quad (2)$$

In this temperature region, the second donor state,  $E_{D2}$ , is assumed completely ionized, while the first donor state,  $E_{D1}$  is partially filled. In range (II), the first donor state is assumed completely filled and the second donor state is partially ionized. The relationship between  $n$  and  $T$  in this temperature range is given by:

$$\frac{n(n + N_A)}{(N_{D2} - N_A - n)} = \frac{1}{g} N_c \exp(E_{D2}/kT) \quad (3)$$

Since  $n \ll N_A$  and  $n \ll N_{D2} - N_A$  for  $T < 77^\circ\text{K}$ , eqn. (3) can be reduced to

$$n \approx \left(\frac{N_C}{g}\right) \left(\frac{N_{D2}}{N_A} - 1\right) \exp(E_{D2}/kT) \quad (3-a)$$

With the aid of Eqs. (2) and (3-a),  $E_{D1}$ ,  $E_{D2}$  and  $N_{D1}$ ,  $N_{D2}$  can be determined by assuming values of  $N_A$ ,  $g$ , and using values of  $n$  determined from the Hall constant. The procedures for determining these parameters are indicated in the legend of Fig. 2.

For temperatures below  $20^\circ\text{K}$ , the impurity band hopping conduction process dominates the conduction mechanism; this is shown in Fig. 1. For  $T < 20^\circ\text{K}$ , the indium levels are completely filled and the second donor state, ( $E_{D2}$ ), is partially filled. Presumably the electron conduction is by hopping from one filled state to the nearest empty state in this level. The hopping conductivity for  $T < 20^\circ\text{K}$  is shown by the dashed line in Fig. 1 for In-doped CdS. The low electron mobility for  $T < 10^\circ\text{K}$  is more evidence for the hopping conduction in this material (e.g., for  $T = 10^\circ\text{K}$ ,  $\mu_H = 10 \text{ cm}^2/\text{V-sec}$ ). The hopping conductivity activation energy observed from conductivity versus inverse temperature curve for  $T < 20^\circ\text{K}$  is found to be  $0.00035 \text{ eV}$ .

Electron mobilities of In-doped and Cu-doped CdS were determined from the conductivity and Hall effect measurements between  $4.2^\circ\text{K}$  and  $300^\circ\text{K}$ , as is shown in Fig. 3. The present results are adequate to permit a study of the dominant scattering mechanisms. From the near equality of the mobilities for  $T > 200^\circ\text{K}$  for samples with different doping and from their fairly rapid increase with decreasing temperature, it appears that the  $\mu_H$  for  $T \gtrsim 200^\circ\text{K}$  are determined by the intrinsic properties of the two samples and not by the crystal defects. The scattering of electrons in this temperature range is most likely by the longitudinal optical phonons<sup>1</sup>. The best fit of the mobility data for  $T \gtrsim 200^\circ\text{K}$  is given by  $\mu_L \approx 110[\exp(300 \pm 10)/T - 1]$ . For both In-doped and Cu-doped CdS samples, the electron mobility reaches a maximum at  $T = 80^\circ\text{K}$ , and then decreases with decreasing temperatures. The doping density of both copper and indium is approximately equal to  $5 \times 10^{17} \text{ cm}^{-3}$ . The significant difference in electron mobility for both samples for  $T < 100^\circ\text{K}$  depends mainly on the effectiveness of the ionized impurity scattering of electrons by both centers. Since indium atoms introduce a shallow donor level in CdS with a single positive charge when it is ionized, the electrons experience a Coulomb attractive potential while being scattered by such centers. On the other hand, the copper atoms introduce a deep acceptor level, and it

will stay as  $\text{Cu}_{\text{Cd}}'$ , with a single negative effective charge. The electrons similarly will experience a Coulomb repulsive potential while being scattered by such centers. In general, the scattering cross-section for the former is much greater than for the latter<sup>14</sup>. As a result, the electron mobility in Cu-doped CdS is much higher than that of In-doped CdS for  $20^\circ\text{K} < T < 100^\circ\text{K}$ . For In-doped CdS, the electron mobility decreases exponentially with temperature for  $T < 15^\circ\text{K}$ , indicating a hopping type conduction takes place in the localized states.

In addition to the conductivity and the Hall effect measurements reported above, we have done an optical transmission measurement on the In-doped CdS sample in the wavelength interval between  $2.5\ \mu\text{m}$  and  $40\ \mu\text{m}$ . A strong absorption peak was observed at  $7.14\ \mu\text{m}$ , corresponding to a defect level at  $0.175\ \text{eV}$  below the conduction band edge (neglecting Frank-Condon shift). No conclusion can be drawn regarding the type of defect involved without further investigation.

#### IV. Conclusions

Electrical conductivity and Hall effect measurements have been made between  $300^\circ\text{K}$  and  $4.2^\circ\text{K}$  on In-doped and Cu-doped CdS single crystals. A two-donor-level model has been proposed for the In-doped CdS in order to interpret the electron concentration data between  $20^\circ\text{K}$  and  $300^\circ\text{K}$ . The results yield  $E_{\text{D1}} = 0.033\ \text{eV}$  for In-level which is in excellent agreement with the recent report by Nassau et al<sup>15</sup>. The ionization energy observed between  $77^\circ\text{K}$  and  $20^\circ\text{K}$  for an unknown donor level is  $E_{\text{D2}} = 0.007\ \text{eV}$ . This energy is smaller than the predicted value by the hydrogenic impurity model which for the case of CdS should be  $0.0305\ \text{eV}$ . Although we have no adequate explanation in this respect, an unknown donor state with identical ionization energy,  $E_{\text{D}} = 0.007\ \text{eV}$ , has been reported by Itakura and Toyada<sup>11</sup> in a high purity undoped CdS between  $50^\circ\text{K}$  and  $10^\circ\text{K}$ . It is believed that the low temperature hopping conduction observed in our In-doped CdS samples is taking place at this unknown donor state because the thermal energy in this temperature range is much smaller than  $E_{\text{D2}}$ . Optical transmission experiments revealed another defect level at  $0.175\ \text{eV}$  below the band edge. The scattering of electrons is independent of the types of impurities for  $T > 200^\circ\text{K}$  and is mainly due to the longitudinal optical mode scattering. Impurity hopping conduction was observed for In-doped CdS for  $T < 20^\circ\text{K}$ . This was not observed for the case of Cu-doped CdS with the same amount of impurity concentration.

### References

1. F. A. Kroger, H. J. Vink and J. Volger, Philips Res. Rept. 10.39 (1955).
2. H. Miyazawa, H. Maeda and H. Tomishima, J. Phys. Soc. Japan 14, 41 (1959).
3. S. S. Devlin, Shiozawa, L. R., and J. M. Jost, Research on II-VI Compound Semiconductors, Final Report, Contract No. ARL-65-98, Aerospace Research Laboratories, Wright-Patterson Air Force Base, Ohio (1965).
4. H. Fujita, K. Kobayashi, T. Sawai and K. Shiga, J. Phys. Soc. Japan, 20, 109 (1965).
5. A. G. Redfield, Phys. Rev. 94, 526 (1954).
6. K. Morikawa, J. Phys. Soc. Japan 20, 1728 (1965).
7. H. H. Woodbury and M. Aven in: Radiation Damage in Semiconductors, 7th International Conf. on the Physics of Semiconductors, p. 179 (1964).
8. G. W. Bradberry and W. E. Spear, Brit. J. Appl. Phys. 15, 1127 (1964).
9. V. Buget and G. T. Wright, Brit. J. Appl. Phys. 16, 1457 (1965).
10. W. W. Piper and R. E. Halsted in: Proc. Intern. Conf. on Semicond. Physics, Prague, Czech., p. 1046 (1960).
11. M. Itakura and H. Toyoda, J. Phys. Soc. Japan 18, 150 (1963).
12. T. H. Geballe, Semiconductors, edited by N. B. Hannay (Reinhold Publ. Corp., New York, 1959) p. 313.
13. See, for example: R. H. Bube, Photoconductivity of Solids, p. 160, Wiley & Sons (1960).
14. A. F. Gibson and R. E. Burgess, Progress in Semiconductors, Vol. 8, p. 80 Wiley & Sons (1964).
15. K. Nassau, C. H. Henry, and J. W. Shiever, Proc. of the 10th International Semicond. Phys. Conf., p. 629 (1970).

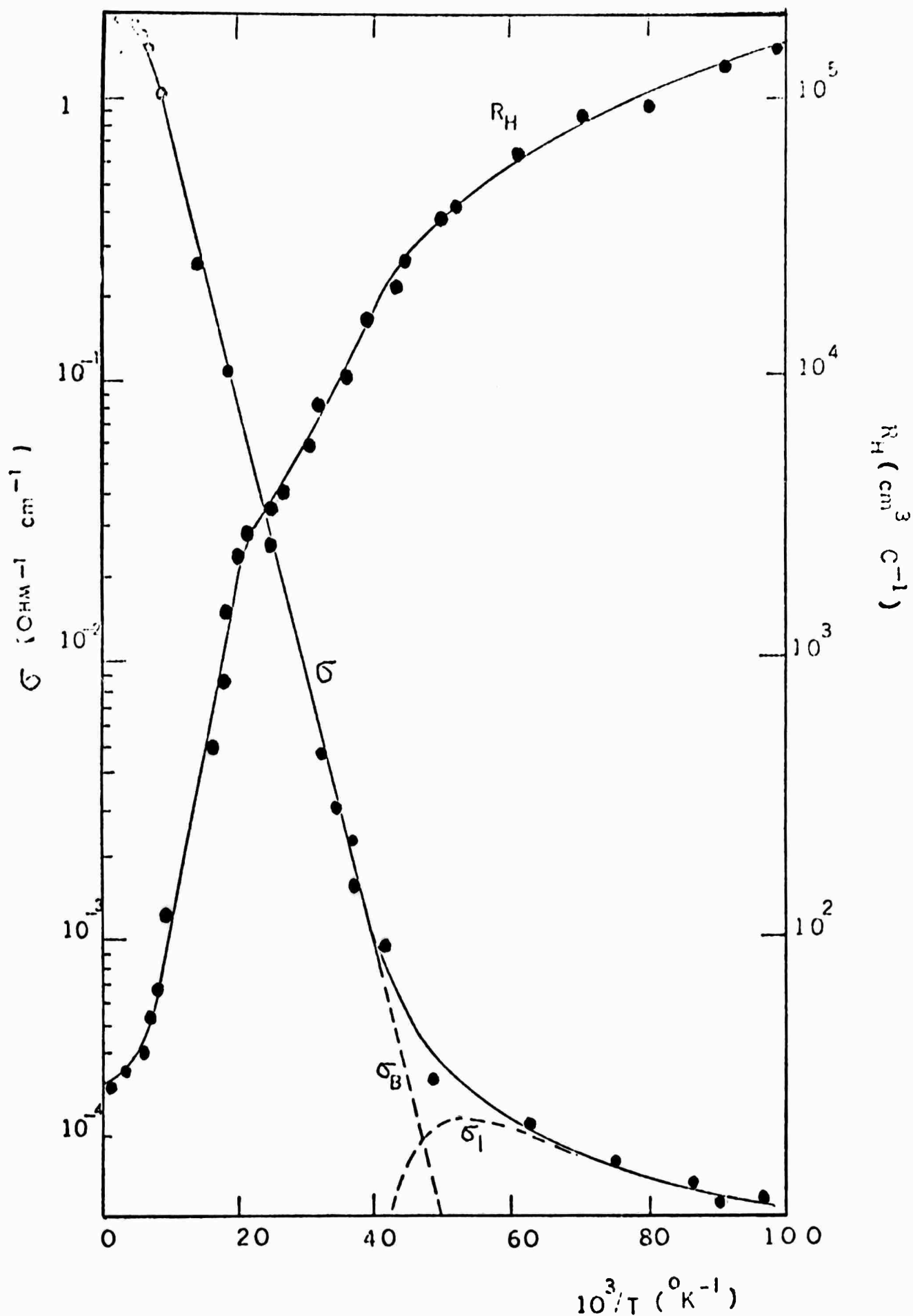


Fig. 1 Electrical conductivity,  $\sigma$ , and Hall coefficient,  $R_H$ , versus  $1/T$  for In-doped CdS, for  $4.2^\circ\text{K} < T < 300^\circ\text{K}$ . For  $T < 25^\circ\text{K}$ , the conductivity data,  $\sigma$ , is decomposed into two parts (dashed line); one due to normal band conduction and the other due to the impurity hopping conduction. The indium concentration is  $X_D \approx 6 \times 10^{17}\text{cm}^{-3}$  and  $\sigma = \sigma_B + \sigma_I$  for  $T < 25^\circ\text{K}$ .



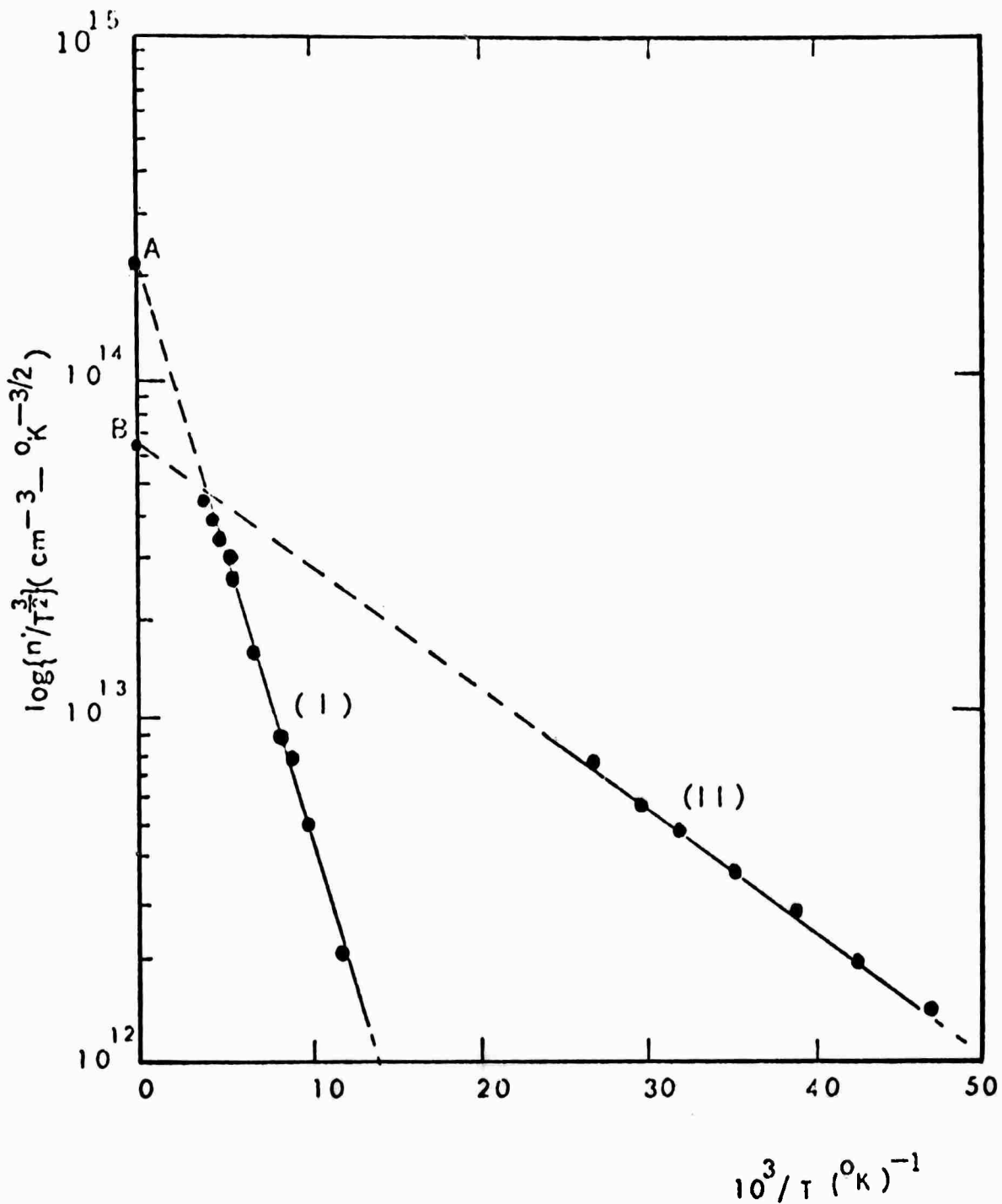


Fig. 2 Region (I) is a plot of  $\ln\{n[n + N_A - N_{D2}]/[N_{D1} + N_{D2} - n] T^{3/2}\}$  versus  $1/T$ . The slope of this straight line yields  $E_{D1} = 0.033$  eV, and the extrapolation of this line to the intercept of the ordinate is  $A = \frac{2}{g} (2\pi m_e k/h^2)^{3/2} = 2.1 \times 10^{14}$ , which yields  $m_e = 0.2 m_0$ . Region (II) is a plot of  $\ln[n/T^{3/2}]$  versus  $1/T$ . The slope of this line yields  $E_{D2} = 0.007$  eV and the intercept of this line with ordinate is  $B = A(\frac{N_{D2}}{N_A} - 1) = 6 \times 10^{17} \text{ cm}^{-3}$  and  $N_{D2} = 1.3 \times 10^{17} \text{ cm}^{-3}$ .

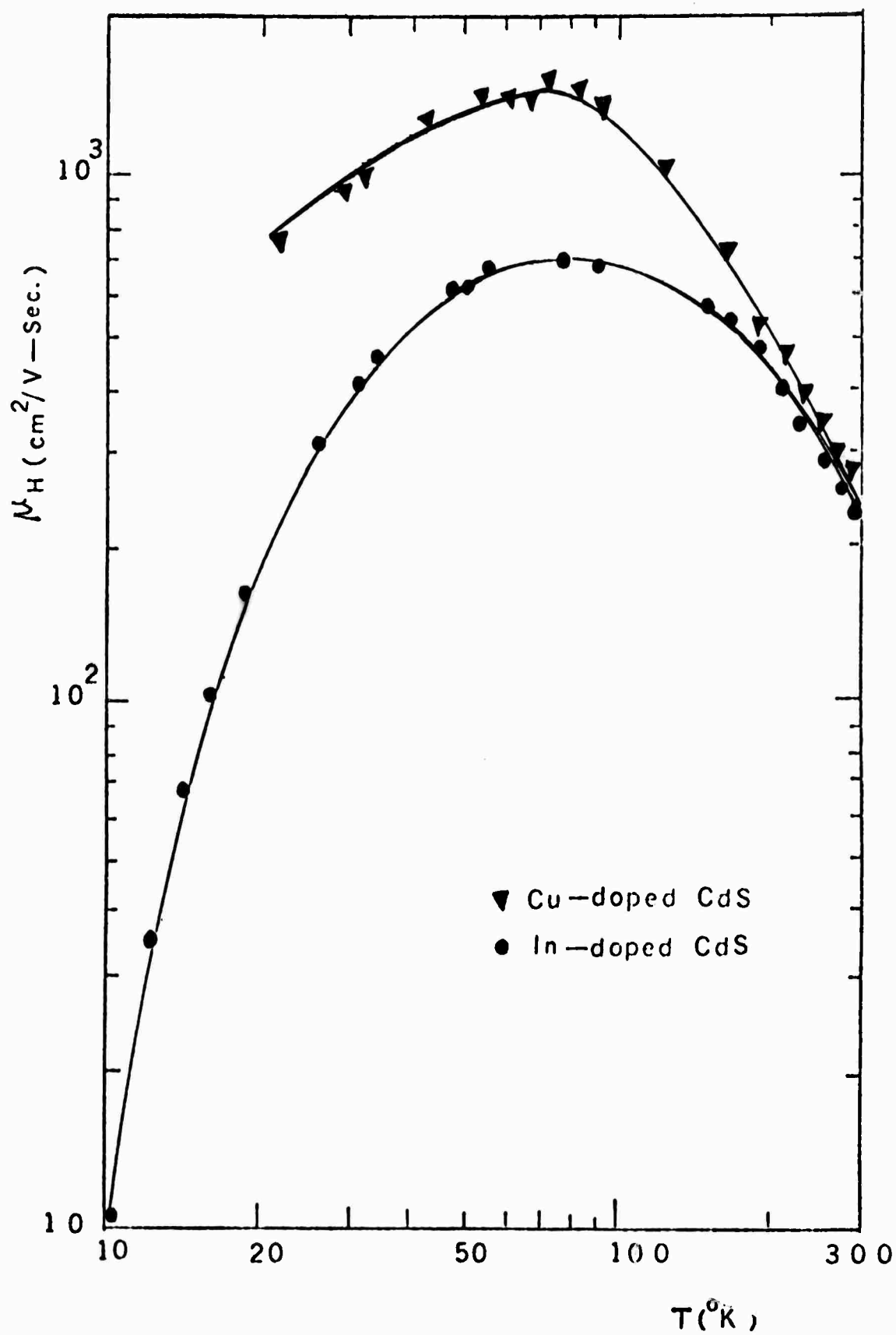


Fig. 3 Electron mobility versus  $T$  for In-doped and Cu-doped CdS.  
 $\mu_L \approx 110[\exp(300 \pm 10/T) - 1] \frac{\text{cm}^2}{\text{V-sec}}$  for  $T > 200^\circ\text{K}$ .

D. STUDY OF ROOM TEMPERATURE PHOTOMAGNETOELECTRIC AND PHOTOCONDUCTIVE EFFECTS IN Au-DOPED SILICON (S. S. Li and H. F. Tseng)

I. Introduction

In our recent study of the low temperature PME and PC effects in gold-doped silicon<sup>1,2</sup>, we reported that at very low temperatures (from 4.2°K to 100°K) a nonlinear quadratic relationship was obtained between  $\Delta p$  and  $\Delta n$  (i.e.,  $\Delta p = \Gamma \Delta n^2$ ) at moderate injection range as a result of the hole trapping at the gold acceptor levels. This results in a 4/3 power law relation between PME short circuit current and the photoconductance (i.e.,  $I_{PME} \propto \Delta G^{4/3}$ ). In this paper, we report the results of room temperature measurements of the PME and PC effects in a relatively thin Au-doped silicon ( $d \approx 0.1$  mm) sample. A method of determining the recombination parameters such as electron and hole lifetimes, the electron and hole capture probabilities at the gold levels using steady state PME and PC effects is demonstrated in the present paper. The results are found in good agreement with the experimental data available in the literature as determined from the Hall effect, photoconductivity decay and photovoltaic effect experiments<sup>3-5</sup>.

II. Theory

The physical model used in developing the room temperature recombination theory and the photomagnetolectric (PME) effect in Au-doped silicon is based on the following assumptions and facts:

1. The samples were overcompensated by gold impurity (i.e.,  $N_{Au} > N_D$  or  $N_{Au} > N_A$ ), and thus in the exhaustion region  $N_{Au} \gg n_0$ , or  $p_0$  is valid.
2. Small injection ( $\Delta n < n_0$ , or  $\Delta p < p_0$ ) and small magnetic field ( $\mu B < 1$ ) conditions are assumed.
3. The generation of electron-hole pairs by incident photons is in the vicinity of the illuminated surface. (i.e.,  $\alpha d \gg 1$ , where  $\alpha$  is the absorption coefficient and  $d$  is the sample thickness).
4. The surface recombination velocity,  $s_0$ , on the illuminated surface is much smaller than the dark surface recombination velocity,  $s_d$ , (i.e.,  $s_0 \ll s_d$ ).
5. One-dimensional analysis is valid ( $l \gg d$ ) and end effect is ignored.

The notations used above, unless otherwise specified, have the conventional meanings<sup>1</sup>.

#### A. Excess Carrier Lifetimes and the Ratio of Excess Carrier Density

In order to interpret the steady state photomagnetolectric and photoconductive effects in gold-doped silicon, it is necessary to develop the expressions for the excess carrier lifetimes and the ratio of injected excess carrier density. In the case of gold over-compensated silicon, the Fermi level is locked near the center of the forbidden gap, and the gold concentration and the shallow donor (or acceptor) density will be much larger than the thermal equilibrium concentration of the free carriers (i.e.,  $N_{Au}, N_D \gg n_o, p_o$  or  $N_{Au}, N_A \gg n_o, p_o$ ). The recombination and trapping mechanism for such samples is that only one of the two levels of the gold atoms in the band gap will be effective in recombination process (i.e., acceptor level for n-type material, and donor level for p-type samples); the other level will act as a trapping center for minority carriers.

The density of gold atoms with different charge states can be expressed by: (a) for n-type material,

$$\begin{aligned} N_{Au}^0 &= N_{Au} - (N_D - n_o) \\ &\approx N_{Au} - N_D \end{aligned} \quad \begin{array}{l} \text{is the density for} \\ \text{neutral gold centers} \end{array} \quad (1)$$

and

$$\begin{aligned} N_{Au}^- &= N_D - n_o \\ &\approx N_D \end{aligned} \quad \begin{array}{l} \text{is the density for nega-} \\ \text{tively charged gold-acceptor} \\ \text{centers} \end{array} \quad (2)$$

(b) for p-type material

$$\begin{aligned} N_{Au}^0 &= N_{Au} - (N_A - p_o) \\ &\approx N_{Au} - N_A \end{aligned} \quad (3)$$

$$N_{Au}^+ = N_A - p_o \approx N_A \quad \begin{array}{l} \text{is the density for positively} \\ \text{charged gold donor centers} \end{array} \quad (4)$$

For small injection case (i.e.,  $\Delta n \ll N_{Au}^0$ ,  $\Delta p + \Delta p_t \ll N_{Au}^-$ ,  $N_{Au}^0$  for n-type;  $\Delta p \ll N_{Au}^0$ ,  $\Delta n + \Delta n_t \ll N_{Au}^+$ ,  $N_{Au}^+$  for p-type), the variation of gold charge states with injection can be ignored. Therefore, the lifetimes of the injected carriers are independent of the light intensity.

For n-type samples, the electron lifetime,  $\tau_n$ , ( $\tau_n$  is defined as the

free time that an electron spends in the conduction band before captured by the neutral gold acceptor level) can be expressed by:

$$\tau_n = \frac{1}{C_n^0 N_{Au}^0} = \frac{1}{C_n^0 (N_{Au} - N_D)} \quad (5)$$

where  $C_n^0$  is the rate of electron capture probabilities ( $\text{cm}^3\text{-sec}^{-1}$ ) by the neutral gold acceptor centers, and  $N_{Au}^0$  is substituted by  $(N_{Au} - N_D)$  using Eq. (1). The hole lifetime,  $\tau_p$ , at the negatively charged gold acceptor centers, can be expressed by:

$$\tau_p = \frac{1}{C_p^- N_{Au}^-} = \frac{1}{C_p^- N_D} \quad (6)$$

where  $C_p^-$  represents the rate of hole capture probabilities by the negatively charged gold acceptor centers, and  $N_{Au}^-$  is substituted by  $N_D$  using Eq. (2).

Similarly, the electron and hole lifetimes at the gold donor level,  $\tau_n$  and  $\tau_p$ , in p-type samples can be defined by:

$$\tau_n = \frac{1}{C_n^+ N_{Au}^+} = \frac{1}{C_n^+ N_A} \quad (7)$$

and

$$\tau_p = \frac{1}{C_p^0 N_{Au}^0} = \frac{1}{C_p^0 (N_{Au} - N_A)} \quad (8)$$

where  $C_n^+$  and  $C_p^0$  represent the capture probabilities for electrons and holes at the positively charged and neutral gold donor levels, respectively. The  $N_{Au}^+$  is substituted by  $N_A$  using Eq. (4), and  $N_{Au}^0$  is substituted by  $(N_{Au} - N_A)$  using Eq. (3).

The reason that the minority carrier trapping at the gold centers does not influence the steady state excess carrier lifetime is quite obvious for small injection cases. To be more specific, let us consider only the case of n-type gold-doped silicon: the gold acceptor levels will act as recombination centers, while the gold-donor levels will act as hole-trap centers. The condition for a trap-level is that the recombination at this level is negligible (compared to the recombination rate at the gold acceptor levels). This means that the probabilities of electrons being captured by the gold donor levels can be neglected. Therefore, we can set the electron recombination rate at the gold donor levels to be zero, i.e.,

$$U_{tn} = 0 \quad (9)$$

while for small injection, the hole recombination rate at the gold donor

levels,  $U_{tp}$  can be expressed by<sup>6</sup>:

$$U_{tp} = C_p^{\circ} (N_{Au}^{\circ} \Delta p - p_{1t} \Delta N_{Au}^{+}) \quad (10)$$

where,  $p_{1t}$  denotes the hole concentration in the valence band when the donor level coincides with the Fermi level, and  $\Delta N_{Au}^{+}$  is the excess density of gold-donor levels being filled by the captured holes. For steady state,  $U_{tp} = U_{tn} = 0$ , since the capture of holes is exactly balanced by their emission. The steady state electron and hole lifetimes  $\tau_n$  and  $\tau_p$  are given by:

$$\tau_n = \frac{\Delta n}{(U_{cn} + U_{tn})} = \frac{\Delta n}{U_{cn}} \quad (11)$$

$$\tau_p = \frac{\Delta p}{(U_{cp} + U_{tp})} = \frac{\Delta p}{U_{cp}} \quad (12)$$

From Eqs. (11) and (12) we know that the steady state excess carrier lifetimes are only controlled by the recombination centers (i.e., the gold acceptor levels). The only effect of these trap-centers is their influence on the a.c. response time of the PME voltage, which will not be discussed in the present paper.

The rates of recombination of electrons and holes through recombination centers are equal in the steady state case<sup>6</sup>:

$$U_{cn} = \frac{\Delta n}{\tau_n} = U_{cp} = \frac{\Delta p}{\tau_p} \quad (13)$$

If we define  $\Gamma$  as the ratio of excess electron and hole density, then from Eqs. (5-8,13) we find:

(a) for n-type material,

$$\Gamma = \frac{\Delta n}{\Delta p} = \frac{\tau_n}{\tau_p} = \frac{C_p^{-} N_D}{C_n^{\circ} (N_{Au} - N_D)} = \frac{N_D}{(N_{Au} - N_D)} \gamma_{1/2} \quad (14)$$

where  $\gamma_{1/2} = \frac{C_p^{-}}{C_n^{\circ}}$  is the ratio of hole and electron capture probabilities at gold acceptor levels and

(b) for p-type material

$$\Gamma = \frac{\Delta n}{\Delta p} = \frac{\tau_n}{\tau_p} = \frac{C_p^{\circ} (N_{Au} - N_A)}{C_n^{+} N_A} = \frac{(N_{Au} - N_A)}{N_A} \gamma_{-1/2} \quad (15)$$

where  $\gamma_{-1/2} = \frac{C_p^{\circ}}{C_n^{+}}$  is the ratio of hole and electron capture probabilities at gold donor levels.

From Eqs. (5-8) and (14-15), it is noted that one can easily control the

lifetimes of excess carriers and the ratio of excess carrier density simply by controlling the compensation ratio of  $N_{Au}$  and  $N_D$  for n-type samples, and  $N_{Au}$  and  $N_A$  for p-type cases.

#### B. The Photomagnetolectric and Photoconductive Effects

The results in part (A) yield the relationship between the injected excess carrier density for Au-doped silicon under small injection conditions. In this section, the results of part (A) will be used in the derivation of the PME effect for gold-doped silicon. The electron and hole current density equations are given by:

$$J_{nx} = q\mu_n n \epsilon_x - \mu_n B J_{ny} \quad (16)$$

$$J_{px} = q\mu_p p \epsilon_x + \mu_p B J_{py} \quad (17)$$

$$J_{ny} = q\mu_n n \epsilon_y + qD_n \frac{d\Delta n}{dy} \quad (18)$$

$$J_{py} = q\mu_p p \epsilon_y - qD_p \frac{d\Delta p}{dy} \quad (19)$$

$$J_{ny} + J_{py} = 0 \quad (20)$$

and the relation between  $\Delta n$  and  $\Delta p$  is given by Eqs. (14) and (15).

The continuity equation for electrons in the y-direction (i.e., the direction of illumination) is given by

$$\frac{1}{q} \frac{d}{dy} J_{ny} - U_{cn} = 0 \quad (21)$$

The boundary conditions at the illuminated and the dark surfaces of the sample are

$$[S_o \Delta n - \frac{1}{q} J_{ny}]_{y=0} = Q \quad (22)$$

$$[S_d \Delta n + \frac{1}{q} J_{ny}]_{y=d} = 0 \quad (23)$$

where  $Q$  is the photon flux density. Solving Eqs. (16-20) and with  $\Gamma = \frac{\Delta n}{\Delta p}$ , we obtain the electron current density in the y-direction

$$\begin{aligned} J_{ny} &\approx \frac{qD_n (n_o \Gamma^{-1} + p_o)}{(n_o b + p_o)} \frac{d\Delta n}{dy} \\ &= qD^* \frac{d\Delta n}{dy} \end{aligned} \quad (24)$$

where

$$D^* = \frac{D (n_o \Gamma^{-1} + p_o)}{(n_o b + p_o)} \quad \text{is the effective diffusion constant.}$$

The PME short circuit current per unit width (by setting  $\epsilon_x = 0$ ) is given by:

$$I_{PME} = \int_0^d (J_{nx} + J_{px}) dy = -B(1+b) \mu_p \int_0^d J_{ny} dy$$

or

$$I_{PME} = qB(1+b) \mu_p D^* \Delta n_o \quad (25)$$

where  $\Delta n_o$  is the excess carrier density at the illuminated surface.  $\Delta n_o$  can be related to the incident photon flux density,  $Q$ , by solving the continuity equation (21) and using the boundary condition at  $y = 0$ . The result yields  $\Delta n = \Delta n_o \exp(-y/L^*)$  and

$$\Delta n_o = \frac{L^* Q}{L^* S_o + D^*} \quad (26)$$

where  $L^* = (D^* \tau_n)^{1/2}$  is the effective diffusion length.

The PME open circuit voltage per unit length,  $V_{PME}$ , can be obtained from the relation<sup>3</sup>

$$V_{PME} = \frac{I_{PME}}{G} \quad (27)$$

Substituting (25) into (27) we obtain:

$$V_{PME} = qB(1+b) \mu_p D^* \Delta n_o / G \quad (28)$$

where  $G = G_o + \Delta G$ , and  $G_o$  is the dark conductance per unit width to length ratio.  $\Delta G$  represents the photoconductance per unit width to length ratio which can be derived from

$$\Delta G = q \mu_p (b + \Gamma^{-1}) \int_0^d \Delta n dy \quad (29)$$

Substituting  $\Delta n = \Delta n_o \exp(-y/L^*)$  into Eq. (29) and using the boundary conditions that  $\Delta n = \Delta n_o$  at  $y = 0$  and  $\Delta n = 0$  at  $y = d$  in Eq. (29), we obtain:

$$\Delta G = q(b + \Gamma^{-1}) \mu_p L^* \Delta n_o \quad (30)$$

The PME open circuit voltage,  $V_{PME}$ , can now be expressed as a function of  $\Delta G$  simply by eliminating  $\Delta n_o$  from Eq. (28) and Eq. (30). The result reads

$$V_{PME} = B \left( \frac{b+1}{b+\Gamma^{-1}} \right) \left( \frac{n_o \Gamma^{-1} + p_o}{n_o b + p_o} \right)^{1/2} \left( \frac{D}{\tau_n} \right)^{1/2} \left( \frac{\Delta G}{G} \right) \quad (31)$$



Eq. (31) predicts that for small injection case (i.e.,  $\Delta G \ll G_0$ ), the PME open circuit voltage,  $V_{PME}$ , should vary linearly with magnetic flux density,  $B$ , and the photoconductance,  $\Delta G$  (or light intensity).

Note that Eq. (31) provides a direct means for determining the electron and hole lifetimes as well as the capture probabilities from the concurrent measurements of the steady state PME and PC effects as long as values of  $\Gamma$  are known. Eq. (31) applies equally well for both p- and n-type samples. For n-type samples,  $\Gamma$  is determined from Eq. (14) and for p-type samples,  $\Gamma$  is determined by Eq. (15).

### III. Results and Analysis

An n-type silicon slab with phosphorus concentration of  $N_D = 10^{16} \text{ cm}^{-3}$  and a p-type silicon bar with boron concentration of  $N_A = 10^{14} \text{ cm}^{-3}$  were used for gold diffusion. The gold impurity was first evaporated on silicon substrates (or using  $\text{AuCl}_3$  plating) and then diffused at  $1200^\circ\text{C}$  for a twenty-four hour period and quenched to room temperature. The gold concentration was then estimated from the resistivity and Hall coefficient data and compared with the diffusion data available for gold in silicon<sup>7</sup>. The results are as follows:

(a) for n-type silicon sample

$$\begin{aligned} N_{\text{Au}} &\approx 5 \times 10^{16} \text{ cm}^{-3} \\ N_D &\approx 10^{16} \text{ cm}^{-3} \\ n_0 &= 1.3 \times 10^{12} \text{ cm}^{-3} \\ p_0 &= 1.5 \times 10^8 \text{ cm}^{-3} \quad \text{at } 300^\circ\text{K.} \\ n_i &= 1.4 \times 10^{10} \text{ cm}^{-3} \end{aligned}$$

(b) and for p-type sample

$$\begin{aligned} N_{\text{Au}} &\approx 10^{16} \text{ cm}^{-3}, \quad N_A \approx 10^{14} \text{ cm}^{-3}, \\ p_0 &= 9.6 \times 10^{12} \text{ cm}^{-3}, \quad n_0 = 2.1 \times 10^7 \text{ cm}^{-3}. \end{aligned}$$

The sample dimensions for n-type are  $7 \times 5 \times 0.1 \text{ mm}^3$  and  $7 \times 5 \times 0.2 \text{ mm}^3$  for the p-type sample. In order to satisfy the assumption (4) made in Sec. II, the front surface of the sample was chemically etched and the dark surface was sand blasted. The experimental set-up and the measuring technique is identical to our previous report<sup>8</sup>.

The results of the PME and PC measurements are shown in Fig. 1 to Fig. 6.

Figs. 1-5 are the results for the n-type sample, and Fig. 6 is for the p-type sample. Similar dependence of  $V_{PME}$  on  $B$ ,  $I_0$  and  $\Delta G$  on  $I_0$  are observed for p-type samples and only  $V_{PME}$  versus  $\Delta G/G_0$  is shown in Fig. 6 for the purpose of evaluation of carrier lifetimes.

Figure 1 shows the variation of  $V_{PME}$  versus  $B$ , with light intensity,  $I_0$ , as parameter. The results indicate that  $V_{PME}$  is directly proportional to  $B$  for various illumination intensities, which is in accord with the prediction of Eq. (31). Fig. 2 shows the variation of  $V_{PME}$  as a function of light intensity with magnetic field,  $B$ , as parameter. The results indicate that at low illumination intensity a linear relation between  $V_{PME}$  and  $I_0$  is obtained for various magnetic field strengths, and a sublinear region is observed for large illumination intensity. Fig. 3 shows a linear relationship between  $V_{PME}$  and  $I_0$  observed for two different wavelengths and magnetic field strengths. The light intensity is rather weak when the monochromator is used for measurements. This can be seen by comparison between Fig. 2 (white light) and Fig. 3 (monochromatic light). Fig. 4 demonstrates the linear relationship between  $\Delta G/G_0$  versus  $I_0$ , which is again in accord with the prediction given by Eq. (30).

In order to compare the results with theoretical prediction of Eq. (31), we plot  $V_{PME}$  versus  $\Delta G/G_0$  from Fig. 2 and Fig. 4. The results are shown in Fig. 5. Fig. 5 demonstrates the variation of  $V_{PME}$  as a function of  $\Delta G/G_0$  with  $B$  as a parameter for the n-type sample. The results indicate that for  $\Delta G/G_0 < 0.2$  a linear relationship between  $V_{PME}$  versus  $\Delta G/G_0$  is obtained, as is predicted by Eq. (31). For  $\Delta G/G_0 > 0.2$ , deviation from linearity was observed. The  $V_{PME}$  should become independent of  $\Delta G/G_0$  at very high injection levels<sup>8</sup>. For the p-type sample,  $V_{PME}$  versus  $\Delta G/G_0$  is shown in Fig. 6. One can again see that the linearity between  $V_{PME}$  versus  $\Delta G/G_0$  is obtained for  $\Delta G/G_0 \lesssim 0.12$ .

In order to calculate the electron and hole lifetimes and the carrier capture probabilities at the gold levels, it is necessary to know the electron and hole capture rate ratios,  $\gamma_{1/2}$  and  $\gamma_{-1/2}$  at gold acceptor and donor levels, respectively. Using the data given by Fairfield and Gokehale<sup>3</sup> for gold-doped silicon, it is found that

$$\gamma_{1/2} = \frac{C_p^-}{C_n} = 70 \text{ and } \gamma_{-1/2} = \frac{C_p^+}{C_n} = 0.38$$

Substituting the above values into Eqs. (14) and (15), one finds

$$\Gamma = 17.5 \text{ for n-type sample}$$

and

$$\Gamma = 38 \text{ for p-type sample.}$$

Using the above data and assuming  $b = 2$  (the electron-hole mobility ratio), the electron lifetime is then computed from Eq. (31) and from the data in the linear region of Figs. 5 or 6. The result yields  $\tau_n = 1.3 \times 10^{-8}$  sec. for the n-type sample. The electron diffusion constant,  $D_n$ , for the n-type sample used in the above calculation, is  $24.9 \text{ cm}^2/\text{sec}$ . and the hole diffusion constant  $D_p$ , for the p-type sample is  $8.8 \text{ cm}^2/\text{sec}$ . These two constants are determined from the Hall effect measurement (We have found  $\mu_n = 960 \text{ cm}^2/\text{V-sec}$  for the n-type sample and  $\mu_p = 340 \text{ cm}^2/\text{V-sec}$  for the p-type sample.) and by using the Einstein relation,  $D_{n,p} = \mu_{n,p} \left( \frac{kT}{q} \right)$ . In determining the scattering factor in the Hall Coefficient, we have assumed that the longitudinal acoustical mode lattice scattering is dominant (i.e.,  $r = 1.18$ ) and the scattering due to the gold impurity is negligible at room temperature. Other parameters such as  $\tau_p$ ,  $L^*$ ,  $C_n^o$ ,  $C_p^-$ ,  $C_n^+$  and  $C_p^o$  are calculated subsequently by using Eqs. (5) to (8), (14) and (15). For comparison, the results are summarized in Table I along with some available data in the literature.

One aspect we need to point out here is the fact that in calculating the carrier lifetimes and capture probabilities from the PME and PC measurements, we used the values of the electron-hole capture rate ratios at gold-acceptor and donor levels given by Fairfield et al.<sup>3</sup>. This discrepancy can be eliminated by concurrent measurements of the PME and PC effects on two specimens (either n-type or p-type) with different gold density or different shallow impurity density, and using the theory developed in the present paper. This would allow us to determine the capture rate ratios independently.

#### IV. Conclusions

The photomagnetolectric and photoconductive effects in gold-doped silicon have been studied at  $T = 300^\circ\text{K}$ . A linear relationship between PME open-circuit voltage versus magnetic field intensity, photoconductance and light intensity has been obtained in both n- and p-type samples under small injection conditions, which is in accord with the theoretical predictions of Eq. (31). This result indicates that the recombination and trapping mechanisms at room temperatures are quite different from those observed at low temperatures, as reported previously<sup>1,2</sup>.

A simple recombination model has been proposed to interpret the observed PME and PC effects in gold-doped silicon at room temperatures. The electron and hole capture probabilities at the gold acceptor and donor levels have been deduced from the PME and PC measurements, using the electron-hole capture rate ratios given by Fairfield et al.<sup>3</sup>, and the results are found in good agreement with those determined from other methods.

### References

1. J. Agraz and S. S. Li, Phys. Rev., B15, Sept. 15 (1970).
2. J. Agraz and S. S. Li, Phys. Rev., accepted (1970).
3. J. M. Fairfield and B. V. Gokehale, J. Solid State Elec. 8, 685 (1965).
4. G. Bemski, Proc. IRE 46, 990 (1958)
5. C. T. Sah, A. F. Tasch, Jr. and D. K. Schroder, Phys. Rev. Letters, 19, 2, 71 (1967).
6. W. Shcokley and W. T. Read, Phys. Rev., 87, 835 (1952).
7. C. B. Collins, R. O. Carlson and C. J. Gallagher, Phys. Rev. 105, 1168 (1957).
8. S. S. Li, Phys. Rev., 188, 1246 (1969).

Table I Recombination Parameters in Gold-doped Silicon at 300°K

Sample	Bemski <sup>4</sup>	Fairfield <sup>3</sup> et al	This Paper
<p>n-type</p> <p><math>N_{Au} \approx 5 \times 10^{16}</math></p> <p>and</p> <p><math>N_D = 10^{16} \text{ cm}^{-3}</math></p>	$C_n^o (\text{cm}^3\text{-sec}^{-1})$	$1.7 \times 10^{-9}$	$1.8 \times 10^{-9}$
	$C_p^- (\text{cm}^3\text{-sec}^{-1})$	$1 \times 10^{-8}$	$1.3 \times 10^{-7}$
	$\tau_n (\text{sec})$	—	$1.3 \times 10^{-8}$
	$\tau_p (\text{sec})$	—	$7.8 \times 10^{-10}$
	$L^* (\text{cm})$	—	$1.0 \times 10^{-4}$
<p>P-type</p> <p><math>N_{Au} \approx 10^{16}</math></p> <p>and</p> <p><math>N_A = 10^{14} \text{ cm}^{-3}</math></p>	$C_n^+$	$3.5 \times 10^{-8}$	$3.6 \times 10^{-8}$
	$C_p^+$	$\geq 10^{-9}$	$2.4 \times 10^{-8}$
	$\tau_n$	—	$2.7 \times 10^{-7}$
	$\tau_p$	—	$7.3 \times 10^{-7}$
	$L^*$	—	$22.1 \times 10^{-4}$

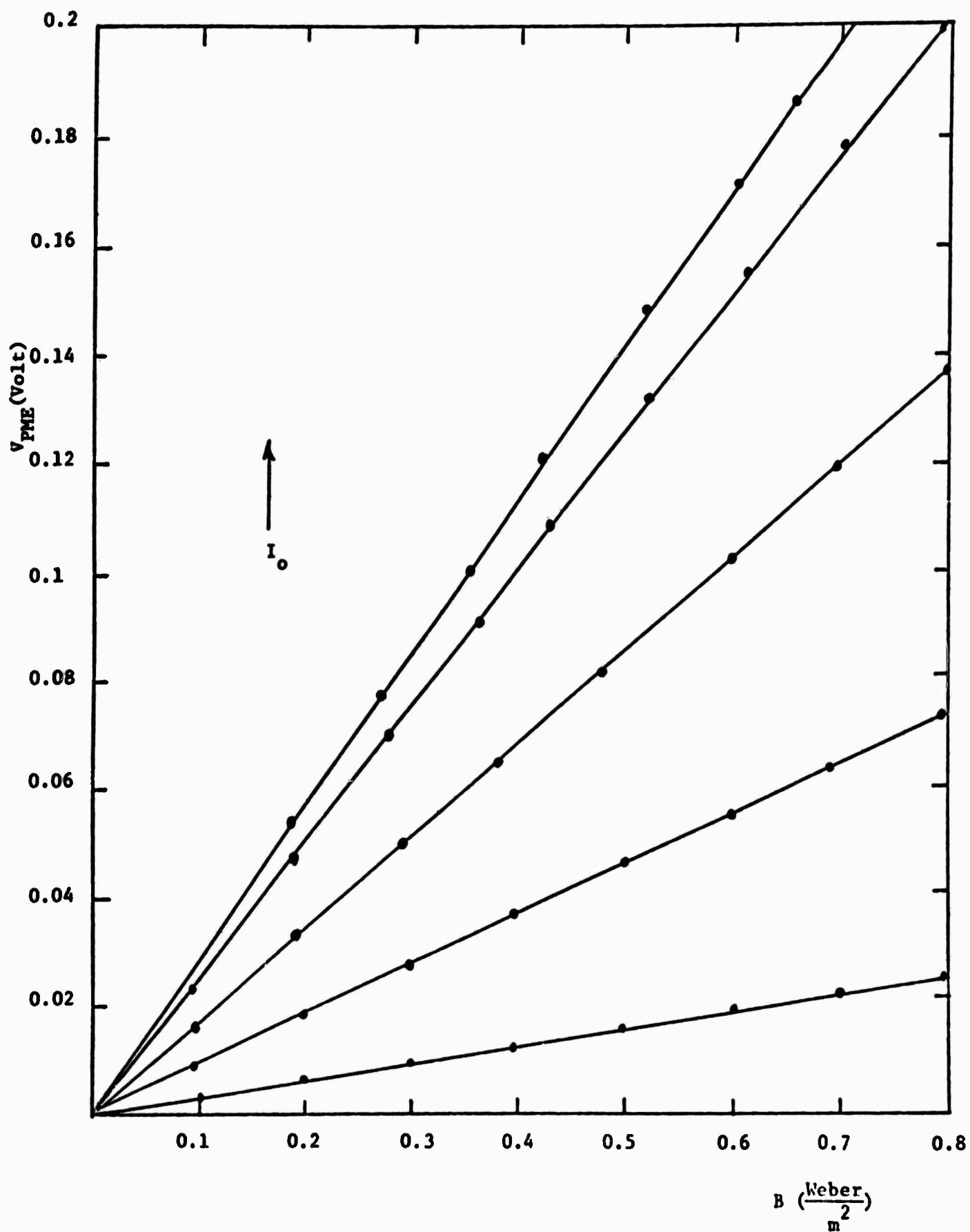


Fig. 1 The PME open circuit voltage,  $V_{PME}$ , versus magnetic flux density,  $B$ , with light intensity,  $I_0$ , as a parameter, at  $T = 300^\circ\text{K}$ . (for n-type sample).

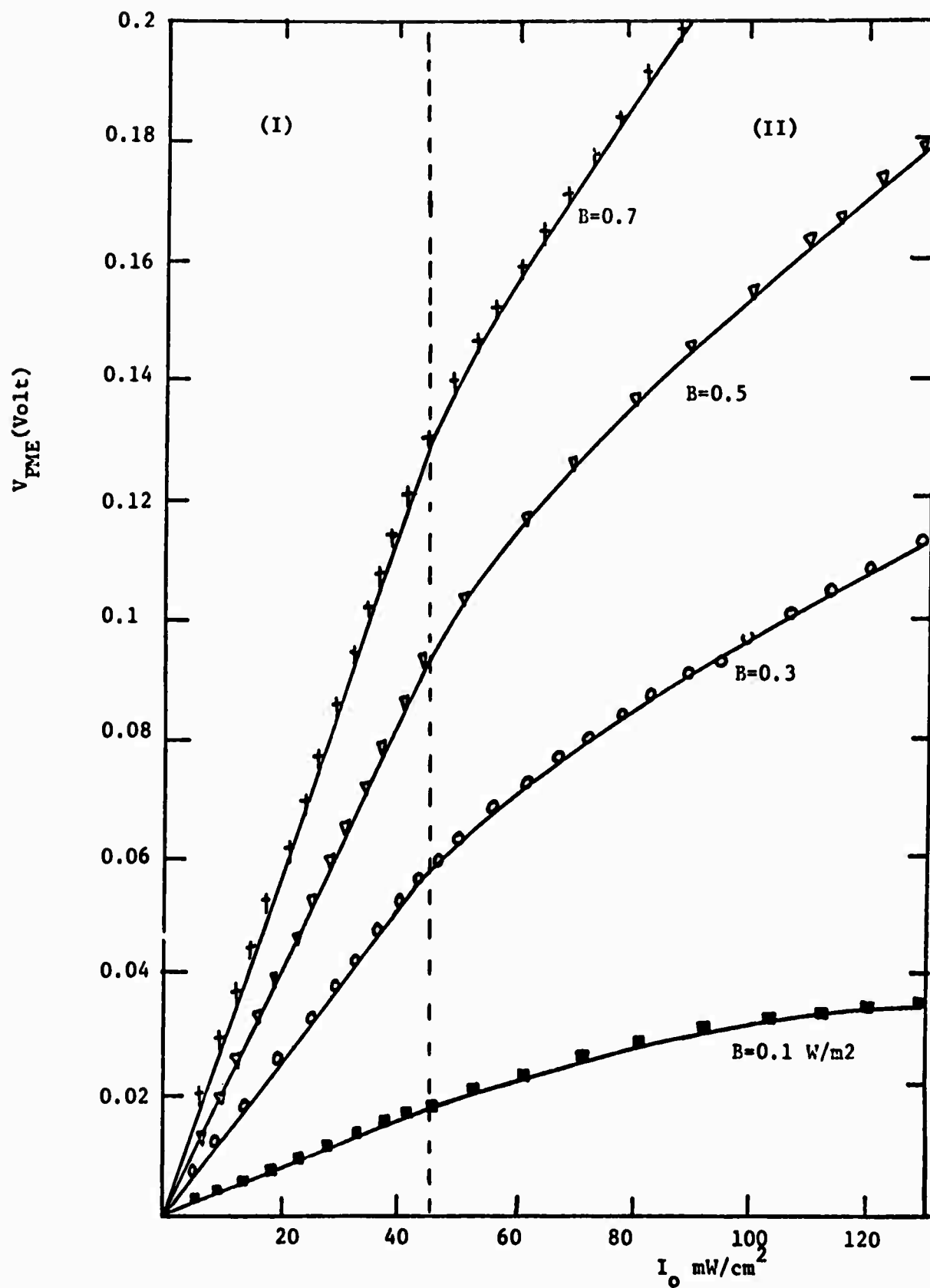


Fig. 2 The PME open circuit voltage,  $V_{PME}$ , versus light intensity,  $I_0$ , with magnetic flux density,  $B$ , as a parameter. (I) linear region, (II) sublinear region. (for n-type sample).  $T = 300^\circ\text{K}$ .

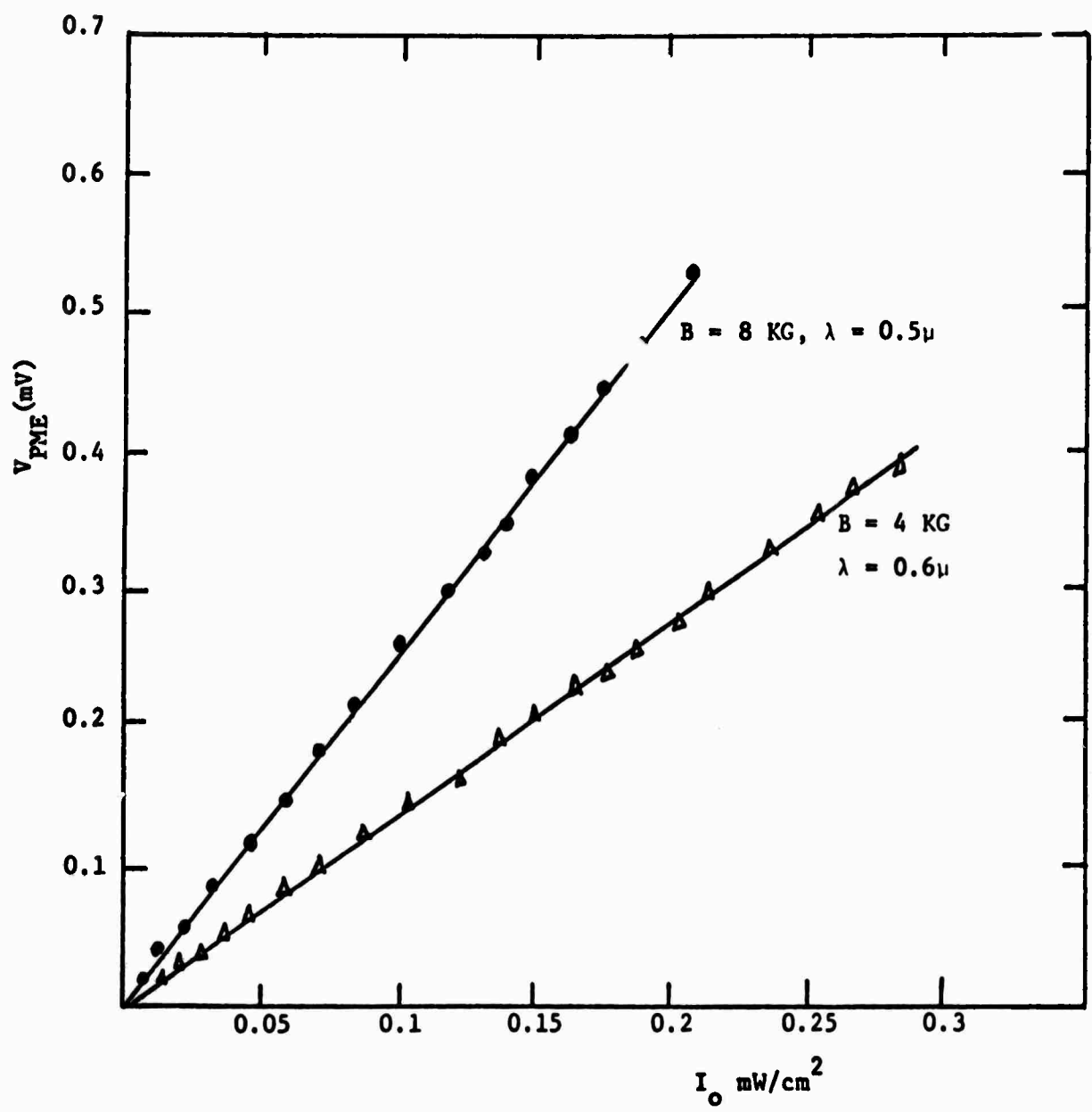


Fig. 3  $V_{PME}$  versus  $I_0$  for two different magnetic flux densities,  $B$ , and photon wavelength,  $\lambda$ . (for n-type sample).  $T = 300^\circ\text{K}$ .



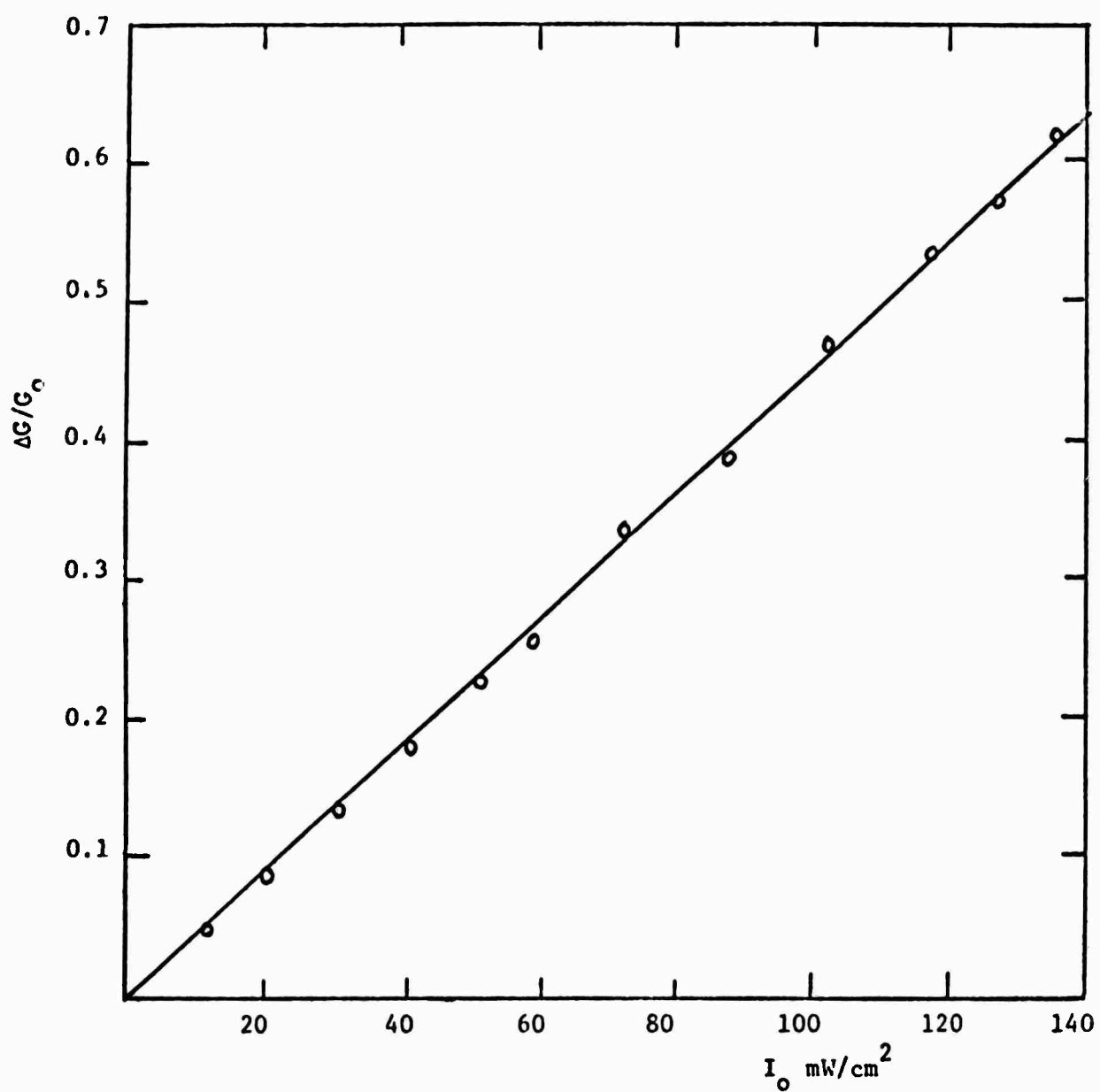


Fig. 4 Variation of the photoconductance,  $\Delta G/G$ , as a function of light intensity,  $I_0$ , at  $T = 300^\circ\text{K}$ . (for n-type sample).

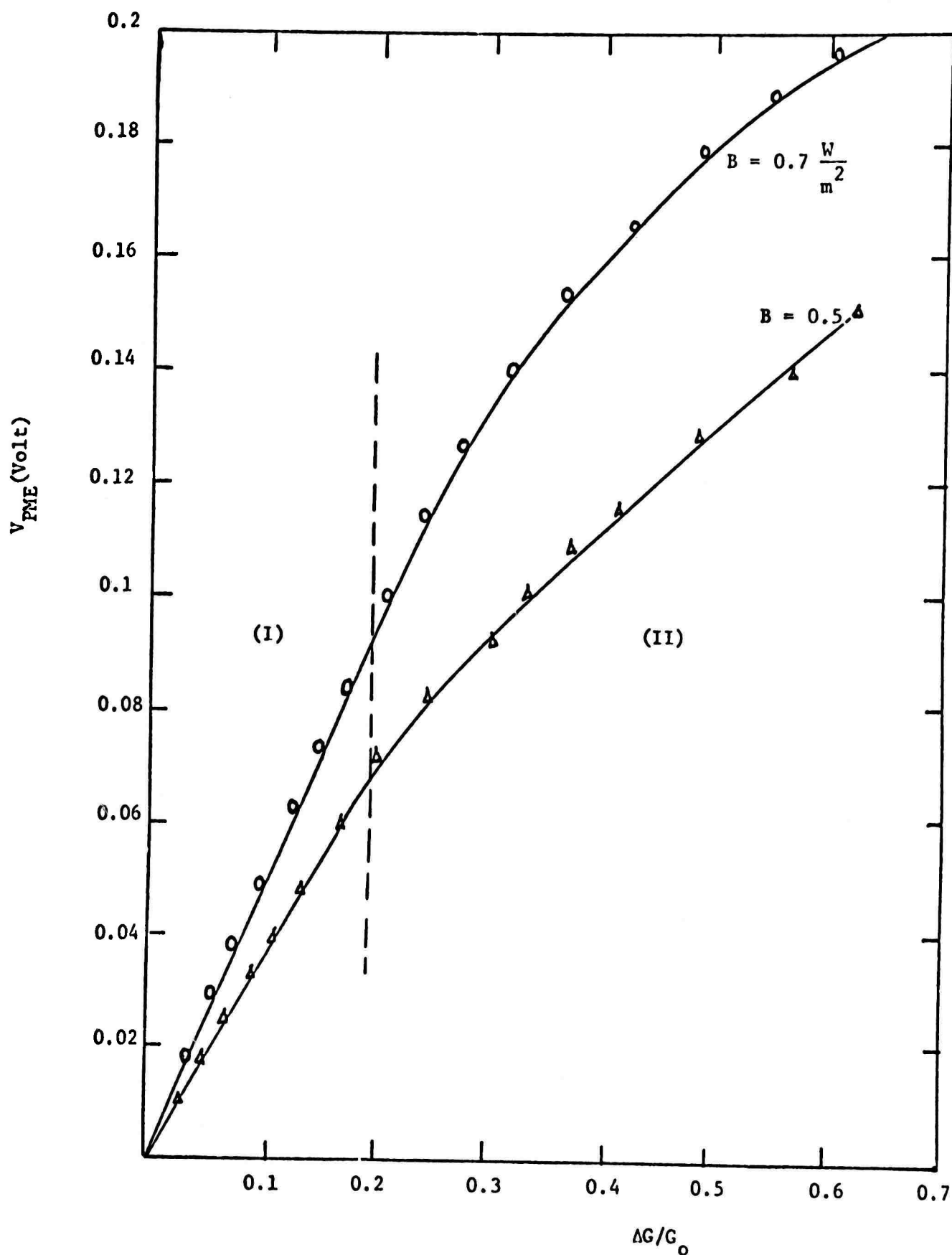


Fig. 5 Variation of the PME open circuit voltage,  $V_{PME}$ , as a function of photoconductance,  $\Delta G/G_0$ , for two different magnetic flux densities,  $B$ . (I) linear region, (II) sublinear region, for n-type sample, with  $N_{Au} \approx 5 \times 10^{16} \text{ cm}^{-3}$  and  $N_D = 10^{16} \text{ cm}^{-3}$ .  $T = 300^\circ\text{K}$ .

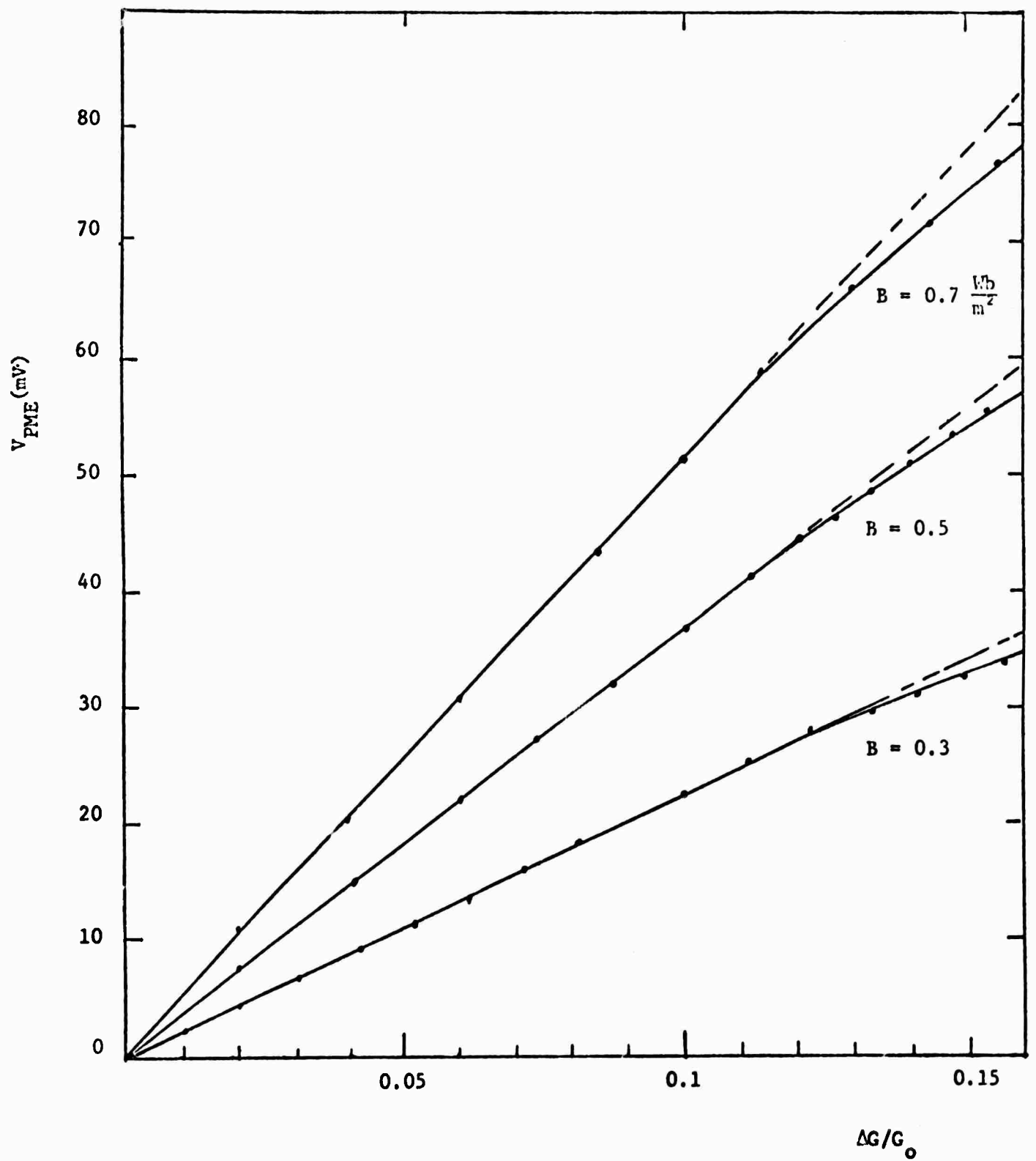


Fig. 6 Variation of the PME open circuit voltage, as a function of  $\Delta G/G_0$ , for various magnetic flux densities,  $B$ , for p-type sample with  $N_{Au} \approx 10^{16} \text{ cm}^{-3}$ ,  $N_A = 10^{14} \text{ cm}^{-3}$ .  $T = 300^\circ\text{K}$ .

## E. ASSESSING MODEL ADEQUACY AND SELECTING MODEL COMPLEXITY IN INTEGRATED-CIRCUIT SIMULATION (F. A. Lindholm, S. W. Director and D. L. Bowler)

### I. Introduction

Success in the simulation and automated design of integrated circuits depends critically on the models chosen to represent the behavior of active devices. The basic consideration involved in the choice is to obtain required accuracy from a model of minimum complexity<sup>1</sup>. Basing calculations on a model of insufficient accuracy will normally lead to meaningless results. On the other hand, use of a model more complex than needed threatens the capability of computer memory, increases c.p.u. time, increases the chance of numerical errors, and limits the size of circuits that the simulation program can accommodate. Moreover, the more complex the model the more time and effort must be spent determining the model parameters. Design using optimization techniques compounds the need for model simplicity because such design requires many circuit analyses.

In simulation of the static behavior of bipolar integrated circuits, the simplest transistor characterization commonly in use is the Ebers-Moll model<sup>2</sup> or its charge-control or Linvill equivalents<sup>3</sup>. The validity of a simulation based on this characterization then depends on how adequately the Ebers-Moll model represents the performance of each transistor in the circuit. This adequacy in turn depends on the approximations that underlie the model. In the original formulation<sup>2</sup> of the Ebers-Moll model, these approximations (or assumptions) are:

1. The transistor consists of space-charge and quasi-neutral regions<sup>4</sup>.
2. Net generation or recombination in the space-charge regions and at the surface is negligible. This includes the neglect both of thermally derived generation and recombination and of generation arising from avalanche multiplication or Zener breakdown<sup>4</sup>.
3. A Boltzmann relation of the form  $\exp(qV/kT)$  describes the dependence between the minority densities at the edges of a space-charge region and the voltage  $V$  applied across that region<sup>4</sup>.
4. The dependence of lifetime on carrier density and current is negligible<sup>4,5</sup>.
5. Conductivity modulation in the base region is negligible, as is degradation of emitter efficiency resulting from conductivity modulation<sup>4,5</sup>.
6. The electric field in quasi-neutral regions is independent of current<sup>4,5,6</sup>.
7. Uniform injection of carriers is assumed across the area of the emitter; that is, emitter crowding is negligible<sup>7,8</sup>.
8. Base widening caused by space-charge limited flow in the collector is negligible<sup>9,10</sup>.
9. Multi-dimensional flow caused by space-charge limited flow in the collector is negligible<sup>10,11</sup>.

These approximations limit the validity of the Ebers-Moll model, as it was originally formulated, to a restricted range of terminal voltages and currents. Because common methods of simulation give no assurance that the currents and voltages in each transistor of the circuit under study lie within this range, one guards against model failure by employing generalizations, to be discussed subsequently. These generalizations extend the range of validity; unfortunately, they increase model complexity.

The Ebers-Moll model fails for currents and voltages below certain critical values. In formulating a generalization that avoids this failure, one must take account of net generation-decombination in the transition regions and at the surface (approximation 2 above). Analytical expressions exist that enable this generalization<sup>12,13</sup> to be made. To establish the pertinent critical current, one can measure the  $I_C$ - $V_{BE}$  characteristics and infer the current above which recombination in the active base predominates in determining the total recombination current.<sup>12,13</sup>

Aside from the lower bound thus established, failure of the Ebers-Moll model normally occurs if voltages and currents exceed certain critical values. Here generalization of the model is more difficult. The difficulty arises because, for large currents and voltages, the phenomena implied by the approximations listed above all tend to interact to determine the device behavior and all are described by nonlinear equations. From an analytical viewpoint, direct solution poses an intractable problem. Several approaches, based on approximations, have been proposed to evade this problem.

One approach consists in retaining the form of the equations describing the Ebers-Moll model but increasing the accuracy by allowing the parameters of the model to vary with voltage and current<sup>1,14</sup>. The functional dependence of this parameter variation is determined by curve fitting, using measurements made at the device terminals. The characterization thus consists of tabulations of the dependence of such parameters as current gain and the charge-control time constants on relevant currents and voltages.

The advantage of this method lies on the side of accuracy. By fitting the parameter dependence to measured data, one ensures that the predicted behavior will match actual device behavior to within a specified error. The accuracy can be increased by increasing the number of data points used in constructing the model. This method, however, has serious drawbacks. The resulting model is complex. Its use requires the storage of many pieces of data to characterize each device. This produces the disadvantages noted earlier: limitations on computer memory, on numerical accuracy and, consequently, on the size of the

circuit that can be simulated. As an additional disadvantage, the parameters for this model derive solely from measurements made at the device terminals. No attempt is normally made to relate device performance to structural and material parameters. To the integrated-circuit designer, this constitutes a serious deficiency.

Gummel and Poon have recently described an alternative approach that offers significant advantages<sup>15</sup>. Their integral charge-control model, described by 21 parameters (excluding parasitic resistances), does not depend for its validity on many of the approximations, cited earlier, upon which the Ebers-Moll model is based. Moreover, their model enables trading simplicity for accuracy, thereby generating a progression of simpler models; in its simplest form the Gummel-Poon model reduces to the Ebers-Moll model. The most important approximation limiting the validity of the Gummel-Poon model is the assumption of one-dimensional current flow. To include a first-order description of the multi-dimensional effects of emitter crowding, Gummel and Poon include in their model an adjustable parameter whose value is chosen to fit measured device behavior. In general, multi-dimensional effects have received much study, although mainly from the viewpoint of device rather than of circuit design<sup>7,8,10,11</sup>.

Thus models of different degrees of accuracy and simplicity exist as candidates for use in simulation programs. Of these the simplest is the Ebers-Moll model, or its charge-control or Linvill equivalents. Other more complicated models take account of one or more of the various phenomena ignored by the Ebers-Moll model: emitter crowding, high injection, etc.

A basic problem left unsolved by previous studies, however, rules out the effective utilization of these models in integrated-circuit simulation and design. This problem is the determination, for each transistor in the circuit under study, of the model of least complexity that will give the accuracy required. A sub-problem is to determine those transistors for which the simplest model -- the Ebers-Moll model -- will provide an adequate description.

The present paper describes a method that offers a solution to these problems. In Section II below, we outline the central ideas of the method. Section III sets forth certain onset voltages and currents that describe the limits of adequacy of the Ebers-Moll model. In Section IV we illustrate the practical utility of the method by applying it to the simulation of an operational amplifier.

## II. The Method

A model may fail to adequately describe device behavior if any of its underlying approximations is violated. If for a particular circuit application

none of these approximations is violated, we say that the model is self-consistent for that application.

The method for model assessment and choice of model complexity presented here is based upon using voltages and currents calculated in a computer simulation of the circuit to test for self-consistency of the models. Each model that fails the test is replaced with a more complex model, and the circuit is again analyzed. This procedure continues until self-consistency prevails for all models in the circuit. When this condition is satisfied, we assume that the models adequately represent device behavior.

Because it is desirable that simulation programs employ the least complex models possible, the first simulation uses the Ebers-Moll model for each transistor. For simplicity we focus attention in this paper on the static behavior of circuits in which all of the transistors operate in the forward-active region; and we assume all the collector currents to be large enough that one can neglect contributions arising from net recombination-generation in the transition regions. Under these constraints -- which apply, for example, to the biasing circuits of many amplifiers -- four onset parameters suffice to describe the limits of adequacy of the Ebers-Moll model. These parameters -- three currents and one voltage -- provide the basis for the self-consistency test. As is described in Section III, each onset parameter corresponds to the onset of failure of various of the approximations underlying the Ebers-Moll model; that is, each corresponds to the onset of various of the phenomena ignored in the formulation of that model.

Figure 1 shows an abbreviated flow diagram of the method. Most existing analysis programs are easily modified to permit incorporation of this method. As in any analysis program, the first step is to read in the network description. Each transistor should be read in as a three-terminal device rather than as a set of interconnecting elements. For the first analysis, an Ebers-Moll model with parasitic resistances added is used to represent each transistor in the circuit; the onset parameters for this model are calculated as is indicated in Section III below. The first analysis gives the collector current and voltage for each transistor in the circuit, which are compared with the appropriate onset parameters to test for self-consistency. If an onset parameter associated with any transistor model is exceeded, the self-consistency test fails. Each such model is made appropriately more complex. Analysis is then repeated and another self-consistency check is made. The procedure continues until all models in the circuit are self-consistent.

Notice that this method ensures use of the simplest model -- the Ebers-Moll model -- wherever possible. It places additional complexity only on those transistors poorly represented by the Ebers-Moll model. Moreover, for

any transistor requiring a model more accurate than the Ebers-Moll model, it encourages adding of no more complexity than that needed to obtain an adequate representation of device behavior. For example, suppose that the Ebers-Moll model for a particular transistor in the circuit fails because the collector current exceeds the onset value describing high injection in the base. Then one replaces the Ebers-Moll model, not with the most complex model available, but rather with a model obtained by adding only the elements needed to account for this high injection.

Thus the method offers a solution to the basic problems described in Section I. For each transistor in a circuit the method selects from among existing models that one of least complexity consistent with an adequate description of the circuit behavior.

### III. Onset Parameters for the Ebers-Moll Model

The onset parameters describe the currents and voltages at which various of the approximations underlying the Ebers-Moll model start to become severely violated. These approximations were listed in Section I.

The onset parameter  $I_{C-CR}$  gives the collector current above which emitter crowding becomes severe, in violation of approximation 7. In specifying the value of this critical current, we assume the absence of the other phenomena implied by the approximations listed in Section I; we make a similar assumption in specifying each of the other onset parameters. The onset parameter  $I_{C-HIB}$  gives the collector current above which high level injection in the base region becomes severe. It thus relates to the onset of conductivity modulation and of current dependence of lifetime and electric field in the base; moreover, for collector current larger than  $I_{C-HIB}$ , a Boltzmann relation of the form  $\exp(qV_{EB}/kT)$  no longer describes the dependence of the minority density at the base edge of the emitter space-charge region. Hence  $I_{C-HIB}$  is concerned with the violation of approximations 3 through 6. The onset parameter  $I_{C-SCL}$  gives the collector current above which space-charge limited flow occurs in the collector region. Space-charge limited flow causes base widening and multi-dimensional flow, violating thereby approximations 8 and 9.

We specify the foregoing onset parameters in terms of collector current. Alternatively, we could specify them in terms of emitter base voltage  $V_{EB}$  inasmuch as the Ebers-Moll model supplies a functional dependence between  $I_C$  and  $V_{EB}$ . For the final onset parameter no such choice is available. This parameter gives the collector voltage at which breakdown begins in the collector space-charge region, in violation of approximation 2.

We now describe each of the onset parameters and discuss its determination



by calculations based upon the transistor make-up and by measurements at the terminals.

#### A. ONSET PARAMETER FOR EMITTER CROWDING

The flow of base current produces a potential gradient that makes the voltage applied across the emitter junction be a decreasing function of distance from the base contact. Because minority carrier injection depends exponentially on this voltage (normalized by the thermal voltage,  $kT/q$ ), the injection occurring at the emitter edges nearest the base contact can greatly exceed that occurring over the rest of the emitter area. This tendency for carrier density, and hence current density, to crowd toward emitter edges is called emitter crowding.

The exponential dependence cited above suggests that the effects associated with emitter crowding will become important when the maximum voltage difference produced by the base current reaches approximately  $kT/q$ . Hauser<sup>7</sup> has shown that this condition occurs when

$$I_B = \frac{2 kT/q}{R_B/m} \quad (1)$$

where  $m = 4$  for a double-stripe base contact and  $m = 1$  for a single-stripe contact. At this value of base current, the current density normal to the active emitter and at the emitter edge nearest the base contact is approximately twice the minimum normal current density<sup>7</sup>. (The minimum normal current density occurs at the center of the emitter for a double-stripe base contact and at the emitter edge farthest from the base contact for a single-stripe geometry).

We use this condition to define the onset parameter  $I_{C-CR}$  for emitter crowding:

$$I_{C-CR} = F_{CR} \frac{2 kT/q}{R_B/m \beta_f} \quad (2)$$

Crowding increases continuously with increasing current, and thus a definition of the current at which crowding "begins" is to some degree arbitrary. The adjustable constant  $F_{CR}$  reflects this arbitrariness. As is discussed later, its value is chosen at the discretion of the analyst, in accord with the maximum error in model prediction that accompanies different choices of  $F_{CR}$ .

In (2),  $\beta_f$  denotes the common-emitter current gain in forward-active operation and  $R_B$  denotes the transverse resistance of the intrinsic base region, which is estimated by

$$R_B \triangleq \frac{\bar{\rho}_B}{W_B} \frac{L}{Z} = \rho_{BS} \frac{L}{Z} \quad (3)$$

In Figure 2 the base width  $W_B$  and the emitter dimensions,  $L$  and  $Z$ , are indicated. By  $\bar{\rho}_B$  we mean the average resistivity of the base and by  $\rho_{BS}$  the sheet resistance underneath the emitter.

In determining the value of  $I_{C-CR}$  for a particular transistor, one must distinguish between the transverse base resistance  $R_B$ , on the one hand, and the intrinsic base resistance  $R_b$  pertinent in a dc large-signal model, such as the Ebers-Moll model, on the other. For current sufficiently low that the approximations underlying the Ebers-Moll model all are valid, the relation between these two resistances is<sup>7,16</sup>

$$R_b = R_B/3m \quad (4)$$

The simplest way to find the value of  $R_B$  is by direct measurement of the sheet resistance  $\rho_{BS}$  using a closed-geometry (JFET) test pattern fabricated on the same chip as the transistors in question. If a test pattern of this kind is unavailable, one may estimate  $\rho_{BS}$  from

$$\rho_{BS} \approx 1/q\mu_{BM}N_B \quad (5)$$

Here  $\mu_{BM}$  denotes the mobility of majority carriers in the base, which can be estimated with fair accuracy, and  $N_B$  is Gummel's number (the number of impurity atoms per unit area in the base), which can be inferred from measurements at the conventional transistor terminals<sup>17</sup>. Alternatively, one can measure the intrinsic base resistance  $r_b$  pertinent to small-signal, low-frequency excitation. Under the same constraints that ensured the validity of (4),

$$r_b = R_b = R_B/3m \quad (6)$$

To determine the value of  $R_B$  from the measured value of  $r_b$ , one then needs only to know whether the base contact has a double-stripe or a single-stripe geometry.

In principle, one can calculate  $\beta_f$  from knowledge of the transistor make-up. In practice, however, one knows the spatial distribution of carrier lifetime to such poor accuracy that the only practical way to determine  $\beta_f$  is by inference from terminal measurements.

The means for determining the value of the onset parameter  $I_{C-CR}$  thus consists in combining calculations based on the transistor make-up with measurements made at the device terminals.

The onset parameter for crowding lends itself to interpretation in relation to the current-voltage characteristics. For  $F_{CR}=1$ ,  $I_{C-CR}$  defines the corner at which the asymptotes for negligible crowding and for significant crowding intersect. Figure 3 shows this interpretation. Notice that the Ebers-Moll model tends to predict a collector current larger than that resulting if the effects of crowding are taken

into account. In the method of Fig. 1, the maximum difference (or error) occurs when  $I_C = I_{C-CR}$ . Using the results of Hauser<sup>7</sup>, one can find the maximum errors attending different choices of the constant  $F_{CR}$ . These values, which appear in Table 1, apply to any transistor whose make-up is consistent with the assumptions used by Hauser in his analysis. For many practical devices, these assumptions hold with good accuracy; the most seriously restrictive of them are the assumption of stripe-contact geometry and the assumption that the length-width ratio of the emitter makes reasonable a two-dimensional (rather than three-dimensional) treatment of crowding.

In the method diagramed in Fig. 1, the first simulation of circuit behavior is based on representing each transistor in the circuit by an Ebers-Moll model with parasitic resistances added. To this point, we have ignored the influence of these resistances. Indeed, however, inclusion of base resistance  $R_b$  reduces the maximum error substantially below the values cited in Table 1.

The reason for this is as follows. Whether predicted by the Ebers-Moll model or by the Hauser model which accounts for crowding, the collector current  $I_C$  depends sensitively on the portion  $V_{EB}'$  of the applied emitter base voltage  $V_{EB}$  that contributes to the potential barrier at the emitter-base junction. The relation between these voltages is

$$|V_{EB}'| = |V_{EB}| - |I_C| \frac{R_b}{\beta_f} \quad (7)$$

(ignoring the voltage across the parasitic emitter resistance  $R_e$ , which is assumed negligible in this discussion). The maximum errors given in Table 1 are computed by comparing collector currents at the value of  $V_{EB}'$  that causes

$$I_C = I_{C-CR}$$

to flow in the Ebers-Moll model. From a practical standpoint, this is an inappropriate comparison, however, because  $V_{EB}'$  is an internal voltage rather than a voltage across transistor terminals. To find more meaningful values of the maximum error, one must compare the collector currents predicted by the Ebers-Moll model and the Hauser model at the terminal voltage  $V_{EB}$  that causes  $I_C$  to equal  $I_{C-CR}$  in the Ebers-Moll model. Doing this, one finds, for example, that the maximum error accompanying the choice  $F_{CR} = 1$  decreases from approximately 70% (see Table 1) to approximately 20%. No general results can be given as to the size of this decrease. The reduction cited holds for a typical transistor employed in our experimental study, described in Sec. IV. As is apparent from (7), determination of the actual error risked in model assess-

ment for a particular transistor requires the specification of  $\beta_f$ ,  $R_b$ , and  $I_{C-CR}$  for that transistor.

Choice of  $F_{CR}$  in the definition of  $I_{C-CR}$  thus rests on the transistor make-up and on the maximum error in model assessment that the analyst is willing to risk. For many circuits,  $F_{C-CR} = 1$  may be a reasonable choice.

#### B. ONSET PARAMETER FOR HIGH INJECTION IN THE BASE

All of the phenomena implied by approximations 3 through 6 listed earlier, which accompany high injection in the base, set in at approximately the same collector current. As this critical current we take the value at which the injected minority charge is some fraction  $F_{HIB}$  of the majority base charge present in thermal equilibrium:

$$\Delta Q_b = F_{HIB} Q_{bo} \approx F_{HIB} q A_E N_B \quad (8)$$

where  $A_E$  is the area of the emitter. From charge-control theory, we express the injected minority charge as the product of the collector current and the forward transit time  $\tau_f$ . Thus

$$I_{C-HIB} \triangleq F_{HIB} q A_E N_B / \tau_f \quad (9)$$

which defines the onset parameter for high injection in the base.

Finding the value of  $I_{C-HIB}$  for a particular transistor requires the determination of the Gummel number  $N_B$  and of the forward transit time  $\tau_f$ . To determine  $N_B$ , any of the methods mentioned earlier can be used. To determine  $\tau_f$ , one can either employ measurements at the device terminals<sup>18,19</sup> or the semi-empirical relation<sup>10,15</sup>

$$\tau_f = W_B^2 / n_t D_{Bm} \quad (10)$$

where  $D_{Bm}$  denotes the diffusivity of minority carriers in the base. For practical transistors, the constant  $n_t$  ranges from 2, appropriate for a homogeneous-base transistor, to 10; it accounts for the influence of built-in electric field on the carrier transit time across the base. As an estimate, one can calculate the value of  $n_t$  from the expression

$$n_t / 2 \approx 1 + \left[ \frac{W_B}{2} \frac{d \ln N}{dx} \right]^{3/2} \quad (11)$$

which pertains to a transistor with exponential doping in the base<sup>20</sup>. Here  $N$  denotes the impurity density in the quasi-neutral base.

In describing transistor beta degradation at high collector currents, Wait and Hauser<sup>21</sup> have proposed an onset current for high injection in the base that differs from that defined above. It can be shown, however, that the

Wait-Hauser onset current results if one sets  $F_{CR} = 1$  and  $n_t = 2$  in our expression for  $I_{C-HIB}$ . The Wait-Hauser current therefore describes the onset of high injection in a homogeneous-base transistor, but is less generally applicable than is the definition given in (9) above.

This definition has different physical meanings depending on the choice made of the fraction  $F_{HIB}$ . For  $F_{HIB} = 1$ ,  $I_{C-HIB}$  corresponds approximately to the intersection of the asymptotes describing high and low injection<sup>15</sup> precisely analogous to the interpretation given to  $I_{C-CR}$  in Fig. 3. For  $F_{HIB} = 0.5$ , it corresponds approximately to the current at which the injected minority density at the emitter edge of the quasi-neutral base region in a homogeneous-base transistor just equals the density of the base impurity atoms.

Gummel and Poon<sup>15</sup> have computed the  $I_C - V_{EB}$  characteristics assuming high injection in the base. From their computations one can infer representative values of the maximum error risked in assessing the adequacy of the Ebers-Moll model in the presence of high injection. Defining the maximum error in a sense analogous to that employed for Table 1, one finds that the approximate maximum error for  $F_{HIB} = 1$  is 85%; for  $F_{HIB} = 0.5$ , it is 25%; and for  $F_{HIB} = 0.25$ , it is 5%. These values result if one ignores the effects of a potential drop in  $R_b$ . As was discussed in connection with the onset parameter for current crowding, these values may therefore substantially overestimate the maximum error actually risked in model assessment.

### C. SPACE-CHARGE-LIMITED FLOW IN THE COLLECTOR

In the conventional treatment of forward-active transistor behavior, which assumes the absence of crowding and of high-level injection in the base, a so-called space-charge region is assumed to straddle the metallurgical collector junction. In this region the space charge density equals the charge density of the impurity ions. The free carriers present are assumed to contribute negligibly to the charge density. As current increases, however, the charge of the free carriers traversing this region can no longer be neglected. Indeed, at a certain critical current density  $J_{Crit}$ , the charge of the free carriers combined with the charge of the impurity atoms will be just large enough to cause the electric field at the collector metallurgical junction to vanish. This occurrence marks the onset of space-charge-limited current flow in the collector space-charge region; current densities exceeding  $J_{Crit}$  require (in a one-dimensional, one-carrier model) the formation of a potential barrier which will reflect some of the carriers that are injected by the emitter and reach the collector junction. In this space-charge-limited mode of flow<sup>22</sup>, the current will increase propor-

tionately as the square of  $V_{CB}$ , if drift flow with constant mobility predominates, or proportionately as  $|V_{CB}|$ , if flow at the scatter-limited velocity  $v_{sat}$  predominates. But in a normal circuit environment  $V_{CB}$  and  $I_C$  will be unable to vary in accord with this dependence; for example, the circuit configuration might hold  $V_{CB}$  essentially constant. Thus the one-carrier, one-dimensional model of the conventional treatment disallows collector currents exceeding  $J_{Crit} A_E$ .

Accommodation of current larger than this value therefore requires a major departure from the one-carrier, one-dimensional model. One possible departure, which retains the assumption of one-dimensional flow, involves the cooperation of holes and electrons to extend the quasi-neutral region that receives injection from the emitter so that its far boundary crosses the metallurgical collector junction into the collector region itself. This is the model of base-widening<sup>9,10</sup>. Another possible departure involves an increase in the effective area of the emitter owing to lateral injection of carriers into the base and consequent multi-dimensional flow<sup>10,11</sup>. In practical transistors, both base widening and lateral injection occur at currents exceeding  $J_{Crit} A_E$ ; both contribute to the degradation of current gain and frequency response<sup>10</sup>.

We now derive an expression for  $J_{Crit}$ , the current density at which space-charge-limited flow in the collector sets in. For concreteness, consider the npn structure shown in Fig. 2. If one ignores crowding, a one-dimensional treatment suffices for current not exceeding  $J_{Crit}$ .

As is stated above, the condition defining the onset of space-charge-limited flow is the vanishing of the electric field at the metallurgical collector junction:

$$E(0) = 0 \quad (12)$$

By definition this occurs at current density

$$J_{Crit} = -qn(x) v(x) = qn(x) \mu_{nc}(E) E(x) \quad (13)$$

The electric field is therefore determined by

$$\frac{dE}{dx} = \frac{\rho}{K_s \epsilon_0} \approx \frac{qN_{DC} + J_{Crit}/v(x)}{K_s \epsilon_0} \quad (14)$$

To find the functional dependence of  $J_{Crit}$  upon  $V_{CB}$  and the transistor make-up, we now introduce an approximation that will put (14) in suitable form for integration. We approximate the dependence of mobility on electric field by the simple empirical relation<sup>23</sup>

$$\mu_{nC}(E) \approx \frac{\mu_{no}}{1 + (\mu_{no} E / v_{sat})} \approx \frac{\mu_{no}}{1 + (\mu_{no} \bar{E} / v_{sat})} \stackrel{\Delta}{=} \overline{\mu_{nC}} \quad (15)$$

in which  $\bar{E} = V_{CBT}/W_C$  is the average electric field in the collector region. Here  $\mu_{no}$  denotes the low-field mobility and  $V_{CBT}$  denotes the total (applied plus contact) potential between base and collector. Combining (14) and (15) and rearranging leads to

$$K_s \epsilon_o dE / (qN_{DC} + J_{Crit} / \overline{\mu_{nC}} E) = dx \quad (16)$$

In their study of space-charge-limited flow, Shockley and Prim<sup>24</sup> have integrated an equation of this form. The result is

$$J_{Crit} = \frac{qN_{DC} (V_{CBT}/W_C) \mu_{no}}{1 + \frac{(V_{CBT}/W_C) \mu_{no}}{v_{sat}}} \quad (17)$$

provided

$$qN_{DC} W_C^2 / K_s \epsilon_o V_{CBT} \gg 1 \quad (18)$$

For integrated-circuit transistors, this condition is easily met.

Despite its simplicity (17) provides a good fit with the functional dependence of Whittier and Tremere's critical current density<sup>10</sup>, which required computer solution. Moreover, it is consistent with the expression of Poon *et al*<sup>25</sup> for critical current. The derivation given here applies more generally than that of Poon<sup>25</sup>, which required the assumption of collector bias so small that at low currents the collector depletion width constitutes only a small fraction of the width  $W_C$  of the collector region.

In accord with (17), we define the onset parameter for space-charge-limited flow in the collector as

$$I_{C-SCL} = F_{SCL} \frac{qN_{DC} A \mu_{no}}{W_C} \left[ \frac{1 + (V_{CBT}/W_C) \mu_{no}}{v_{sat}} \right]^{-1} V_{CBT} \quad (19)$$

The factor  $F_{SCL}$  provides the analyst with an adjustable constant that plays a role similar to the adjustable constants associated with the onset parameters for crowding and for high injection in the base.

The simplest method to determine the value of  $I_{C-SCL}$  is by calculation based on knowledge of the doping of the collector region, of its width, and of its junction contact potential.

Notice that, in contrast to  $I_{C-CR}$  and  $I_{C-HIB}$ , the value of  $I_{C-SCL}$  cannot

be found prior to the first simulation. For any transistor in the circuit under study, its value depends on the value of  $V_{CB}$  computed for that transistor.

#### D. ONSET PARAMETER FOR VOLTAGE BREAKDOWN

For a transistor biased in the forward-active mode, the smallest of the breakdown voltages conventionally defined is typically  $BV_{CEO}$ , the breakdown voltage between collector and emitter with the base open-circuited. Thus we normally take this voltage to be the onset parameter describing breakdown. However, for certain diode-connected transistors<sup>26</sup> and for transistors in which the circuit environment imposes close approximations to either short-circuit or open-circuit conditions between emitter and base, violation of the constraint

$$V_{CE} < BV_{CEO}$$

may not necessarily imply failure of the Ebers-Moll model. Voltage ratings such as  $BV_{CBO}$  or  $BV_{CES}$  may more appropriately serve as the breakdown onset parameter for these devices. Often the circuit configuration makes the appropriate choice obvious; the results of the computer simulations of circuit behavior also offer guidance.

The breakdown voltages can be measured at the device terminals<sup>27</sup> or calculated from the transistor make-up<sup>26-29</sup>

#### IV. Illustrative Example

The effectiveness of the proposed procedure was studied by the simulation of an altered version of the  $\mu A$  702 operational amplifier shown in Fig. 4. Values for the transistor model parameters are assumed to be those given by Gummel and Poon<sup>15</sup>. The onset parameters associated with each transistor can be computed from knowledge of these parameters.

The first step is to establish that if none of the onset parameters is exceeded, the Ebers-Moll<sub>model</sub> adequately predicts circuit behavior. Towards this end two computer simulations were performed: one using the 6-parameter\* Ebers-Moll model for each transistor and one using the full 24 - parameter\* Gummel-Poon model. The results of these simulations are shown in Table 2. As can be seen, both simulations predict essentially the same node voltages and it can be shown that for this circuit none of the onset parameters is exceeded. (For this case,  $I_{C-H1B} \approx I_{C-CR} < I_{C-SCL}$ .) It is interesting to note the increase in cost of the simulation using the Gummel-Poon model when the Ebers-Moll model will suffice. The simulation using the Ebers-Moll model required 4 Newton iterations for con-

\* This count includes the extrinsic emitter, base, and collector resistors.



vergence to three significant places while the simulation using the Gummel-Poon model required 18 Newton iterations.

The next step is to show that if an onset parameter for one transistor model is exceeded, that by appropriately increasing the complexity of this model meaningful results are obtained. We can show the desired result by again studying the operational amplifier of Fig. 4, but this time modifying the transistors used so as to force the onset parameter,  $I_{C-H1B}$ , of one transistor model, to be exceeded. In particular we assume the transistors used have an emitter area 1/20th as large as the emitter area of the transistors studied in the previous simulations. Moreover, this area reduction is assumed to be realized while maintaining the same emitter length-to-width ratio. Thus we are assured that while  $I_{C-H1B}$  is decreased by a factor of 20,  $I_{C-CR}$  remains as before. Although  $I_{C-SCL}$  is also decreased by a factor of 20 it still remains greater than  $I_{C-H1B}$ . Finally, to guarantee that  $I_{C-H1B}$  for T4 is exceeded, it is assumed that the base width of this transistor is twice as large as the base widths of the other transistors. As can be seen from Eqs. (9) and (10),  $I_{C-H1B}$  for T4 is therefore one fourth as large as the  $I_{C-H1B}$ 's for the other transistors.

Four simulations of the modified operational amplifier were carried out. In the first simulation, all transistors were characterized by the 6-parameter Ebers-Moll model. As expected, only the onset parameter  $I_{C-H1B}$  for transistor T4 is exceeded (see Table 3). This run took four Newton iterations. Second, a simulation of the circuit with each transistor characterized by the full 24-parameter Gummel-Poon model was performed. This run took 22 Newton iterations and the results are shown in Table 4. Note the differences in values between this run and the run using the Ebers-Moll models. The third and fourth simulations involved using the Ebers-Moll model for each transistor until convergence, (4 Newton iterations), checking the onset parameters, <sup>INCREASING</sup> the complexity of the model for which the onset parameter was exceeded, (i.e., the model used for T4), and allowing the simulation to continue until convergence. For the third run, the model for T4 was increased to a Gummel-Poon model which accounted for only high level injection in the base. This run took a total of 8 Newton iterations. For the fourth run, the model for T4 was increased to the full 24-parameter Gummel-Poon model. This run took a total of 22 Newton iterations. The results of all runs are summarized in Table 4.

It would appear that for this circuit at least, the use of the onset parameters as a means for determining model complexity is justified for two reasons.

First, clearly a savings of computer time is realized if a simple model can be used. Second, if a complex model is required, no additional cost is involved if an initial simulation using the Ebers-Moll model is made and then model complexity is increased as necessary.

#### V. Discussion

In this paper we have proposed a method for selecting, for each transistor in a circuit, the model of least complexity that will give acceptable accuracy. At the heart of the method is the capability to assess model adequacy. This capability derives from a self-consistency test in which the values of the currents and voltages computed in a simulation of the circuit behavior are compared with onset parameters. We have set forth the onset parameters for the Ebers-Moll model and have discussed their determination by terminal measurement and by calculation based on the transistor make-up.

If the self-consistency test fails for a particular Ebers-Moll model in the circuit, this model is replaced with a more complex model chosen in accordance with which of the onset parameters were violated. Among the models presently available as replacements for the Ebers-Moll model, we believe the single most comprehensive and useful model to be that proposed recently by Gummel and Poon<sup>15</sup>. In part its utility derives from the fact that the Gummel-Poon formulation contains a set of models, which enables trading between accuracy and simplicity. Particular members of the set offer descriptions appropriate when certain of the approximations underlying the Ebers-Moll model, but not all, are violated.

For example, suppose that the result of a circuit simulation indicates that the Ebers-Moll model for a particular transistor fails because the collector current exceeds a single onset parameter: that pertaining to high injection in the base. Then one replaces that Ebers-Moll model with a Gummel-Poon model abbreviated to contain only those parameters necessary to describe high injection. As a second example, suppose that either  $I_{C-CR}$  or  $I_{C-SCL}$  is violated. Then an appropriate replacement is a Gummel-Poon model containing the full set of "push-out"<sup>15</sup> and related parameters. The complexity of the resulting description arises in part because multi-dimensional effects accompany either crowding or space-charge-limited flow. As was noted earlier, the Gummel-Poon formulation, which is based on the assumption of one-dimensional flow, takes multi-dimensional effects into account through an adjustable constant  $n_p$ , whose value is chosen to fit measured characteristics. If the crowding onset

parameter alone is violated, the Gummel-Poon model for crowding may provide a less compact description than that obtained by adopting a circuit model patterned after the work of Ghosh<sup>8</sup>.

We have described the onset parameters for the Ebers-Moll model only. Once one of these parameters is exceeded, the other onset parameters change because the occurrence of one set of phenomenon may either hasten or delay the onset of another set. We defer the description of these changes to a later paper.

Failure of the approximations underlying the Ebers-Moll model, which were listed in Section I, establishes the bounds on current and voltage within which the Ebers-Moll model provides a satisfactory description of device behavior. Two exceptions to this statement exist. First, as is implicit in the derivation of Gummel<sup>30</sup>, one can demonstrate device behavior in accord with the Ebers-Moll model without assuming the device is resolvable into space-charge and quasi-neutral regions. Second, for forward-active operation, the Early effect<sup>31</sup> is present independent of the value of the collector current; and this effect the Ebers-Moll model ignores. For some circuits, as our experimental evidence suggests, its neglect will cause negligible error in the simulation of dc circuit behavior. If desired, one can take approximate account of the Early effect in the forward-active mode while still retaining basically an Ebers-Moll formulation. This is done by multiplying the collector current predicted by the Ebers-Moll model by the factor:  $1 + (|V_{CE}|/|V_A|)$ . The additional parameter  $V_A$  is termed the Early voltage<sup>15</sup>, and can be easily determined by measurement.

In this paper we have focussed attention on the use of onset parameters to enable model selection by the method illustrated in Fig. 1. The onset parameters might also be used for other purposes. For example, the severe violation of one or more onset parameters may suggest the desirability of redesigning the transistors or the circuit under study.

#### ACKNOWLEDGEMENT

For instructive discussions, we thank Professors Arthur Brodersen and Doug Hamilton. We are indebted to Robert Martin, Frank Hewlett and James Smith, who aided in the phases of our work concerned with circuit simulation and device fabrication and measurement.

## REFERENCES

1. F. A. Lindholm, "Device Modeling for Computer-Aided Analysis and Design of Integrated Circuits," Solid State Electronics, vol. 12, pp. 831-840, Nov. 1969.
2. J. J. Ebers and J. L. Moll, "Large signal behavior of junction transistors," Proc. IRE, vol. 42, pp. 1773-1784, Dec. 1954.
3. D. J. Hamilton, F. A. Lindholm, and J. A. Narud, "Comparison of large-signal models for junction transistors," Proc. IEEE, vol. 52, pp. 239-248, March 1964.
4. For example, see:  
 A.S. Grove, Physics and Technology of Semiconductor Devices, Wiley, New York, 1967.  
 A. K. Jonscher, Principles of Semiconductor Device Operation, Wiley, New York, 1960.  
 P. E. Gray, D. DeWitt, A. R. Boothroyd, and J. F. Gibbons, Physical Electronics and Circuit Models of Transistors, Wiley, New York, 1964
5. L. E. Clark, "High current-density beta diminution," IEEE Trans. on Electron Devices, vol. ED-17, pp. 661-667, Sept. 1970 (contains extensive review of prior work).
6. G. C. Ebner and P. E. Gray, "Static V-I relationships in transistors at high injection levels," IEEE Trans. on Electron Devices, vol. ED-13, pp. 692-701, Oct. 1966.
7. J. R. Hauser, "The effects of distributed base potential on emitter current injection density and effective base resistance for stripe transistor geometries," IEEE Trans. on Electron Devices, ED-11, pp. 238-242, May 1964.
8. H. N. Ghosh, "A distributed model of the junction transistor and its application in the prediction of the emitter-base diode characteristic, base impedance, and pulse response of the device," IEEE Trans. on Electron Devices, vol. ED-12, pp. 513-531, Oct. 1965.
9. C. T. Kirk, Jr., "A theory of transistor cutoff frequency falloff at high current densities," IRE Trans. Electron Devices, vol. ED-9, pp. 164-174, March 1962.
10. R. J. Whittier and D. A. Tremere, "Current gain and cutoff frequency falloff at high currents," IEEE Trans. Electron Devices, vol. ED-16, pp. 39-57, Jan. 1969.
11. A. van der Ziel and D. Agouridis, "The cutoff frequency falloff in UHF transistors at high current," Proc. IEEE (Letters), vol. 54, pp. 411-412, March 1966.
12. J. D. Meindl, Micropower Circuits, Wiley, 1969.
13. C. T. Sah, R. N. Noyce, and W. Shockley, "Carrier generation and recombination in pn junctions and pn junction characteristics," Proc. IRE, vol. 45, pp. 1228-1243, Sept. 1957.  
 C. T. Sah, "Effect of surface recombination and channel on pn junction and transistor characteristics," IRE Trans. Electron Devices, vol. ED-9, pp. 94-108, Jan. 1962.
14. For example, see:  
 A. F. Malmberg and F. N. Cornwell, "NET-1 Network Analysis Program LA-3119," Los Alamos Scientific Laboratory, Sept. 1964.

14. Continued

- L. D. Milliman, W. A. Massena, and R. H. Dickhaut, "CIRCUS, A Digital Computer Program for Transient Analysis of Electronic Circuits - User's Guide," Harry Diamond Laboratories, 346-1, Jan. 1967.
15. H. K. Gummel and H. C. Poon, "A Compact Bipolar Transistor Model," 1970 ISSCC Technical Digest, vol. 13, pp. 78-80, Feb. 1970.
- H. K. Gummel and H. C. Poon, "An integral charge control model of bipolar transistors," BSTJ, vol. 49, pp. 827-852, May-June 1970.
16. R. D. Thornton, D. DeWitt, P. E. Gray, and E. R. Chenette, Characteristics and Limitations of Transistors, Wiley, 1966, p. 64.
17. H. K. Gummel, "Measurement of the number of impurities in the base layer of a transistor," Proc. IRE, vol. 49, pp. 834-835, 1961.
18. R. D. Thornton, J. G. Linvill, E. R. Chenette, H. L. Ablin, J. N. Harris, A. R. Boothroyd, J. Willis, C. L. Searle, Handbook of Basic Transistor Circuits and Measurements, Wiley, N. Y., 1966, Ch. 8.
- P. E. Gray and C. L. Searle, Electronic Principles, Wiley, 1969, pp. 824-832.
19. C. S. Meyer, D. K. Lynn, and D. J. Hamilton (eds.), Analysis and Design of Integrated Circuits, McGraw-Hill, 1968, pp. 95-100.
20. A. N. Daw, R. N. Mitra and N. K. D. Choudhury, "Cutoff frequency of a drift transistor," Solid State Electronics, vol. 10, pp. 359-364, 1967.
21. J. T. Wait and J. R. Hauser, "Beta falloff in transistors at high collector currents," Proc. IEEE (Letters), vol. 56, pp. 2087-2088, Nov. 1968.
22. R. H. Tredgold, Space Charge Conduction in Solids, Elsevier Publishing Co., N. Y., 1966.
23. H. K. Gummel, "A Charge control relation for bipolar transistors," B.S.T.J., vol. 49, pp. 115-120, Jan. 1970.
24. W. Shockley and R. C. Prim, "Space-charge-limited emission in semiconductors," Phys. Rev., vol. 90, pp. 753-758, 1953.
25. H. C. Poon, H. K. Gummel, and D. L. Scharfetter, "High injection in epitaxial transistors," IEEE Trans. on Electron Devices, vol. ED-16, pp. 455-458, May 1969.
26. R. M. Warner, Jr. and J. N. Fordemwalt, Integrated Circuits: Design Principles and Fabrication, McGraw-Hill, 1965.
27. A. B. Phillips, Transistor Engineering, McGraw-Hill, N. Y., 1962.
28. S. M. Sze, Physics of Semiconductor Devices, Wiley, N. Y., 1969.
29. F. van de Wiele, R. van Overstraeten and H. de Man, "Graphical method for the determination of junction parameters and of multiplication parameters," Solid State Electronics, vol. 13, pp. 25-36, Jan. 1970.
30. H. K. Gummel, "A self-consistent iterative scheme for one-dimensional steady state transistor calculations," IEEE Trans. on Electron Devices, vol. ED-11, pp. 455-465, October 1964.
31. J. M. Early, "Effects of space charge layer widening in junction transistors," Proc. I.R.E., vol. 46, pp. 1141-1152, November 1952.

$F_{CR}$	Max error (approximate)
1	70% (decreases to 20% if include $R_b$ )
0.5	30%
0.25	10%

Table 1. The maximum error associated with different choices of  $F_{CR}$  if one ignores the potential drop in the base resistance  $R_b$ . The maximum error is defined as

$$\frac{I_{C-CR} - (I_C)_{\text{with crowding}}}{(I_C)_{\text{with crowding}}}$$

in which  $(I_C)_{\text{with crowding}}$  denotes the collector current that results if one takes account of crowding. Both  $(I_C)_{\text{with crowding}}$  and  $I_{C-CR}$  occur at the same value of  $V_{EB}$  (if one neglects the potential drop in base resistance  $R_b$ ).

NODE	ALL	ALL
	EBERS-MOLL	GUMMEL-POON
1	-.0039	-.0063
2	-0.607	-0.612
3	0.664	0.671
4	-.000208	-.00125
5	-0.609	-0.614
6	0.668	0.670
7	0.844	0.852
8	6.00	6.00
9	2.49	2.45
10	1.84	1.80
11	0.288	0.131
12	-1.96	-1.95
13	-2.58	-2.57
14	-2.62	-2.62
15	-2.60	-2.60
16	-2.71	-2.71
17	-3.00	-3.00
18	-0.374	-0.512
19	-0.603	-0.607
20	.0188	.0187
21	.0243	.0246

Table 2 A comparison of the node voltages predicted by simulations using the Ebers-Moll model and Gummel-Poon model for each transistor. The simulation using the Ebers-Moll model required 4 Newton iterations and the simulation using the Gummel-Poon model required 18 Newton iterations.

TRANS. NO.	ALL EBERS-MOLL	$I_{C-HIB}$
1	0.170	0.938
2	0.086	0.938
3	0.084	0.938
4	0.448	0.234
5	0.419	0.938
6	0.414	0.938
7	0.862	0.938
8	0.440	0.938
9	0.785	0.938

Table 3 A comparison of transistor collector currents as predicted by the Ebers-Moll model with the onset parameter  $I_{C-HIB}$ .



RUN	1	2	3	4
NODE	ALL EBERS-MOLL	ALL GUMMEL-POON	EBERS-MOLL & PARTIAL GUMMEL-POON	EBERS-MOLL & GUMMEL-POON
1	-.00386	-.0103	-.00885	-.00117
2	-0.684	-0.696	-0.687	-0.688
3	0.742	0.785	0.769	0.787
4	-.000202	-.000562	-.000219	-.000229
5	-0.686	-0.698	-0.689	-0.69
6	0.745	0.761	0.748	0.750
7	0.915	0.955	0.933	0.943
8	6.0	6.0	6.0	6.0
9	2.55	2.33	2.31	2.17
10	1.83	1.63	1.58	1.44
11	0.37	-0.252	-0.141	-0.435
12	-1.89	-1.86	-1.89	-1.89
13	-2.59	-2.57	-2.59	-2.59
14	-2.63	-2.64	-2.63	-2.63
15	-2.61	-2.61	-2.62	-2.62
16	-2.71	-2.73	-2.73	-2.75
17	-3.0	-3.0	-3.0	-3.0
18	-0.37	-0.989	-0.875	-1.16
19	-0.68	-0.69	-0.682	-0.683
20	.0186	.0181	.0185	.0185
21	.0238	.0251	.0256	.0265

Table 4 The results of simulations on a modified version of the circuit of Fig. 4 using different transistor models. Run 1 required 4 Newton iterations, run 2 required 22 Newton iterations, run 3 required 8 iterations, and run 4 required 21 iterations.



Fig. 1 Flow diagram of the method.

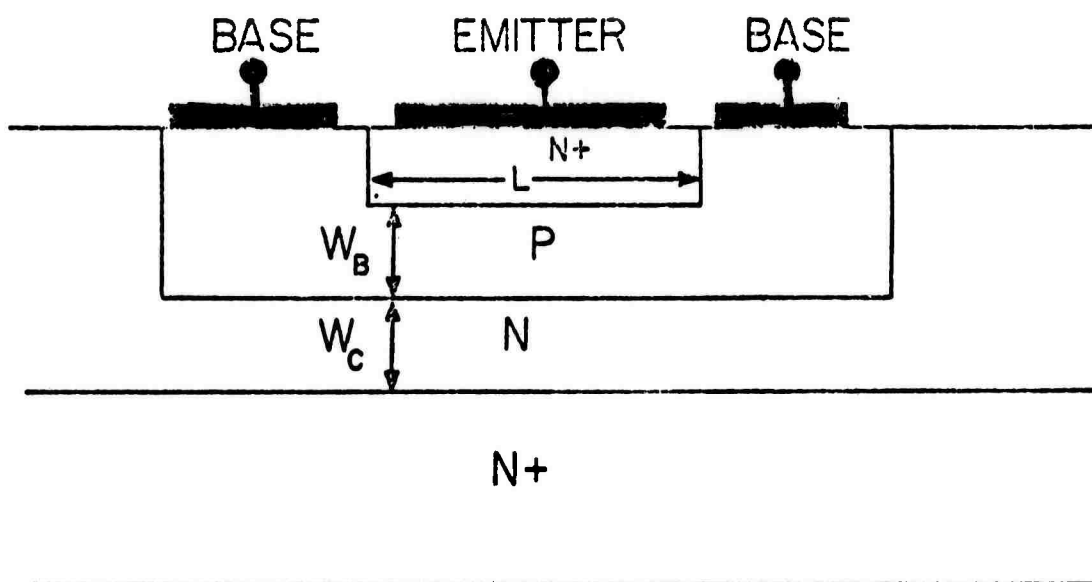


Fig. 2 Pertinent structural features. The emitter depth into the paper is denoted by  $Z$ . The figure shows a double-stripe base contact.

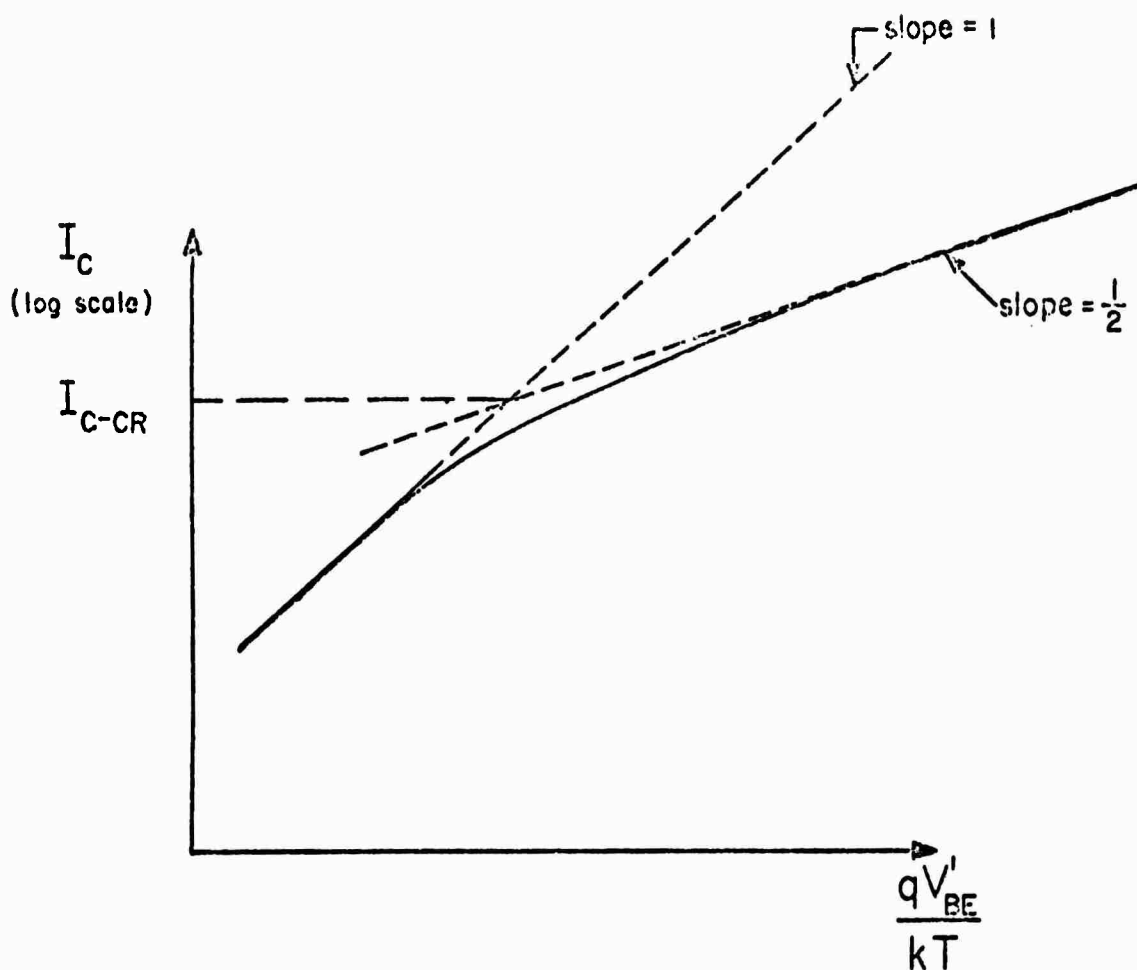


Fig. 3 Interpretation of  $I_{C-CR}$  with  $F_{CR} = 1$ . In this figure, the bending of the curve results from crowding alone. The effects of high injection in the base, space-charge-limited flow in the collector, voltage breakdown, and potential drops in the base resistance are ignored. A wholly analogous interpretation holds for the onset parameter  $I_{C-HIB}$  (with  $F_{HIB} = 1$ ).

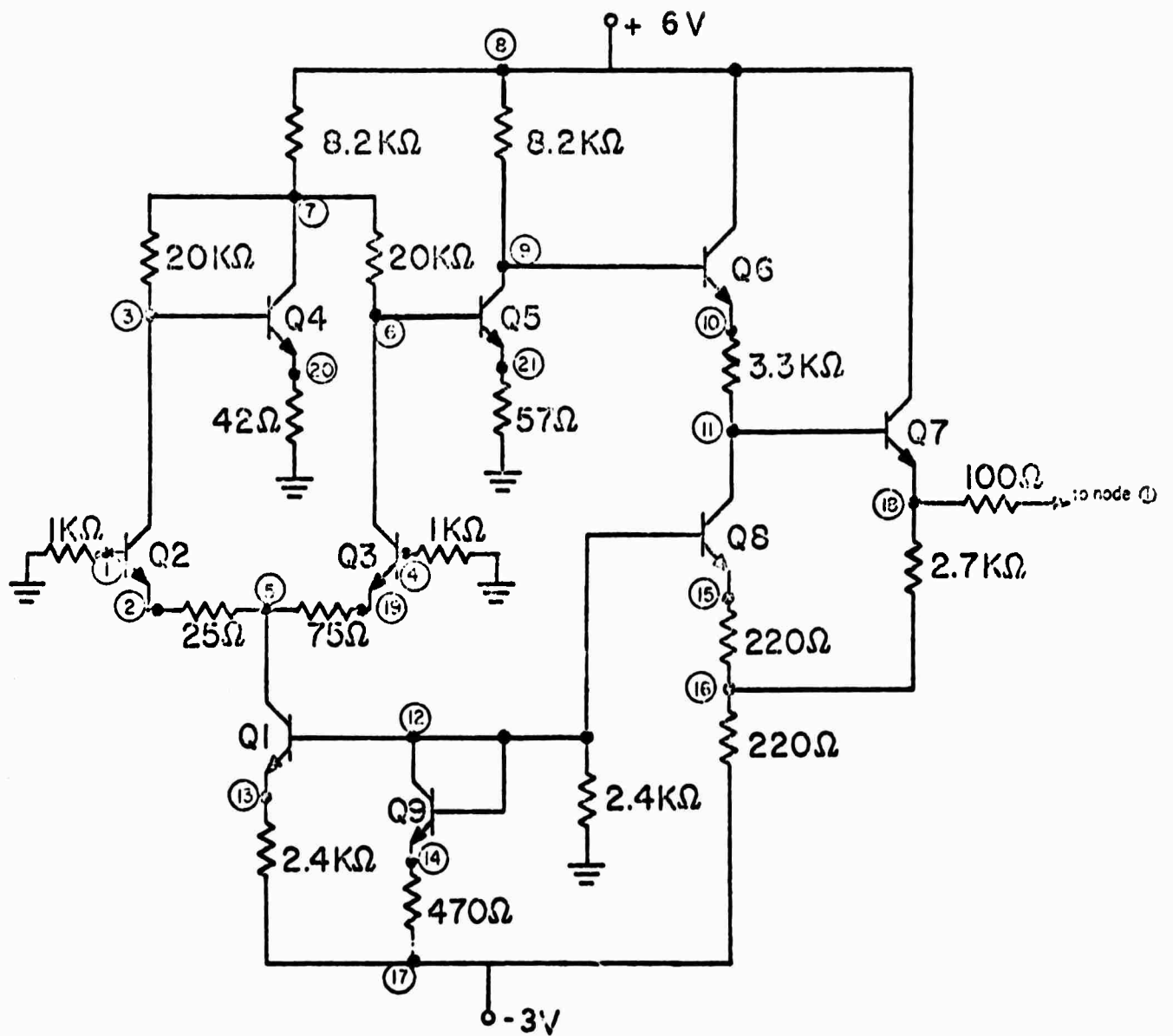


Fig. 4 The  $\mu A 709$  operational amplifier circuit.

F. INCORPORATION OF THE EARLY EFFECT IN THE EBERS-MOLL MODEL  
(F. A. Lindholm)

The Ebers-Moll model<sup>1</sup> is widely used in simulating the static behavior of bipolar transistor circuits. A main attribute of this model is its mathematical simplicity. Its major defect is the neglect of various phenomena that can occur in transistors: high injection in the base, emitter crowding, breakdown, space-charge-limited flow in the collector, appreciable net recombination in junction transition regions, etc. Within a certain determinable range of terminal currents and voltages, however, most of these phenomena can indeed be neglected<sup>2</sup>. The one major exception to this statement involves the Early effect<sup>3</sup> (base-width modulation), which persists for all currents in the forward-active region of transistor operation. The Ebers-Moll model takes no account of the non-zero slope of the output characteristics resulting from the Early effect.

We show here that the addition of a single parameter, which is easily measurable, enables incorporation of the Early effect in the Ebers-Moll formulation. This parameter is the Early voltage  $V_A$ , defined in Figure 1.

As this figure illustrates, extrapolations of the forward-active characteristics all intersect approximately at  $V_A$  for a given temperature<sup>4</sup>. Idealization of the characteristics by neglect of the saturation voltage, as shown in Figure 2, may give adequate accuracy in calculating forward-active performance for many transistor circuits. From Figure 2

$$I_C = [I_C/(V_{CE} + V_A)] V_{CE} + I_S[\exp(qV_{BE}/kT) - 1] \quad (1)$$

Thus the expressions

$$I_C = I_S[\exp(qV_{BE}/kT) - 1] [1 + (V_{CE}/V_A)] \quad (2)$$

$$I_E = -I_C \left\{ 1 + \frac{1}{\beta_{fo} [1 + (V_{CE}/V_A)]} \right\} \quad (3)$$

$$I_E + I_C + I_B = 0 \quad (4)$$

constitute the Ebers-Moll description of forward-active operation, altered to take account of the Early effect. As is evident, the alteration involves simply multiplying the collector currents and the forward-active gain  $\beta_{fo}$  in the original Ebers-Moll formulation by the factor

$$1 + (V_{CE}/V_A) .$$

The notation used in the above expressions is that conventionally employed. The polarities used for voltages and currents apply for an npn transistor. Appropriate sign changes make the expressions valid for a pnp transistor.

In passing, we observe that the dependence on bias of the output small-signal conductance is given approximately by

$$\begin{aligned}\frac{\partial I_C}{\partial V_{CE}} &= \frac{I_S \exp[qV_{BE}/kT - 1]}{V_A} \\ &= \frac{I_C}{V_{CE} + V_A} \\ &= \frac{I_C}{V_A (\beta_f / \beta_{fo})}\end{aligned}\quad (5)$$

In (5)

$$\beta_f = \beta_{fo} [1 + (V_{CE}/V_A)] = I_C/I_B \quad (6)$$

denotes the forward-active current gain including the influence of Early effect.

If greater accuracy is desired than that afforded by (2) - (4), one can idealize the characteristics as shown in Figure 3. Here we approximate saturated operation by a straight line of slope  $1/R_{SC}$  and write, instead of (1),

$$I_C = \frac{I_C(V_{CE} - I_C R_{SC})}{V_{CE} + V_A} + I_S [\exp(qV_{BE}/kT) - 1], \quad V_{CE} > I_C R_{SC} \quad (7)$$

Solution of the resulting quadratic equation for  $I_C$  will then lead to expressions analogous to (2) - (4), but more complex. It is doubtful for most circuits that the gain in accuracy warrants troubling with the increased complexity of description.

The values of the parameters  $V_A$ ,  $\beta_{fo}$ , and  $R_{SC}$  are most easily found from empirical observation of the transistor current-voltage characteristics. As is implied by (6), measurement of the current gain in the forward-active region but for collector voltages so small that

$$V_{CE} \ll V_A$$

determines an approximate value for  $\beta_{fo}$ .

#### REFERENCES

1. J. J. Ebers and J. L. Moll, "Large-signal behavior of junction transistors," Proc. IRE, vol. 42, pp. 1773-1784, Dec. 1954.
2. F. A. Lindholm and S. W. Director, "Assessing model adequacy in integrated-circuit simulation," Technical Digest of 1971 International Solid State Circuits Conference, pp. 44-45, Feb. 1971.  
  
F. A. Lindholm, S. W. Director, and D. L. Bowler, "Assessing model adequacy and selecting model complexity in integrated-circuit simulation," IEEE Journal of Solid State Circuits, to appear Aug. 1971.
3. J. M. Early, "Effects of space charge layer widening in junction transistors," Proc. I.R.E., vol. 46, pp. 1141-1152, Nov. 1952.
4. H. K. Gummel and H. C. Poon, "An integral charge control model of bipolar transistors," BSTJ, vol. 49, pp. 827-852, May-June 1970.



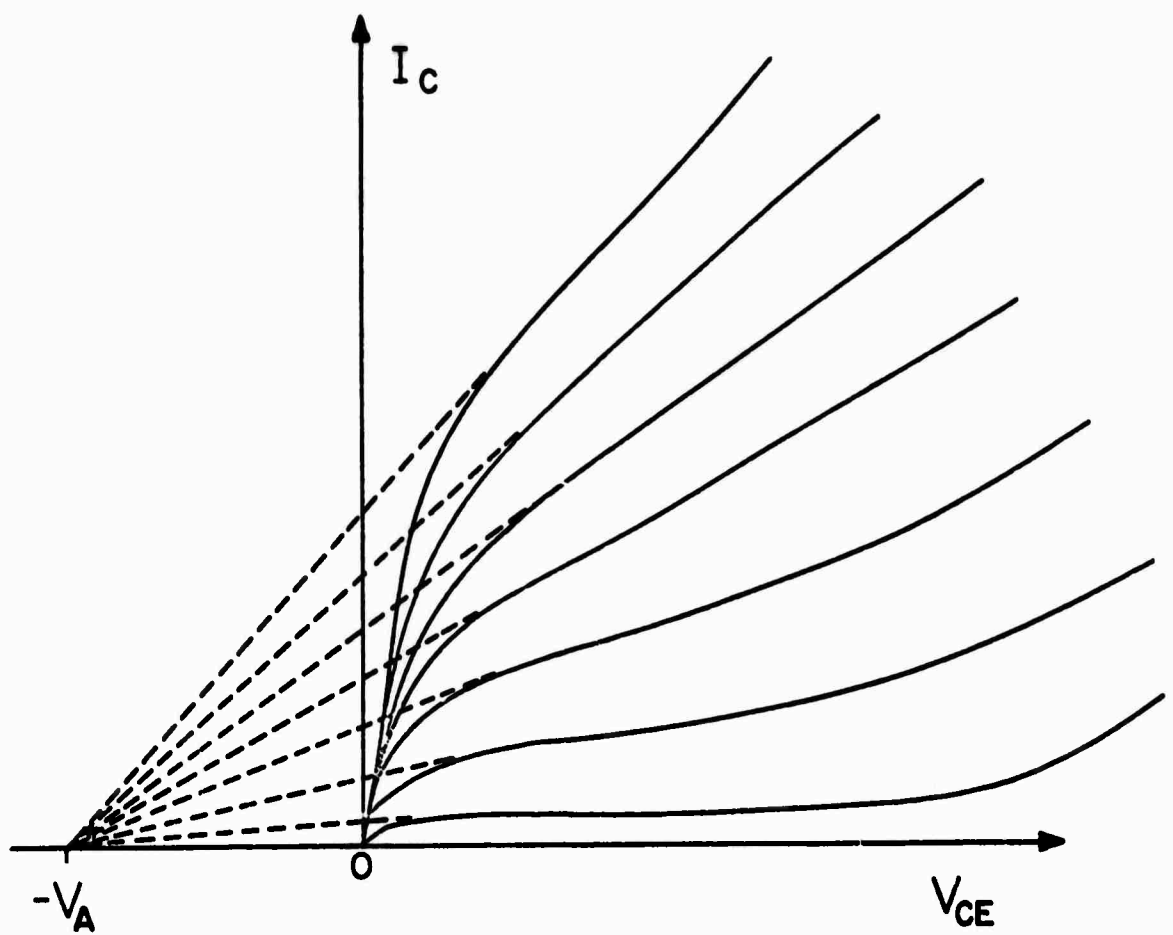


Fig. 1 Illustrating the Early voltage  $V_A$  for an npn transistor.

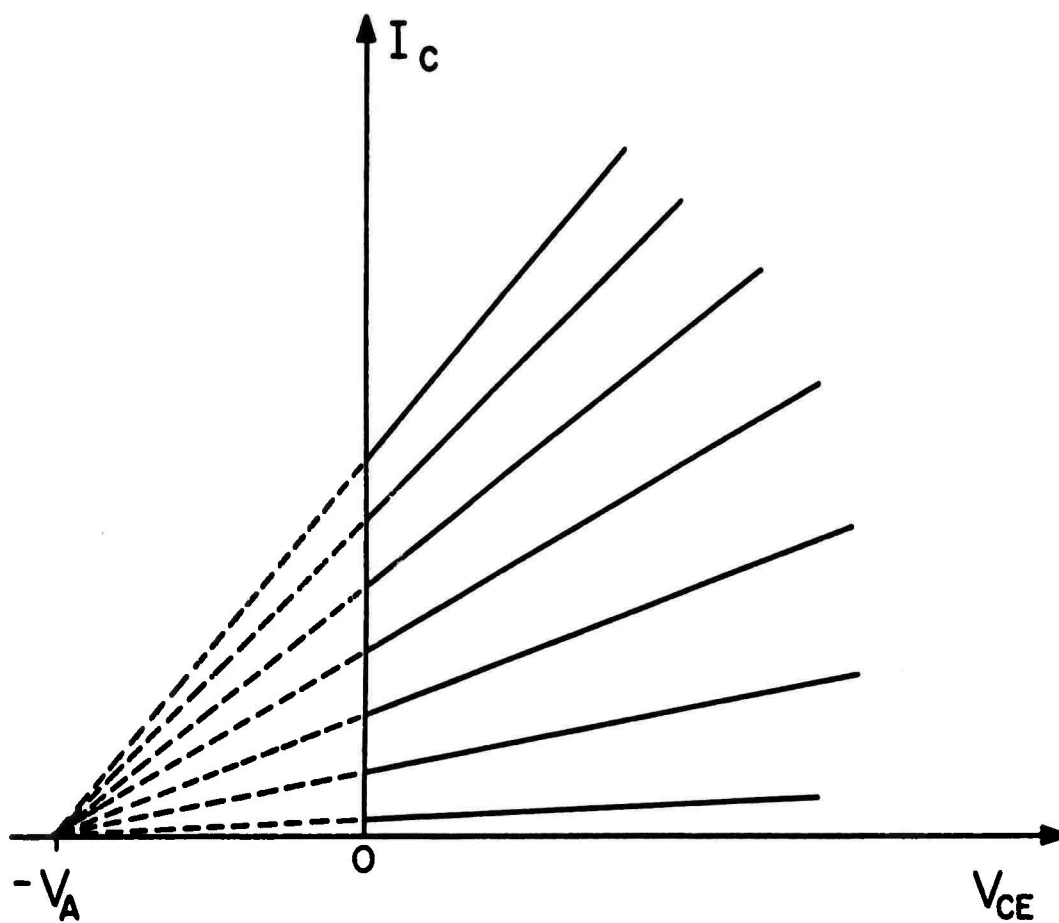


Fig. 2 Idealization of the characteristics enabling simple incorporation of the Early effect in the Ebers-Moll model.

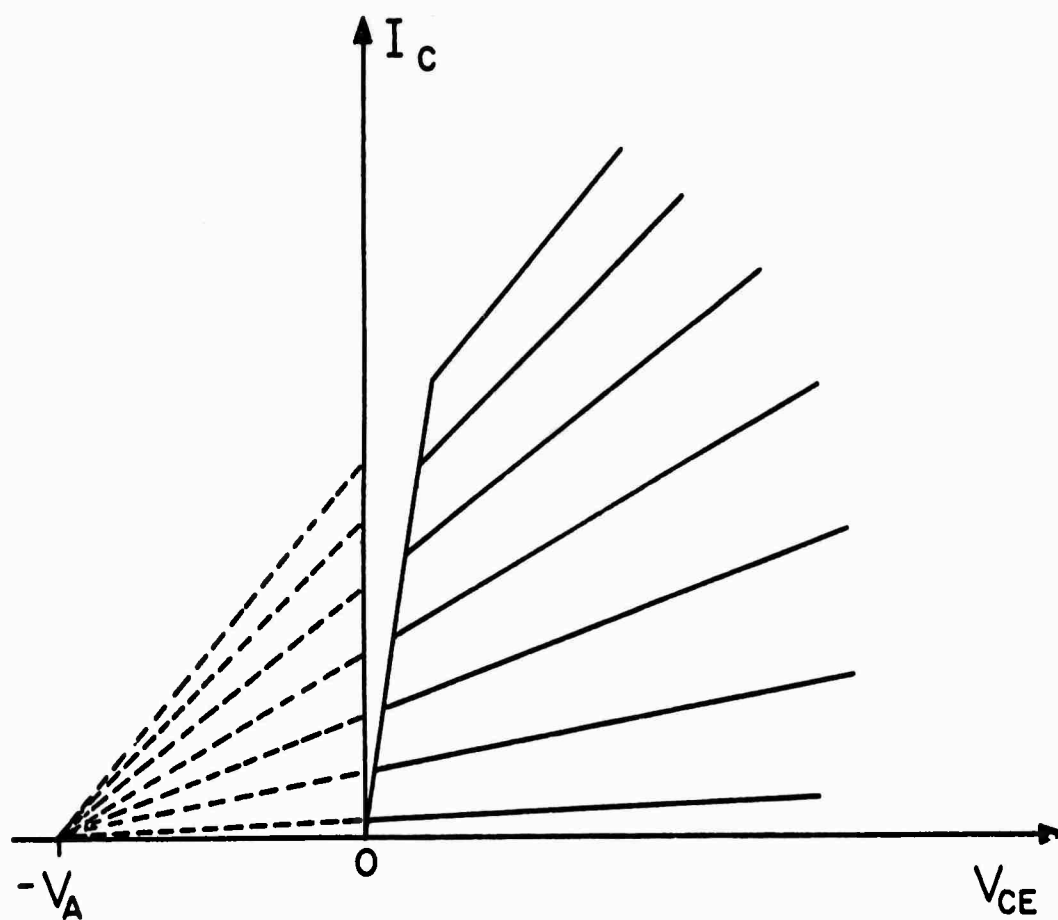


Fig. 3 A second idealization of the transistor characteristics.

### III. Insulating and Semiconducting Glasses (L. L. Hench, R. W. Gould)

#### A. FAST NEUTRON EFFECTS IN GLASS-CERAMICS AND AMORPHOUS SEMICONDUCTORS (L. L. Hench, W. D. Tuohig and A. E. Clark)

##### I. Introduction

The unique range of properties exhibited by both insulating glass-ceramics and amorphous semiconductors makes them potentially useful in a variety of applications which may involve exposure to nuclear irradiation. Although the neutron radiation sensitivity of insulating glasses<sup>1</sup> and various crystalline ceramic materials<sup>2-4</sup> have been investigated in some detail, relatively little is known about neutron damage in glass-ceramics or semiconducting glasses.

Several recent reports have been made concerning neutron and  $\gamma$ -ray effects on the behavior of switching devices made of chalcogenide glasses<sup>5,6</sup>. The studies have shown device insensitivity from fluences of  $10^{16}$  n/cm<sup>2</sup> nvt fast neutrons and  $10^{11}$  rads/sec of  $\gamma$ -rays. The electrical conductivity of liquid chalcogenides has been found<sup>7</sup> to be unaffected by fast neutron dosages of as much as  $1.8 \times 10^{20}$  cm<sup>-2</sup>. Considering that the measurements were made on liquids, this result is not surprising.

Results from this laboratory<sup>8</sup> have shown that the electrical conductivity of solid semiconducting glasses in the  $V_2O_5$ - $P_2O_5$  system are relatively unaffected by fast neutron fluences of up to  $4 \times 10^{17}$  nvt. However, an approximately 10% increase in

electrical conductivity was observed after a dose of  $1.25 \times 10^8$  rads of  $\text{Co}^{60}$   $\gamma$ -ray irradiation. This behavior was attributed to an increase in the concentration of quasi-free charge carriers due to Compton scattering of electrons. Additional evidence in support of this argument will be presented in this paper.

Studies of the influence of fast neutrons on the stability of the electrical properties of heterogeneous  $\text{KPO}_3\text{-V}_2\text{O}_5$  semiconducting glasses have been recently reported by one of the authors.<sup>(9)</sup> An important observation in the study was the degradation of electrical characteristics associated with 100 Å to 200 Å ordered heterogeneities within the glass matrix. After a  $2.7 \times 10^{17}$  nvt fluence the electrical conductivity had decreased by a factor of 7, A.C. conductivity characteristics of the disordered glass had appeared, and a large dielectric loss peak was destroyed. An objective of the present paper is to discuss the importance of crystallite size on the fast neutron damage threshold in heterogeneous amorphous semiconductors.

Ionically conducting  $\text{Li}_2\text{O-SiO}_2$  glasses containing sub-micron crystalline regions have also been shown by the authors to be strongly influenced by fast neutron exposure.<sup>(10)</sup> A fluence of  $1 \times 10^{17}$  nvt was sufficient to decrease the magnitude of the dielectric loss peak exhibited by the material. The radiation exposure also accelerated the sequence of crystallization reactions occurring during thermal treatment of the glass. The dissolution rate of lithium metasilicate crystals which appear as a precursor to equilibrium crystallization was enhanced by the fast neutron damage.

A final objective of this paper is to report the effects of increasing the cumulative fast neutron dosage on the electrical properties of the nucleated  $\text{Li}_2\text{O-SiO}_2$  glasses.

## II. Experimental Procedure

All three glasses discussed were melted in electric muffle furnaces in covered Pt crucibles and formed into specimens approximately 1.8 cm in diameter and 0.5 cm thick by quenching

into steel molds. The compositions studied, melting and annealing schedules are given in Table I.

Table I

Glass Composition	Melting Temp. and Time	Annealing Temp. and Time
80 mole % $V_2O_5$ - 20 mole % $P_2O_5$	966°C/10 hr.	300°C/30 min.
33 mole % $KPO_3$ - 67 mole % $V_2O_5$	550°C/8 hr.	200°C/2 hr.
33 mole % $Li_2O$ - 67 mole % $SiO_2$	135°C/24 hr.	300°C/1 hr.

Electrical measurements were made in vacuum on polished samples with vacuum evaporated gold electrodes in a double guard ring configuration using an apparatus previously described.<sup>(8,10,11)</sup>

Gamma-ray irradiation experiments were performed using 30,000 Ci  $Co^{60}$  source at the University of Florida. The  $\gamma$ -ray dose was determined by using the photometric  $Fe^{2+} \rightarrow Fe^{3+}$  reaction as detailed in ASTM procedure D-1671-63.<sup>(12)</sup> Specimen temperature during  $\gamma$ -radiation was approximately 25°C.

Both the  $V_2O_5$ - $P_2O_5$  and  $Li_2O$ - $SiO_2$  glasses were given neutron irradiation exposures in the Wright-Patterson Air Force Base test reactor. The Wright-Patterson AFB reactor has a fast neutron flux capability of  $1.5 \times 10^{13}$  n/cm<sup>2</sup> (>0.1 meV). The fast neutron flux was measured using a 58 nickel [n,p] 59 cobalt reaction with a 2.9 meV threshold energy. Fluxes reported are based on activations measured 48 hours after removal of the samples from the reactor. Cadmium wrapping was employed to protect the gold electrodes. Temperature monitoring of the reactor indicated that sample temperatures were in the range of 50°C throughout the exposures. Approximately four weeks lapse at 25°C between exposure and measurement was necessary to reduce activity to a tolerable level.

V<sub>2</sub>O<sub>5</sub>-P<sub>2</sub>O<sub>5</sub> Amorphous Semiconductors. Previous reactor exposures of 80 mole % V<sub>2</sub>O<sub>5</sub> - 20 mole % P<sub>2</sub>O<sub>5</sub> glasses resulted in a slight increase in the electrical conductivity.<sup>(8)</sup> Separate Co<sup>60</sup> γ-ray experiments indicated this behavior was due to γ-ray ionization of charge carriers. The net effect was only a 10% increase in conductivity. However, additional data presented in Figure 1 shows that the γ-ray exposure strongly influences the dielectric losses in the glasses.

The dielectric loss angle,  $\tan \delta$ , plotted as a function of log measuring frequency, Hz, increases due to the  $6.8 \times 10^7$  rads γ-ray exposure. Well resolved dielectric loss peaks also appear. The frequency location of the loss peaks and their magnitude both suggest that appreciable interfacial polarization is occurring in the irradiated glasses.<sup>(13)</sup> Analysis of the temperature dependence of the frequency location of the dielectric loss peak,

$$f_{\max} = f_0 \exp[-Q/RT], \quad (1)$$

results in a measured activation energy for the loss process of 0.6 ev. This is the same value calculated for the temperature dependence of the D.C. conductivity of this glass.<sup>(9)</sup> Therefore, it is reasonable to assume that similar electronic carriers are involved in the relaxation process as contribute to the D.C. conductivity.

Since the γ-irradiation should not produce structural heterogeneities in the glass, the interfacial barriers involved in the relaxation process must be associated with heterogeneities already present or the sample electrodes. As discussed in a recent paper concerning the theory of heterogeneous semiconductors,<sup>(14)</sup> either internal heterogeneities or partially blocking electrodes can give rise to dielectric loss peaks in these materials.

A γ-ray dosage of  $1.25 \times 10^8$  rads produced an unusual low frequency resonance-like response which also appears to be an interfacial phenomena. Figure 2 summarizes a series of measurements of the frequency dependent capacitance of the 80/20 V<sub>2</sub>O<sub>5</sub>-P<sub>2</sub>O<sub>5</sub> glass exposed to  $1.25 \times 10^8$  rads. After irradiation an

appreciable increase in the capacitance is observed even at 23°C. At 40°C, post radiation, a large increase in capacitance occurs, followed at 65°C by a wide low frequency resonance-like effect. The capacitance of the sample is negative over the range from  $2.7 \times 10^3$  Hz to  $4.5 \times 10^5$  Hz, as measured by the -C scale on the Wayne Kerr B-221 bridge and the L scale on the B-61 bridge. From  $3 \times 10^4$  Hz to  $1 \times 10^5$  Hz the negative C values are too large to be measured.

At a higher temperature, 87°C, the resonance-like behavior appears to be damped and is measurable over the entire frequency range. At 114°C the negative capacitance behavior disappeared during the measurements, indicating a rapid annealing process at this temperature. Post annealing data is shown in Figure 2 at a measurement temperature of 86°C. After annealing, capacitance values are nearly equivalent to the pre-radiation values for the glass and are not shown for the sake of clarity.

It seems that the data of Figures 1 and 2 can be interpreted in one of two ways. Either the ionizing radiation produces extra charge carriers which are trapped at previously existing barriers in the glass or at the electrode-glass interface. Or, the radiation could create traps at interfacial regions which are populated with "normal" carriers, the traps being created by ionization of deep-lying electrons. The fact that the activation energy for the relaxation loss process is the same as for D.C. conduction would appear to favor the latter alternative. One would expect a lower activation energy for a large number of ionized electrons. Also, if pre-existing traps at interfaces were present, the relaxation process should occur with "normal" carriers as well.

Creation of a wide distribution of deep-lying traps at interfacial regions also provides a reasonable explanation for the observed resonance behavior at  $1.25 \times 10^8$  rads. In such a model, the resonance-like behavior is associated with thermally activated and field directed oscillations between trapping sites. At low temperatures, the oscillations simply contribute an additional interfacial polarization to the capacitance. At



sufficiently high temperatures, resonance oscillations through the barriers become possible. A portion of the population obtains irreversible sites on one side of the barrier, thus producing a temperature dependent annealing of the phenomena.

Partially Crystallized Semiconducting Glasses. Previously reported investigations of fast neutron effects in heterogeneous 33 mole %  $\text{KPO}_3$  - 67 mole %  $\text{V}_2\text{O}_5$  semiconducting glasses involved crystallites in the 100-200 Å size range.<sup>(4,15)</sup> A heat treatment at 288°C of glasses rapidly quenched from 800°C was employed in the nucleation and growth of the crystallites. The studies showed that fast neutron fluences of less than  $1.0 \times 10^{17}$  were required to destroy dielectric loss peaks associated with the high conductivity crystallites.

It is also possible to produce a small volume fraction, <1%, of sub-micron crystals in the  $\text{KPO}_3$ - $\text{V}_2\text{O}_5$  glasses by casting from temperatures of 550°C or below.<sup>(9)</sup> Dielectric loss peaks are exhibited by such materials as shown in Figure 3. The loss peaks have been attributed to high conductivity  $\text{PV}_2$  crystals, giving rise to Maxwell-Wagner-Sillars (MWS) interfacial polarization.<sup>(16)</sup> Similar behavior has been observed in the  $\text{FeO-P}_2\text{O}_5$  system.<sup>(17)</sup> The size of the crystals in the sample of Figure 3 are in the range of 0.1 μm, a factor of 10 larger than in the previously reported study.<sup>(9)</sup>

The effect of the exposure of the heterogeneous glass to a  $1.7 \times 10^{17}$  nvt fast neutrons is also shown in Figure 3. Two major changes are readily apparent. The magnitude of the loss peak is markedly reduced and the location of the loss peak is shifted to a higher frequency. In terms of the MWS interfacial polarization model, the decrease in loss peak height indicates that either the volume fraction of crystallites has decreased or the conductivity difference between the phases is reduced, or the phase boundary has been degraded sufficiently that it will not sustain a space charge.

The frequency location of the loss peak is controlled by the morphology of the dispersed phase and consequently, a shift in frequency is evidence that morphological changes have occurred.

Consequently, the loss behavior observed indicates that there is cumulative disordering of the dispersed sub-micron crystals within the glass matrix from the fast neutron irradiation. The damage threshold for the larger crystals appears to be in the range of an order of magnitude greater than the 100-200 Å crystals. Consequently, these results would suggest that the damage threshold for crystals dispersed in a glass matrix may be linearly proportional to the size of the crystals. Additional studies to extend the range of validity of this conclusion are in progress.

Li<sub>2</sub>O-2SiO<sub>2</sub> Glass-Ceramics. Previous investigations have established that heat treating 33 mole % Li<sub>2</sub>O-SiO<sub>2</sub> glasses at 500°C for 5-6 hours precipitates metastable lithium metasilicate crystals that are ~200 Å long and 50 Å wide.<sup>(18,19)</sup> A MWS dielectric loss peak appears in the glass concurrent with the presence of the crystals. Additional heat treatment causes the metastable crystals to resorb and nucleate the equilibrium lithium disilicate crystal phase in the process. The dielectric loss peak decreases in magnitude and shifts to a higher frequency as a result of the resorption.

A recent paper by the authors showed that the metastable nucleation process was unaltered by a  $1.0 \times 10^{17}$  nvt irradiation of the glass prior to heat treatment.<sup>(10)</sup> However, the metasilicate dissolution process was shown to be significantly accelerated by the fast neutron irradiation. The explanation proposed was that the Li<sup>+</sup> mobility was enhanced by the irradiation, making the structure more susceptible to thermal alteration. An enhanced mobility of the Li ions would also decrease the conductivity difference between the matrix and the crystals, thereby reducing the magnitude of the loss peak, as shown in Figure 4. The absence of a shift in frequency of the peak with the  $1.0 \times 10^{17}$  nvt exposure indicates that appreciable morphological changes did not occur.

Additional evidence to support this conclusion of enhanced Li<sup>+</sup> ion mobility is presented in Figure 5. The A.C. conductivity of the Li<sub>2</sub>O-SiO<sub>2</sub> glasses after a 500°C/6-hour heat treatment is

plotted as function of measuring frequency at various measuring temperatures. The pre-neutron irradiation conductivity is lower than the conductivity after the  $1.0 \times 10^{17}$  exposure. The radiation enhancement of the conductivity appears to be due to an increase in the pre-exponential term,

$$\sigma = \sigma_0 \exp - [Q/RT] \quad (2)$$

rather than a decrease in activation energy for the ionic conduction. Figure 6 shows that the activation energy for the glass before and after the  $1.0 \times 10^{17}$  nvt radiation remains at approximately 15 kcal/mole, which is equivalent to that previously reported for this material.

Increasing the fast neutron fluence to  $1.8 \times 10^{17}$  continues the degradation of the dielectric loss peak, Figure 4, to one-third the magnitude of the pre-radiation peak. In addition, the location of the peak is shifted to higher frequencies.

It can be seen in Figures 5 and 6 that the magnitude of the glass conductivity is decreased by the additional neutron exposure, primarily by an increase in the activation energy to approximately 20 kcal/mole. Such a decrease in activation energy may be a result of densification of the glass structure such as observed in  $\text{SiO}_2$  even at  $10^{17}$  nvt.<sup>(20)</sup> It is also reasonable that the  $\text{Li}^+$  ions would be appreciably influenced by densification because of their lower bonding energy.

Thermal variation of the loss peak location for the  $1.8 \times 10^{17}$  irradiated sample is given in Figure 7. A plot of the logarithm of the frequency of maximum loss vs.  $1/T$  (eq. 1) yields the activation energy for the relaxation process. As shown in Figure 8, the activation energy is not appreciably changed by the radiation.

Because of the decrease in bulk conductivity of the  $1.8 \times 10^{17}$  nvt sample, a consistent explanation for the destruction of the loss peak requires a degradation of the metasilicate crystals that give rise to the peak. The shift in the frequency of the loss peak suggests that the axial ratio of the metasilicate

crystals is reduced by the radiation in a like manner to that produced by additional 500°C thermal treatments. (10,18)

Consequently, it can be concluded that the change in the electrical properties of the nucleated glasses is a result of enhanced ionic mobility at low dosages ( $1.0 \times 10^{17}$  or less) followed by neutron destruction of the sub-micron crystal nuclei at larger dosages.

### III. Conclusions

The major point to be re-emphasized is that electrical properties of heterogeneous glasses that are governed by sub-micron crystals are susceptible to fast neutron damage at fluences of  $1-2 \times 10^{17}$  nvt. The size of the crystals affects the damage threshold. Ionizing radiation produces electronic complications in addition to the neutron related structural changes for semi-conducting glasses.

## REFERENCES

1. E. Lell, N. J. Kreidl and J. R. Hensler, "Radiation Effects in Quartz, Silica and Glasses," Progress in Ceramic Science, Vol. 4, p. 73 (J. Burke, editor, Pergamon Press, 1966).
2. W. Primak and R. Kampfworth, "Radiation Compaction of Vitreous Silica," J. Appl. Phys., 39 [12] 5651-5658 (1968).
3. M. Nachman, L. Cojocaru and L. Ribco, Nukleonik, 10 Band, 1. Heft (1967), p. 1.
4. Barber, "Effects of Nuclear Radiation on Electrical Properties of Non-stoichiometric NiO," J. Am. Cer. Soc., 51, 611 (1968).
5. (a) S. R. Ovshinsky, E. J. Evans, D. L. Nelson, H. Fritzsche, "Radiation Hardness of Ovonic Devices," IEEE Trans. on Nuclear Science, Dec. 1968.  
  
(b) R. R. Shanks, J. H. Helbers and D. L. Nelson, "Ovonic Computer Circuits Development," Technical Report AFAL-TR-69-309, June 1970  
  
(c) R. R. Shanks, D. L. Nelson, R. L. Rowler, H. C. Chambers and D. J. Niehaus, "Radiation Hardening Circuitry Using New Devices," Technical Report AFAL-TR-70-15, March 1970.
6. E. J. Evans, "A Feasibility Study of the Applications of Amorphous Semiconductors to Radiation Hardening of Electronic Devices," Picatinny Arsenal Technical Report 3698.
7. J. T. Edmond, J. C. Male and P. F. Chester, J. Sci. Inst. (J. of Physics E), 1 [2] 373 (1968).
8. L. L. Hench and G. A. Daughenbaugh, J. Nuclear Materials, 25, 58-63 (1968).
9. L. L. Hench, J. Non-crystalline Solids, 2, 250-277 (1970).
10. W. D. Tuohig and L. L. Hench, J. Nuclear Materials, 31, 86-92 (1969).
11. L. L. Hench, "Dielectric Relaxation in Materials Analysis," Society of Aerospace Materials and Process Engineers, Proceedings of the 14th Annual Symposium, Cocoa Beach, Florida, November 1968; reprinted as Technical Paper 428, Engineering Progress at the University of Florida, Gainesville.
12. Test for absorbed gamma radiation dose in the Fricke dosimeter, ASTM Standards, 29, 719 (1963).

13. (a) L. K. H. von Beek, in Progress in Dielectrics, Vol. 7 (CRC Press), p. 69.
14. (b) L. L. Hench and H. F. Schaake, "Electrical Properties of Glass," in Introduction to Glass Science, D. Pye and H. Simpson, editors, Plenum Press (in press).  
  
H. F. Schaake, "Theory of Heterogeneous Semiconductors," in Physics of Electronic Ceramics, L. L. Hench and D. B. Dove, editors, M. Dekker, Inc. (1971), (in press).
15. L. L. Hench, A. E. Clark and D. L. Kinser, "Neutron Irradiation Effects in Partially Crystallized Semiconducting Glasses," submitted to J. Non-crystalline Solids.
16. A. Fuwa, "Electrical Properties of Glasses and Crystals in the  $K_2O-V_2O_5-P_2O_5$  System," M.S. Thesis, University of Florida, 1970.
17. D. L. Kinser, J. Electrochem. Soc., 117 [4] 546 (1970).
18. D. L. Kinser and L. L. Hench, J. Am. Cer. Soc., 52, 445 (1968).
19. D. L. Kinser and L. L. Hench, J. Materials Sci., 5, 369 (1970).
20. R. E. Jaeger, J. Am. Cer. Soc., 51, 57 (1970).

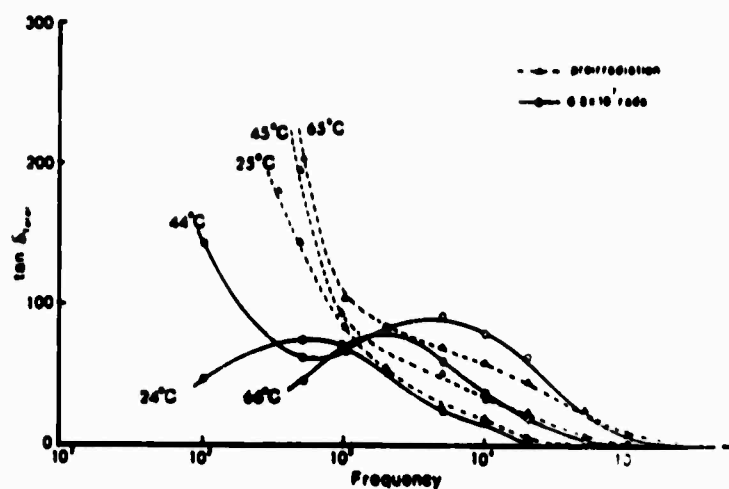


Fig. 1. Development of dielectric loss peaks in an 80 mole %  $V_2O_5$  - 20 mole %  $P_2O_5$  semiconducting glass with  $6.8 \times 10^7$  rads  $^{60}Co$   $\gamma$ -ray exposure.

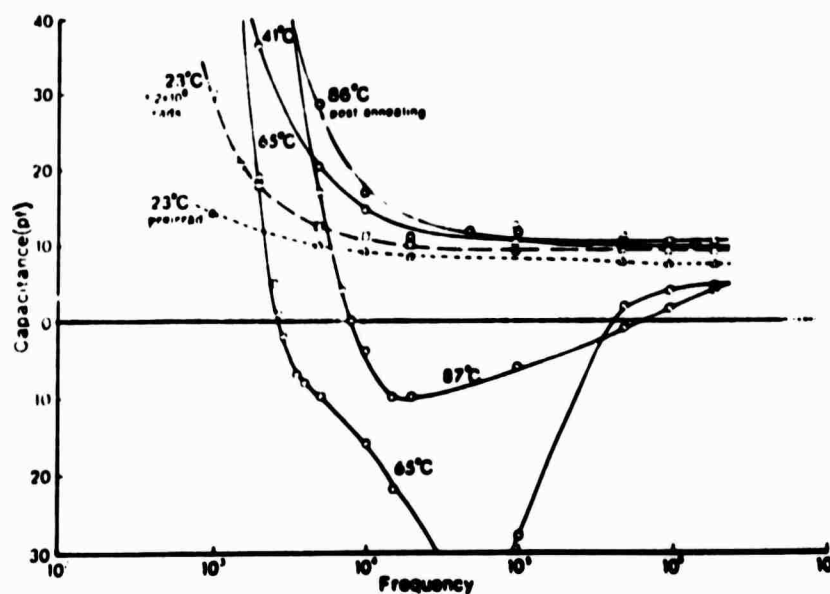


Fig. 2. Sequence of capacitance behavior of our 80/20  $V_2O_5/P_2O_5$  semiconducting glass after  $1.2 \times 10^8$  rads  $^{60}Co$   $\gamma$ -ray irradiation. Sequence: 23°C pre-rad; 23°C post-rad; 65°C post-rad; 87°C post-rad; 86°C post-rad, post 119°C annealing; 41°C post-rad, post annealing.

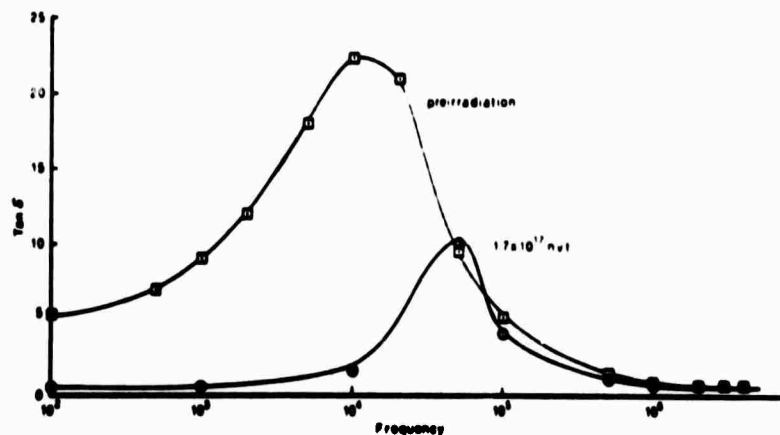


Fig. 3. Dielectric loss peaks, before and after  $1.7 \times 10^{17}$  nvt irradiation, exhibited by a 33 mole %  $\text{KPO}_3$  - 67 mole %  $\text{V}_2\text{O}_5$  semiconducting glass-ceramic.

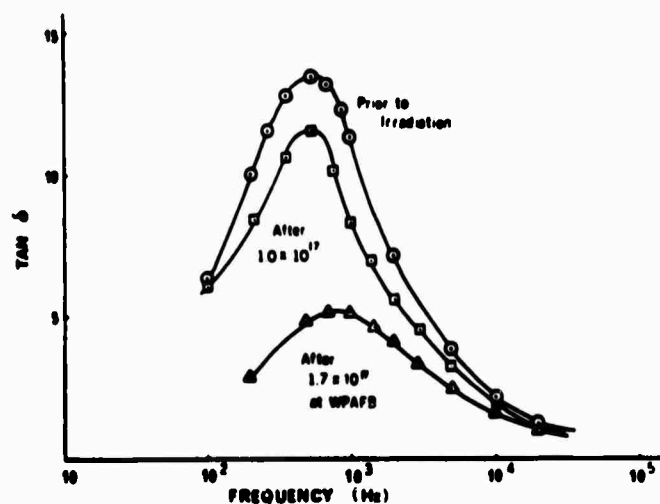


Fig. 4. Influence of cumulative fast neutron exposure on the dielectric loss peak of a  $500^\circ\text{C}/6$  hr. heat treated  $\text{Li}_2\text{O}-2\text{SiO}_2$  glass.



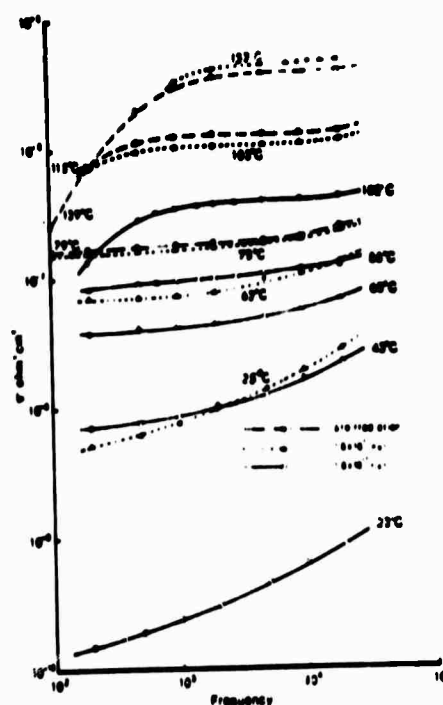


Fig. 5. Change in electrical conductivity-temperature-frequency behavior of a nucleated  $\text{Li}_2\text{O}-2\text{SiO}_2$  glass with cumulative fast neutron exposure.

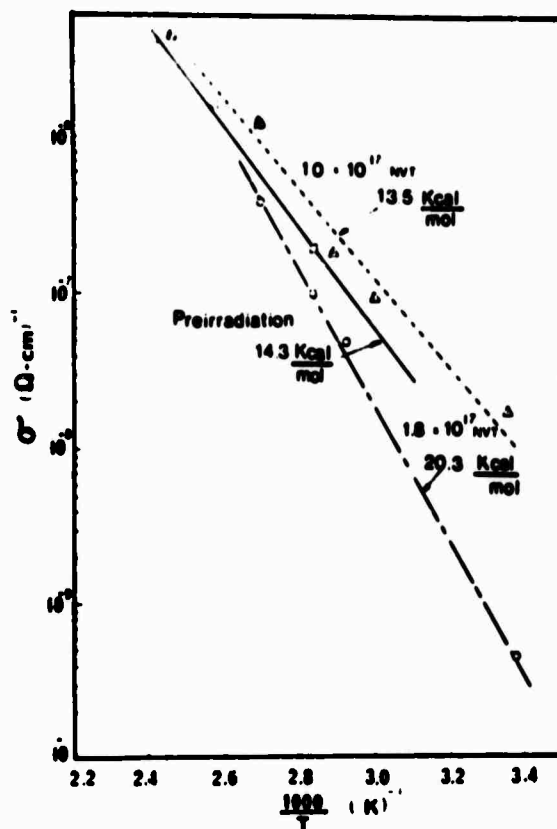


Fig. 6. Fast neutron dependent changes in the conductivity temperature dependence of a  $500^\circ\text{C}/6$  hr. heat treated  $\text{Li}_2\text{O}-2\text{SiO}_2$  glass.  $\sigma$  measured at  $5 \times 10^3$  Hz.

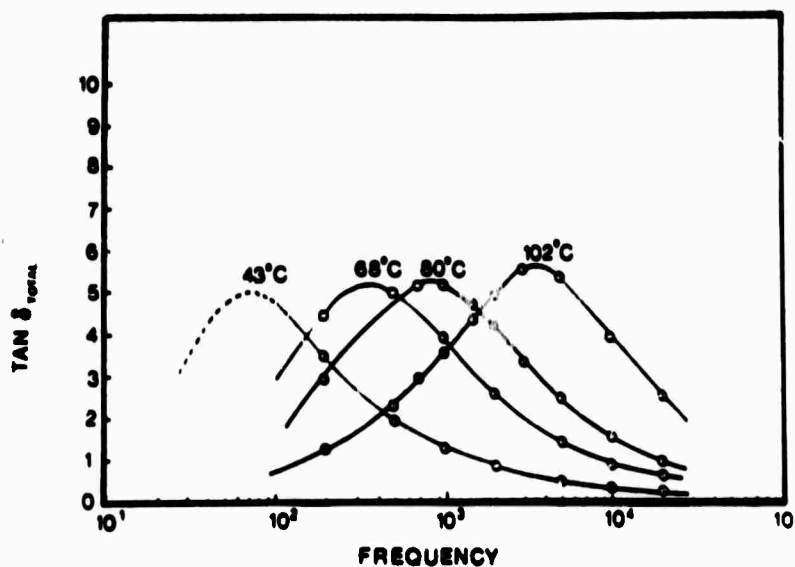


Fig. 7. Temperature dependent variation in dielectric loss peak location for a  $\text{Li}_2\text{O}-2\text{SiO}_2$  nucleated glass after  $1.8 \times 10^{17}$  nvt irradiation.

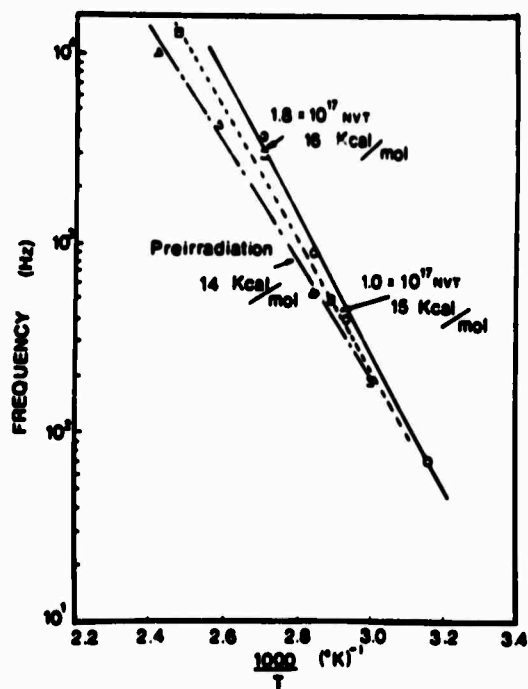


Fig. 8. Fast neutron effects on the temperature dependence of the dielectric loss peak location of a nucleated  $\text{Li}_2\text{O}-2\text{SiO}_2$  glass.

## B. CHARACTERIZATION OF POWDER SURFACES (L. L. Hench)

### I. Introduction

Analyzing the surface character of powders is perhaps one of the most important and most difficult procedures in ceramics. The importance of a powder's surface is that it can control the extent of agglomeration or aggregation of the particles and the strength of the interparticle bond. The state of powder aggregation or agglomeration strongly influences the morphology developed in sintering, particularly the tendency towards an "end-point density."<sup>(1)</sup> Recent theoretical sintering studies<sup>(2)</sup> have proven that the initial number and distribution of interparticle contacts establishes the entire course of morphological changes occurring in sintering and hot pressing steps. Alterations in the interparticle topology during forming processes also are directly related to the number and strength of interparticle bonds. In addition, the reactivity of powders is largely related to surface structure and therefore sintering kinetics, catalysis, and the ion exchange behavior of ceramics are functions of the particle surfaces. Therefore, it would seem that surface characterization should be a well established procedure in the manufacture of many ceramic products.

However, the understanding of powder surfaces is perhaps the least developed of any field of science and technology. Consequently, specific powder surface characterization methods are not well established at all. Correlations of powders with well characterized surfaces and various ceramic processing methods are practically non-existent. There is good reason for the lack of development in the field of powder surface characterization. The scale of observation required for surface structure analysis is beyond the resolution limits of existing instrumental techniques.

## II. Direct Means of Characterization

Direct transmission electron microscopy (TEM) comes the closest to detecting and analyzing surface structures. But even this method cannot detect atomistic surface irregularities, amorphous surface films several atom layers thick, and of critical importance, TEM analysis requires vacuum measurements. In-situ analysis of surface hydrosphere structures, which exist for most ceramic powders under standard humidity conditions, is therefore impossible.

Sampling problems in TEM are obviously formidable and analysis of the agglomeration or aggregation state of the powder is extraordinarily laborious due to particle overlap problems. In order to distinguish whether a group of particles (a clump) are sintered together (aggregate) or bonded by physisorbed layers, van der Waals bonds, or electrostatic charges (agglomerates), it is necessary to obtain a 3-D view of the interparticle contacts. This requires the use of a goniometer stage and the tilting of every pair of particles in the clump to insure that particle overlap is not responsible for the apparent bonding. There are several difficulties associated with such an analysis. It is restricted to clump sizes of 10-15 particles in order to obtain transmission images. If the number of particles per clump is too large, the sample will appear opaque to the electron beam. Also, if two or more

phases are present as particles it is necessary to use quantitative stereological analysis of the TEM images to determine volume fraction distributions per clump, surface areas, mean free paths, etc. (See Chapter 19.) Such analysis must use the mathematical corrections for overlap errors<sup>(3)</sup> and also must apply thickness error corrections.<sup>(4)</sup> As recently shown,<sup>(4)</sup> if sampling thickness effects are ignored errors of as much as 300% can be introduced. (See Chapter 20 for details of these and other possible errors in quantitative analysis of TEM and SEM images.)

Direct TEM analysis of particle surface layers is not particularly encouraging for several reasons. The resolution of selected area diffraction is insufficient to isolate surface layers of 5-20 Å thick. The disordered and potentially amorphous structure of the surface layers also is unfavorable for diffraction analysis.

Other direct means of surface characterization have been developed and successfully applied to single crystal surfaces as discussed in Chapter 21. These techniques include low energy electron diffraction (LEED),<sup>(5)</sup> Auger spectroscopy,<sup>(6)</sup> field emission microscopy (FEM),<sup>(7)</sup> field ion emission microscopy (FIM),<sup>(8)</sup> and scanning electron diffraction (SED).<sup>(9)</sup> Each of these tools share the difficulty with TEM that a vacuum is required. The experimental difficulties of applying these methods to the analysis of powders has not been overcome at the present time. In fact, quantitative data interpretation of well characterized, clean, single crystal surfaces is still in its adolescence.<sup>(8,10)</sup>

### III. Indirect Means of Characterization

The above discussion emphasizes the need for indirect methods of analysis if the characterization of powder surfaces is to be accomplished. A variety of such tools have been developed by physical chemists over the years and the various methods generally fall into two categories: 1) interaction of the

powder with a liquid, and 2) interaction of the powder with a gas. Different techniques arise by analyzing different types of interactions in each of the above cases and by varying the nature of liquid or gas employed. All such indirect methods have in common the requirement that experimental results must be interpreted in terms of a surface structural model. Although the experimental methods in themselves may be reasonably straightforward and reproducible, it is in the interpretative models that difficulties and controversy arises.

The reason for ambiguity in interpretation is simple and implied in the previous section. There is at present no valid, direct means of characterizing most ceramic powders which can be used as standards in evaluating the models for indirect characterization. This difficulty is beginning to be overcome, as shown by recent gas absorption studies on directly characterized carbon<sup>(11)</sup> and silica powders.<sup>(12)</sup> Once agreement as to model interpretations for these and several oxide powders has been achieved, then indirect means of characterizing ceramic surface structures may become standard tools. Granted the enormity of the need for powder surface characterization and assuming future development of standardization procedures, let us examine the type of information that may be potentially achieved by indirect methods.

#### IV. Surface Forces

Types of forces. Surface phenomena are a consequence of asymmetrical or unbalanced forces between atoms and molecules at the interface of the particle. Consequently, in order to develop methods of surface characterization it is necessary to understand the various types of surface forces and their range of spatial influence.

Surface forces are electronic in origin and may be either attractive or repulsive. As discussed in a variety of sources,<sup>(13)</sup> the electrostatic potential energy of interaction between two ions of unlike charge,  $-Z_1e_1$  and  $+Z_2e_2$ , separated by a distance

(x) is

$$\epsilon_1(x) = -Z_1 e_1 Z_2 e_2 / x \quad (1)$$

The potential energy between a surface ion of charge  $Ze$  and a dipole of moment  $\mu$  can also be shown<sup>(13)</sup> to be

$$\epsilon_2(x) = -Ze \mu / 2x^2 \quad (2)$$

Interaction between a surface dipole and a dipole at distance  $x$  away involves an interaction energy<sup>(13)</sup> of

$$\epsilon_3(x) = -\mu^2 / 4x^4 \quad (3)$$

However, thermal agitation tends to randomize the motion of the dipoles in each of the above cases which increases the distance dependence. For example, the temperature dependent orientation energy<sup>(13)</sup> of interaction for polar molecules at a surface is

$$\epsilon_4(x) = -2\mu^4 / 3x^6 kT \quad (4)$$

Induced dipole-quadrupole interactions give rise to an energy term related to the inverse eighth power of distance and dipole-octapole or quadrupole-quadrupole interactions give a term involving  $x^{-10}$ .

A general attraction at a particle interface will also arise due to London-van der Waals dispersion forces<sup>(14)</sup> regardless of how dissimilar the particles and environmental molecules may be chemically. London dispersion forces arise from the interaction of fluctuating electron dipoles within a material with induced electron-nuclei dipoles in the atoms or molecules comprising a neighboring substance. It can be shown<sup>(13,14)</sup> that the mutual attraction energy due to dispersion forces of two particles of polarizabilities  $\alpha_1$  and  $\alpha_2$  and average vibrational energies of  $h\nu_1$  and  $h\nu_2$  is:

$$\epsilon_5(x) = -\frac{3}{2} \frac{a_1 a_2}{x^6 \left( \frac{1}{h\nu_1} + \frac{1}{h\nu_2} \right)} \quad (5)$$

Potential covalent contributions to surface bonding may also exist. The calculations of mutual sharing of electrons between nuclei show that the distance dependence,  $x$ , is of the order of the radii of the ions or atoms involved in the bond. The covalent bond energy is expressed qualitatively as:

$$\epsilon_6(x) = -\frac{C_6 \mathcal{K}}{x^n} \quad (6)$$

where  $\mathcal{K}$  is the exchange energy due to a positive quantum electron interaction and  $C_6$  and  $n$  are constants dependent on the number of electrons, nucleus charge, and symmetry of atom arrangements in the covalent bond. For a detailed analysis of covalent bonding the reader is referred to Slater.<sup>(15)</sup>

Each of the interactions in equations (1-6), with the exception of the coulomb force between isolated charges, are short range and thereby contribute to the system's energy only over a few Å distance. These short range forces constitute the binding that holds the solid together and, being additive, give rise to the total potential energy of solid, as discussed in the next section. It is the extension of these surface forces to atoms or molecules in the proximity of a particle that results in monolayer chemisorption or physisorption at the particle surface.

Although the distinction between chemisorption and physical adsorption is somewhat arbitrary, it is generally considered that chemisorbed species form a chemical bond nearly as strong as the substrate. Chemisorbed surface interactions with ceramics therefore will normally involve ionic-covalent interaction energies  $\epsilon_1$  and  $\epsilon_6$ . On the other hand, more weakly bonded, physical adsorption species on ceramic particles will usually involve interaction energies  $\epsilon_2$ ,  $\epsilon_3$ ,  $\epsilon_4$ ,  $\epsilon_5$ . Because of the



secondary or induced nature of these surface forces, physisorption can also occur on top of a chemisorbed layer.

Long range interactions. By the very specific nature of the surface interactions involved, chemisorption is usually restricted to a monolayer of coverage or less with the extent of the surface forces limited to several Angstroms. However, there is considerable evidence that appreciably long range forces are also present at the surface of particles. For example, platelike  $\text{Fe}_2\text{O}_3$  or  $\text{WO}_3$  hydrates arrange themselves in horizontal layers upon settling with as much as 8,000 Å thick layers of water between the platelets.<sup>(16)</sup> Brownian motion of the platelets also suggests long range attractive forces.<sup>(17)</sup> Clay minerals also exhibit the well known property of arranging in highly ordered "card pack" formations with large layers of water between the particles.<sup>(18)</sup>

Three major contributions to long range forces have been established. They are the primarily electrostatic interactions of electrical double layer systems, dispersion force interactions, and dipole-dipole interactions. Calculations of the extended dispersion or van der Waals attractions between particles of specific geometries have been made. To illustrate, in the case of two spheres of radius  $r$ , the energy of van der Waals attraction will be

$$\epsilon'_5 = - \frac{rH}{12x} \quad (7)$$

when the distance of separation of the spheres,  $x$ , is less than  $r$ .  $H$  in equation (7) is known as the Hamaker constant and is equal to  $\frac{3}{4} \pi^2 n^2 h \nu_0 \alpha^2$ , where  $n$  is the number of atoms/cc and the other terms are as defined in equation (5). Since  $H$  is on the order of  $10^{-13}$  erg, the energies so calculated from equation (7) show that the interaction energy from this source is comparable to that of thermal motion when the particles are separated by distances of the order of their dimensions. Equation (7) also shows that the dependence of  $\epsilon'_5$  is inverse first power; consequently, two particles need only to come within a

distance of separation of approximately  $2r$  in order to be bonded by dispersion forces. Although only weakly bonded agglomerates arise from such interactions, additional shorter range interactions become more favorable as the particles are brought closer together by the dispersion interaction.

Direct measurement of  $\epsilon_5$  has been made between macroscopic plates of glass,<sup>(19)</sup> quartz,<sup>(20)</sup> and mica<sup>(21)</sup> using delicate balance type arrangements. Forces of the order of  $10^{-2}$  dynes/cm<sup>2</sup> were obtained at distances of  $1\mu$ m or so. Experimental verification of the relative magnitude of the dispersion force contribution to the surface reactivity of ceramic powders has not been obtained to the author's knowledge.

Another potentially significant contribution to the long range interaction between ceramic particles is due to the extension of surface charge induced dipoles throughout many layers of an adsorbed species.<sup>(13)</sup> Extending the interaction energy  $\epsilon_2$  of a polarizable species adsorbed on charged surface sites to the  $i^{\text{th}}$  layer leads to a locus of  $\epsilon_2$  values represented by an exponential relationship

$$\epsilon_2(x) = \epsilon_{2(0)} e^{-ax} \quad (8)$$

where  $x$  represents the distance from the surface and  $a$  is given by

$$a = -\left(\frac{1}{d_0}\right) \ln(\alpha/d^3) \quad (9)$$

where  $d_0$  is the atomic diameter of the molecule of polarizability  $\alpha$  at a distance of separation from the surface of  $d$ .

Adsorption of inert gases on alumina and graphite can be interpreted to be due to such a polarization of the adsorbate by strong electrostatic surface fields.<sup>(22)</sup> Long range orientational interactions in multilayer adsorbed water films on ceramic powders in air or in suspension may also be interpreted in terms of such an induced dipole orientational model. It is

the transmission of such long range interactions between particles that produce agglomerates.

Surface charges in liquids. In liquid suspension many ceramic powders develop an electrical double layer in response to surface charges on the particles. The electrical double layer is usually negatively charged and repulsive towards other particles. However, dispersion and dipole attractive forces will be arithmetically additive to the repulsive force of the double layer in the total response of the interparticle system.

Let us first consider the Guoy-Chapman model for the diffuse double layer at a charged planar surface.<sup>(13,23)</sup> The electrical potential at the surface is taken to be  $\psi_0$ ; it decreases into the solution and at any point is a value  $\psi(x)$ . Any ion in the electric field will thus have a potential energy  $Ze\psi$ , where  $Z$  is the ion valence and  $e$  is the electron charge. Consequently, the probability of finding an ion at distance  $x$  from the surface,  $n^\pm$ , in a total concentration of  $n_0$ , is proportional to the Boltzmann factor; i.e.,

$$n^+ = n_0 e^{-Ze\psi/kT} \quad (10)$$

$$\text{and } n^- = n_0 e^{+Ze\psi/kT} \quad (11)$$

By using suitable boundary conditions and integrating the ion distribution as a function  $x$ , it is possible to achieve the functional decrease in  $\psi$  from the surface value  $\psi_0$ . For the simplest case, when  $\psi_0$  is less than  $kT$ , the result is

$$\psi = \psi_0 e^{-kx} \quad (12)$$

where  $k$  is defined as  $[(4\pi e^2/DkT) \sum_i n_i Z_i^2]^{1/2}$ ,  $D$  is the dielectric constant of the medium containing  $n_i$  ions of valence  $Z_i$ . At 25°C,  $kT$  has a value of 25.7 mv, so for singly charged ions at room temperature the above equation will hold for  $\psi_0 < 25$  mv.

The exponential dependence of  $\psi$  on  $x$  is shown in Figure 1 for several concentrations of the solution medium. The quantity  $1/k$  is the distance at which the potential has reached  $1/e^{\text{th}}$  of its value at the surface. Since this distance coincides with the center of gravity of the space charge, the plane at  $x = 1/k$  is taken as the thickness of the diffuse double layer. Figure 1 shows that the double layer thickness decreases as the ionic concentration increases. This is because the probability of finding a charge compensating ion close to the surface increases proportionally with ionic concentration. A comparison of two different valences of ions in the solution at equivalent concentrations is also shown in Figure 1. As expected from equation (12), the thickness of the double layer decreases as the charge per ion increases.

The total surface charge  $\Sigma$  can be obtained from the gradient of the potential with respect to  $x$  as

$$\Sigma = - (D/4\pi)(d\psi/dx)_{x=0} \quad (13)$$

which leads to the relation between the total surface charge and the surface potential as

$$\Sigma_G = Dk \psi_0 / 4\pi \quad (14)$$

At the other limiting condition when  $\psi_0$  is much larger than  $kT$ , the distance dependence of  $\psi$  reduces to

$$\psi = (4kT/Ze) e^{-kx} \quad (15)$$

as long as  $x \gg 1/k$ . In this case the potential falls away in the manner of equation (12) but only at some distance from the surface and with an apparent  $\psi_0$ . For singly charged ions at 25°C the apparent  $\psi_0$  is fixed at approximately 100 mv. The breakdown of the Guoy-Chapman theory close to the surface at high  $\psi_0$  values is a result of neglecting ionic diameters in the model. The Stern layer modification eliminates this difficulty. (24)

Stern suggested that the double layer should consist of two parts. Close to the surface is an absorbed layer of ions forming a compact double layer of a thickness  $d$  reducing  $\psi_0$  to a value of  $\psi_d$ . The Gouy diffuse layer then extends outward from  $\psi_d$ , as shown in Figure 2. The potential gradient in the compact layer will thus be

$$d\psi_s/dx = \frac{\psi_0 - \psi_d}{d} \quad (16)$$

and, therefore, the charge density for the compact layer will be

$$\Sigma_S = (D'/4\pi)(\psi_0 - \psi_d) \quad (17)$$

$D'$  is a local dielectric constant which may differ from that of the bulk solvent.  $D'/4\pi d$  represents the capacitance of the compact Stern layer and is experimentally accessible by electrocapillarity measurements and other techniques to be discussed.

The total surface charge density will be  $\Sigma_S + \Sigma_G$  and the total electrical capacitance will be given by the series addition

$$\frac{1}{C} = \frac{1}{C_S} + \frac{1}{C_G} \quad (18)$$

In concentrated solutions  $C_G$  becomes large so the surface capacitance is almost entirely due to the compact Stern layer, i.e.,  $C \approx C_S$ .

An additional variable that influences the surface charge is the adsorption of charged ions at the surface of the particle at a concentration proportional to their concentration in solution. Such ions drastically alter the intrinsic surface potential  $\psi_1$  to a new value  $\psi_0$  and can even change the sign of the surface charge. Since  $\psi_0$  is thus a function of the concentration of such ions in solution, they are termed the potential

determining ions. The Stern and diffuse layers are preceded by a potential determining layer of ions as shown in Figure 2. Examples of potential determining ions includes  $\text{Ag}^+$  ions on silver iodide,  $\text{Cl}^-$  ions on gold sols,  $\text{H}^+$  ions on clays, and  $\text{H}^+$  ions on proteins and biological macromolecules. A schematic of the ion distributions at the surface of a clay particle that are responsible for the three charge layers is also shown in Figure 2.

Because of the relatively strong electrostatic and van der Waals bonding of the ions in the Stern layer to the particle surface, they will be relatively immobile if a force is applied to the particle. Motion of the particle in response to the force consequently will occur at a shear plane at some distance in the diffuse layer. The surface potential that exists at this shear plane is termed the zeta potential. Various electrokinetic phenomena can be used to obtain a measurement of the zeta potential and therefore it is a parameter for surface structure characterization. However, as described above, the zeta potential is only indirectly related to the intrinsic surface charges of the particle and is dependent on the liquid medium employed in the measurement.

## V. Surface Energy

The various ionic and atomic bonding forces described in the previous section are generally uniformly distributed within the bulk of a solid and give rise to a lattice energy which can be fairly accurately calculated and measured.<sup>(25)</sup> However, at the surface of a solid the local atomic arrangements are not maintained, coordination shells are unfilled, and unsatisfied bonds are present. Consequently, the solid surface energy can be defined as the energy required to restore the bulk lattice configuration at the surface of a perfect crystal. It is a potential energy which is often expended in the chemisorption and physisorption of ions in the medium within which the particle is suspended. For this reason the measurement of surface

the surface energy would be 25.8% from the 0.1 $\mu$  particles, 74.1% from the 0.01 $\mu$  particles, and 0.1% from the 0.1 $\mu$  particles. Because of the disproportionate percentage of surface energy for the small particles, it is essential that the low side of the size distribution be well characterized. However, it is these particles that will be most easily agglomerated and most difficult to isolate into small enough clumps for direct size analysis by TEM and most difficult to disperse for indirect size analysis.

Another important factor is that the density of crystal defects will also vary with the particle size. It is to be expected that edge steps, kinks, ledges, etc., will be much more prominent on very small particles. Consequently, the edge energy contribution listed in Table 3 probably becomes underestimated by as much as a factor of 2-10 for 0.01 $\mu$  particles. For these reasons, a complete surface energy characterization of a ceramic powder should involve an energy distribution analysis including surface, edge, and local defect contributions. The fraction of the energy contribution "tied up" in agglomerates would also need to be included. This level of direct characterization lies many years in the future and may seldom ever be practical for commercial powders. However, as shown in a later section, indirect adsorption techniques can be used to obtain a good approximation to the site energy distribution of ceramic powders.

An additional complication is the well documented decrease in surface energy associated with adsorbed gas films.<sup>(29)</sup> Reduction in surface energies by as much as 5 have been reported when adsorbed water layers are present on ceramics. Such adsorption effects on surface energy may or may not be dependent on the particle size of the powders. If they are, the energy distribution curves for the powders will be shifted. This type of information is presently not available but is critical if powder characterizations are to be related to processing and end use behavior.

energies can be an important characterization step for many ceramic powders or products.

As suggested by Duga,<sup>(26)</sup> the various techniques for measuring surface energies can be divided into two categories: 1) mechanical, and 2) thermodynamic. The concept applied in the mechanical methods is that new surfaces are created during the fracture of a brittle solid, as most ceramics are at room temperature.<sup>(27)</sup> The surface energy of the solid thus is simply the energy required to effect fracture divided by the area of the newly formed surfaces. The thermodynamic methods involve the interaction of the solid surface with a liquid of known properties. Measurements of the solid-liquid contact angle or the heats evolved during immersion or dissolution can be used to calculate the surface energy of the solid.

Various techniques in each of these categories are summarized in Table 1 adapted from Duga.<sup>(26)</sup> The crack propagation methods, when applied to completely brittle single crystals in high vacuum, yields the most reliable surface energy values for ceramics available.<sup>(28)</sup> Highly reliable data on the change in surface energy due to adsorbed films are also achieved when the mechanical method is applied in a controlled environment.<sup>(29)</sup> Accurate surface energy measurements of powders have not been achieved using mechanical methods.

Thermodynamic measurements appear to offer the widest application for all types of solids, including powders over wide temperature ranges. However, the proper choice of a series of liquids is difficult. Impurities localized at particle surfaces or adsorbed films must be removed in order for the measurements to represent equilibrium conditions. Diffusion of the solid or liquid across the interface, or chemical reactions at the interface invalidate the thermodynamic analysis.

A brief review of several of the most reliable methods of surface energy measurement follows:

The Griffith criterion<sup>(30)</sup> for crack propagation is the basis of later developments of mechanical techniques for surface energy measurement. The Griffith equation



$$\sigma = \sqrt{\frac{4E\gamma}{\pi c}} \quad (19)$$

stems from a balance between the rate of decrease in strain energy associated with the growth of the crack under stress and the rate of increase of surface energy due to the two new surfaces being created at the crack. The parameters in equation (19) are:  $\sigma$  = minimum applied stress required for crack growth;  $E$  = Young's modulus;  $\gamma$  = surface energy; and  $c$  = length of ideally grown crack.

An excellent experimental application of the Griffith concept to the measurement of surface energy was advanced by Gilman.<sup>(31)</sup> A schematic of the cantilever beam method is shown in Figure 3 where various terms and dimensions are defined. The Gilman analysis of the relationship between the force ( $F$ ) required to propagate the crack and the surface energy of the solid ( $\gamma$ ) is given in equation (20).

$$\gamma = \frac{6F^2 L^2}{Ew^2 t^3} \left[ 1 + \frac{\alpha E}{4G} (t/L)^2 \right] \quad (20)$$

This equation also includes a second term developed by Westwood and Hitch<sup>(32)</sup> which accounts for contributions from end effects and shearing forces;  $G$  is the shear modulus, and  $\alpha$  is a parameter determined by the boundary conditions in the vicinity of the crack tip. One value of the Westwood and Hitch modification is that measurements made as a function of  $t/L$  enable  $\alpha$  to be calculated and therefore errors in  $\gamma$  due to plastic relaxation at the crack tip can be eliminated. Table 2 gives surface energy values for a number of ceramic crystals obtained by this method.

Of the thermodynamic methods, the critical angle of wetting technique yields perhaps the most accurate and most easily interpreted values of the surface energy. However, this technique is also restricted to single crystals of dense bodies and is therefore more appropriately discussed in Chapter 21.

The heat of immersion method is particularly suited for evaluating the surface energy of powders. The technique involves the calorimetric measurement of the heat evolved when a higher energy solid-vapor surface is replaced by a lower energy solid-liquid surface. By knowing the surface area involved ( $A$ ), the change in energy per unit area of surface can be determined, i.e.,

$$q_{im} = A(H_{sv} - H_{lv}) \quad (21)$$

For details of the technique and applications of this method to a number of solids, the reader is referred to Zettlemoyer. (33,34)

Heat of solution measurements are a similar calorimetric technique for evaluating the surface energy of powders. The method involves the measurement of the small differences between the heat of solution of coarse powders and of finely divided powders. By measuring the heat capacities of the fine versus coarse material down to low temperatures, the heat capacity difference,  $C_p$ , can be used to calculate the temperature dependence of the surface energy. The surface entropy and free energy also can be obtained from the calculation as:

$$\bar{H}_T^s = H_{298^\circ K}^s + 1/A \int_{298^\circ K}^T \Delta C_p dT \quad (22)$$

$$\bar{S}^s = 1/A \int_0^T \Delta C_p d \ln T \quad (23)$$

$$\bar{G}^s = H^s - T\bar{S}^s \quad (24)$$

The bars on the quantities above reflect the fact that surface energy measurements on powders represent average energy values of the local surfaces exposed on the particles. The variations in surface energy associated with different crystallographic planes, (35) as well as edges and corners, dislocations, and other imperfections are averaged into one representative quantity. The influence of such averaging can be important, for as

Bruce has shown,<sup>(36)</sup> the surface energy of an FCC structure such as MgO can vary as much as a factor of 1.225 from the minimal energy (110) plane.

Examples of the application of the heat of solution method to ceramic materials include a series of studies conducted on MgO. Giaque and Archibald<sup>(37)</sup> prepared coarse and fine MgO by calcination from the hydroxide. A difference in heat of solution of 388 cal/mole was determined. A surface area measurement of 86 m<sup>2</sup>/g was made by Jura and Garland for fine MgO powder prepared in a similar manner. On combination of the two results, a surface energy of 1090 ergs/cm<sup>2</sup> for MgO is obtained.<sup>(13)</sup> By employing equations (22-24), and temperature dependent specific heat data, they concluded that the average surface free energy of MgO decreased from 1040 ergs/cm<sup>2</sup> at 0°K to 1000 ergs/cm<sup>2</sup> at 298°K.

For purposes of characterization, it may often be desirable to know the surface energy of a material at a specific temperature in either the solid or liquid state. Bruce<sup>(38)</sup> has developed a procedure for estimating the surface energy temperature dependence of ceramics if experimental values are unavailable. The surface energy at 0°K can be estimated from the relation:

$$\gamma_s^0 = H_s b / ZcN \quad (25)$$

Between 0°K and the melting point,  $T_m$ :

$$\gamma_s^T = \gamma_s^0 - \left( \frac{\gamma_s^0}{T_c} \right) T \quad (26)$$

$$\text{At } T_m, \gamma_s^{T_m} - \gamma_L^{T_m} = \Delta\gamma = \eta H_f / AN \quad (27)$$

and between  $T_m$  and the critical temperature,  $T_c$ :

$$\gamma_L^T = k(1 - T/T_c)^n \quad (28)$$

The terms in equations (25-28) are:

$H_s$  = molar heat of sublimation (ergs/mole)

$N$  = Avogadro's number

$b$  = # bonds/cm<sup>2</sup> of the lattice plane considered

$c$  = # bonds/molecule

$A$  = surface area of a molecule

$\eta$  = ratio of free bonds to normal coordinate bonds

$n$  = adjustable exponent, about 1.2

$H_f$  = latent heat of fusion

$$k = \frac{H_s b (1 - T_m/T_c) - (2\eta c/bA) H_f/H_s}{2Nc (1 - T_m/T_c)^n}$$

If the critical temperature is unknown, Bruce has shown that the following ratios of critical temperature to boiling point are approximately equal for several classes of oxides:  $T_c/T_b \approx 1.52$  for MO,  $T_c/T_b \approx 1.50$  for MO<sub>2</sub>, and  $T_c/T_b \approx 1.40$  for M<sub>2</sub>O<sub>3</sub>.

Application of Bruce's method to MgO yields the following results which are in reasonable agreement with experimental evidence:

$$\gamma_o = 1300 \text{ ergs/cm}^2$$

$$\gamma_s^{T_m} = 1300 - 0.238T$$

$$\gamma_s^{T_m} = 1300 - 0.238(3075) = 565 \text{ ergs/cm}^2$$

$$\Delta\gamma = 270 \text{ ergs/cm}^2$$

$$\gamma_L^{T_m} = 295 \text{ ergs/cm}^2$$

$$\gamma_L^T = 2(295)(1 - \frac{T}{5470}) = 590 - 0.108T$$

Several other techniques have been applied to determine the surface energy of powders including Ostwald ripening of dissolving powders,<sup>(39)</sup> equilibrium shapes of crystals,<sup>(40)</sup> expansion of lattice parameters from x-ray diffraction.<sup>(41)</sup> The latter method appears to hold the most promise, although strain contributions to the lattice parameters must be eliminated (see Chapter 14). The reader is referred to Bickerman<sup>(42)</sup> for a critical discussion of these as well as each of the above methods for measuring surface energy.

## VI. Surface Structure

As pointed out earlier, structural features at an atomistic level can appreciably affect local surface charges and the local surface energy of a particle. Such features include vacancies, interstitials, impurity ions, dislocations, subgrain boundaries, twin boundaries, surface ledges, steps, etc. Stran-ski<sup>(43)</sup> catalogs several dozen types of surface energy perturbing features and estimates their energy on a sodium chloride crystal structure. Observation and analysis of most of these contributions to the surface energy is possible only with field ion microscopy (Chapter 8) or transmission electron microscopy (Chapters 7 and 8), if then. For most ceramic powders such analyses are presently impossible. Even if examination were possible, sampling problems for powders with real size distributions are nearly unsurmountable.

For example, consider the surface energy of a subdivided 1 g cube of MgO. In addition to the 1,000 ergs/cm planar surface energy, determined in a manner cited above,<sup>(44)</sup> there will be an edge energy which can be estimated as  $1 \times 10^{-5}$  ergs/cm. The change in total surface energy and edge energy (ergs/g) of the cube as it is subdivided is shown in Table 3. Small particles in the 100 Å range exhibit a very large surface and edge energy. Consequently, if the size distribution of a 0.1μ commercial MgO powder is represented as 70%, 0.1μ particles; 10%, 1.0μ particles; and 20%, 0.01μ particles, the distribution of

## VII. Powder-Liquid Interface Techniques

A variety of methods have been developed to measure the electrical behavior of powder surfaces in a powder-liquid system. The methods involve the relative motion between a charged surface and the bulk solution at the plane of the zeta potential. If an electric field is applied, the particles move in response to the applied force and their velocity is related to the charge on the particles. Or, if the charged particles are mechanically made to move, an electrical potential will be induced proportional to the particle charge density. The different methods are summarized in Table 4, after Adamson.<sup>(13)</sup>

## VIII. Electrophoresis

A potential gradient,  $X$ , is established in a solution containing the charged particles and the resulting velocity,  $v$ , of the particles is measured by a microscope or a moving boundary apparatus. The force exerted on the particle surface, per  $\text{cm}^2$ , is  $\Sigma X$  and at steady state is balanced by the viscous drag,  $\eta v/\tau$ .  $\tau$  is the thickness of the diffuse double layer from the shear plane out, Figure 2, and  $\eta$  is the viscosity of the solution.

Although the total charge of the particle is not known,  $\Sigma$  will be related to the zeta potential at the shear plane as

$$\Sigma = D\xi/4\pi\tau \quad (29)$$

Equation (29) is the equation for a parallel plate condenser with a thickness  $\tau$  and dielectric constant  $D$ .

Equating the force applied with the viscous drag, and substituting equation (29) yields the desired expression for the particle velocity

$$v = \xi DX/4\pi\eta \quad (30)$$

Consequently, a measure of the velocity per unit field gives the zeta potential ( $\xi$ ).

The reader is referred to several sources for a discussion of a more detailed theory<sup>(45,46)</sup> and the complicating effects of electrophoretic retardation and relaxation contributions.

#### IX. Sedimentation Potential

An applied mechanical force such as developed by a centrifuge will cause the particles to move relative to the solution inducing a potential  $E$ . If the mass of dispersed substance per cc,  $C_m$ , is rotated with an angular velocity  $w$ , the sedimentation potential between two points  $R_2$  and  $R_1$  along the axis of rotation will be given by<sup>(13)</sup>

$$E = (C_m/k)(D\xi/6\pi\eta)(w^2/R)(R_2^2 - R_1^2) \quad (31)$$

#### X. Electroosmosis

This method involves measuring the velocity of a liquid moving past an immobile charged surface. Particles possessing a certain zeta potential are compacted into a cylinder with pores of a radius,  $r$ . When the cylinder is located as a plug in a solution bath (see Figure 4) and a potential  $X$  is applied, the mobile diffuse double layer will move through the pores. The volume flow  $V$  is cc/sec is related to the size of the pore,  $r$ , and the linear velocity of the liquid in the pores,  $v$ , as:

$$V = \pi r^2 v \quad (33)$$

and by applying equation (30)

$$V = r^2 \xi DX / 4\eta \quad (32)$$

Observation of the liquid transport can be by the motion of an air bubble in the capillary providing the return path as shown in Figure 4. For example, if  $\psi_0$  is 100 mv, a field of 1,500

v/cm will produce a velocity of 1 cm/sec in water where  $D = 80$  at  $25^{\circ}\text{C}$ .

### XI. Shearing Potential

When the solution is caused to flow through the pores past the charged surface a potential,  $E$ , is induced. The relationship between the applied pressure,  $P$ , the  $\xi$  potential and the induced field is<sup>(13)</sup>

$$E = \xi PD / 4\pi\eta k \quad (34)$$

where  $k$  is the specific conductance of the solution.

### XII. Powder-Gas Interface Techniques

Ceramic powders are in equilibrium with a gaseous environment throughout most processing steps. Consequently, understanding the powder-gas interface is a vital characterization requirement. As discussed earlier, direct means of studying this interface are not available because of the 4-20 Å thickness involved. For this reason, a variety of indirect methods have been developed which employ variations of the gaseous atmosphere itself as an analytical tool. The major analytical variables are the types of gases used (molecular size, polar or nonpolar), temperature of the powder, and partial pressure of the gas. Most techniques involve measuring the volume of gas sorbed onto the powder surface as a function of the above variables.<sup>(13,47,48)</sup> It is also possible to combine the fundamental data on variations in the volume of sorbed gases with other physical property measurements such as dielectric losses,<sup>(49,50)</sup> capacitance,<sup>(49)</sup> conductance,<sup>(51)</sup> NMR\*<sup>(52)</sup> or IR\*\*.<sup>(53)</sup> Such combined experiments offer the most powerful approach to powder surface characterization available today.

---

\*Nuclear Magnetic Resonance

\*\*Infra-Red Analysis



### XIII. Types of Adsorption

Gas-surface interactions can be divided into two somewhat arbitrary categories: physical adsorption (physisorption) and chemical adsorption (chemisorption). A physisorbed gas is bonded to the surface primarily through general van der Waals-London forces with a bond strength of approximately 7 kcal/mole or less. Chemisorbed species on ceramics, however, will have developed a strong chemical bond with the surface of 10-40 kcal/mole or more. The origin of the differences in bond energy between the two types of adsorption can be seen from Figure 5.

Figure 5, from Hayward and Tropnell,<sup>(54)</sup> represents the variation in potential energy of a gas species as it approaches a planar surface. As the molecule  $X_2$  approaches the surface, the van der Waals attraction of physical adsorption will lower the energy, curve 1, to a minimum,  $q_p$ , established at a distance  $r_{vw}$ . The value of  $r_{vw}$  will be the sum of the van der Waals radii of the surface atom and the adsorbate molecule. At distances less than  $r_{vw}$ , quantum repulsion is experienced by the adsorbate molecule and the potential energy rises. There is no activation barrier for physisorption; therefore, it is very rapid (except when transport is limited as in a porous substance). It is reversible and the gas may be many layers thick because of the nonspecific nature of the forces involved.

It is also possible that the gaseous species  $X_2$  will dissociate on the surface, M, by forming a chemical bond. This process is depicted in Figure 5 by curve 2. The bond strength formed on chemisorption will be  $q_c$ , which is much larger than the physisorbed minimum,  $q_p$ , and therefore chemisorption will be a stable process. The potential curves cross and become rounded at the crossing region because of a wave mechanical mixing of electron energy states. The adsorbate will follow the lowest energy curve and thus can cross from the physisorbed to the chemisorbed state. However, the potential changes involved may be such that an appreciable energy barrier, E, exists

between the two states. If this is the case, the transition time from physisorption to chemisorption will be very long and may not be statistically significant for a powder, as long as total processing times are short. However, the transition may take place in calcined powders within the period of hours to days and produce drastic aging effects on surface reactivity.<sup>(55,56)</sup> Table 5, after Adamson,<sup>(13)</sup> summarizes the adsorption spectra in terms of surface bond energy,  $Q$ , transition time,  $\tau$ , and surface concentration,  $r$ .  $\tau$  will also be affected by the particle size of the powder and the partial pressure of the gas. For example, the author<sup>(57)</sup> has shown that  $MgO$  prepared by calcination from  $Mg(OH)_2$  will hydrate at room temperature within 30 hours at 85% relative humidity, whereas the surface is nearly unchanged after 10 days at 25% relative humidity. Even if the chemisorption rate is unimportant at room temperature, at a higher temperature it may dominate.

As the powder temperature is increased to  $T_c$  for the adsorbate, the physical adsorption becomes progressively less, curve 1 in Figure 6, because of the low adsorption energy. The chemisorption rate may still be appreciable, curve 2 in Figure 6, so a transition will occur following a path dependent on the equilibration time. Such a transition may occur for adsorbed water on the surface of ceramic powders during drying, mixing, and grinding steps or in the early stages of sintering.

#### XIV. Langmuir Model

The approach that can be used to characterize the fraction of surface covered by a chemisorbed layer was first developed by Langmuir.<sup>(58)</sup> The rate of condensation on the surface is proportional to the number of unoccupied surface sites,  $S_o$ , and the gas pressure,  $P$ , i.e.,

$$R_c = k_c P S_o \quad (35)$$

Evaporation of the gas from the surface is proportional only to

the number of occupied surface sites,  $S_1$ , of a total number  $S$ , or

$$R_e = k_e S_1 \quad (36)$$

At equilibrium  $R_c$  and  $R_e$  can be equated and upon rearrangement yields,

$$\frac{S_1}{S} = \frac{k_c P}{k_e + k_c} \quad (37)$$

$S_1/S$  is the fraction of surface covered,  $\theta$ , and the ratio  $k_c/k_e$  is known as the Langmuir constant  $b$ . Thus, equation (37) can be written as

$$\theta = bP/(1+bP) \quad (38)$$

which is the Langmuir adsorption isotherm. Alternatively, if  $\theta$  is replaced by  $v/v_m$ , where  $v$  is the volume of adsorbed gas at  $P_1$  and  $v_m$  is the volume, cc/g at STP, adsorbed at the monolayer point, the Langmuir equation reads as

$$v = v_m bP/(1+bP) \quad (39)$$

The temperature dependence of adsorption enters in equation (39) through the Langmuir constant,  $b$ . The rate of evaporation,  $k_e$ , is the reciprocal of the adsorption time, or

$$k_e = (1/\tau_o)_e - Q/RT \quad (40)$$

The rate of molecules impinging on the site area  $\sigma_o$  will describe the adsorption rate. From gas kinetic theory,  $k_c$  will then be

$$k_c = N\sigma_o/(2\pi MRT)^{1/2} \quad (41)$$

The ratio of equations (41) and (42) yields  $b$ , which is most handily written as a product of a frequency factor,  $b_o$ , where

$$b_o = N\sigma_o\tau_o/(2\pi MRT)^{1/2} \quad (42)$$

with thermal activation; i.e.,

$$b = b_o e^{Q/RT} \quad (43)$$

A plot of Langmuir isotherms at several temperatures is shown in Figure 7.

For a more formal statistical mechanical derivation of the monolayer adsorption isotherm, the reader is referred to Fowler and Guggenheim<sup>(59)</sup> or Adamson.<sup>(13)</sup> The major difference in the final equation is that the kinetic Langmuir model assumes equal internal partition functions for the adsorbed and desorbed states. This assumption is not valid because the gas species loses rotational degrees of freedom on adsorption.

Although chemisorption does reasonably occur as a monolayer phenomena, experimental results often do not follow the Langmuir relation. This is because of surface heterogeneity and lateral interaction effects and the lack of accounting for entropy changes between states, mentioned above. Detailed discussions of these modifications are given in Adamson,<sup>(13)</sup> and Bickerman.<sup>(42)</sup> The Langmuir adsorption model is also appropriate for describing sub-monolayer physical adsorption and has, in fact, been successfully applied to a large number of materials.<sup>(60)</sup> Data are usually plotted as  $P/v$  vs.  $P$  according to the linear form of equation (39),

$$P/v = 1/bv_m + P/v_m \quad (44)$$

The constants  $b$  and  $v_m$  can be calculated from the best linear fit. Assuming a value for  $\sigma_o$ , usually taken from the liquid density of the adsorbate, the value of  $v_m$  can be related to the surface area of the solid,  $S$ , as

$$v_m = Sv_o/N\sigma_o \quad (45)$$

where  $v_o$  is the STP number 22,400 cc/mole. Values of  $\sigma_o$  in square Å/molecule normally used are:  $N_2$  (16.2);  $O_2$  (14.1); A (13.8); Kr (19.5); and  $n-C_4H_{10}$  (18.1).

#### XV. Multilayer Models

A major difficulty of the Langmuir model is that it is inappropriate for describing multilayer formation so characteristic of physical adsorption. Brunauer<sup>(61)</sup> has considered that there are five principal types of adsorption isotherms, as illustrated in Figure 8. Type I is the Langmuir type, Type II is that usually observed for multilayer physisorption, Type III occurs rarely when the heat of adsorption is less than the heat of liquefaction of the adsorbate, and Types IV and V reflect capillary condensation phenomena. The adsorbate condensation causes the adsorbed volume to level off prior to the saturation pressure and often results in hysteresis effects.

The Brunauer, Emmett, and Teller analysis of the Type II isotherm<sup>(62)</sup> for  $N_2$  adsorption at 77°K is the basis for the now classic method of surface areal analysis of powders. Use of the BET method was discussed in Chapter 12. Although the BET equation covers Types I, II and III isotherms, it should be kept in mind that the fit is usually valid only over the range of  $P/P_o = 0.05$  to 0.3.

Because of the relatively gross assumptions involved in the BET derivation, a large literature of criticism, modifications, and rebuttals has evolved.<sup>(47)</sup> Most changes have involved the introduction of another variable parameter accounting for lateral interactions within the molecules of the multilayer.

A number of other models for multilayer adsorption have also been developed, including ones based on two-dimensional film pressures,<sup>(63)</sup> a two-dimensional equation of state employing the ideal gas law<sup>(64)</sup> or the van der Waals equation,<sup>(65)</sup>

and a condensed film model.<sup>(66)</sup> None of these appear to offer significant improvement over the BET results for surface area analysis, however.

Another approach to multilayer adsorption which leads to structural interpretation of the adsorbed surface film is called the potential theory.<sup>(61)</sup> The model is basically that of a liquid film condensed on the surface of the particles by a van der Waals-dispersion force potential field. If one assumes that the liquid has negligible compressibility, the thickness of the film,  $x$ , is related to the adsorbed volume  $v$  as:

$$v = Sxv_o/V_1 \quad (46)$$

where  $S$  is surface area,  $v_o$  is 22,400 cc/mole,  $V_1$  is the molar volume of the liquid.

The potential,  $\epsilon_x$ , which will produce condensation at a distance  $x$  from the surface is related to the gas pressure in equilibrium with the adsorbed film,  $P$ , by

$$\epsilon_x = RT \ln P_o/P \quad (47)$$

As discussed earlier, the dispersion potential function of a planar surface can be approximated by an inverse cube power of the distance, or

$$\epsilon(x) = \epsilon_o/(a+x)^3 \quad (48)$$

where  $a$  is a distance of the order of a molecular radius. Upon combination of equations (47) and (48) one obtains

$$RT \ln(P_o/P) = \epsilon_o/(a+x)^3 \quad (49)$$

which on solving for  $x$  and substituting into equation (46) yields

$$v = -\alpha + \beta [\ln P_0/P]^{-1/3} \quad (50)$$

with  $\alpha = av_0S/V_1$  and  $\beta = (v_0S/V_1)(\epsilon_0/RT)^{1/3}$ .

Equation (50) fits Type II adsorption isotherms over a wide range of  $P/P_0 = 0.1$  to  $0.8$ . Equation (50) has the further advantage of yielding surface area measurements by plotting  $v$  vs.  $[\ln P_0/P]^{-1/3}$ , which are decidedly less dependent on the adsorbate used than the BET method.<sup>(13)</sup> A modification is known as the Frenkel-Halsey-Hill<sup>(67)</sup> equation. Surface heterogeneity effects have also been included by Halsey.<sup>(68)</sup>

When either the surface potential at a distance  $x$  from the surface or the density of the gas film at  $x$  is plotted as a function of the volume of gas adsorbed at thickness, the plot is termed a characteristic curve.<sup>(69)</sup> An example of such a characteristic curve for the adsorption of  $SO_2$  on silica gel is shown in Figure 9. Two features of the curve are especially significant. First, an extensive surface volume of adsorbed gas is required to decrease the surface potential from a value of 4 kcal/mole to zero. The thickness of the adsorbed layer could be calculated using equation (46) to be a value of approximately 10 Å. Secondly, the characteristic curve is temperature independent; i.e., the adsorbate remains gaseous and is merely compressed in the potential field. At a sufficiently lower temperature the adsorbate pressure will reach the vapor pressure of liquid,  $P_0$ , and condensation will occur. Equation (50) will describe the adsorption isotherm of the solid.

Another approach that has been taken to describe the theoretical variation of  $\epsilon$  with  $x$  is that of surface induced polarization of nonpolar adsorbate molecules.<sup>(70)</sup> The surface polarization model described earlier, equation (8), when combined with equations (46) and (47) results in the polarization adsorption isotherm. This approach has been suggested as the explanation for the adsorption of gases on alumina<sup>(71)</sup> and carbon surfaces.<sup>(13)</sup> A significant consequence of the polarization models is that it predicts strong orientational effects within

multilayers and a perturbation from the normal liquid structure which may be expected from contact angle phenomena.<sup>(13)</sup>

Analysis of the thickness of adsorbed surface layers is most easily achieved by employing the t-curve, discussed recently in detail by Broekhoff and Linsen.<sup>(72)</sup> Shull<sup>(73)</sup> was the first to show for a number of nonporous solids that a straight line results when the ratio of the adsorbed volume,  $V_a$ , to the volume of a unimolecular layer,  $V_m$ , is plotted as a function of the relative pressure. Consequently, if the thickness of the layer is known at one pressure, the linear relationship permits the thickness of the adsorbed layer to be calculated for the entire range of pressures. Broekhoff and Linsen<sup>(72)</sup> have proposed the use of a statistical thickness,  $t$ , based on the assumption that the adsorbed liquid layers have the same density as condensed capillary liquid. The defining equation for  $t$  is

$$t = (MV_{sp}/22400) \cdot (V_a/S) \cdot 10^4 \text{ \AA} \quad (51)$$

where  $V_a$  is the adsorbed volume of the adsorbate in ml gas STP/g of adsorbent,  $V_{sp}$  is the specific volume of the adsorbate in ml/g,  $M$  is the molecular weight of the adsorbate, and  $S$  is the specific surface area in  $m^2/g$  adsorbent.

For nitrogen, equation (51) reduces to

$$t = 15.47(V_a/S) \text{ \AA} \quad (52)$$

By substituting  $S$ , obtained from a BET analysis, and  $V_a$  for a given relative pressure,  $P/P_0$ , into equation (52),  $t$  can be calculated as a function of  $P/P_0$  for a powder. The  $t$  vs.  $P/P_0$  curve for  $N_2$  adsorption on a number of nonporous powders, e.g.,  $TiO_2$ ,  $BaSO_4$ ,  $ZrO_2$ ,  $Al_2O_3$ ,<sup>(74)</sup> all show a common t-curve (Figure 10). However, a porous  $SiO_2$  gel (Aerosil)<sup>(75)</sup> shows a marked departure from the common t-curve. The relative pressure at which departures occur can be used to evaluate the powder porosity.



It is also apparent that a series of  $t$ -values calculated from equation (52) will produce a straight line when plotted against  $V_a$ , the total volume adsorbed at the given relative pressure. Such a  $V_a$ - $t$  plot for anatase  $TiO_2$  is shown in Figure 11. The slope of the line so obtained is a measure of the surface area of the powder,  $S_t$ . A number of investigators<sup>(76-78)</sup> have found that  $S_t$  values were in good agreement with  $S_{BET}$  values.

Broekhoff and Linsen<sup>(72)</sup> have provided a handy tabulation of the functional dependence of  $t$  on  $P/P_0$  for nonporous samples. Their table is reproduced in part in Table 5.

Deviations from the calculated linear  $t$  vs.  $V_a$  plots provide an important indication of the powder's pore structure. No deviation implies no surface pores. If the curve bends upward at a given pressure (see Figure 12), capillary condensation is occurring in pores of a certain shape and dimension. A downward bend to the curve is indicative of slit-shaped pores or large holes being filled. A number of detailed interpretations of pore shapes and dimensions have been made using such  $V_a$ - $t$  plots.<sup>(76-78)</sup>

Broekhoff and Linsen<sup>(72)</sup> have recently reviewed the detailed calculations of adsorption and desorption from various shaped pores that provide the quantitative evaluation of the adsorption behavior of porous powders. A basic concept in the analysis is that the thermodynamic potential of the adsorbed phase of thickness  $t$  is determined by the distance of the interface between the adsorbate in a condensed state and the vapor in a gaseous state; i.e.,

$$\mu_a = \mu_L - F(t) \quad (53)$$

where  $\mu_L$  is the thermodynamic potential of the liquid in the bulk state at the same temperature and  $F(t)$  is a function which can be determined from a  $t$ -curve of multimolecular adsorption. The analytical method is too involved to be presented here and

the reader is referred to the original reference. The approach has been successfully applied to calculating the pore size distributions in powders of alumina,<sup>(79)</sup> zirconia,<sup>(80)</sup> porous glasses,<sup>(81)</sup> graphite oxides,<sup>(82)</sup> a nickel-silica catalyst,<sup>(75,83)</sup> MgO,<sup>(84)</sup> various SiO<sub>2</sub> gels,<sup>(85)</sup> sol-gel ThO<sub>2</sub>,<sup>(86)</sup> and sol gel (U, Th) oxides.<sup>(87)</sup>

The adsorption isotherms of the above powders also exhibit an interesting and useful hysteresis behavior. Three of the types of hysteresis loops categorized by de Boer<sup>(64)</sup> are also of particular importance in interpreting sorption isotherms. They are designated Types A, B and E and are shown in Figure 13. Type A is characteristic of a powder with particles that contain cylindrical pores open at each end. Tubular pores with widened sections and ink-bottle shaped pores with narrow necks and small bodies will result in distorted Type A hysteresis.

Ink-bottle pores with very wide bodies and narrow necks or slit shaped pores open at all sides give rise to B-type hysteresis. The E-type loop is intermediate to A and B and is due to a distribution of pores with narrow necks of approximately uniform diameters, but with wide bodies of varying diameters. Separation of these structural types is obviously difficult and should be accompanied by TEM analysis of the powders.

#### XVI. Applications

Although obtaining fundamental information of the surface behavior of powders is fraught with the assumptions cited above, comparative studies utilizing this technique can be especially revealing. Consider the following examples among many others cited in recent volumes on this subject.<sup>(47,48,50,13,34)</sup>

The  $V_a$  vs.  $t$  N<sub>2</sub> adsorption curve for anatase TiO<sub>2</sub> shown in Figure 11 was measured as a function of pre-adsorbed layers of water. The change in the powder surface to that of a hydro-sphere does not change the nature of the multilayer N<sub>2</sub> adsorption. Since the slope of the curves decreases, the adsorbed

water acts to decrease the surface area of the powder, presumably due to blocking  $N_2$  from micropores.<sup>(75,88)</sup> However, a change in the density of the adsorbed  $N_2$  layer due to the  $H_2O$  substrate would produce a similar effect. A density distribution analysis discussed earlier could be used to distinguish between these two possibilities. At a particular thickness of the  $N_2$  layer the curves depart downward from linearity, indicating capillary condensation of the  $N_2$  which indicates micropores in the powder. The increasing thickness of  $N_2$  required for condensation is further indication that the pre-adsorbed water has filled micropores.

The variations in surface area and pore structure of  $Al_2O_3$  powders produced by thermal decomposition of bayerite<sup>(89)</sup> are shown in Figure 14. As temperature is increased above the decomposition temperature,  $>230^\circ C$ , the surface area (slope of the  $V_a-t$  plot) rapidly increases and then decreases as sintering of the powders occurs. The  $t$  plots show an appreciable amount of micropores giving rise to high surface areas,  $480\text{ m}^2/\text{g}$ . After sintering occurs, the pore structure changes as shown by the change in slope of the curve.

Characterization of porous silica gels has also been accomplished using  $N_2$  adsorption analysis.<sup>(85)</sup> For example, Figure 15 illustrates that the hysteresis loops for  $SiO_2$  gels change from Type E to Type A as the pH of precipitation of the gel is changed from 4.2 to 6.6. This is due to a large variation in the pore size distribution (Figure 16) associated with the kinetics of precipitation.

Redistributions of  $MgO$  pore sizes associated with varying the thermal decomposition of magnesites have been calculated using adsorption isotherm analysis<sup>(84)</sup> and are illustrated in Figure 17. Another particularly dramatic example of the use of adsorption methods is the characterization of sintered (U, Th) oxide powders produced by sintering gels at different temperatures.<sup>(87)</sup> The change in the isotherms with increasing sintering temperature is shown in Figure 8.

## XVII. Dielectric Techniques

Dielectric measurements offer a potentially powerful technique to use in conjunction with adsorption isotherms. Measurements of conductance and capacitance can be made on the same sample as the adsorption measurements.<sup>(50)</sup> By being able to vary the measuring frequency and applied voltage under conditions of constant temperature and constant amount of adsorbate, dielectric analysis can be employed to probe the structure of the adsorbed layer.

Several series of dielectric adsorption studies have been made on  $\gamma$ -alumina powders using water as the adsorbate.<sup>(90,91,50)</sup> The results obtained show that there is a frequency and temperature sensitive maximum in the dielectric loss,  $\epsilon''$ , at a particular amount of surface coverage,  $\theta$ . The charging constant,  $\epsilon'$ , also exhibits breaks in plots of  $\epsilon'$  vs. amounts adsorbed at similar values of  $\theta$ , see Figure 9. A consistent interpretation of the various studies does not seem to have been reached by the authors cited. However, the most plausible explanation appears to be one associating the appearance of loss peaks with capillary condensation producing an isolated high conductivity phase, thus satisfying the Maxwell-Wagner-Sillars<sup>(92)</sup> requirements for losses in a heterogeneous dielectric.

## XVIII. Conclusions

The various direct and indirect surface characterization methods discussed provide a large armamentarium for the physical ceramist. However, there have been few efforts to employ a variety of methods on a series of systematically varied ceramic powders. When such studies are conducted and interpreted in terms of the several theoretical surface models, it will be possible to develop a structural theory of ceramic surfaces. Such a theory can be used as a basis for understanding the changes in behavior associated with the handling and wet or dry processing of ceramic powders.

## REFERENCES

1. R. L. Coble, Ceramic Microstructures, J. Pask and R. Fulrath, eds., J. Wiley and Sons (1969), p. 658.
2. R. T. DeHoff and F. N. Rhines, "Topology of Sintering," Proceedings of Powder Metallurgy Conference, Stuttgart (1969), p. 1.
3. A. N. Holmes, Petrographic Methods and Calculations, Thomas Marby and Co., London (1927).
4. C. V. Gokularathnam, S. W. Freiman, R. T. DeHoff and L. L. Hench, J. Am. Ceram. Soc., 52, 327-331 (1969).
5. The Structure and Chemistry of Solid Surfaces, G. A. Somorjai, ed., J. Wiley and Sons, Inc. (1969), papers 1-57, 19, 21, 23, 28, 30, 31, 33-35, 37, 50, 63, 69, 70-73, 77, 78.
6. The Structure and Chemistry of Solid Surfaces, G. A. Somorjai, ed., J. Wiley and Sons, Inc. (1969), papers 13, 29.
7. R. Gomer, Field Emission and Field Ionization, Harvard University Press (1961).
8. J. J. Hren and S. Ranganathan, Field Ion Microscopy, Plenum Press, New York (1968).
9. C. W. B. Grigson and D. B. Dove, Journal of Vacuum Science and Technology, 3 [3] (1966) 120-132.
10. The Structure and Chemistry of Solid Surfaces, G. A. Somorjai, ed., J. Wiley and Sons, Inc. (1969).
11. J. C. P. Broekhoff and R. H. van Dongen, Physical and Chemical Aspects of Adsorbents and Catalysts, B. G. Linsen, ed., Academic Press, New York (1970), pp. 63-146.
12. G. Hochstrassers, J. F. Antonini and I. Peyches, "MS and ESR Studies of Dangling Bonds and Adsorbed Ions on the Pristine Surface of Silica," in The Structure and Chemistry of Solid Surfaces, G. A. Somorjai, ed., J. Wiley and Sons, Inc. (1969), pp. 37-41.
13. A. W. Adamson, Physical Chemistry of Surfaces, 2nd ed., Interscience, New York (1967).
14. E. M. Lifshitz, Soviet Physics, 2 [1] (1956) 73-83.
15. J. C. Slater, Quantum Theory of Atomic Structure, Vol. 1, McGraw-Hill (1960), p. 166.

16. S. Levine, Trans. Faraday Soc., 42B, 102 (1946).
17. S. Hachisu and K. Furusawa, Sci. Light (Tokyo), 12 [1] (1963) 157.
18. Ceramic Fabrication Processes, W. D. Kingery, ed., J. Wiley and Sons, Inc., Cambridge, Mass., The Technology Press (1958), Chapters 1 and 2.
19. W. Black, J. G. V. de Jongh, J. Th. G. Overbeck and M. J. Sparnaay, Trans. Faraday Soc., 56 (1960) 1597.
20. I. I. Abrekossova and B. V. Denjaguin, Phys. Chem. Solids, 5 (1958) 1.
21. D. Tabor and R. H. S. Winterton, Proc. Roy. Soc., A312 (1969) 435.
22. S. W. Benson and J. W. King, Jr., Science, 150 (1965) 1710.
23. G. Guouy, Ann. Phys., 7 [9] (1917) 129.
24. O. Stern, Z. Elektrochem, 30 (1924) 508.
25. J. C. Slater, Insulators, Semiconductors and Metals: Quantum Theory of Molecules and Solids, Vol. 3, McGraw-Hill, New York (1967), p. 206.
26. J. J. Duga, "Surface Energy of Ceramic Materials," Defense Ceramic Information Center Report 69-2, Battelle Memorial Institute, Columbus Laboratories (1969).
27. R. J. Stokes, "Mechanical Behavior of Polycrystalline Ceramics," in Ceramic Microstructures, R. Fulrath and J. Pask, eds., J. Wiley and Sons (1968), p. 379.
28. S. M. Weiderhorn, "Fracture of Ceramics," in Mechanical and Thermal Properties of Ceramics, J. B. Wachtman, Jr., ed., NBS Publication 303 (1969), p. 217.
29. D. J. Bryant, L. H. Taylor and P. L. Gutshall, "Cleavage Studies of Lamellar Solids in Various Gas Environments," in Trans. Tenth National Vacuum Symposium (1963), pp. 21-26.
30. A. A. Griffith, Phil. Trans. Roy Soc. (London), A221 (1920) 163.
31. J. J. Gilman, J. Appl. Phys., 31 (1960) 2208.
32. A. R. C. Westwood and T. T. Hitch, J. Appl. Phys., 34 (1963) 3085.

33. A. C. Zettlemoyer, "Hydrophobic Surfaces," in Hydrophobic Surfaces, F. M. Fowkes, ed., Academic Press, New York (1969), pp. 1-28.
34. Z. C. Zettlemoyer and K. S. Narayan, "Heats of Immersion and the Vapor/Solid Interface," in The Solid-Gas Interface, Vol. 1, E. A. Flood, ed., M. Dekker, Inc., New York (1966), pp. 145-175.
35. W. L. Winterbottom, "Crystallographic Anisotropy in the Surface Energy of Solids," in Surfaces and Interfaces, Vol. 1, J. J. Burke, N. L. Reed and V. Weiss, eds., Syracuse University Press (1967), pp. 133-169.
36. R. H. Bruce, "Aspects of Surface Energy of Ceramics: I. Calculation of Surface Free Energies," in Science of Ceramics, Vol. 2, G. H. Stewart, ed., Academic Press, London (1965), p. 359.
37. W. F. Giaque and R. C. Archibald, J. Am. Chem. Soc., 59 (1937) 561.
38. R. H. Bruce, "Aspects of Surface Energy of Ceramics: II. Calculation of the Average Surface Free Energy and the Effect of Some Variables," in Science of Ceramics, Vol. 2, G. H. Stewart, ed., Academic Press, London (1965), p. 368.
39. J. P. Borel, Compt. Rend., 257 (1963) 1847.
40. B. E. Sundquist, Acta Met., 12 [67] (1964) 585.
41. M. M. Nicholson, Proc. Roy. Soc. A228 (1955) 490.
42. J. J. Bickerman, Physical Surfaces, Academic Press (1970).
43. I. N. Stranski, Z. Physik Chem., 136 (1928) 259.
44. A. W. Adamson, Physical Chemistry of Surfaces, 2nd ed., Interscience Publishers, Inc. (1967), p. 278.
45. H. R. Kruyt, Colloid Science, Elsevier, New York (1952).
46. J. Th. Overbeek, Advances in Colloid Science, Vol. III, Interscience, New York (1950), p. 97f.
47. Physical and Chemical Aspects of Adsorbents and Catalysts, B. G. Linsen, ed., Academic Press (1970).
48. Fundamentals of Gas-Surface Interactions, H. Saltsburg, J. N. Smith, Jr. and M. Rogers, eds., Academic Press (1967).
49. N. K. Nair and J. M. Thorp, Trans. Faraday Soc., 61, Part 5 (1965) 962-989.

50. R. L. McIntosh, Dielectric Behavior of Physically Adsorbed Gases, M. Dekker, Inc. (1966).
51. A. J. Mountvala, G. Y. Onoda, E. J. Onesto and A. G. Pincus, "Characterization of Ceramic Particles: Analysis of Alumina by Dielectric Measurements," ONR Report, Contract No. N00014-68-C-0305, Nov. 1969.
52. W. S. Brey, Jr. and K. D. Lawson, J. Phys. Chem., 68 (1964) 1474.
53. M. R. Basila, T. R. Kantner and K. H. Rhee, J. Phys. Chem., 68 (1964) 3197.
54. D. O. Hayward and B. M. W. Trapnell, Chemisorption, Butterworths, London (1964).
55. S. J. Gregg, The Surface Chemistry of Solids, Reinhold Publishing Corp., New York (1961), pp. 300-328.
56. L. L. Hench, "Sintering and Reactions of MgO and Cr<sub>2</sub>O<sub>3</sub>," Dissertation Abstracts, University of Michigan Microfilm (1964).
57. L. L. Hench, "Dielectric Relaxation in Materials Analysis," Society of Aerospace Materials and Process Engineers, Proceedings of the 14th Annual Symposium, Nov. 1968.
58. I. Langmuir, J. Am. Chem. Soc., 40 (1918) 1361.
59. R. H. Fowler and E. A. Guggenheim, Statistical Thermodynamics, Cambridge University Press, Cambridge, England (1952).
60. D. M. Young and A. D. Growell, Physical Adsorption of Gases, Butterworths, London (1962),
61. S. Brunauer, The Adsorption of Gases and Vapors, Vol. 1, Princeton University Press, Princeton, New Jersey (1945).
62. S. Brunauer, P. H. Emmett and E. Teller, J. Am. Chem. Soc., 60 (1938) 309.
63. S. J. Gregg, J. Chem. Soc. (1942) 696.
64. J. H. de Boer, The Dynamical Character of Adsorption, The Clarendon Press, Oxford (1953).
65. S. Ross and J. P. Olivier, On Physical Adsorption, Interscience, New York (1964).
66. W. D. Harkins and G. Jura, J. Am. Chem. Soc., 66 (1944) 1366.



67. T. L. Hill. *Advan. Catalysis*, 4 (1952) 211.
68. G. D. Halsey, Jr., *J. Am. Chem. Soc.*, 73 (1951) 2693.
69. J. McGavack, Jr., and W. A. Patrick, *J. Am. Ceram. Soc.*, 42 (1920) 946.
70. J. H. de Boer and C. Zwikker, *Z. Physik Chem.*, B3 (1929) 407.
71. S. W. Benson and J. W. King, Jr., *Science*, 150 (1965) 1710.
72. J. C. P. Broekhoff and B. G. Linsen, "Studies on Pore Systems in Adsorbents and Catalysts," in Physical and Chemical Aspects of Adsorbents and Catalysts, B. G. Linsen, ed., Academic Press, New York (1970), pp. 1-63.
73. C. G. Shull, *J. Am. Chem. Soc.*, 70 (1948) 1405.
74. J. H. de Boer, B. G. Linsen, Th. van der Plas and G. J. Zondervan, *J. Catalysis*, 4 (1965) 649.
75. J. H. de Boer, B. G. Linsen, J. C. P. Broekhoff and Th. J. Osinga, *J. Catalysis*, 11 (1968) 46.
76. B. C. Lippens, B. G. Linsen and J. H. de Boer, *J. Catalysis*, 3 (1964) 32.
77. J. H. de Boer and B. C. Lippens, *J. Catalysis*, 3 (1964) 38, 44.
78. W. F. N. M. de Vleerschauer, "Active Magnesia," Thesis, Delft University of Technology, The Netherlands (1967).
79. B. C. Lippens, "Structure and Texture of Aluminas," Thesis, Delft University of Technology, The Netherlands (1961).
80. a) J. H. de Boer, B. G. Linsen and Th. J. Osinga, *J. Catalysis*, 4 (1965) 643.  
b) H. Th. Rijnten, "Formation, Preparation and Properties of Hydrous Zirconia," in Physical and Chemical Aspects of Adsorbents and Catalysts, B. G. Linsen, ed., Academic Press, New York (1970), pp. 315-371.
81. P. H. Emmett and M. Cines, *J. Phys. Colloid Chem.*, 51 (1947) 1260.
82. A. B. L. van Dorn, "Grafietoxyde," Thesis, Delft University of Technology, The Netherlands (1957).
83. B. G. Linsen, "The Texture of Nickel-Silica Catalysts," Thesis, Delft University of Technology, The Netherlands.

84. W. F. N. M. de Vleerschauwer, "Active Magnesia," in Physical and Chemical Aspects of Adsorbents and Catalysts, B. G. Linsen, ed., Academic Press, New York (1970), pp. 265-316.
85. C. Okkerse, "Porous Silica," in Physical and Chemical Aspects of Adsorbents and Catalysts, B. G. Linsen, ed., Academic Press, New York (1970), pp. 213-265.
86. E. G. P. Cornelissens, in Physical and Chemical Aspects of Adsorbents and Catalysts, B. G. Linsen, ed., Academic Press, New York (1970), p. 420.
87. M. E. A. Hermans, "Hydrolytic Phenomena in U(VI)-Preparation," in Physical and Chemical Aspects of Adsorbents and Catalysts, B. G. Linsen, ed., Academic Press, New York (1970), pp. 373-423.
88. F. E. Karasz, W. M. Champion and G. D. Halsey, Jr., J. Phys. Chem., 60 (1956) 376.
89. B. C. Lippens and J. H. de Boer, J. Catalysis, 4 (1965) 319.
90. M. G. Baldwin and J. C. Morrow, J. Chem. Phys., 36 (1962) 1591.
91. G. Ebert, Kolloid Z., 184 (1962) 148.
92. L. K. H. von Beek, in Progress in Dielectrics, Vol. 7, CRC Press (1966), p. 69.

Table 1  
Experimental Techniques (26)  
for Determining Surface Energy

<u>Mechanical Methods</u>	<u>Thermodynamic Methods</u>	<u>Miscellaneous</u>
Crack Propagation	Contact Angle	X-ray Lattice
Strain Energy Release	Heat of Immersion	Parameter Shift
Crushing	Heat of Solution	
Drilling	Dissolution and Ostwald Ripening	
Bent Wafer	Equilibrium Shapes	
Fiber Stress		

Table 2  
Surface Energies of Selected  
Ceramic Single Crystals  
Using Double Cantilever Method

Crystal	Plane	Temp. °C	Surface Energy ergs/cm <sup>2</sup>
Al <sub>2</sub> O <sub>3</sub>	(10 $\bar{1}$ 1)	25	6,000
Al <sub>2</sub> O <sub>3</sub>	(10 $\bar{1}$ 0)	25	7,300
CaCO <sub>3</sub>	(10 $\bar{1}$ 0)	-196	230
CaF <sub>2</sub>	(111)	25	355
	(111)	-196	450
	(111)	-273	542
	(110)	-273	1,081
LiF	(100)	25	563
	(100)	-196	340
MgO	(100)	25	1,700
NaCl	(100)	25	310
NaCl	(100)	-196	280
Si	(111)	-196	1,240
SiO <sub>2</sub> (quartz)	(11 $\bar{2}$ 0)	25	760
SiO <sub>2</sub> (quartz)	(10 $\bar{1}$ 1)	25	450
SiO <sub>2</sub> (quartz)	(10 $\bar{1}$ 0)	25	1,030

Table 3  
Surface Energy of a Subdivided 1 g cube of MgO

Number of Particles	Single Particle Weight g	Single Particle Volume cc	Side Length cm	Total Area cm <sup>2</sup>	Total Edge Length cm	Surface Energy ergs/g	Edge Energy ergs/g
1	1.0	0.27	0.65	2.5	7.8	$2.5 \times 10^3$	$7.8 \times 10^{-5}$
2702	$3.7 \times 10^{-3}$	$1 \times 10^{-3}$	0.1	28	550	$2.8 \times 10^4$	$5.5 \times 10^{-3}$
$2.7 \times 10^5$	$3.7 \times 10^{-6}$	$1 \times 10^{-6}$	0.01	280	$5.5 \times 10^4$	$2.8 \times 10^5$	0.55
$2.7 \times 10^8$	$3.7 \times 10^{-9}$	$1.10^{-9}$	0.0001	$2.8 \times 10^3$	$5.5 \times 10^6$	$2.8 \times 10^6$	55
$2.7 \times 10^{11}$	$3.7 \times 10^{-12}$	$1 \times 10^{-12}$	$10^{-4}$ (1 $\mu$ )	$2.8 \times 10^4$	$5.5 \times 10^8$	$2.8 \times 10^7$ (0.76 cal)	$5.5 \times 10^3$
$2.7 \times 10^{14}$	$3.7 \times 10^{-15}$	$1 \times 10^{-15}$	$10^{-5}$ (.1 $\mu$ )	$2.8 \times 10^5$	$5.5 \times 10^{10}$	$2.8 \times 10^8$ (6.6 cal)	$5.5 \times 10^5$
$2.7 \times 10^{17}$	$3.7 \times 10^{-18}$	$1 \times 10^{-18}$	$10^{-6}$ (100 $\text{\AA}$ )	$2.8 \times 10^6$	$5.5 \times 10^{12}$	$2.8 \times 10^9$ (66 cal)	(0.13 cal) $5.5 \times 10^7$ (1.3 cal)

**Table 4**  
**Powder-Liquid**  
**Electro-characterization Methods**

<b>Potential</b>	<b>Nature of Solid Surface</b>	
	<b>Stationary</b>	<b>Moving</b>
<b>Applied</b>	<b>Electroosmosis</b>	<b>Electrophoresis</b>
<b>Induced</b>	<b>Streaming ; tential</b>	<b>Sedimentation potential</b>

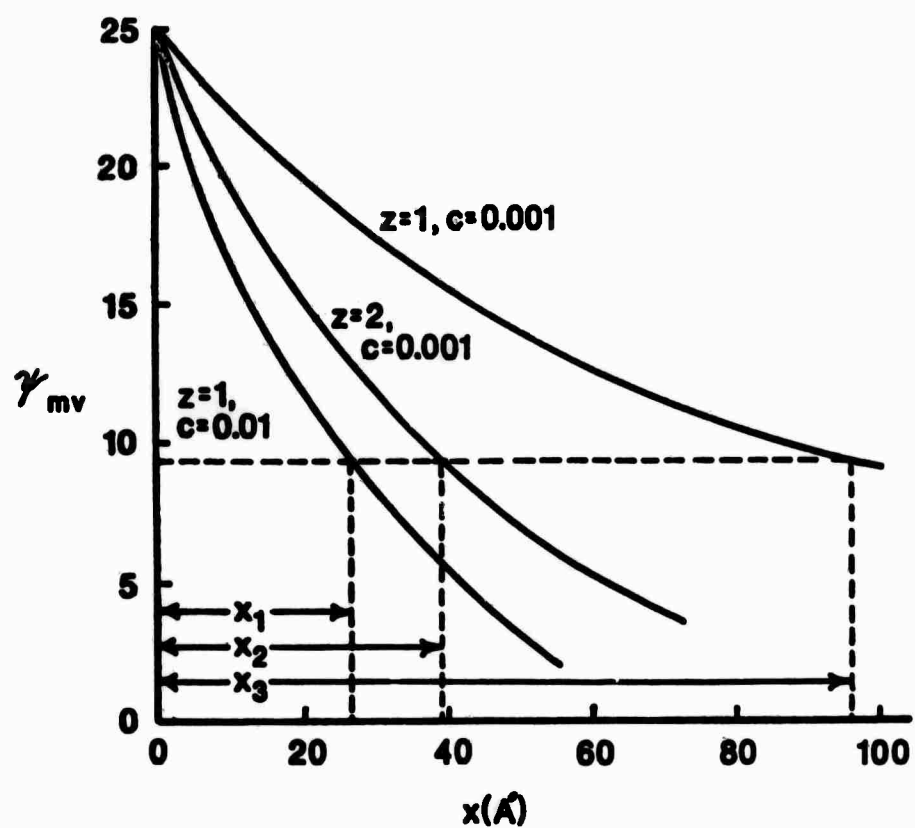


Figure 1. Change in powder surface potential,  $\psi$ , with distance from the surface,  $x$ , for various electrolyte concentrations,  $c$ , and valences,  $z$ .

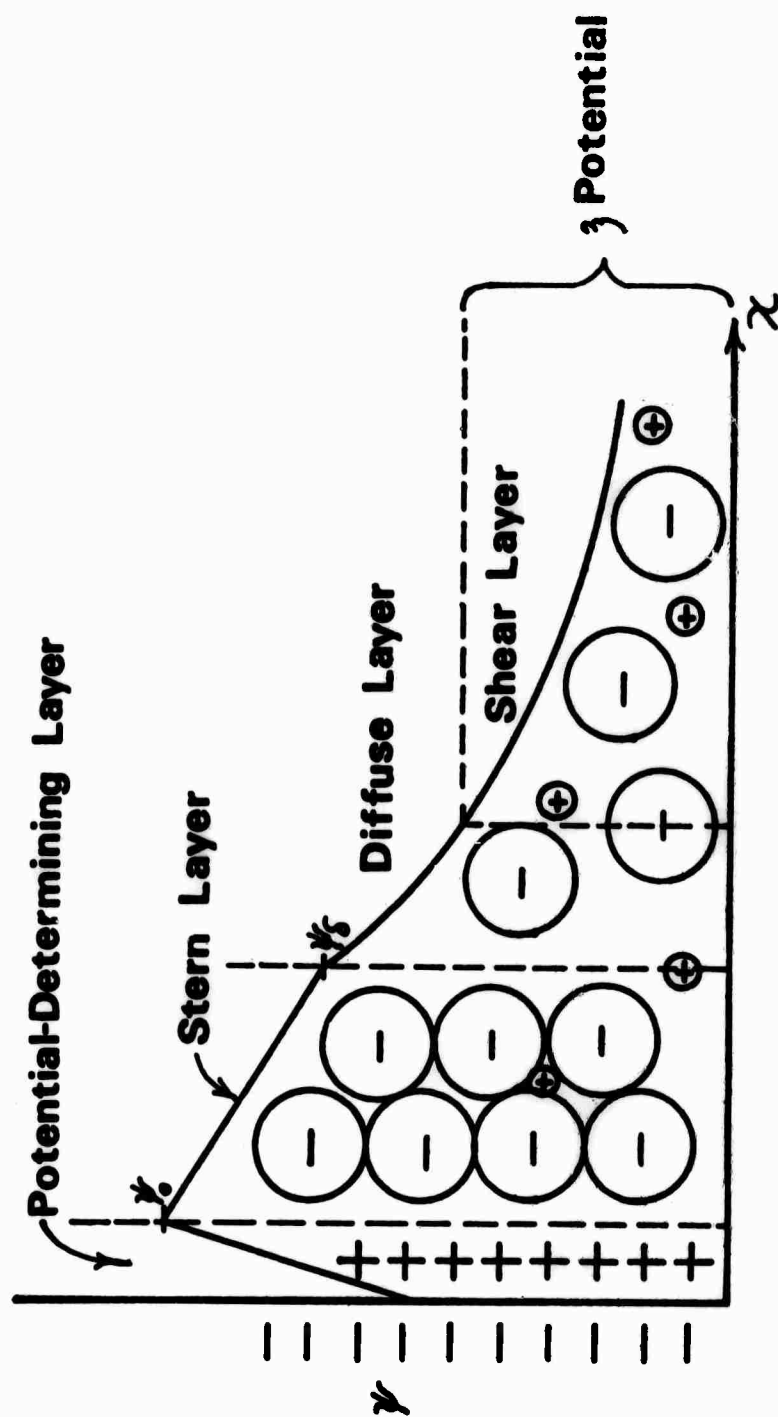


Figure 2. Surface charge model for a powder in an electrolytic solution.



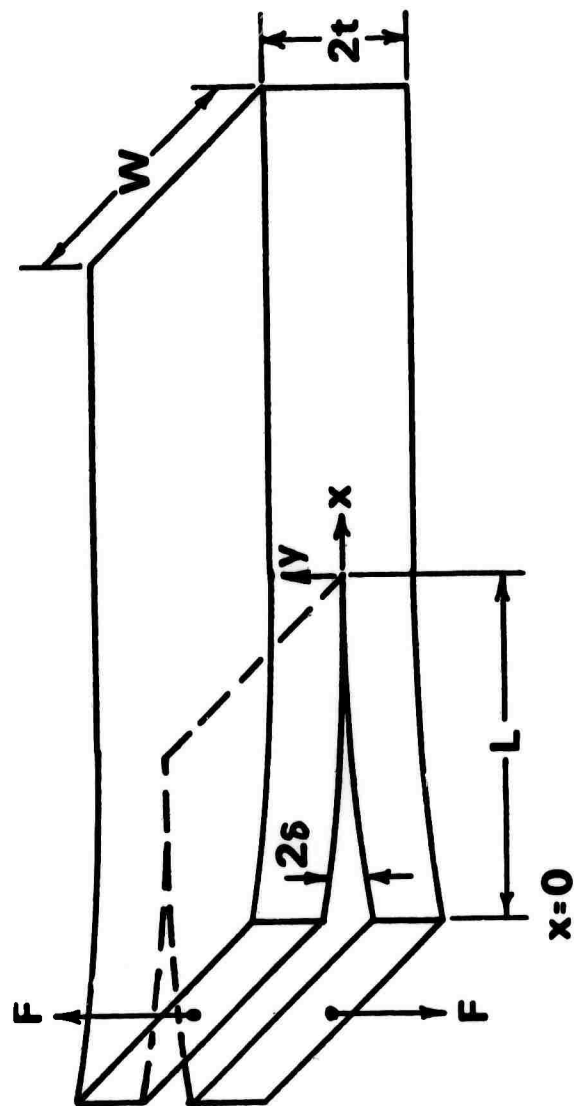


Figure 3. Double cantilever method for determining surface energies.

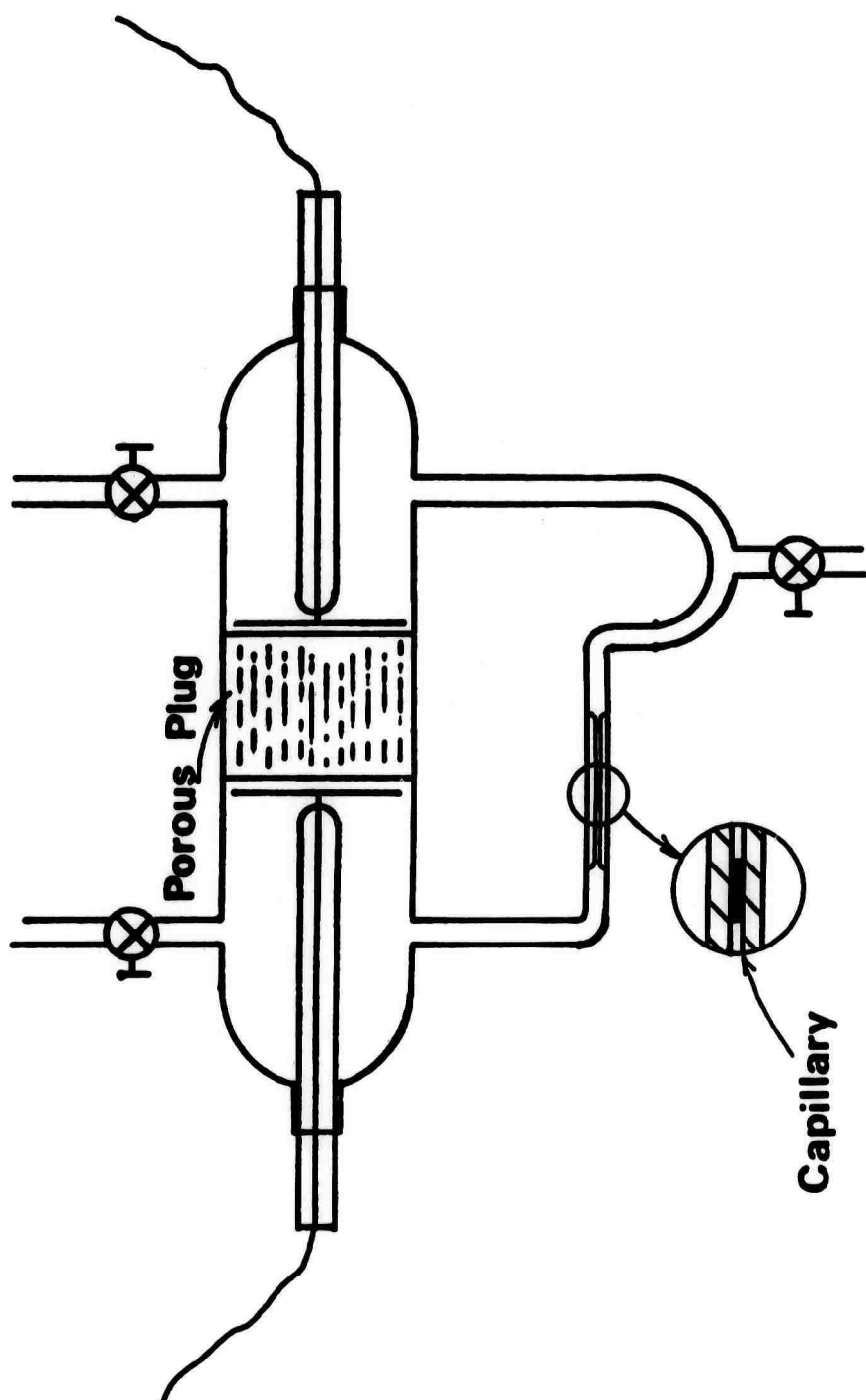


Figure 4. Electroosmosis method for analyzing the zeta potential of a powder.

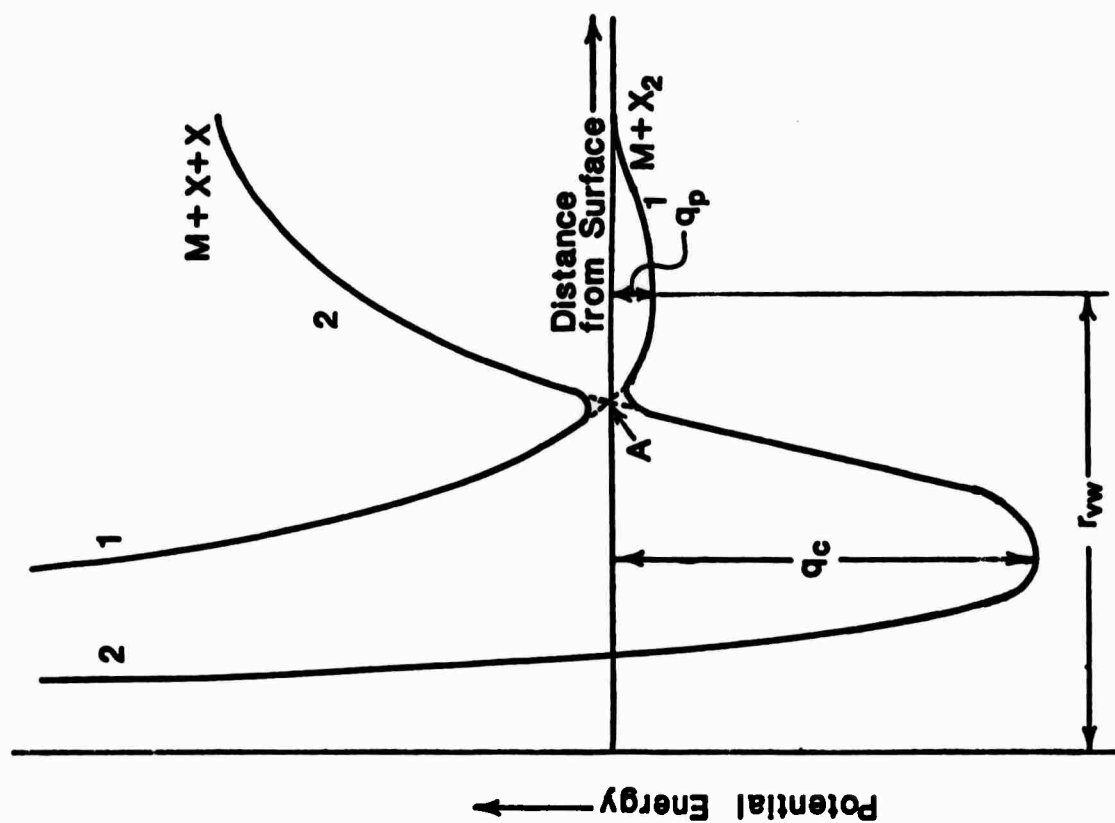


Figure 5. Energy model for chemisorption,  $q_c$ , and physisorption,  $q_p$ , of a gas,  $X_2$ , on a surface.

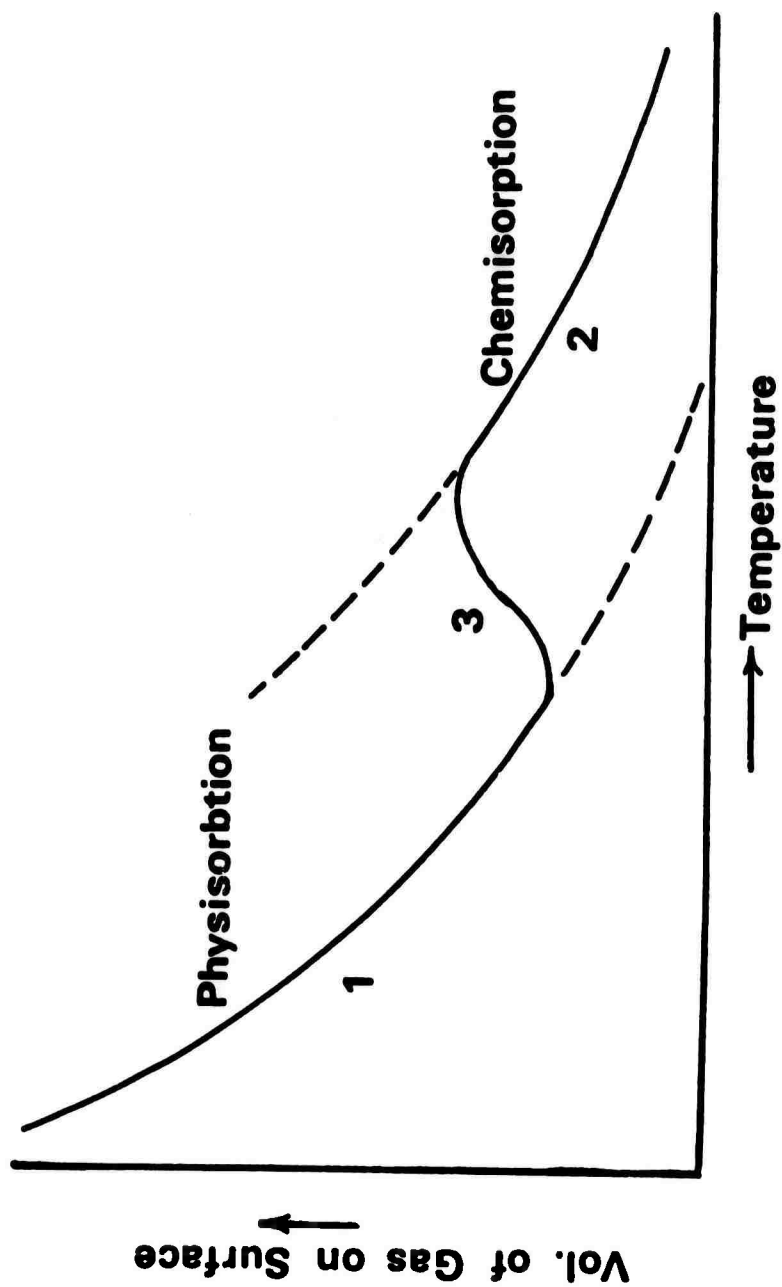


Figure 6. Temperature dependence of surface adsorption.

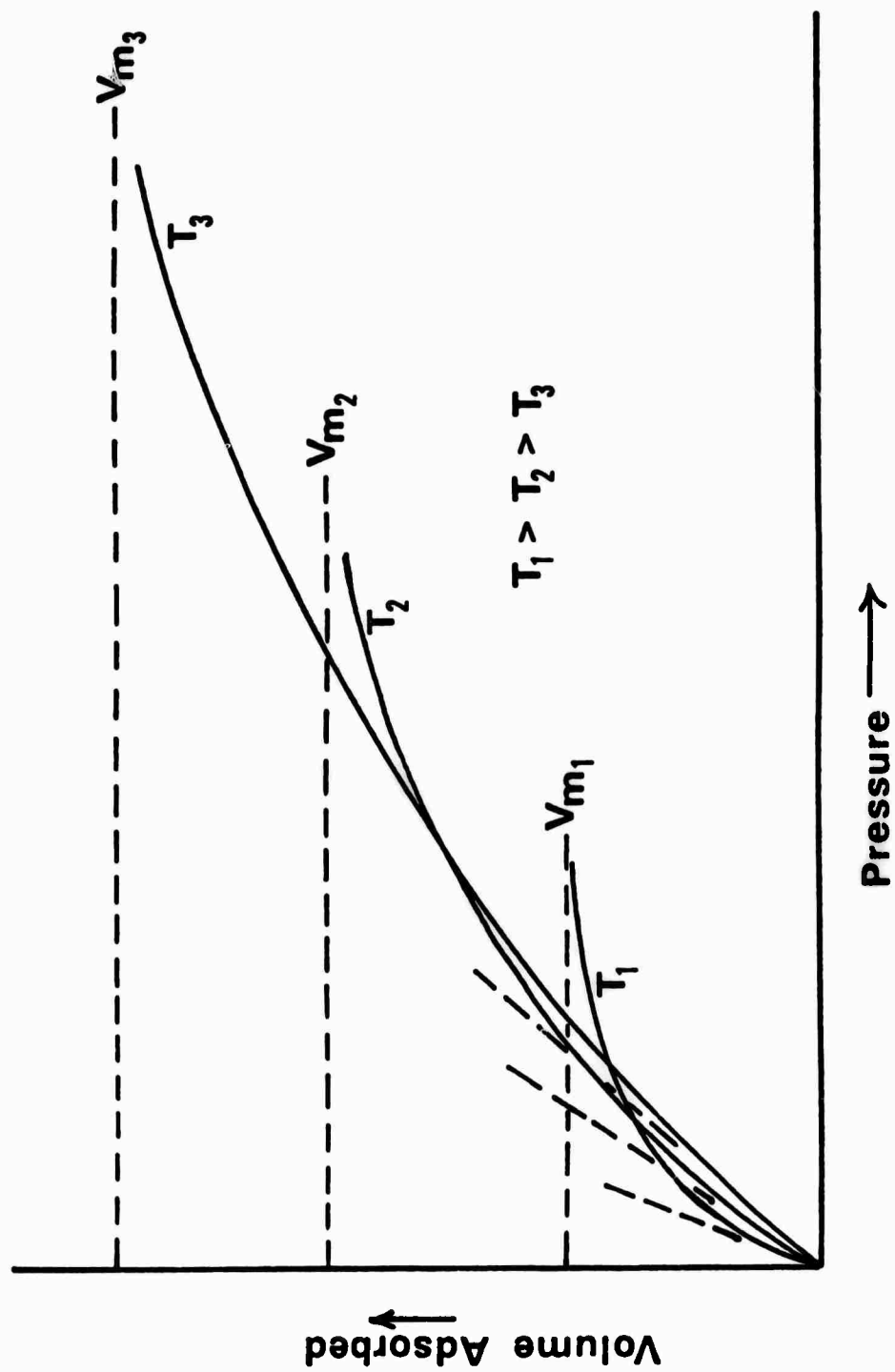


Figure 7. Typical Langmuir isotherms.

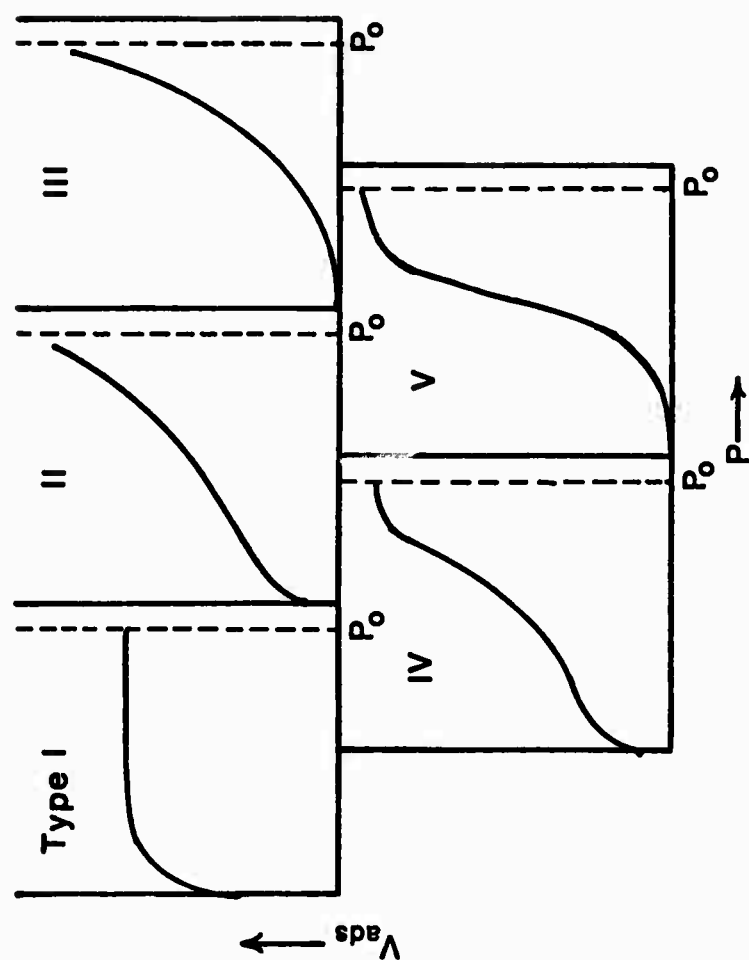


Figure 8. Five types of adsorption isotherms.

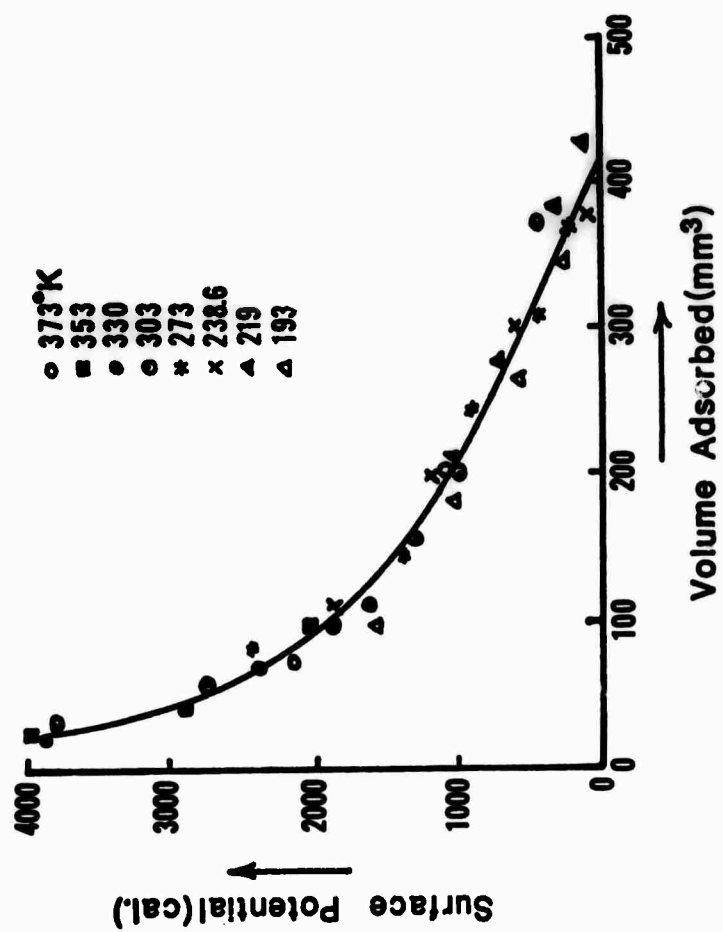


Figure 9. Characteristic curve for the adsorption of  $\text{SO}_2$  on silica gel.

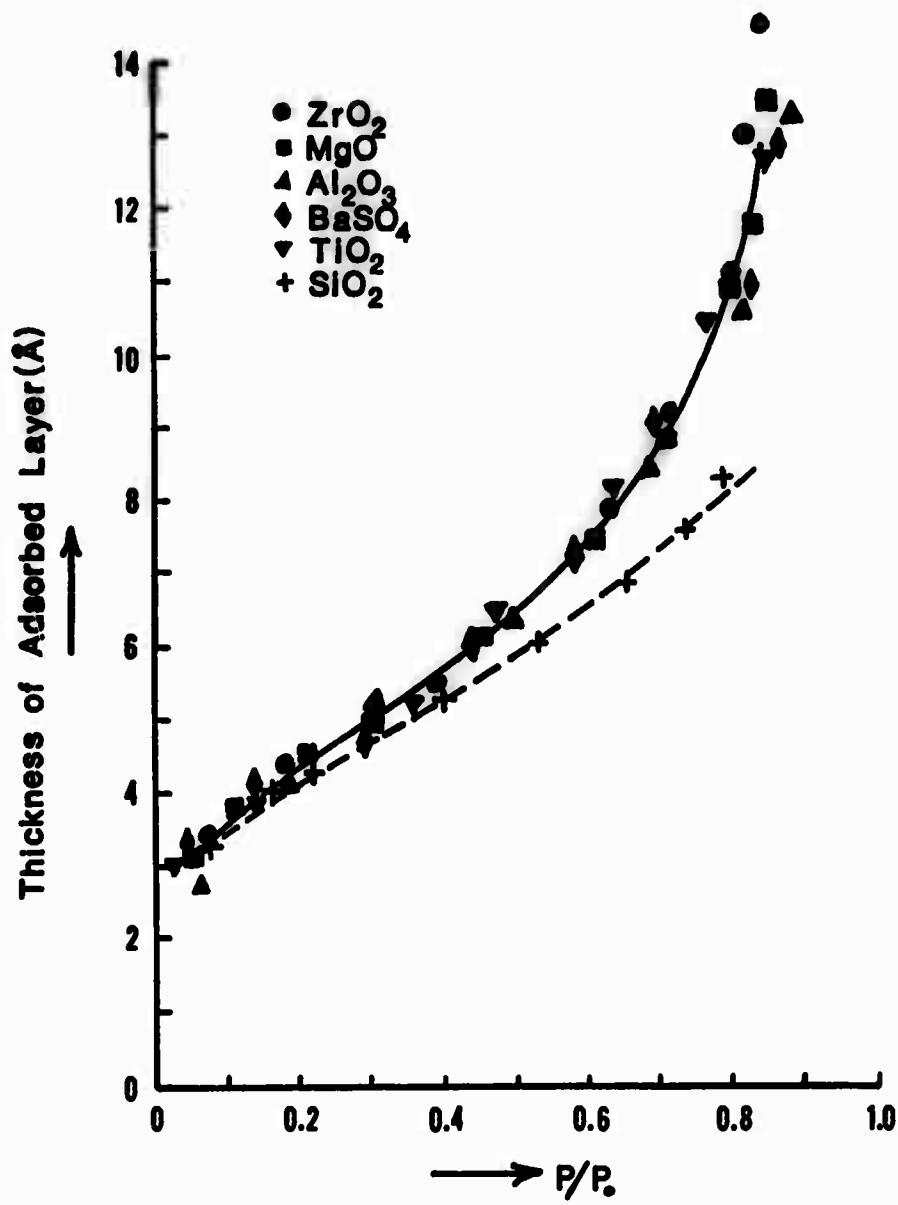


Figure 10. t-curves of various ceramic powders as a function of relative pressure of  $N_2$ ,  $77^\circ K$ .



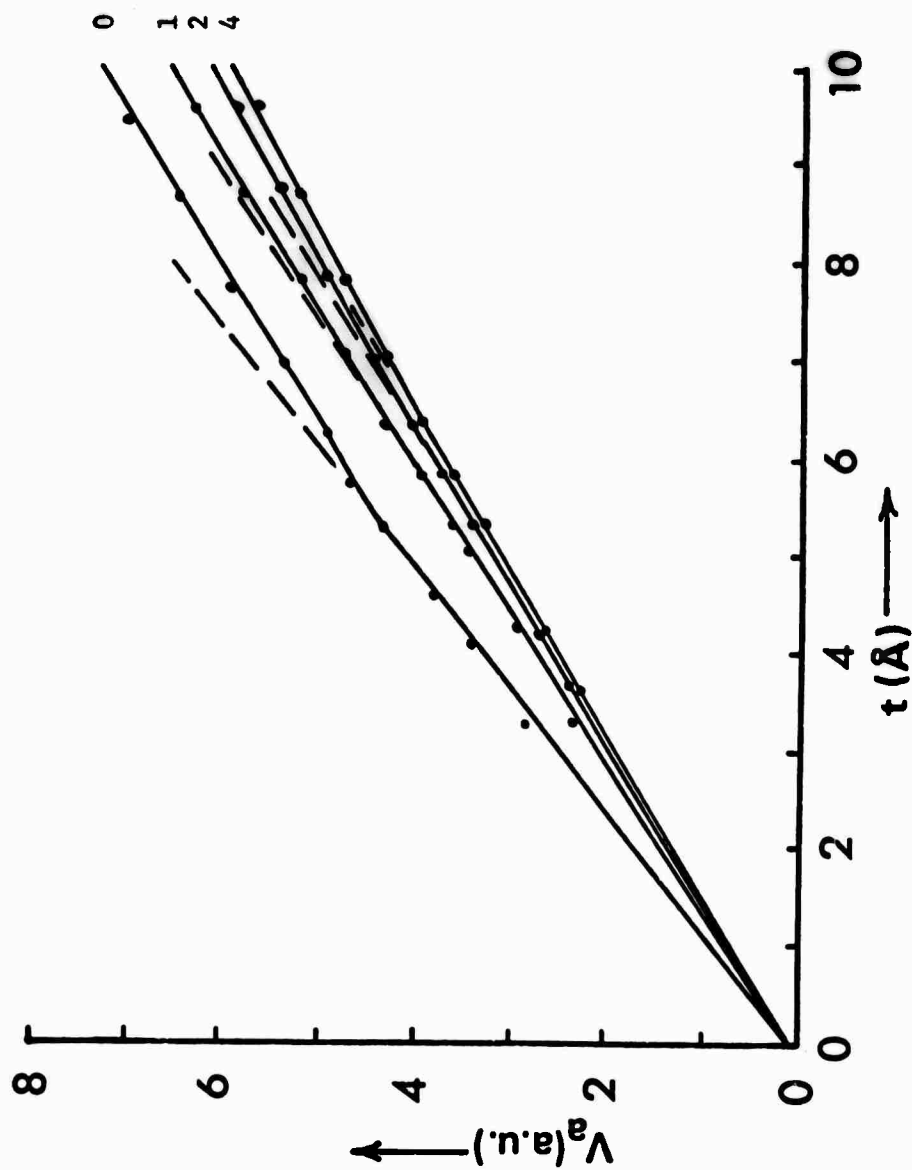


Figure 11. Effect of 0, 1, 2 and 4 layers of water pre-adsorbed on the total volume  $N_2$  adsorbed, 78°K, vs. layer thickness for anatase  $TiO_2$  powder.

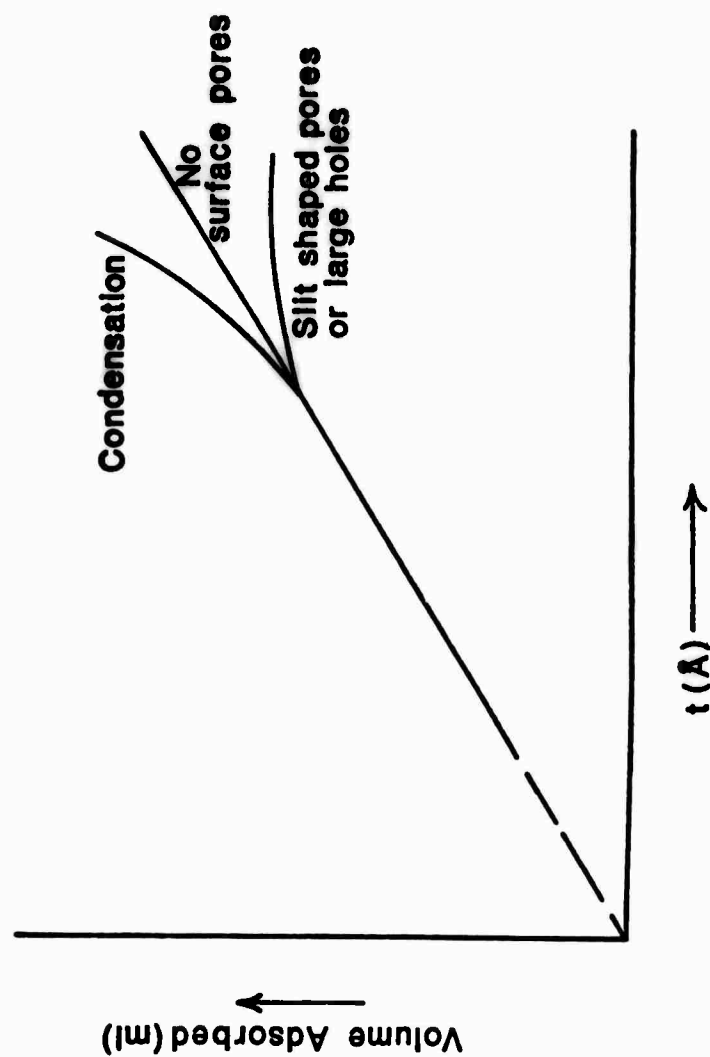


Figure 12. Three fundamental shapes of the total volume adsorbed vs. layer thickness plot.

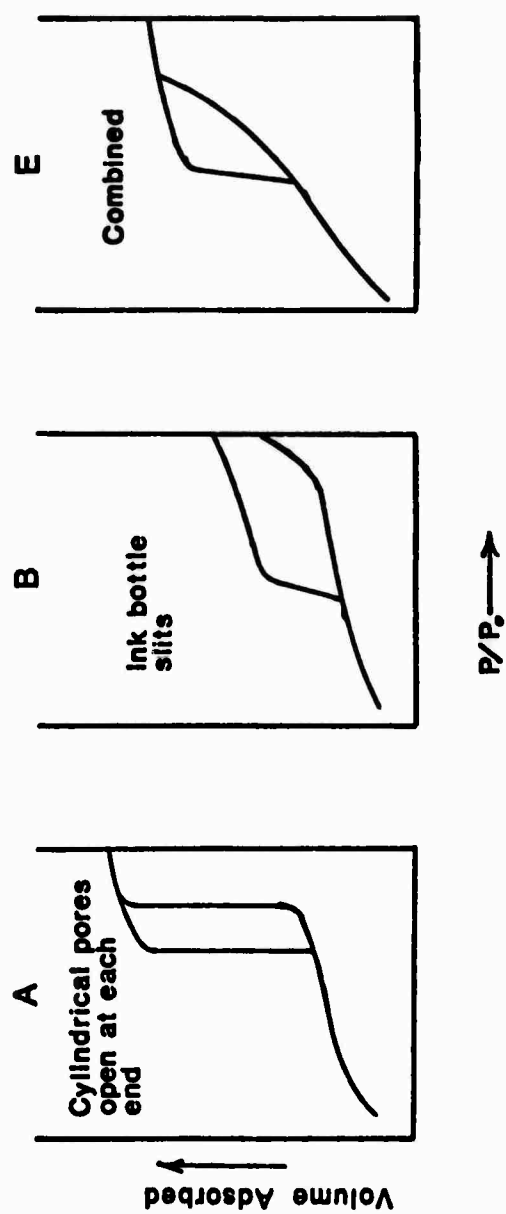


Figure 13. Three types of adsorption hysteresis loops according to de Boers' classification.

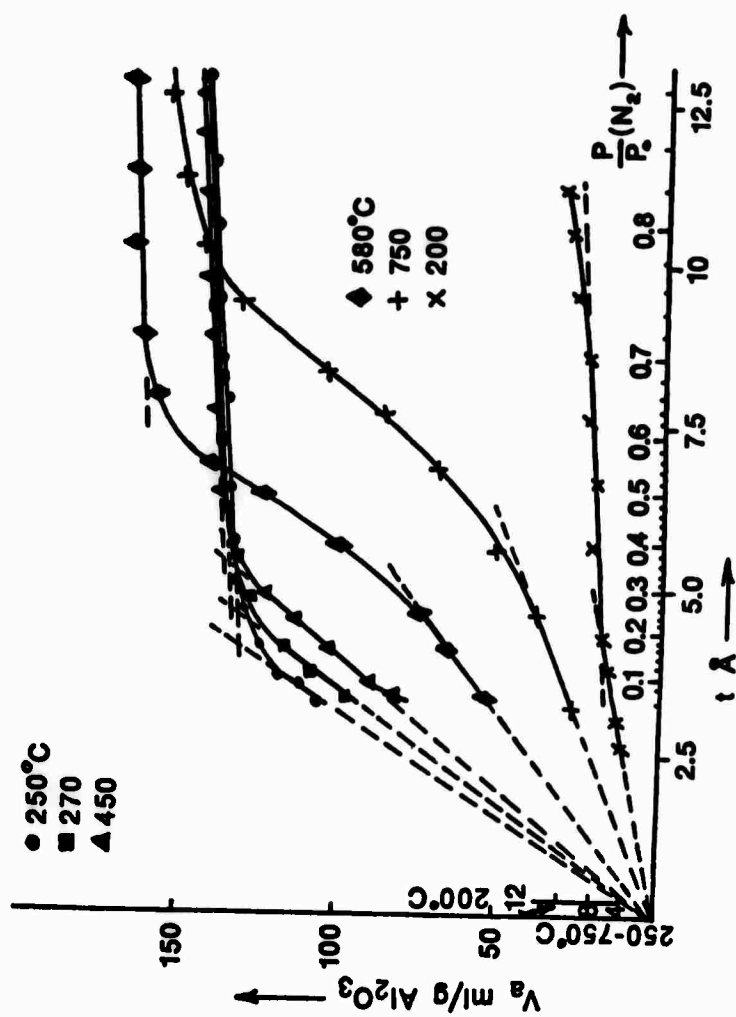


Figure 14. Influence of heating Bayerite  $\text{Al}_2\text{O}_3$  powder on the volume of adsorbed  $\text{N}_2$  vs. thickness dependence of the gas layer.

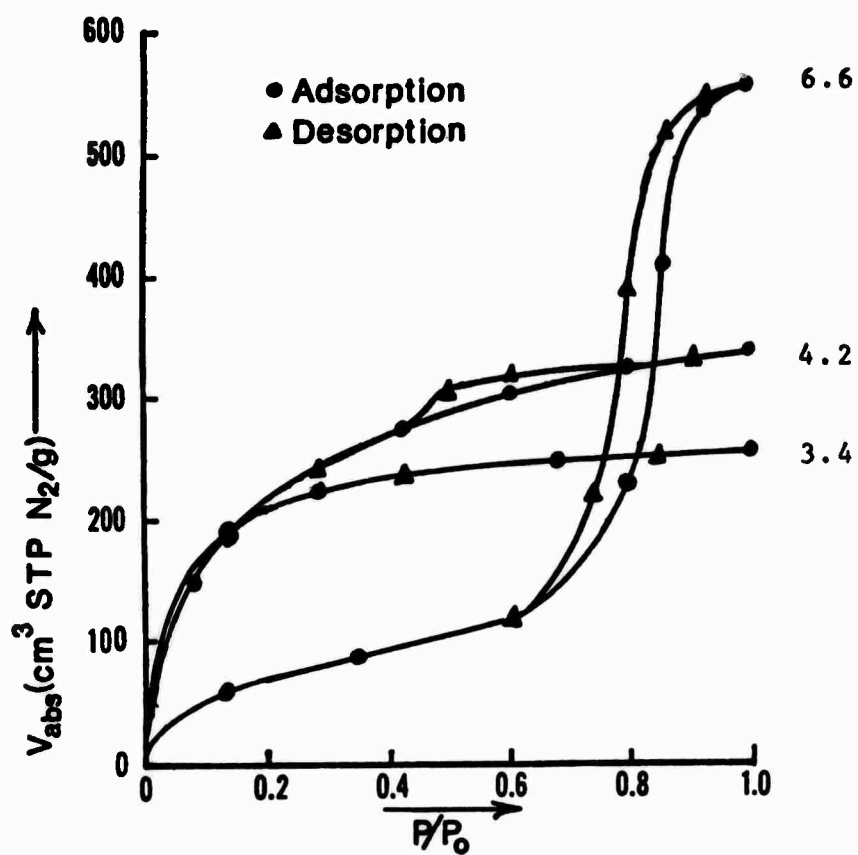


Figure 15. Effect of precipitation pH on the  $N_2$  adsorption isotherms,  $-196^\circ\text{C}$ , of silica powders.

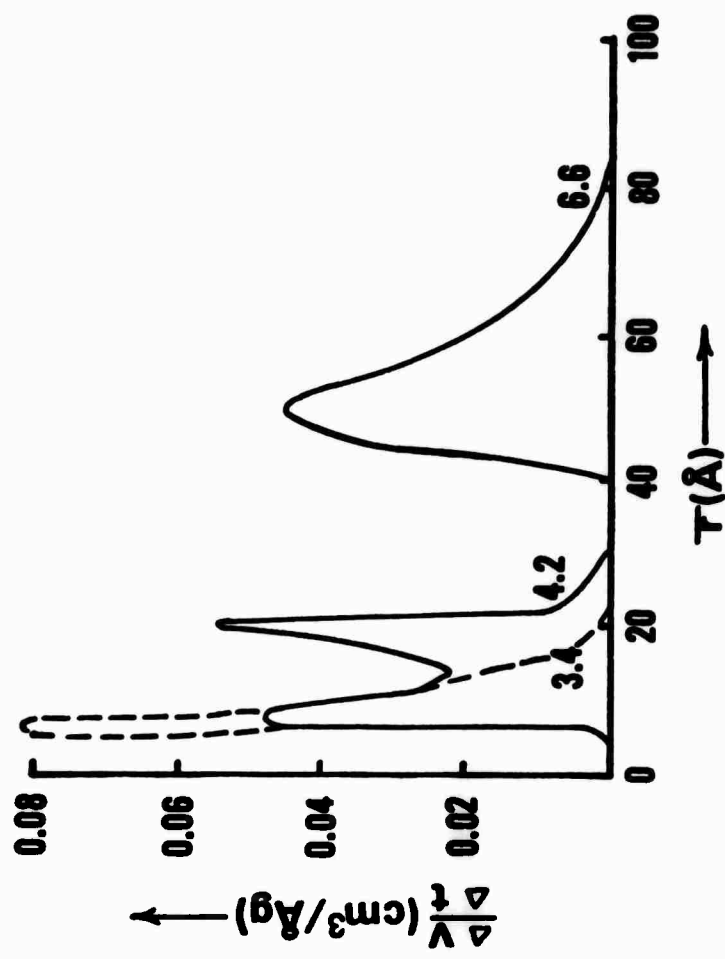


Figure 16. Variations in pore size distributions of  $\text{SiO}_2$  powders resulting from differences in precipitation pH's.

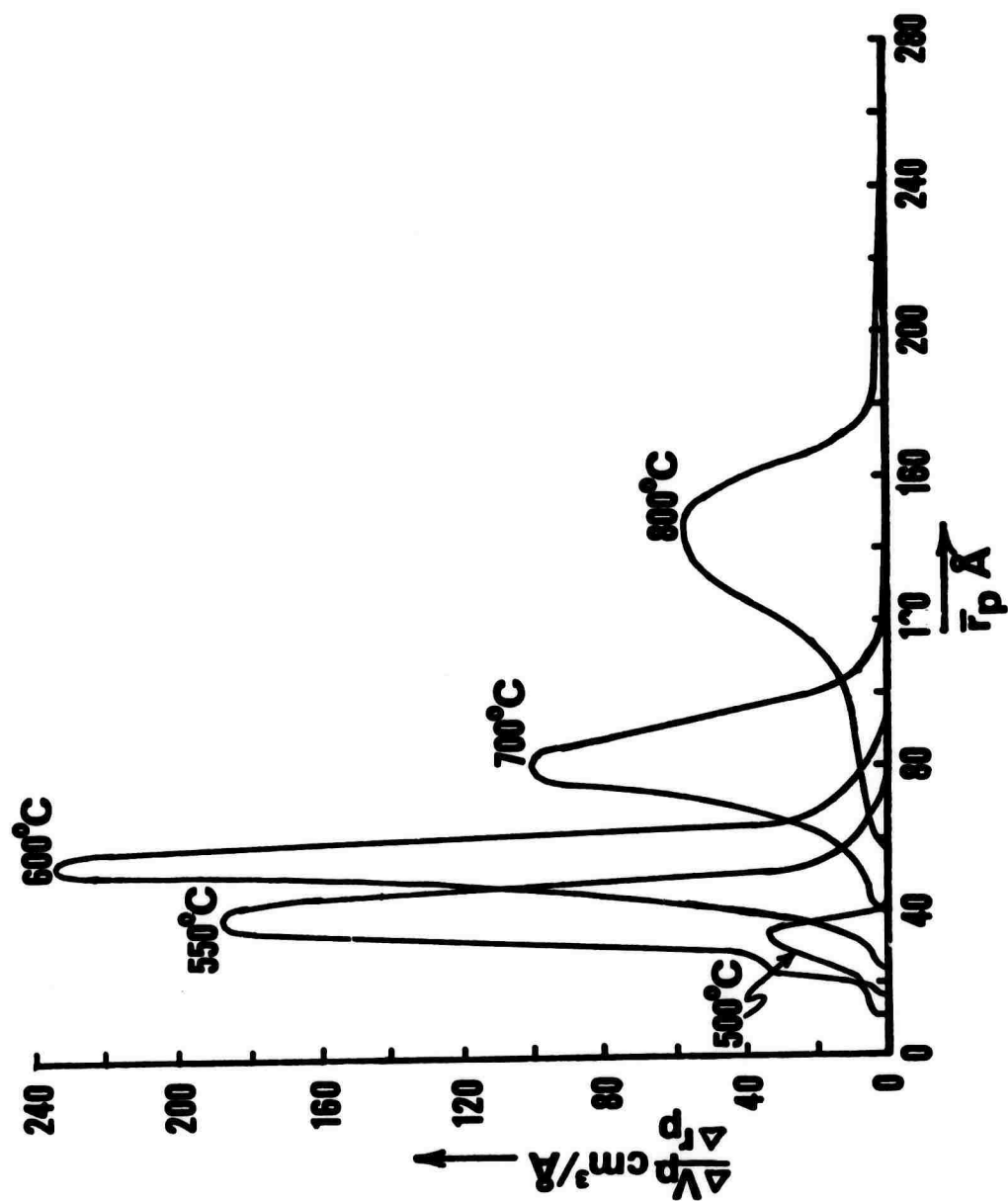


Figure 17. Change in pore size distributions due to heating MgO powder to various temperatures.

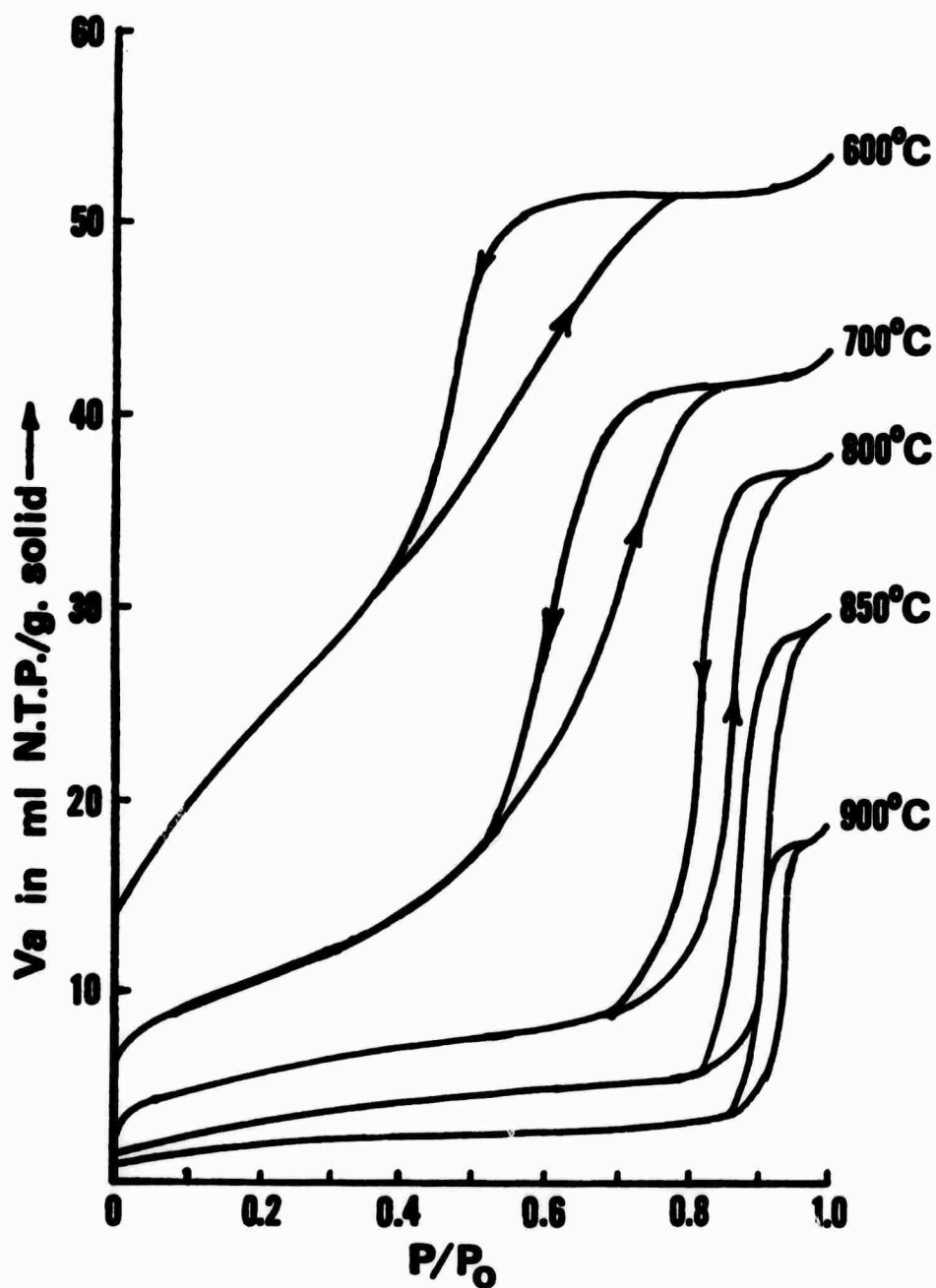


Figure 18. Influence of sintering temperature on the  $N_2$  adsorption isotherms of sol-gel (U, Th) oxide containing 11% U.



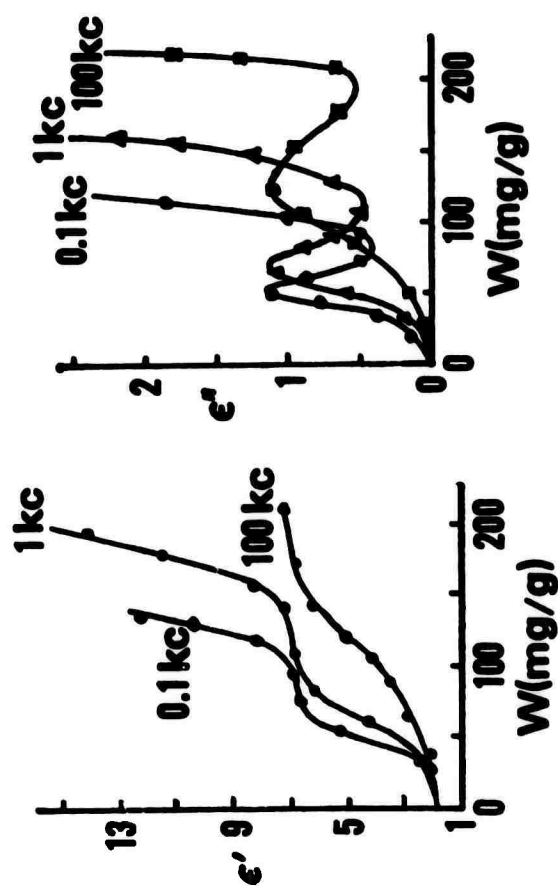


Figure 19. Dependence of the dielectric charging constant,  $\epsilon'$ , and loss constant,  $\epsilon''$ , of porous  $\gamma$  alumina on the adsorption of  $H_2O$ .

## C. DIELECTRICS COMPUTING PROGRAMS (G. J. Scott and L. L. Hench)

### Introduction

The humidity dependence of electronic substrates, insulators, radomes, and other electronic ceramic materials was shown in a previous report to be a very important electrical parametric. Changes in the loss factor by as much as  $10^4$  were observed, for example. The dielectric constant and capacitance were likewise affected by many orders of magnitude through variations in relative humidity over the range of 0-100%.

Analysis of humidity dependent dielectric data can be very time-consuming. Consequently, it was the objective of this study to write and activate an automatic computer program which will calculate and plot the humidity dependent dielectric data. The results of this study follow.

The first programs in the series aid exploratory research by producing report-ready plots of loss tangent vs. log frequency, with up to three parametric curves per graph. Descriptions of operation, detailed structures of data decks, and program listings follow. All programs are coded in IBM 360 FORTRAN LV.

I. The "Tan Delta" set has two programs, "TDPUNCH" for data reduction and "TDDRAW" for graph drawing.

#### A. TDPUNCH

1. Purpose-- produce a printout of the data and resulting calculated percent relative humidity and tan delta values, and punch a new data deck.
2. Input--a manually keypunched deck containing the samples' dimensions and designations, partial pressure of ambient and saturated water, and frequency-conductivity-capacitance data.
3. Operation--read a case heading card, then calculate the relative humidity pertaining to the case. The machine then prints and punches the case heading information. Each case heading, including column titles, appears on a new sheet of the printout.

Read the first of a series of cards on which values of frequency, conductivity and capacitance have been punched.

Test to see that the capacitance value is non-zero.

For non-zero capacitances, calculate  $\tan \delta = 10^6 G/2\pi fC$ , and percent relative humidity, then print and punch frequency, conductivity, capacitance,  $\tan \delta$  and percent relative humidity values. (The frequencies have been set up in decreasing order, about 10 per case.)

When a card with both capacitance and frequency = 0 is encountered, this is the signal for the program to start another case. Again, it reads a data card of the first type (with sample thickness, etc., values) and calculates, punches and prints as above.

The signal that no more cases follow is that  $C = 0$  and  $F = 5$ . Note that these signals are used throughout the series of programs.

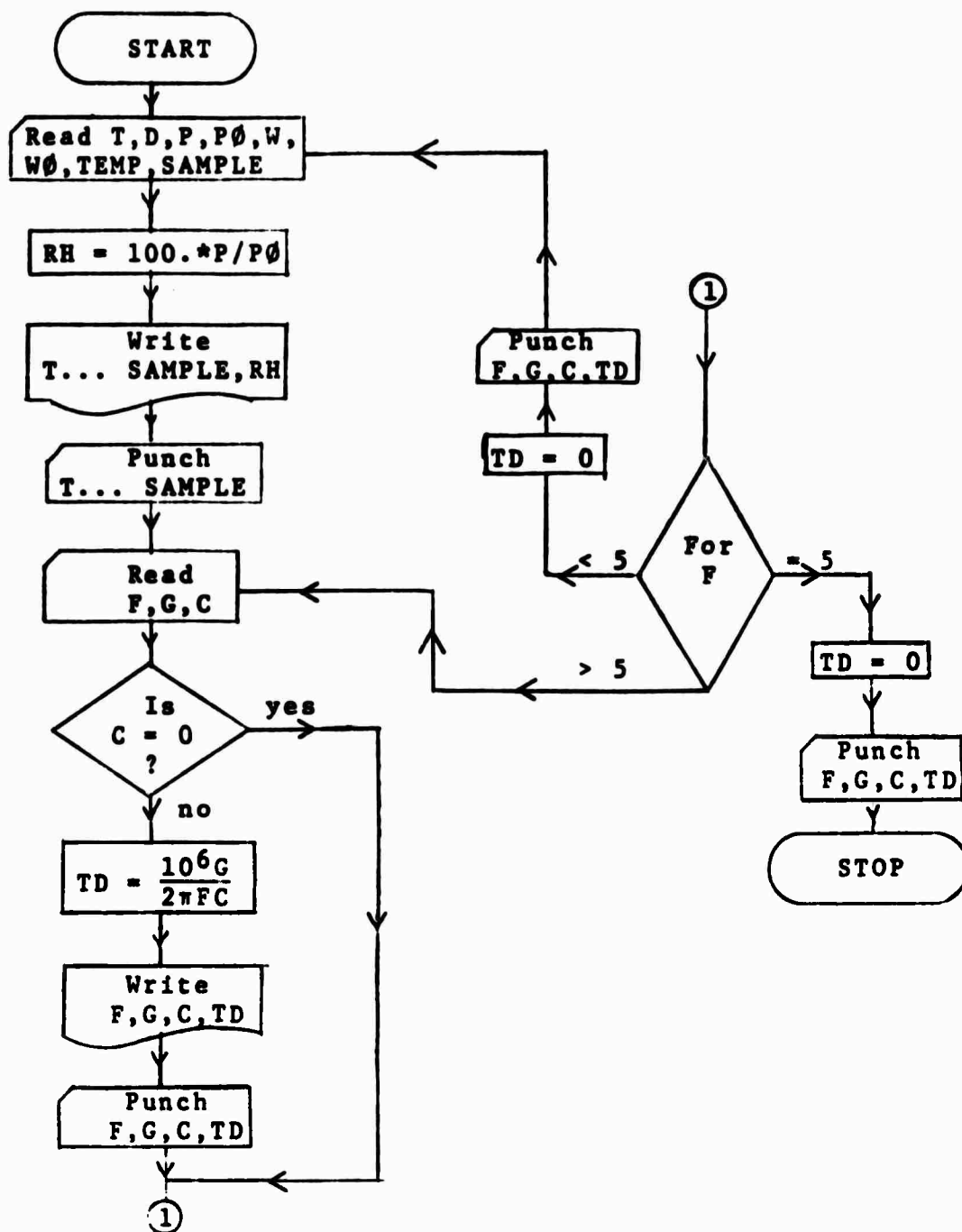
#### 4. Meaning of Symbols:

- T = sample thickness, measured by micrometer
- D = sample diameter, by ID micrometer on the pressing die
- P =  $p_{H_2O}$ , by control over temperature of cold bath in thermal equilibrium with the sample atmosphere
- PØ\* = saturated  $p_{H_2O}$  at the sample's temperature, from tables
- W = mg  $H_2O$  adsorbed/gram of samples
- WØ = vacuum weight of sample, measured by vacuum recording microbalance
- TEMP = sample temperature, controlled to  $\pm 0.5^\circ C$ , measured by Hg bulb thermometer
- SAMPLE = sample number
- F = frequency, Hertz, from Wayne Kerr signal generator
- G = sample conductivity, micromhos, from Wayne Kerr bridge
- C = sample capacitance, picofarads, from Wayne Kerr bridge
- TD =  $\tan \delta = 10^6 G/2\pi fC$
- RH = relative humidity =  $100 * p_{H_2O} / p_o(T)$

---

\*"Ø" in symbols means alphabetic "o"; "0" means "zero".

Flowchart - TDPUNCH



## 6. The Data Deck

Card Type	Format	Columns (inclusive)	Variable Code Name	Remarks
1	8F10.5	1-10	T	See "Meaning of Symbols"
		11-20	D	
		21-30	P	
		31-40	P0	
		41-50	W	
		51-60	W0	
		61-70	TEMP	
		71-80	SAMPLE	
				Must have decimal point.

Note that the decimal points are in columns 5, 15, 25, etc.

---

2	3F20.10	1-20	F	None equal to zero.
		21-40	G	
		41-60	C	

Decimal points in columns 10, 30 and 50. Several of these cards per case.

---

3	3F20.10	1-20	F	All equal 0. This is the "end of case" signal card.
		21-40	G	
		41-60	C	

---

4	3F20.10	1-20	F	= 5.
		21-40	G	= 0.
		41-60	C	= 0.

Replaces the type 3 card after the last case.

---

## B. TDDRAW

1. Purpose: To produce Calcomp plotter drawing of graphs of  $\tan \delta$  versus log frequency. The graphs are centered on 8-1/2" x 11" blocks of the Calcomp sheets, and have up to three relative humidities' curves. Curves for different samples (with respect to composition or processing) do not appear on the same graph.

2. Input: The deck of cards punched by the TDPUNCH program.

3. Output: The Calcomp graphs.

4. Symbols:

F = frequencies at which  $\tan \delta$  is determined, hertz.  
TD =  $\tan \delta$ , the loss angle tangent, dimensionless.  
NF = the number of frequencies associated with a given sample and relative humidity.  
 $\emptyset$  = the set of origin locations, taken with respect to the one immediately preceding.  
 $\emptyset X, \emptyset Y$  = initializing variables for location of the next origin.  
NLT = the number of letters in a title.  
TITLE, TL = 2 and 1 dimensional arrays containing the alphabetic information which constitutes the titles of the axes.  
SD = the tic-Scale-Division array; for example, the log frequency axis has a tic every 0.25 log-frequency-units.  
S = the actual tic spacing on the axis, inches.  
ZS = the x and y axis scale factors, with dimensions "inches of axis per unit variable plotted on the axis".  
TDM, FLM = the maximum values of  $\tan \delta$  and log frequency encountered in a particular set of data. Determine by inspecting the printed output of TDPUNCH.  
XMNIN = the array containing the minimum values of the variables which are to be recorded on the axis, similarly determined.

**NFIRST** = the tic number which is to receive the first tic label, which is an integer multiple of tic-Scale-Division.  
**NG** = the current graph number.  
**ØLSAMP** = the number of the sample for which all the graphs have not yet been drawn. It is "old" from the point of view of the second and subsequent curves.  
**SAMPNØ** = the sample number of the present case.  
**NAX** = the axis number; x = 1, y = 2.  
**MISS** = a signal to assure reading of a new sample number's data deck in proper order--the value of MISS may be zero or one, and equals the number of "sample" cards to be read.

5. Operation: Establish blocks of storage for the sub-scripted variables. Read NG, the NLT and NFIRST arrays, then the TDM, FLM, the SD matrixes, the initial ØLSAMP, and the XMIN array. Read the axis titles, "LOG FREQUENCY" and "TAN DELTA." Calculate the locations of the origins, so that axes are properly placed on 8-1/2" x 11" areas of the 30" x 720" Calcomp sheet. These areas are numbered in the sequence:

3	4	9	10	
2	5	8	11	
1	6	7	12	

Initiate the plotting routines. Scale the x and y axes (see the description of Subroutine SCALIN to follow). Establish the first origin, and write a program identification on the sheet.

Initialize NG and MISS. NG is stepped when a new graph is to be drawn. Draw axes at the current origin, label them and the ticks, per Subroutine PREP, description to follow.

For each of three cases (specific to a particular sample and relative humidity per graph):

Read the heading card, which contains the sample number. If the sample number hasn't changed (i.e., if  $SAMPN\emptyset = \emptyset LSAMP$ ), read a card which has the values of F and  $\tan \delta$ . Test F to see that it is a data value (i.e.,  $>5$ ) and not just a signal (meanings same as before).

Calculate the location of the point, according to the algorithm:

inches distance along "x" or "y" axis  
= scale factor (inches/unit) x [(current  
value of  $\log F$  or  $\tan \delta$ ) - (minimum or  
"origin" value of  $\log F$  or  $\tan \delta$ )].

Print a triangle centered on this location for the first curve on these axes, a square for the second, and a diamond for the third. Note that we have calculated  $\log_{10} f$  while establishing the axis distance.

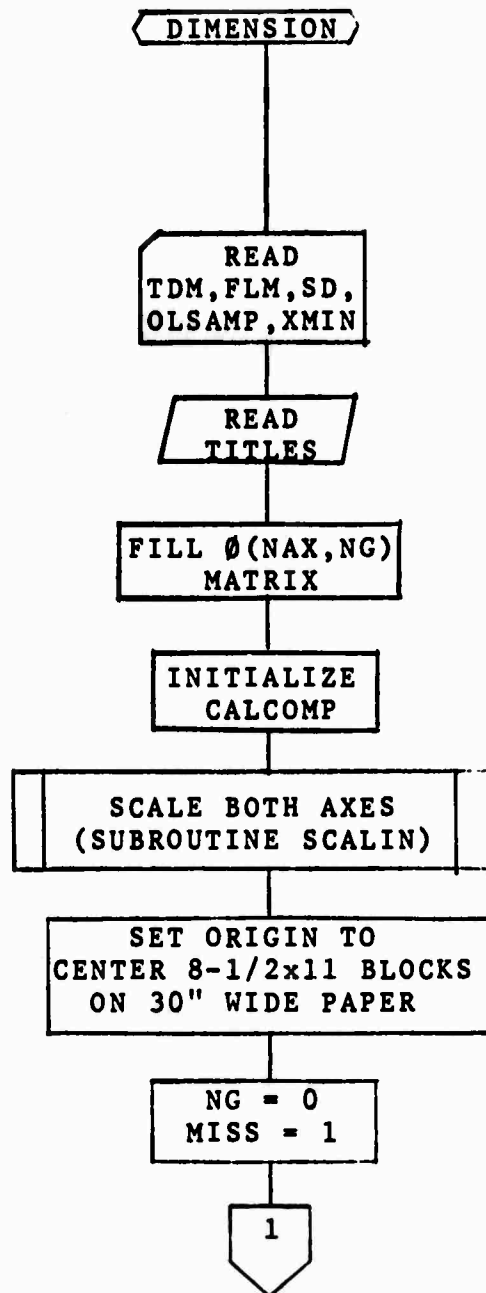
Read another frequency- $\tan \delta$  card, and print points until the signal to change cases ( $F = 0$ ) is encountered. Then read a  $SAMPN\emptyset$  card, and draw the curve for the second (and third if necessary) case.

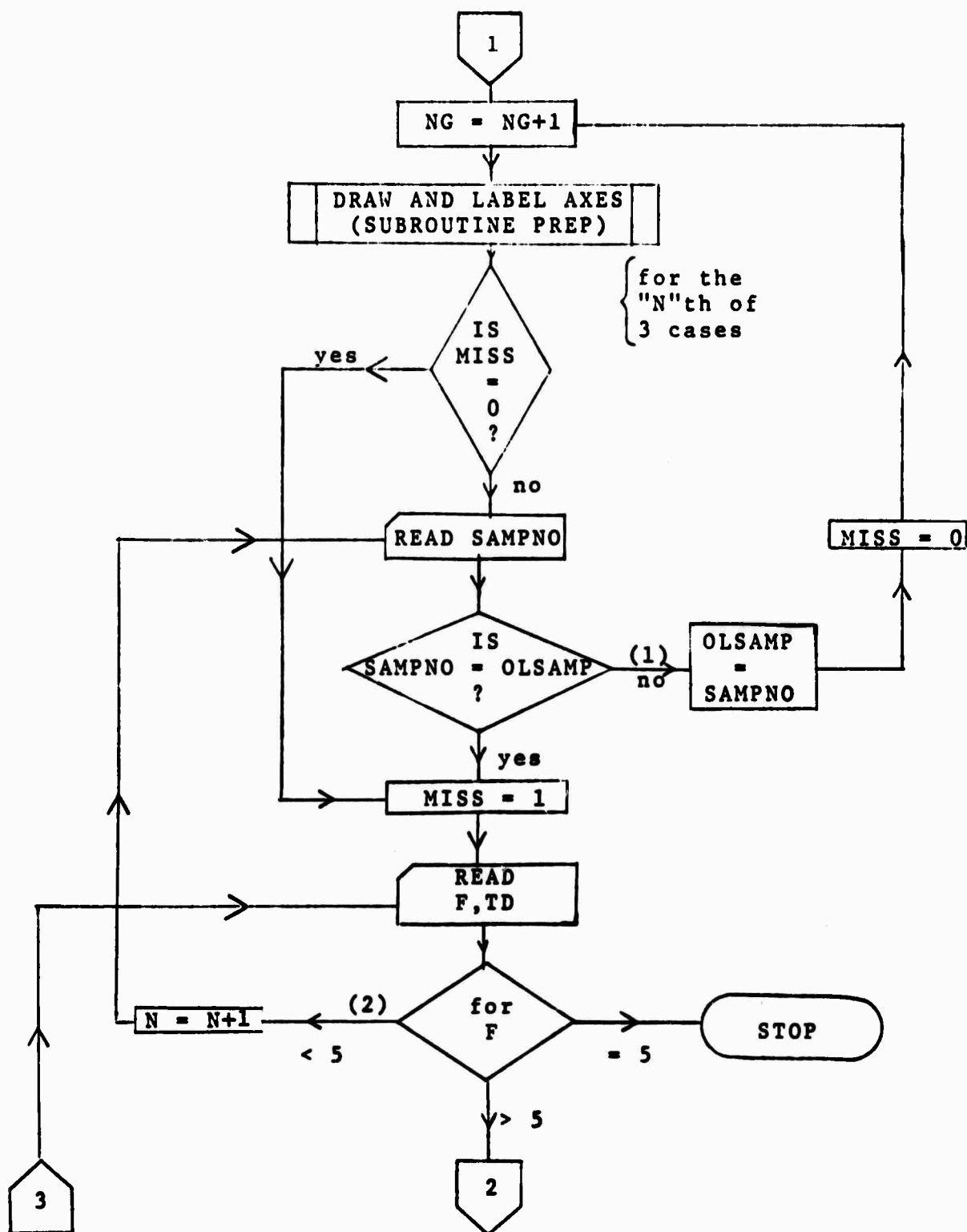
Should the sample number change, change the value of  $\emptyset LSAMP$  to this new present  $SAMPN\emptyset$  value. Set  $MISS = 0$  (lest the program seek another sample card) and return to draw another set of labeled axes. After drawing the axes, reset  $MISS = 1$ , read the F, TD pair and put the points on the new graph.

Carry on making three curves per graph, changing for each sample, until the  $F = 5$  card is read, signaling the end of the plotting.



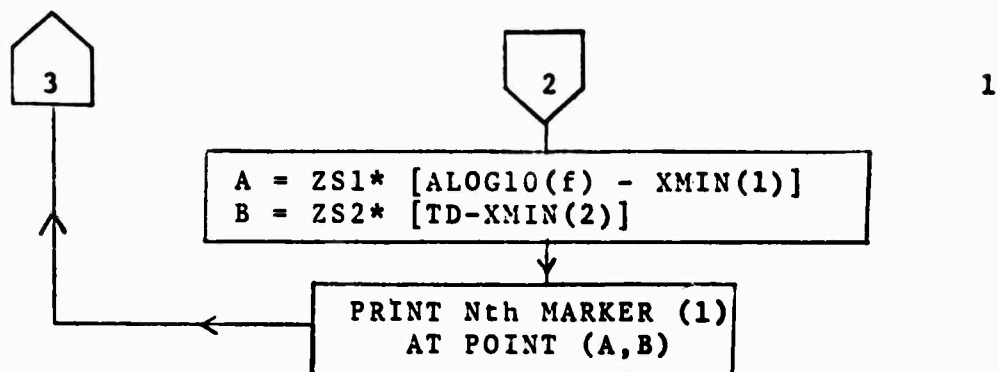
TDDRAW





(1) Therefore, the data following is for a new sample and a new graph must be started.

(2) I.e., equal to 1, marking the end of a case.



(1) Marker "1" is a triangle, "2" a square and "3" a diamond.

#### Data Deck

Card Type	Format	Columns	Variable Code Name	Remarks
1	7F10.0	1-10	TDM	Punch decimal point in the correct place, or right-justify.
		11-20	FLM	
		21-30	XSD	
		31-40	YSD	
		41-50	ØLSAMP	
		51-60	XMIN(1)	When no data below 100 Hz is taken, XMIN(1,1) = 1.75.
		61-70	XMIN(2)	

2 and 3, The output deck from TDPUNCH, without additions or alterations.

## **8. Subroutines**

### **A. SCALIN**

- 1) Purpose: to calculate values of parameters which give an orderly scaling to an axis. SCALIN is called once per axis: i.e., twice per run.
- 2) Input: from the point of view of MAIN--
  - a) the maximum value occurring on the axis in question
  - b) the tic-Scale-Division, in fractional multiples of unit variable
  - c) the axis number ( $x = 1$ ,  $y = 2$ )
  - d) the minimum value occurring on the axis in question.

These are, respectively, the first, second, third and fourth, then last of the arguments in the argument list.

- 3) Output (per MAIN):
  - a) revised values of the minimum and maximum values, so that they equal integral multiples of the tic-Scale-Division
  - b) the tic spacing, in inches
  - c) the scale factor, in (inches/unit variable).

These are the first, and fourth and fifth arguments in that list. The sixth argument is a two-dimensional array, storing the minimum tic value on the axis in a form for simple use by the axis-preparing and point-drawing routines. The tic spacing and scale factor are in terms of the interval over which the variable is actually plotted.

- 4) Symbols, as used by SCALIN:
  - X: a minimum value on the axis
  - SDE: a tic-Scale-Division-array-element
  - N: axis number; 1 for abscissas (log P),  
2 for ordinates (tex  $\delta$ )
  - SE: tic-spacing-array-element
  - ZSE: scale factor array element
  - Y: minimum value on the axis.

5) Operation: Calculate the number of tics required to bound the maximum coordinate value by one tic division and the number to reach to the first integral tic division less than the minimum coordinate value. Calculate the coordinate values at these numbers-of-tics.

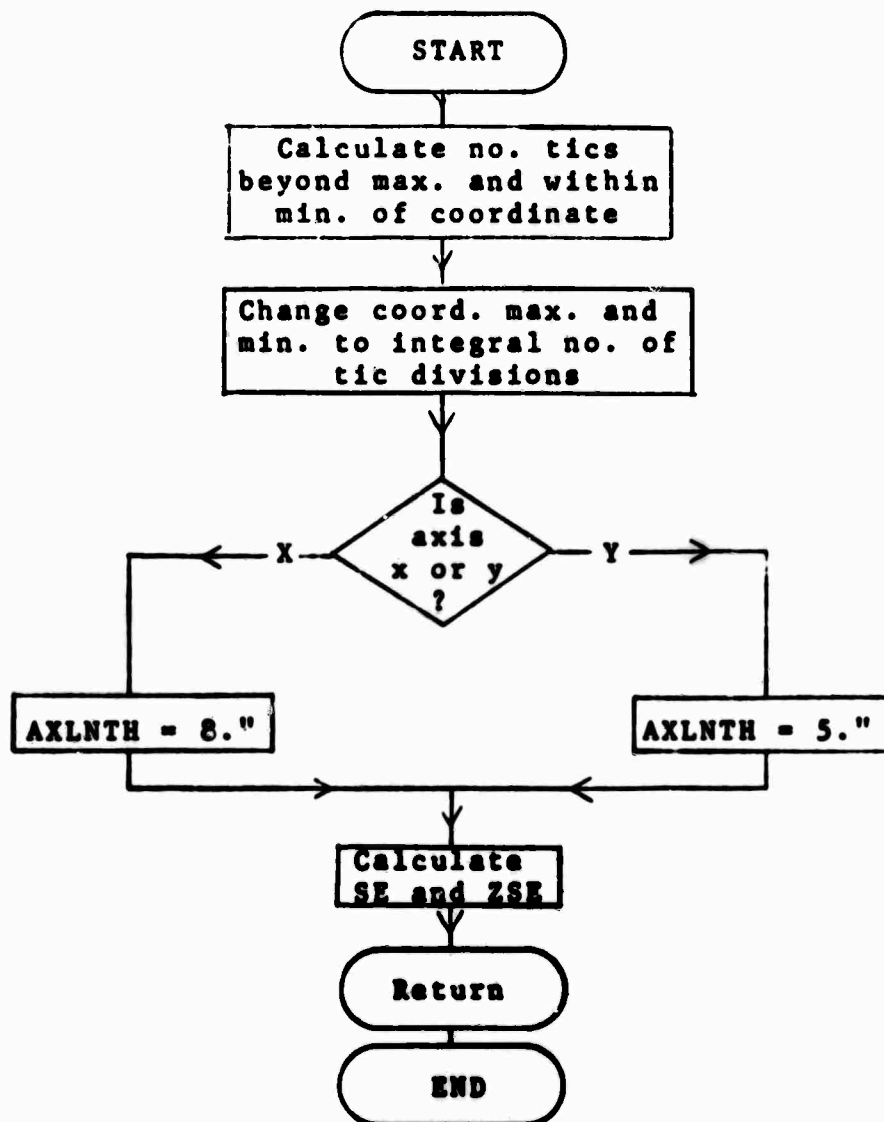
Set the axis length for log F at 8.0", or for tan  $\delta$  = 5.0". Calculate the tic spacing and scale factor per:

$$SE = \frac{\text{axis length (inches)}}{\text{axis range/tic-division}}$$

and  $ZSE = \frac{\text{axis length (inches)}}{\text{axis range}}$

Both axis range and tic-division have dimensions of coordinate units.

6) Flowchart: Subroutine SCALIN



**B. PREP**

1) Purpose: to cause Calcomp drawing of a set of ticked and labeled axes.

2) Input:

NG: graph number to be drawn by this call of PREP

Ø: location of origins on the paper, with respect to the last

NLT: Number of Letters in the Titles for the axes

TITLE: the array containing those alphabetic characters which spell out the title specific to the axis and graph type

S, SD, XMIN: as for SCALIN

NFIRST: the tic number at which the first numeric label will be written.

3) Output: the ticked and labeled axes

4) Symbols not already named

R: the axis length

A: the axis angle from the conventional zero

XST, YST: coordinates of the lower left hand corner of the axis labels' titles

AL: angle at which the titles are to be drawn

AXIS2: the Calcomp routine which draws axes of the length, and at the angle desired. Tic marks 0.1" long are placed at the interval designated ("g")

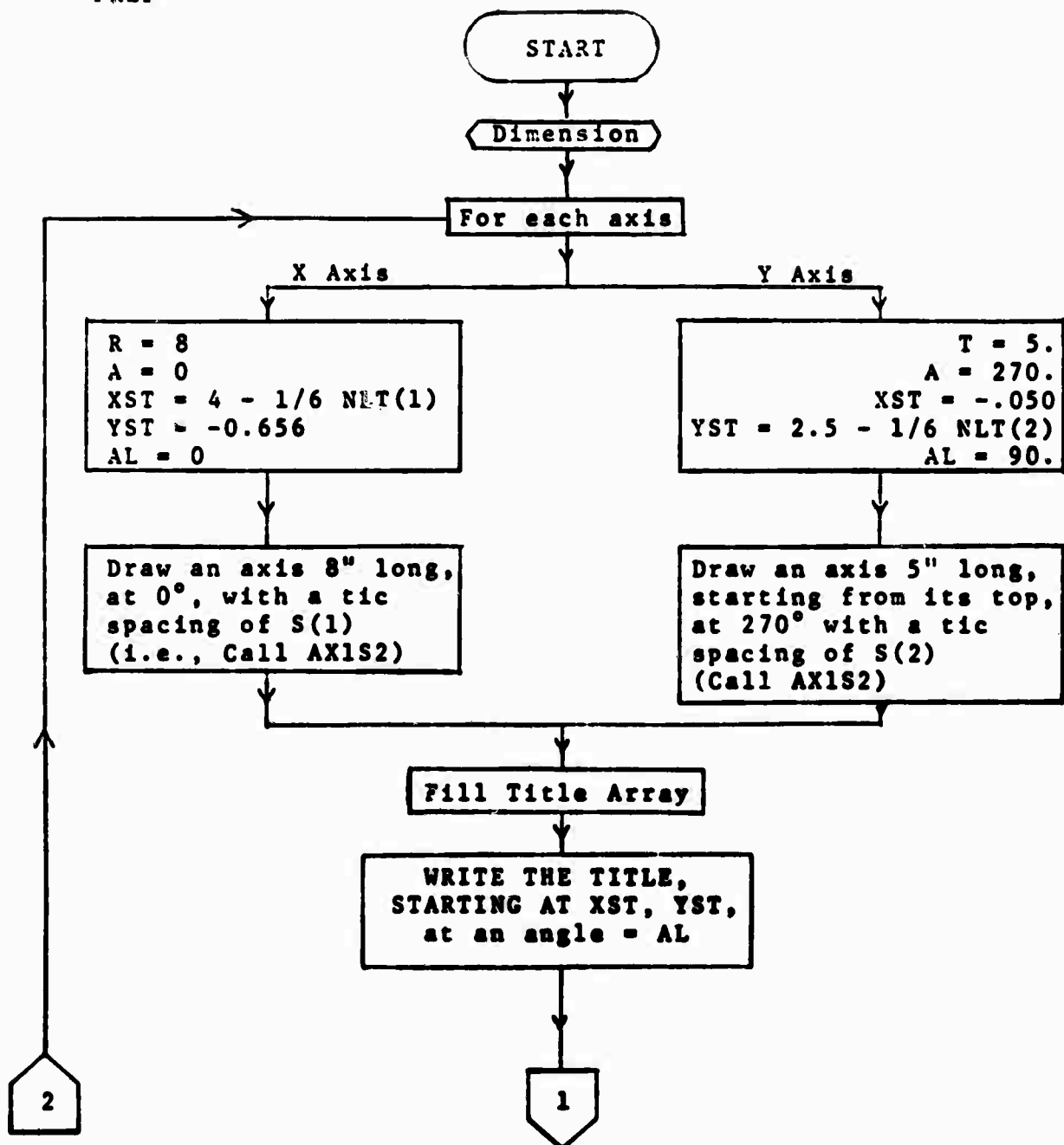
TL: one-dimensional array containing the titles, per requirements of the title drawing routine

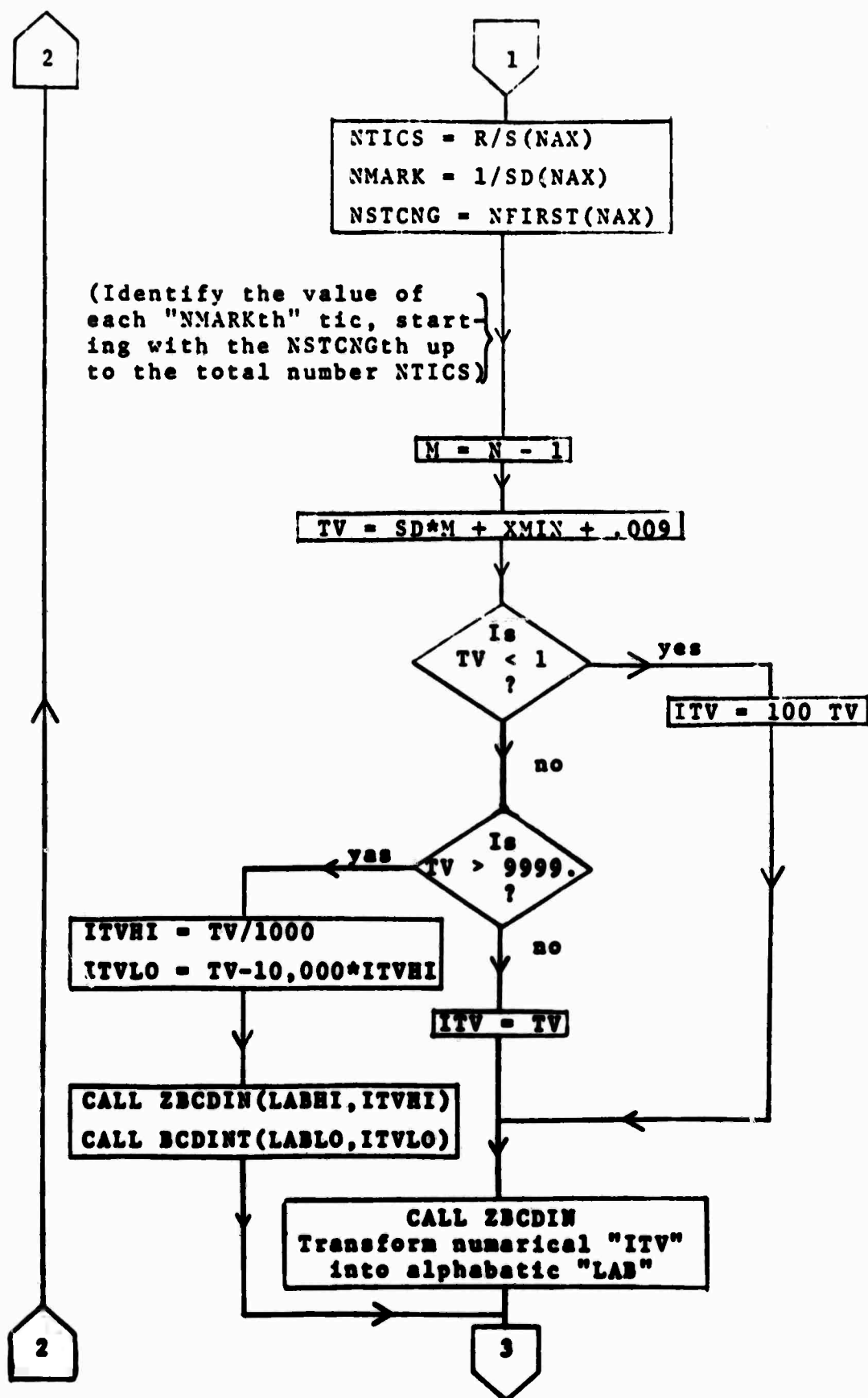
**CPRINT:** the Calcomp routine which draws characters at the location and angle, and of the height desired  
**NTICS:** the number of tics to be placed on the axis  
**NMARK:** every "NMARKth" tic is labeled with its value  
**NSTCNG:** scalar form of NFIRST, telling the Calcomp "the tic Number at which it should Start Tic labeling  
**TV:** the "tic value," in decimal form  
**ITV:** the integer tic value, required as input to. . .  
**ZBCDIN:** a Calcomp routine in which an integer number is converted to a block of four alphabetic characters, with leading zeros suppressed  
**ITVHI:** that part of an integer tic value greater than 10,000  
**ITVL0:** as above, except less than 10,000  
**NC:** the number of characters in a tic value's label  
**CTR:** the displacement of the four space block of ZBCDIN output required to "center" the tic value on the tic  
**Xl, Yl:** the location of the lower left-hand corner of the tic label block  
**XHI, XL0:** the above location for the large and small blocks of tic values 10,000.

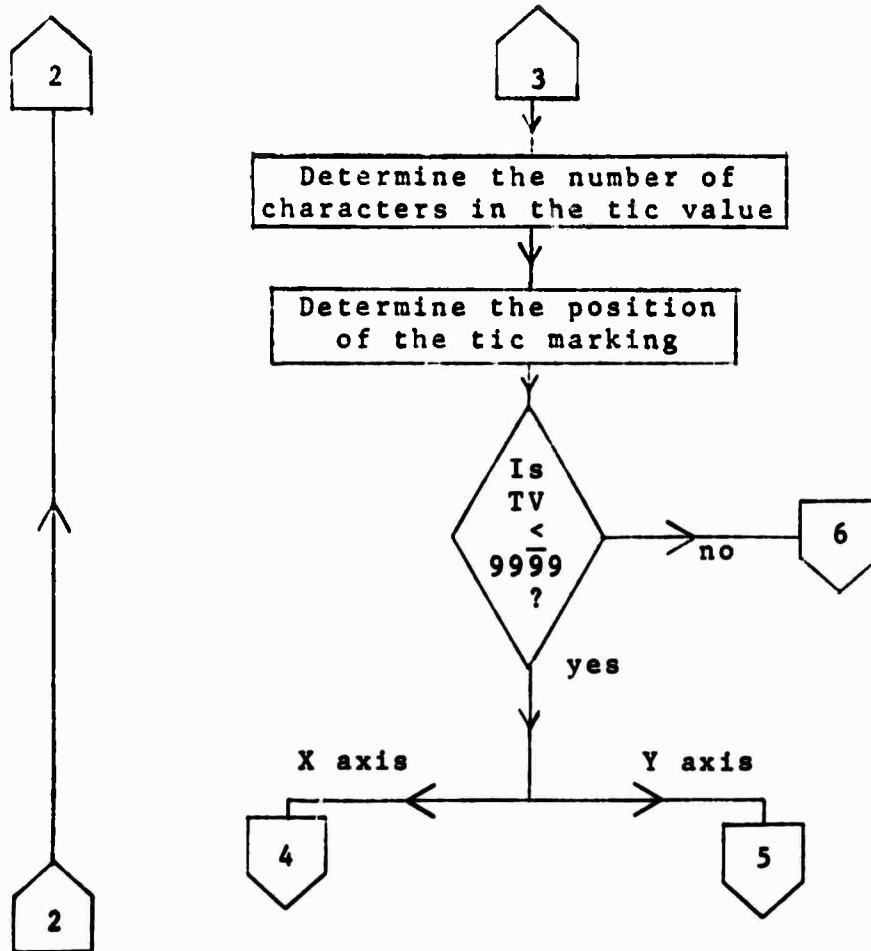
5) Operation (per axis): First, the arguments for the axis drawing and ticking are defined and/or calculated, then drawn per AXIS 2. The title array is then filled, and the title written by "CPRINT." The tic labeling parameters are determined, and tic labels calculated for conversion to alphabetic symbols by ZBCDIN. Tic label locations are calculated, then appropriate tics are labeled. The labels are centered at the tic. Labels of up to 8 characters in length can be handled.

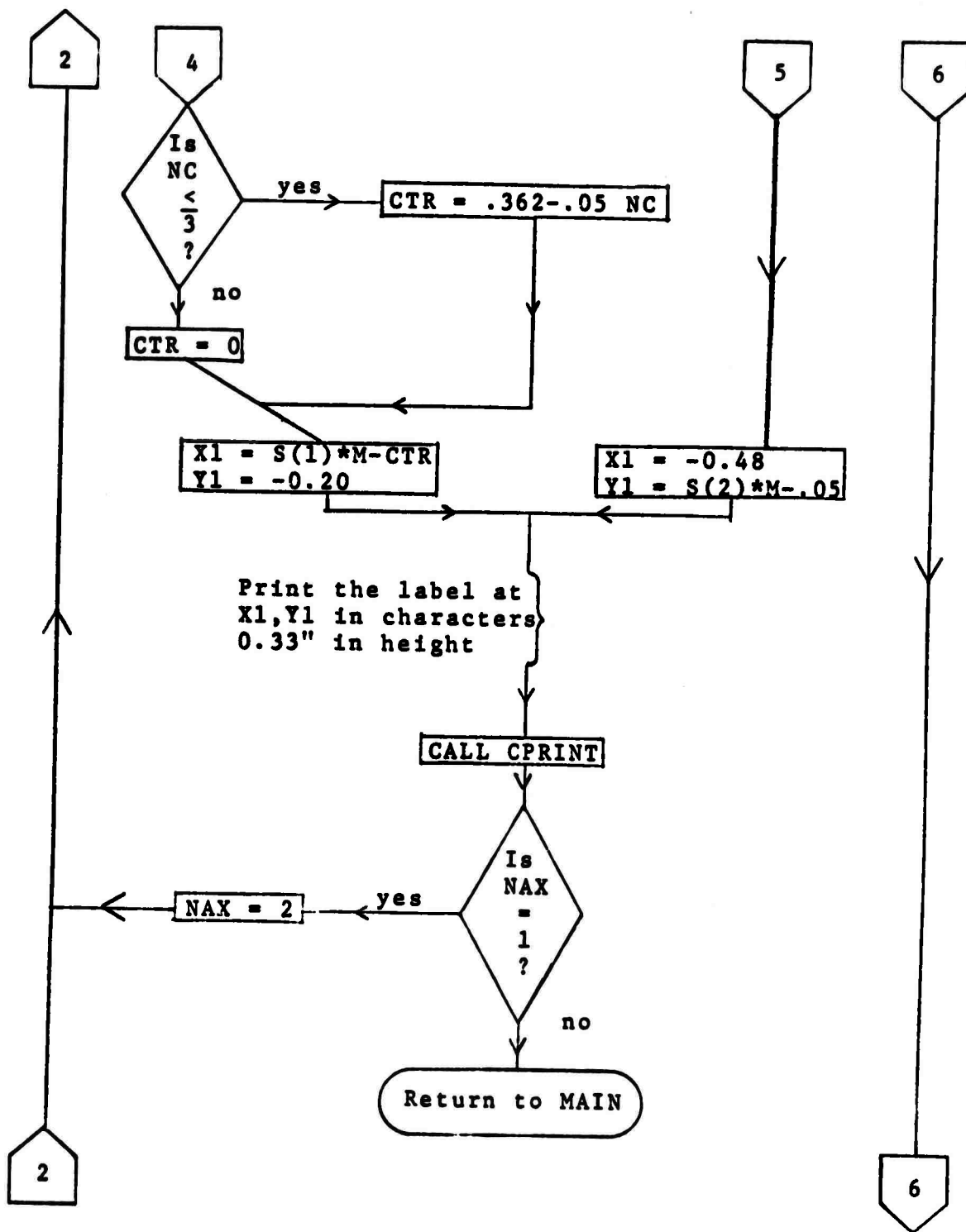


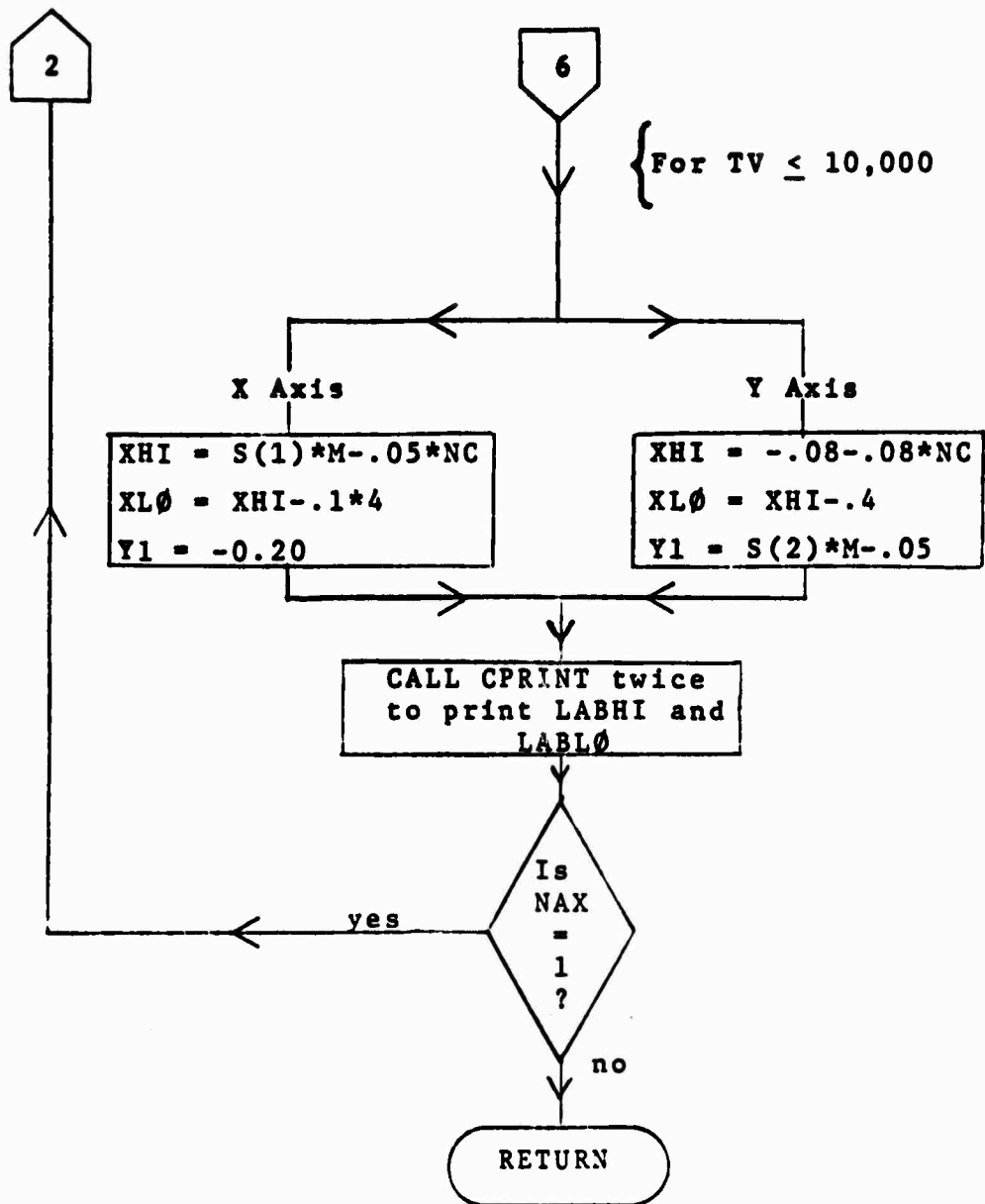
PREP











TDPUNCH REFINES INSTRUMENTAL DATA FOR USE BY A CALCOMP GRAPH DRAWING ROUTINE. THE HEART OF THE EFFORT IS CALCULATING TAN DELTA VALUES FOR ALL TESTS, AND PUNCHING A NEW DATA DECK FOR THE DRAWING PROGRAM.

TO USE TDPUNCH--

KEYPUNCH A 'CASE' CARD AND THE 'FREQUENCY' CARDS FOR EACH CASE, WHICH USUALLY REFERS TO ONE RELATIVE HUMIDITY. NOTE THAT THE TDDRAW PROGRAM ALLOWS USING UP TO EIGHT DIGITS IN THE SAMPLE NUMBER, FOR VERSATILE CATALOGUING OF DIFFERRING EXPERIMENTAL CONDITIONS, NOT NECESSARILY LIMITED TO RELATIVE HUMIDITY VALUES.

THE OUTPUT OF TDPUNCH IS--

- 1) A PRINTED LISTING, WITH HEADINGS, OF THE DATA AND CALCULATED INFORMATION, AND
- 2) A DECK OF MACHINE-PUNCHED CARDS WITH THE SAME INFORMATION.

2) A DECK OF MACHINE-PUNCHED CARDS WITH THE SAME INFORMATION.

```

C      READ THE CASE HEADING CARD
C
1 READ(5,2)T,D,P,PO,W,WO,TEMP,SAMPLE
2 FORMAT(8F10.5)
  RH=100.*P/PO
C
C      PRINT, AND THEN...
C
  WRITE(6, 3)T,D,P,PO,W,WO,TEMP,SAMPLE,RH
3 FORMAT(' THICKNESS      DIAM      PP H2O      SAT P H2O'22X,'TE'
'S'MP, C  SAMPLE      REL HUM, '//8F10.5,F10.3,/'      FREQ,HERT'
2'Z      G, MUMHOS      C,PICOFARADS      TAN '
3DELTA'//)
C
C      ...PUNCH EACH CASES'S HEADING.
C
  WRITE(7,2)T,D,P,PO,W,WO,TEMP,SAMPLE
C
C      READ A 'FREQUENCY' CARD.
C
4 READ(5,5)F,G,C
5 FORMAT(3F20.10)
  IF(C)6,10,6
C
C      CALCULATE TAN DELTA.
C
6 TD=1.E6*G/6.28318/(F*C)

```

```

C
C      PRINT AND PUNCH THE TAN DELTA WITH THE DATA.
C
      WRITE(6, 7)F,G,C,TD
7  FORMAT(4F20.10/)
      WRITE(7,8)F,G,C,TD
8  FORMAT(4F20.10)

C
C      TEST TO DETERMINE THE SIGNALLING EFFECT OF THE
C      FREQUENCY VALUE JUST READ. ALL THE SUBSEQUENT COMMENTS
C      REFER TO THIS TEST'S RESULT.
C
10 IF(F-5.)11,15,13

C
C      IF F IS LESS THAN 5, START A NEW PAGE FOR THE NEXT
C      CASE.
C
11 WRITE (6,12)
12 FORMAT(1H1,////)

C
C      IF F IS GREATER THAN 5, CARRY ON READING 'FREQUENCY' C
C      CARDS. C
C
C      IF F IS LESS THAN OR EQUAL TO 1, THE CASE HAS ENDED.
C      PUNCH THIS CARD, AND RETURN TO READ A NEW CASE CARD.
C
13 IF(F-1.) 14,14,4
14 TD=0.
      WRITE(7,8) F,G,C,TD
      GO TO 1

C
C      IF F = 5, THIS IS THE LAST CARD FOR THIS RUN. PUNCH
C      THIS CARD AND END EXECUTION.
C
15 TD=0.
      WRITE(7,8) F,G,C,TD
      STOP
      END

```

TCDRAW IS A PROGRAM TO DRAW GRAPHS OF TAN DELTA VS.  
LOG FREQUENCY WITH THE CALCOMP MODEL 563 PLOTTER.

GENERAL NOTES--

TCDRAW PLOTS THREE CURVES, NORMALLY FOR DIFFERENT  
RELATIVE HUMIDITIES, PER GRAPH. OTHER DISTINC-  
TIONS, SUCH AS WHETHER A CASE IS IN THE ADSORPTIVE  
OR DESORPTIVE MODE, CAN BE MADE BY SUITABLE DESIGN  
OF THE SAMPLE NUMBERS WHILE CONSTRUCTING THE INPLT  
TO THE TDPUNCH PROGRAM.

THERE IS NO LIMIT TO THE NUMBER OF BASES FOR DRAW-  
ING OR CHANGING GRAPHS. HOWEVER, ONLY 51 GRAPHS  
MAY BE DRAWN.

SCALING THE AXES IS DONE ONCE FOR THE ENTIRE RUN,  
SO THAT SOME GRAPHS, OR EVEN ENTIRE SECTIONS OF THE  
RUN, MAY USE ONLY A SMALL FRACTION OF THE TAN DELTA  
AXIS. WIDE EXTENTS OF HIGHEST-TAN-DELTA-GROUPS, SAY  
BY MORE THAN A FACTOR OF TEN, ARE BEST RUN INTO THE  
COMPUTER IN SEPARATE GROUPS OF LARGE AND SMALL  
MAXIMUM-TAN-DELTA.

RESTRICTIONS--

THE MINIMUM FREQUENCY AT WHICH DATA IS TAKEN MUST  
BE 100 HERTZ.  
SAMPLE NUMBERS MUST BE IN ASCENDING ORDER, NO MORE  
THAN FOUR DIGITS BEYOND THE DECIMAL POINT.  
THE TIC DIVISIONS PARAMETER ('SD') MUST BE LESS THAN  
UNITY.  
NO MORE THAN 51 GRAPHS PER RUN.

TO USE TCDRAW--

MANUALLY PUNCH TWO CARDS, CONTAINING--

1) THE VALUE OF THE LARGEST LOG-TO-THE-BASE-10  
OF FREQUENCY APPLIED TO THE SAMPLE(S), IN THE ENTIRE  
TDPUNCH PRINTOUT, IN COLUMNS 1-10. (THIS VALUE IS  
NORMALLY 6.0).

THE SIMILAR VALUE OF TAN DELTA, IN COLUMNS 11-20.  
0.25 IN COLUMNS 21-24.

0.9999 IF THE MAXIMUM VALUE OF TAN DELTA IS 20.0  
OR GREATER, 0.50 IF THE MAXIMUM TAN DELTA IS 5 OR  
GREATER, 0.25 IF BETWEEN 2.0 AND 5.0 OR 0.10 IF LESS  
THAN 2.0, IN COLUMNS 31-40.

THE SAMPLE NUMBER OF THE FIRST SAMPLE IN COLUMNS  
41-50.

2.0 IN COLUMNS 51-59.

THE SMALLEST VALUE OF TAN DELTA IN THE TDPUNCH  
PRINTOUT, COLUMNS 61-70.





```

C
C      CALCULATE THE AXES' SCALING PARAMETERS, AND
C      PRINT THEM OUT.
C
      CC 4 NAX=1,2
4 CALL SCALIN(XMAX(NAX),SC(NAX),NAX,S(NAX),ZS(NAX),XMIN(NAX))
  WRITE(6,5) XMAX,XMIN,SC,S,ZS
5 FCRPAT(' XMAX==) '2F8.2,' XMIN ==) '2F8.2,' SD ==) '2F9.2
  S/' S==) '2F6.2,' ZS ==) '2F8.2)
  MISS=1

C
C      DRAW TICKED AND LABELED AXES AT THE NEXT ORIGIN LOCA-
C      TION IN SEQUENCE.
C
6 NG=NG+1
  CALL PREPING(O,ALT,TITLE,S,XMIN,NFIRST,SC)
  WRITE(6,7) NG,OLSAMP
7 FCRPAT(/' GRAPH '12,' REFERS TO SAMPLE 'F7.3)

C
C      DRAW THREE CURVES PER GRAPH...
C
      CC 17 N=1,3
      IF(MISS) 8,11,8
8 READ(5,9) SAMPNC
9 FCRPAT(70X,F10.5)

C
C      ...BUT CHANGE GRAPHS TO PLOT A NEW SAMPLE'S DATA.
C
      IF(SAMPNC-CLSAMP-1.E-4) 11,11,10
10 CLSAMP=SAMPNC
  MISS=0
  GC TO 6
11 MISS=1
12 READ(5,13)F,TD
13 FCRPAT(F20.10, 40X,F20.10)

C
C      CHECK TO SEE IF THE CARD JUST READ SIGNALS THE END OF
C      A CASE(F.LT.5), OR THE END OF THIS RUN'S DATA (F=5).
C
      IF(F=5.) 17,19,14

C
C      DETERMINE THE COORDINATES (A,B) OF EACH POINT.
C
14 A=ZS(1)*(ALCG10(F)-XMIN(1))
  B=ZS(2)*(TD-XMIN(2))

```

```

C
C      INDICATE EACH POINT BY DRAWING A TRIANGLE FOR THE
C      FIRST CURVE, A SQUARE FOR THE SECOND, AND A DIAMOND
C      FOR THE THIRD, ALL CENTERED ABOUT (A,B).
C
      IF(N-3) 15,16,16
15 CALL TPRINT(N,A,B,C.1)
   GC TC 12
16 CALL TPRINT(6,A,B,C.2)
   GC TC 12
17 WRITE(6,18) N,A,B
18 FORMAT(' CURVE NO. '11,') 'S LAST POINT IS AT ( 'F4.2,', 'F5.
   $2,') INCHES.')
   GC TC 6
C
C      COMPLETE THE GRAPH AND END EXECUTION.
C
19 CALL PLTEND
   STCF 1
   END

```

```

SUBROUTINE SCALIN(X,SCE,N,SE,ZSE,Y)
CCCCCCCCCCCCCCCCCCCCCCCCCCCCCCCCCCCCCCCCCCCCCCCCCCCCCCCCCCCC
C
C
C      SCALIN CALCULATES THE TIC SPACING AND SCALE FACTOR
C      FOR BOTH AXES, ONCE PER RUN.
C
C      CN ENTRY--
C          X IS THE MAXIMUM DATA VALUE ON THE PRESENT AXIS
C          AS READ BY MAIN.
C          SCE IS THE TIC-DIVISION VALUE, AS READ BY THE
C          MAIN.
C          N IS THE NUMBER OF THE AXIS OF CALCULATION--1
C          FOR THE LOG FREQUENCY AXIS, 2 FOR THE TAN DELTA AXIS.
C          SE AND ZSE ARE CUMPIES.
C          Y IS THE LEAST DATA VALUE ON THE PRESENT AXIS.
C
C      CN RETURN--
C          X AND Y HAVE BEEN CHANGED TO THE INTEGER
C          MULTIPLES OF SCE ONE HIGHER AND ONE LOWER THAN THE
C          DATA VALUES.
C          SCE AND N ARE UNCHANGED IN VALUE.
C          SE AND ZSE ARE THE VALUES OF TIC SPACING AND
C          SCALE FACTOR CALCULATED IN LINES 23 AND 24.
C
CCCCCCCCCCCCCCCCCCCCCCCCCCCCCCCCCCCCCCCCCCCCCCCCCCCCCCCCCCCC
C
C      ROUND THE MAXIMUM AND MINIMUM VALUES ON EACH AXIS,
C      DETERMINED BY VISUAL INSPECTION OF THE PRINTED
C      OUTPUT FROM THE TDPUNCH PROGRAM.
C
C      NTX=IFIX(1+(X/SCE))
C      NTY=IFIX(Y/SCE+.001)
C      X=SCE*FLOAT(NTX)
C      Y=SCE*FLOAT(NTY)
C
C      DESIGNATE THE AXIS LENGTH, IN INCHES.
C
C      IF(N-1) 1,1,2
C      1 AXLNTH=8.
C      GO TO 3
C      2 AXLNTH=5.
C
C      'SE' IS THE TIC SPACING , IN INCHES. 'ZSE' IS THE
C      SCALE FACTOR, IN INCHES PER UNIT TAN DELTA OR LOG
C      FREQUENCY.
C
C      3 SE=AXLNTH*SCE/(X-Y)
C      ZSE=AXLNTH/(X-Y)
C      RETURN
C      ENC

```

```

SUBROUTINE PREP(NG, NLT, TITLE, S, XMIN, NFIRST, S
CCCCCCCCCCCCCCCCCCCCCCCCCCCCCCCCCCCCCCCCCCCCCCCCCCCCCCCCCCCC
C
C      FREF CRAWLS, TICS AND LABELS EACH AXIS IN TURN, ONCE
C      PER GRAPH NUMBER.
C
C      CN ENTRY--
C      NG IS THE ORDINAL OF THE CURRENT GRAPH.
C
C      THE FOLLOWING ARE THE NAMES OF ARRAYS CONTAINING
C      THE VALUES OF--
C      C--ORIGIN LOCATIONS, WITH RESPECT TO THE IMME-
C      DIATELY PRECEDING ONE.
C      NLT--NUMBER OF LETTERS IN THE AXIS TITLE
C      TITLE--THE ALPHABETIC INFORMATION CONSTITUTING
C      THE AXIS NAME.
C      S--TIC SPACINGS ON EACH AXIS.
C      XMIN--LOWER BOUNDS OF EACH AXIS.
C      NFIRST--THE NUMBER OF THE TIC AT WHICH LABEL-
C      LING IS TO START, FOR EACH AXIS.
C      SC--THE FRACTIONAL NUMBER OF UNITS EACH TIC DE-
C      NOTES.
C
C      ON RETURN--
C      NO VARIABLE MEANINGS OR ARRAY LOCATIONS OR VALUES
C      HAVE BEEN CHANGED.
C
CCCCCCCCCCCCCCCCCCCCCCCCCCCCCCCCCCCCCCCCCCCCCCCCCCCCCCCCCCCC
      INTEGER TITLE, TL
      DIMENSION O(2,51), NLT(2), TITLE(2,4), S(2), TL(16), XMIN(2),
      NFIRST(2), SC(2)
C
C      CHANGE ORIGIN LOCATIONS, SUCH THAT THE SUBSEQUENT
C      POSITION IS REFERRED TO THIS PRESENT ORIGIN.
C
      CALL PLOT(O(1,NG), C(2,NG), -3)
C
C      THEN, ON EACH AXIS, SET UP TO...
C
      DO 24 NAX=1,2
      IF(NAX-1) 1,1,2
1  R=6.
      A=0.
      XST=4.-(FLOAT(NLT(NAX))/6.)
      YST=-0.656
      AL=C.
C
C      DRAW THE X-AXIS, WITH TICS...

```

```

      CALL AXIS2(C.,0.,R,A,S(NAX))
      GO TO 3
2  R=5.
   A=270.
   XST=-0.5C
   YST=2.5-(FLOAT(NLT(NAX))/6.)
   AL=+9C.

```

```

C
C      ...CR THE Y-AXIS
C

```

```

      CALL AXIS2(0.,5.,R,A,S(NAX))
3  NL=NLT(NAX)
   NL4=1+NL/4
   DO 4 N=1,NL4
4  TL(N)=TITLE(NAX,N)

```

```

C
C      PRINT THE AXIS VARIABLE'S NAME.
C

```

```

      CALL CPRINT(TL,NL,XST,YST,.328,AL)
5  NTICS=IFIX(R/S(NAX))+1
   NMARK=IFIX(1./SC(NAX))
   IF(SC(NAX).GE.1.) NMARK=4
   NSTONG=NFIRST(NAX)

```

```

C
C      ...AND AT EACH APPROPRIATE TIC...
C

```

```

      DC 24 N=NSTONG,NTICS,NMARK
      M=N-1

```

```

C
C      ...DETERMINE THE TIC VALUE...
C

```

```

      TV=SC(NAX)*FLOAT(M)+XMIN(NAX)+C.COS
      IF(TV-1.) 6,7,7
6  ITV=IFIX(TV*100.)
   GO TO 9
7  IF(TV-5559.) 8,E,1C
8  ITV=IFIX(TV)

```

```

C
C      CONVERT THE NUMERIC INFORMATION 'ITV' TO ALPHABETIC
C      'LAB', FOR USE AS TIC LABELS.
C

```

```

9  CALL ZBCDIN(LAB,ITV)
   GO TO 11
10 ITVHI=IFIX(TV/1.E4)
   ITVLC=IFIX(TV-1.E4*FLOAT(ITVHI))
   CALL ZBCDIN(LABHI,ITVHI)
   CALL BCCINT(LABLC,ITVLC)

```

```

C
C      DETERMINE THE LOCATION OF THE TIC LABEL, ACCORDING
C      TO ITS VALUE, AXIS, AND NUMBER OF CHARACTERS...
C

```

```

11 NC=1+(I)/(ABS(ALOCIC(TV)))
12 IF(I10-9999) 13,13,20
13 IF(NAX-1) 14,14,18
14 IF(NC-3) 15,15,16
15 CTR=.362-.05*FLOAT(NC)
   GC TO 17
16 CTR=0.
17 X1=S(NAX)*FLCAT(M)-CTR
   Y1=-0.2C
   GC TC 19
18 X1=-0.46
   Y1=S(NAX)*FLCAT(M)-.05
C
C       PRINT SHORT TIC LABELS (FOUR OR LESS CHARACTERS)...
C
19 CALL CPRINT(LAB,4,X1,Y1,0.1C,0.)
   GC TC 24
20 IF(NAX-1) 21,21,22
21 XH1=S(NAX)*FLOAT(M)-.05*FLCAT(NC)
   XLC=XH1+C.1*4.
   Y1=-0.2C
   GC TO 23
22 XH1=-.08-.1C*FLCAT(NC)
   XLC=XH1+C.4
   Y1=S(NAX)*FLOAT(M)
C
C       CR LONG CNES (FIVE TO EIGHT CHARACTERS).
C
23 CALL CPRINT(LABHI,4,XH1,Y1,C.1C,C.)
   CALL CPRINT(LABLC,4,XLC,Y1,C.1C,C.)
24 CONTINUE
   RETURN
   END

```

#### IV. Discussion

The research of this seventh semiannual period has yielded results of technical significance that bear on problems of interest to the Department of Defense.

The noise research reported here describes an extensive analytical and experimental study of the noise performance of phototransistors -- devices that potentially find wide application in military detection systems. We have demonstrated that the most important fluctuations may be represented by simple additions to the conventional noise model used to describe junction transistors. Moreover, this study has shown that from measurement of the noise spectra one can infer the current gains and Beta cut-off frequencies, which are critical parameters needed in characterizing the phototransistor.

Materials research described in earlier reports in this sequence is applied here to study the feasibility of the design of a fast solid-state light detector using the photomagnetolectric in gold-doped silicon. This study, together with those describing fundamental electronic parameters in In-doped and Cu-doped CdS and of the photomagnetolectric and photoconductive effects in Au-doped Si at room temperature, all bear on the design of new types of detectors that potentially may be of interest in many military applications.

The method described in this report that provides for the automatic selection of transistor model complexity relates directly to the design of complex circuits of types useful in many military applications. It provides a first approach for avoiding the use of extraordinarily complex models to ensure accuracy. In the absence of this method the analyst needed to use complex models to describe each transistor in a circuit with the attendant disadvantages: increased cpu time and, most important in many applications, a severe limitation on the size of circuit that can be analyzed. We intend that extensions of this research will focus on the problem of designing large circuits for operation in severe environments.

The unique range of properties exhibited by insulating glass-ceramics and amorphous semiconductors makes them potentially useful in a variety of applications that may involve exposure to nuclear irradiation. From the study reported here of the fast neutron effects in glass-ceramics and amorphous semiconductors has come data important in assessing the potentiality of these materials.